DTU Physics
Department of Physics

Non-equilibrium phenomena in nanostructured and low-dimensional correlated systems

Ph.D. thesis by Nicklas Walldorf

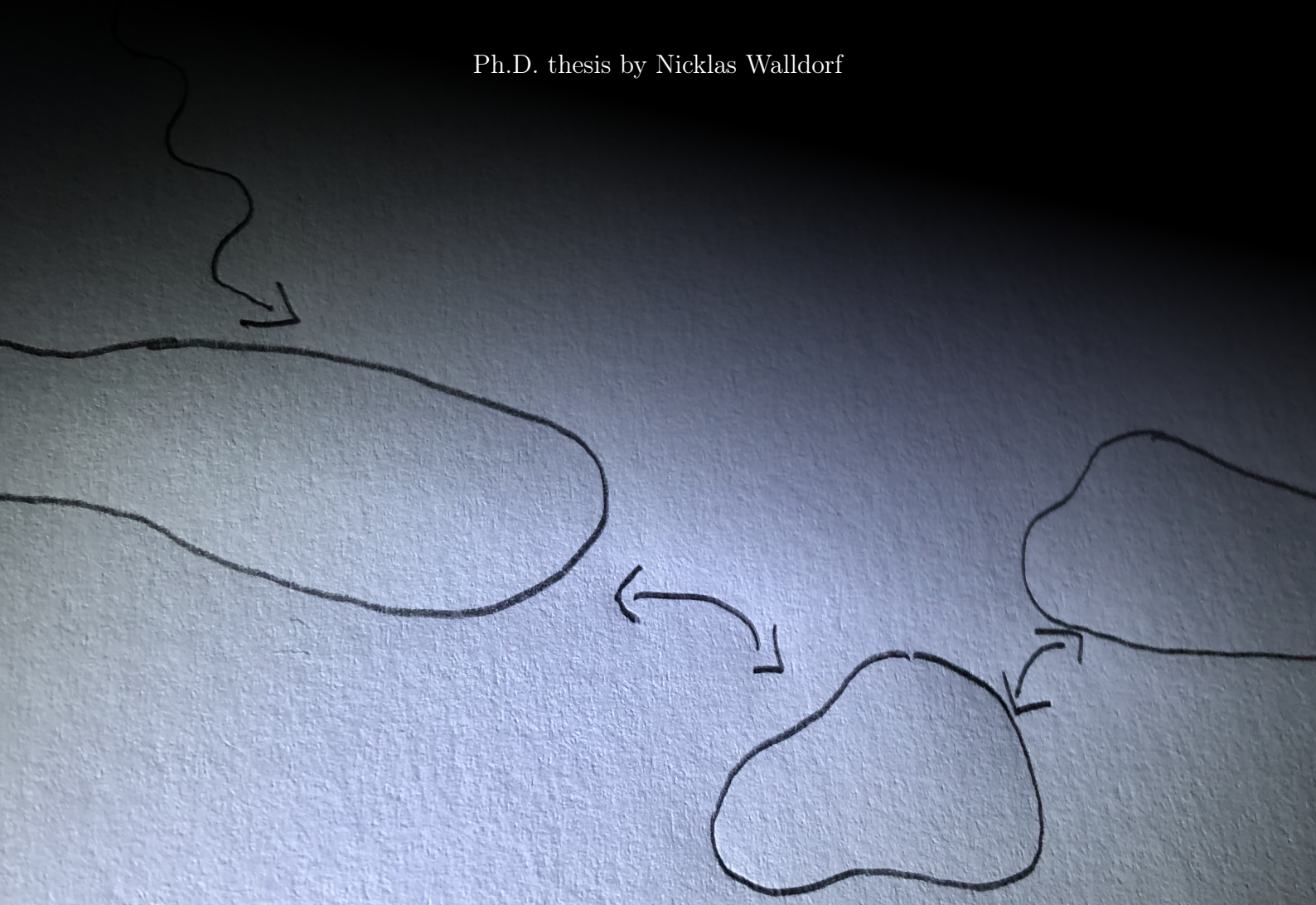

$$\langle \hat{O} \rangle(t) = \mathrm{Tr}[\hat{O}\hat{\rho}(t)]$$

$$\frac{d}{dt}\hat{\rho}(t) = -\frac{i}{\hbar}[\hat{H}(t), \hat{\rho}(t)]$$

August 28, 2020

Non-equilibrium phenomena in nanostructured and low-dimensional correlated systems

August 28, 2020

By Nicklas Walldorf

Principal supervisor:	Professor Antti-Pekka Jauho (DTU)
Co-supervisor:	Associate Professor Jens Paaske (University of Copenhagen)

Published by:	DTU, Department of Physics, Fysikvej, 2800 Kongens Lyngby Denmark `www.fysik.dtu.dk`

Preface

This work is submitted in candidacy for the Ph.D. degree at the Technical University of Denmark (DTU). The work has been carried out during three years at the Department of Micro and Nanotechnology (DTU Nanotech) from September 2016 to July 2018, and at the Department of Physics (DTU Physics) from August 2019 to August 2020. The project is jointly funded by the Center for Nanostructured Graphene (CNG), which is sponsored by the Danish Research Foundation, Project DNRF103, and DTU Nanotech/DTU Physics. The project was supervised by Professor Antti-Pekka Jauho (DTU) and Associate Professor Jens Paaske (University of Copenhagen).

I am grateful to Antti-Pekka Jauho for his great supervision during the three years of working together on this project, and for letting me be guided by my own curiosity, which has enabled several external collaborations and research stays. I am also grateful to Jens Paaske for his great support and for inviting me to the Condensed Matter Theory Group at the University of Copenhagen. I have enjoyed and benefited significantly from hours of fruitful discussions with both of you about physics and non-physics. Thank you!

Furthermore, I would like to thank my collaborators on various interesting projects during my Ph.D. studies. I am thankful to Professor Andrew J. Millis for a great collaboration and for hosting me during my stay at Columbia University, Department of Physics, in the fall 2017. The stay included frequent visits to the Center for Computational Quantum Physics at the Flatiron Institute; thank you for the hospitality. I am also thankful to Associate Professor Christian Flindt and the group at Aalto University, Department of Applied Physics, for hosting me during several visits and for great collaborations. Furthermore, I thank Kristen Kaasbjerg and Dante M. Kennes for many fruitful discussions about physics and life as a Ph.D. student.

Furthermore, I would like to thank members of the Theoretical Nanotechnology and Nanoelectronics groups at DTU and the Condensed Matter Theory group at University of Copenhagen for contributing to a great working environment.

During my work, I have also benefited from fruitful discussions with J. P. Pekola, M. Wegewijs, T. Novotný, M. Leijnse, C. Timm, F. Brange, R. S. Souto, P. Ribeiro, C. Padurariu, N. M. Gergs, and many more during inspirational research stays, conferences, etc.

Finally, I am grateful to my family and friends for their support during my Ph.D. A big heartfelt thanks to Kathrine.

Nicklas Walldorf
Department of Physics
Technical University of Denmark
August 28, 2020

Abstract

The prospects of inducing and engineering novel properties in condensed-matter systems by external perturbation have stimulated a significant interest in the field of non-equilibrium condensed-matter physics, which also benefit from the recent experimental progress in the fabrication and control of nanostructures and low-dimensional materials. In this thesis, we study a selection of steady-state phenomena in interacting nanostructured and low-dimensional condensed-matter systems out of equilibrium within two main lines of research: I) quantum transport in two particular nanostructures engineered for thermoelectric and information science purposes, and II) periodically driven low-dimensional systems.

In the first part of the thesis we discuss two projects where electron currents between reservoirs with different electrochemical potentials drive the non-equilibrium behavior: i) interaction-mediated thermoelectric effects in Coulomb-coupled quantum dots, and ii) non-local transport properties of a Cooper pair splitter. In project i), we set up a master equation with rates calculated from the T matrix. This enables us to discuss the role of higher-order (cotunneling) processes in the general case of energy-dependent couplings to external leads. Both aspects (higher-order processes and energy-dependent couplings) become important in discussing the optimization of the interaction-mediated energy-exchange that enables a cooling-by-current behavior in the device. In project ii), we propose to characterize a Cooper pair splitter in terms of the distribution of electron waiting times between tunneling events, and we show how such transport statistics, including analytical results for the more conventional finite-frequency shot noise, can provide valuable insights into the transport processes.

In the second part of the thesis, we study condensed-matter systems perturbed by periodically oscillating electric fields. We first consider the periodically driven non-interacting single level and square-lattice, where for the former we provide an explicit example of how the periodically driven system approaches a non-equilibrium steady state. Thereafter, we turn our attention to the Coulomb-interacting case in the two-dimensional square-lattice Hubbard model. Guided by our knowledge in equilibrium, we consider fluctuations around the antiferromagnetic mean field and discuss how properties of the system change with a periodic drive. We show examples of how the drive can induce dynamics in the antiferromagnetic mean field and tune the magnon velocity. We highlight the importance of collective-mode excitations which, as we show, in general have a non-thermal distribution, which in turn may destabilize antiferromagnetism. Finally, we outline a route for future studies, in particular by deriving analytical results for fluctuations in the periodically driven level, which we show provide valuable insights into the on-set of mean-field configurations also out of equilibrium.

Resumé

Udsigten til at inducere og designe nye egenskaber i faststofsystemer ved ekstern påvirkning har stimuleret en stor interesse i feltet uligevægts faststoffysik, der også nyder gavn af nylige eksperimentelle fremskridt i fabrikationen og kontrollen af nanostrukturer og lav-dimensionelle materialer. I denne afhandling studerer vi et udvalg af steady-state fænomener i vekselvirkende nanostrukturerede og lav-dimensionelle faststofsystemer ude af ligevægt indenfor to hovedspor: I) kvantetransport i to specifikke nanostrukturer designet for termoelektriske og informationsvidenskabelige formål, og II) periodisk drevne lav-dimensionelle systemer.

I den første del af afhandlingen diskuterer vi to projekter hvor strømme af elektroner mellem reservoirer med forskellig elektrokemiske potentialer driver uligevægts effekten: i) vekselvirkningsmedierende termoelektriske effekter i Coulomb-koblede kvantedots, og ii) ikke-lokale transport egenskaber i en Cooper par splitter. I projekt i) etablerer vi en master-ligning med rater beregnet fra T matricen. Dette muliggør en diskussion af højere-ordens processers (cotunnelering) rolle i det generelle scenarie med energi-afhængige koblinger til eksterne ledere. Begge aspekter (højere-ordens processer og energi-afhængige koblinger) er vigtige i en diskussion af optimeringen af den vekselvirkningsmedierende energy-udveksling der giver systemet dets køling-ved-strøm egenskaber. I projekt ii) foreslår vi at karakterisere en Cooper par splitter ved hjælp af fordelingen af elektron ventetider mellem tunnelerings events, og vi viser hvordan sådan transport statistik, inklusiv analytiske resultater for den mere konventionelle endelig-frekvens støj, kan give værdifuld indsigt i transport-processerne.

I anden del af afhandlingen studerer vi faststofsystemer perturberet af periodisk oscillerende elektriske felter. Vi undersøger først det periodisk drevne niveau og kvadratiske gitter uden Coulomb vekselvirkninger, hvor vi i førstnævnte tilfælde ser et eksplicit eksempel på hvordan det periodisk drevne system går mod en periodisk steady-state opførsel. Dernæst vender vi opmærksomheden mod situationen med Coulomb vekselvirkninger i den to-dimensionelle kvadratisk-gitter Hubbard model. Guidet af vores viden i ligevægt undersøger vi fluktuationer omkring det antiferromagnetiske middelfelt og diskuterer hvordan egenskaberne i systemet ændres under den periodiske drivning. Vi ser eksempler på hvordan drivning kan inducere dynamik i det antiferromagnetiske middelfelt og ændre magnon hastigheden. Vi understreger vigtigheden af kollektive eksitationer, som vi viser generelt har en ikke-termisk fordelingsfunktion, som kan destabilisere antiferromagnetisme. Til sidst skitserer vi en vej for fremtidige undersøgelser, konkret ved at udlede analytiske resultater for fluktuationer i det periodisk drevne niveau, som vi viser giver vigtig indsigt i opbygningen af middelfelter også ude af ligevægt.

List of contributions

Publications

Publication I (attached in App. B.1):
Thermoelectrics in Coulomb-coupled quantum dots: Cotunneling and energy-dependent lead couplings
Authors: Nicklas Walldorf, Antti-Pekka Jauho, and Kristen Kaasbjerg
Physical Review B 96, 115415 (2017)
Cited as Ref. [1] in the thesis.

Publication II (attached in App. B.2):
Electron Waiting Times of a Cooper Pair Splitter
Authors: Nicklas Walldorf, Ciprian Padurariu, Antti-Pekka Jauho, and Christian Flindt
Physical Review Letters 120, 087701 (2018)
Cited as Ref. [2] in the thesis.

Publication III (attached in App. B.3):
The antiferromagnetic phase of the Floquet-driven Hubbard model
Authors: Nicklas Walldorf, Dante M. Kennes, Jens Paaske, and Andrew J. Millis
Physical Review B (Rapid Communication) 100, 121110(R) (2019)
Cited as Ref. [3] in the thesis.

Publication IV (attached in App. B.4):
Noise and full counting statistics of a Cooper pair splitter
Authors: Nicklas Walldorf, Fredrik Brange, Ciprian Padurariu, and Christian Flindt
Physical Review B 101, 205422 (2020)
Cited as Ref. [4] in the thesis.

Publications I–IV have been published during the Ph.D. project.

Conference contributions

Thermoelectric effects in capacitively coupled quantum dots: The role of multi-electron tunneling, International School & Conference on Nanoscience and Quantum Transport 2016, Kiev, Ukraine
Nicklas Walldorf (poster presentation), Antti-Pekka Jauho, and Kristen Kaasbjerg

Electron waiting times of a Cooper pair splitter, Frontiers of Quantum and Mesoscopic Thermodynamics 2017, Prague, Czech Republic
Nicklas Walldorf (poster presentation), Ciprian Padurariu, Antti-Pekka Jauho, and Christian Flindt

Electron waiting times of a Cooper pair splitter, 28th International Conference on Low Temperature Physics 2017, Gothenburg, Sweden
Nicklas Walldorf (poster presentation), Ciprian Padurariu, Antti-Pekka Jauho, and Christian Flindt

The antiferromagnetic phase of the Floquet-driven Hubbard model, Workshop on Ordering and Dynamics of Correlated Quantum Systems 2019, Évora, Portugal
Nicklas Walldorf (poster presentation), Dante M. Kennes, Jens Paaske, and Andrew J. Millis

The antiferromagnetic phase of the Floquet-driven Hubbard model, CNG 1 day seminar 2019, Helsingør, Denmark
Nicklas Walldorf (oral presentation), Dante M. Kennes, Jens Paaske, and Andrew J. Millis

Contents

1 | Introduction

We constantly encounter non-equilibrium phenomena: From the flow of water in rivers, and the firing of neurons in our brain, to the transport of electrons in electronic devices. Arguably, 'non-equilibrium' is an unbounded set emerging from the scarcely realized limit of equilibrium towards far-from-equilibrium, and within this spectrum phenomena occur in a delicate balance between drive and dissipation.

The non-equilibrium behavior of Nature is not only of scientific interest. Historically, technology has developed around exploiting classical macroscopic principles and perturbing these in new ways, like Thomas Edisons search for materials that would light up for hours upon applying an electric potential [5]. The desire to engineer and tailor the properties of materials has driven a significant interest in understanding condensed matter out of equilibrium [6]. On a microscopic level, Nature is governed by the principles of quantum physics, which have, more recently, provided us with insights into the origin of exotic phenomena such as superconductivity and magnetism. Hence, from both a fundamental and technological point of view, it is natural to ask: What kind of fascinating and perhaps useful phenomena can the microscopic laws that govern condensed matter reveal out of equilibrium?

In this thesis we will study a selection of phenomena in interacting nanostructured and low-dimensional condensed-matter systems out of equilibrium.

1.1 Non-equilibrium steady state

A system out of equilibrium is most easily defined as a system that does not satisfy equilibrium conditions characterized by a) a set of time-independent variables which b) remain unchanged after isolation from an external environment [7]. When brought out of equilibrium, the system will show a transient response that violates both conditions[1], after which it may end up in a stationary non-equilibrium steady state that violates the latter condition only, or a dynamical non-equilibrium steady state that violates both conditions but with variables varying periodically in time. We will consider stationary and dynamical non-equilibrium steady-state phenomena within two main lines of research in this thesis: I) quantum transport in (two particular) nanostructures engineered for thermoelectric and information science purposes, and II) periodically driven low-dimensional systems. The former is rooted in the significant progress in engineering nanostructures where static differences in electrochemical potentials and temperatures between electron reservoirs induce stationary (mean) electron currents in the nanostructures (illustrated in the left panel in Fig. 1.1), and the latter is rooted in the interest and recent progress in also controlling many-body aspects of condensed-matter systems by means of a periodic drive, e.g., with an external periodically oscillating electric field (illustrated in the right panel in Fig. 1.1) [6].

Below, we provide a brief introduction to the different topics discussed in this thesis, and a more detailed introduction to each topic is provided in the following chapters. Common for the systems considered is that they are coupled to external electron reservoirs. In our study of stationary non-equilibrium phenomena the reservoirs establish the non-equilibrium conditions through differences in

[1] Quench dynamics and transient behaviors are important topics on their own, however, are only discussed to a limited degree in this thesis.

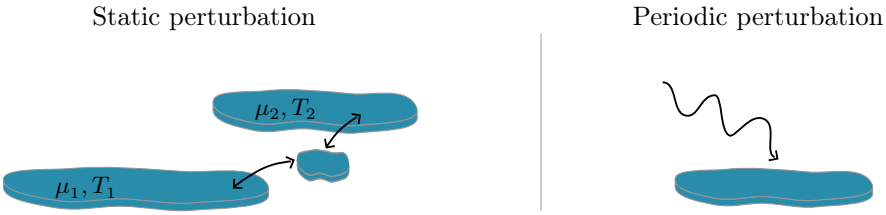

Figure 1.1: Examples of condensed-matter systems driven out of equilibrium. Left panel: Sketch of nanostructures where electronic transport processes are induced by coupling to large reservoirs with different electrochemical potentials, μ_ℓ, and temperatures, T_ℓ (here $\ell \in \{1, 2\}$). Right panel: Sketch of a periodically driven system, e.g., by means of a periodically oscillating electric field.

electrochemical potentials, and in our discussion of dynamical non-equilibrium phenomena a reservoir acts to stabilize a dynamical non-equilibrium steady state.

1.2 Low-dimensional systems and interactions

The miniaturization of electronic devices and the prospect of precise control of the behavior of condensed-matter systems have spurred significant interest in nanostructures and low-dimensional systems. An immediate consequence of the spatial confinement in quantum systems is the importance of energy quantization. Ultimately, when electrons are confined in all three spatial dimensions in a region of size in the order of nanometers to a few microns, the confining boundary conditions cause the electrons to occupy discrete energy levels. Such 'zero-dimensional' structures are referred to as quantum dots (QDs) or artificial atoms. In the first part of this thesis, we study transport processes through quantum dots in specific nanostructures. The effect of confinement in a quantum dot depends on how strongly it is isolated from the surrounding environment[2], and for a finite coupling the electrons can tunnel to and from external electron reservoirs whereby the quantum dot acts as an energy filter in the electron transport process. This provides an important ingredient in controlling the transport processes.

Another key factor in nanostructures and low-dimensional materials is the importance of interactions. One such interaction that is responsible for many interesting properties of condensed-matter systems is the repulsive Coulomb interaction between electrons, also referred to as electronic correlations, which naturally become of upmost importance when confining electrons closely together in nanostructures. This is ultimately exemplified in one-dimensional Luttinger liquids [8], and Coulomb blockade [9] and the Kondo effect [10] in quantum dots. Another type of interaction that is crucial in a non-equilibrium context is the interaction of the system with its surroundings. Quantum systems are highly sensitive to external perturbations [11], and this becomes even more apparent in lower dimensions where the surface-to-bulk ratio increases. This provides an opportunity for external perturbation of the system, e.g., by means of electromagnetic fields or in coupled systems interacting via electron tunneling processes.

In the first part of the thesis we discuss two projects where the above-mentioned factors are crucial: i) thermoelectric effects in Coulomb-coupled quantum dots (publication I), and ii) non-local transport properties of a so-called Cooper pair splitter [12, 13] (publication II and publication IV). In project i), Coulomb-interaction mediates an energy-exchange between otherwise (tunnel-) decoupled systems which has been studied for energy harvesting [14, 15] and cooling [16] purposes. The mechanism (which we will describe in Sec. 3.1) can to first approximation be described in terms of incoherent sequential tunneling of individual electrons between external reservoirs and the quantum dots. In this thesis, we will discuss the role of higher-order tunneling processes and energy-dependent couplings to

[2]Throughout the thesis, 'environment' refers to macroscopic electron reservoirs.

the external reservoirs, both of which become important in optimizing the studied effects. In project ii), the strong Coulomb-interaction in quantum dots is utilized to split Cooper pairs originating from a superconductor. Cooper pairs are proposed as natural candidates of spin-entangled electron pairs for solid state entanglement experiments, with potential application in quantum communication [17]. We discuss the transport characteristics of a Cooper pair splitter in terms of the current, noise spectrum, and electron waiting times between tunneling events.

In the second part of the thesis we study periodically driven low-dimensional systems. In the above-mentioned examples, the particular behaviour is engineered from a complex composition and interplay of the different components in the nanostructures, like Lego blocks put together. However, it has also been suggested to engineer the properties of a material by perturbing the material periodically in time [18, 19]. This rapidly growing field is commonly referred to as Floquet-engineering, and low-dimensional materials which may avoid shielding of the drive fields [20] provide an interesting platform for studies in this field [21]. Just as electron-electron correlations are important in quantum dots, extended materials with strongly correlated electrons can give rise to fascinating ordered phases thanks to a collective behaviour of the electrons. An interesting question is how a periodic drive may affect or perhaps even induce collective phases [6]. This is still a largely unexplored area of research, however, some interesting examples include light-induced superconductivity [22] and phase transitions in magnetic materials [23]. In the generic situation, however, if too many excitations are created, the ordered phases can be destabilized [24, 25]. In publication III, we study the antiferromagnetic phase of the periodically driven Hubbard model. We show that the periodic drive can induce dynamics in the mean-field order parameter and lead to a highly excited, generically non-thermal, distribution of fluctuations around the mean field, which in turn may destabilize the antiferromagnetic order.

1.3 Observables and time-evolution

The phrasing "to drive a system out of equilibrium" has a built-in sense of dynamics: How does the system evolve out of equilibrium? The (pure) state of a quantum system at time t is described by its normalized ket $|\psi(t)\rangle$ such that a measurement of some observable $\mathcal{O}$ will return an eigenvalue o_i of the associated Hermitian operator[3] $\hat{\mathcal{O}}$ with probability $P_i(t) = |\langle O_i|\psi(t)\rangle|^2$, where $|O_i\rangle$ is the eigenket corresponding to the eigenvalue o_i. Hence, the quantum average is defined as [26]

$$\langle\hat{\mathcal{O}}\rangle(t) = \sum_i o_i P_i(t) = \sum_i o_i \langle\psi(t)|O_i\rangle\langle O_i|\psi(t)\rangle = \langle\psi(t)|\hat{\mathcal{O}}|\psi(t)\rangle, \tag{1.1}$$

where we have used the completeness relation of the eigenkets $|O_i\rangle$. If the system is coupled to the outside world (in practice it is indeed difficult to uncouple from the world), its state is uncertain, and we describe the system by the probability p_λ to be in the state $|\psi_\lambda(t)\rangle$, with $\sum_\lambda p_\lambda = 1$. In this case, we define the ensemble average of the operator $\hat{\mathcal{O}}$ as [27]

$$\langle\hat{\mathcal{O}}\rangle(t) = \sum_\lambda p_\lambda \langle\psi_\lambda(t)|\hat{\mathcal{O}}|\psi_\lambda(t)\rangle = \mathrm{Tr}[\hat{\mathcal{O}}\hat{\rho}(t)], \tag{1.2}$$

where we have defined the *density operator*

$$\hat{\rho}(t) = \sum_\lambda p_\lambda |\psi_\lambda(t)\rangle\langle\psi_\lambda(t)|, \qquad \mathrm{Tr}[\hat{\rho}(t)] = 1. \tag{1.3}$$

In some complete orthonormal basis, diagonal components of the matrix elements of the density operator describe populations of the basis states [28] whereas off-diagonal components are referred to as coherences. We will discuss particular examples in Ch. 3.

[3] We denote operators with a hat. The operator $\hat{\mathcal{O}}$ could have an explicit time dependence [26], which for notational simplicity is omitted here.

Say we know $\hat{\rho}(t_0) = \hat{\rho}_0$ at some time t_0, and we want to find the expectation value of $\hat{\mathcal{O}}$ at some later time t where states have evolved according to the Schrödinger equation

$$i\hbar \frac{d}{dt}|\psi(t)\rangle = \hat{H}(t)|\psi(t)\rangle. \tag{1.4}$$

We are then interested in the expectation value [26]

$$\langle\hat{\mathcal{O}}\rangle(t) = \sum_\lambda p_\lambda \langle\psi_\lambda(t_0)|\hat{U}_{t_0,t}\hat{\mathcal{O}}\hat{U}_{t,t_0}|\psi_\lambda(t_0)\rangle = \mathrm{Tr}[\hat{U}_{t_0,t}\hat{\mathcal{O}}\hat{U}_{t,t_0}\hat{\rho}_0], \tag{1.5}$$

where the time-evolution operator $\hat{U}_{t,t_0}$ that solves the Schrödinger equation reads

$$\hat{U}_{t,t_0} = \begin{cases} Te^{-\frac{i}{\hbar}\int_{t_0}^{t} dt' \hat{H}(t')} = \lim_{N\to\infty} e^{-\frac{i}{\hbar}\hat{H}(t_0+(N-2)\delta)\delta} \cdots e^{-\frac{i}{\hbar}\hat{H}(t_0+\delta)\delta} e^{-\frac{i}{\hbar}\hat{H}(t_0)\delta} & t > t_0, \\ \bar{T}e^{\frac{i}{\hbar}\int_{t}^{t_0} dt' \hat{H}(t')} = \lim_{N\to\infty} e^{\frac{i}{\hbar}\hat{H}(t)\delta} \cdots e^{\frac{i}{\hbar}\hat{H}(t+(N-3)\delta)\delta} e^{\frac{i}{\hbar}\hat{H}(t+(N-2)\delta)\delta} & t < t_0, \end{cases} \tag{1.6}$$

with $\delta = |t - t_0|/(N-1)$, and

$$\hat{U}_{t,t} = \mathbb{1}, \qquad \hat{U}^\dagger_{t,t_0} = \hat{U}_{t_0,t}, \qquad \hat{U}_{t'',t'}\hat{U}_{t',t} = \hat{U}_{t'',t}. \tag{1.7}$$

The time (anti-time) ordering operator T ($\bar{T}$) in Eq. (1.6) orders operators evaluated at later times to the left (right) [29]

$$T\{\hat{A}(t)\hat{B}(t')\} = \theta(t-t')\hat{A}(t)\hat{B}(t') \pm \theta(t'-t)\hat{B}(t')\hat{A}(t), \tag{1.8a}$$

$$\bar{T}\{\hat{A}(t)\hat{B}(t')\} = \theta(t'-t)\hat{A}(t)\hat{B}(t') \pm \theta(t-t')\hat{B}(t')\hat{A}(t), \tag{1.8b}$$

where + (−) is valid for bosonic (fermionic) operators. We note from Eq. (1.5) that $\langle\hat{\mathcal{O}}\rangle(t) = \mathrm{Tr}[\hat{\mathcal{O}}\hat{\rho}(t)] = \mathrm{Tr}[\hat{\mathcal{O}}(t)\hat{\rho}(t_0)]$, where in the latter representation, $\hat{\mathcal{O}}(t) \equiv \hat{U}_{t_0,t}\hat{\mathcal{O}}\hat{U}_{t,t_0}$ is expressed in the Heisenberg picture, and in the Schrödinger representation, the density operator evolves according to

$$\hat{\rho}(t) = \hat{U}_{t,t_0}\hat{\rho}(t_0)\hat{U}^\dagger_{t,t_0}. \tag{1.9}$$

Upon differentiation, Eq. (1.9) gives the *von Neumann equation* of motion [27]

$$\frac{d}{dt}\hat{\rho}(t) = -\frac{i}{\hbar}[\hat{H}(t), \hat{\rho}(t)] \equiv \mathcal{L}[\hat{\rho}(t)], \tag{1.10}$$

where $\mathcal{L}$ is the Liouville super-operator, also referred to as the Liouvillian[4]. Using the identity [30, p. 94] $e^{\hat{O}}\hat{A}e^{-\hat{O}} = e^{[\hat{O},\,\cdot\,]}\hat{A} = \hat{A} + [\hat{O},\hat{A}] + \frac{1}{2}[\hat{O},[\hat{O},\hat{A}]] + \cdots$, the evolution of the density operator can also be expressed in terms of the Liouvillian as [27]

$$\hat{\rho}(t) = T\exp\left(\int_{t_0}^{t} dt' \mathcal{L}(t')\right)\hat{\rho}(t_0) \equiv A_{t,t_0}\hat{\rho}(t_0), \tag{1.11}$$

which in the case of a time-independent Hamiltonian, and hence a time-independent Liouvillian, reduces to $\hat{\rho}(t) = \exp(\mathcal{L}(t-t_0))\hat{\rho}(t_0)$.

1.4 Master equations and non-equilibrium Green functions

The time-evolution of quantum systems is the central starting point for non-equilibrium theories. The section above sets the formal stage for the time-evolution of quantum systems, however, from here

[4] Denoted without a hat.

various methods are developed to evaluate the introduced expressions in practice. In particular, we will apply two different methods: master equations and non-equilibrium Green functions.

Master equations take the evolution of the density operator in Eq. (1.10) as starting point. In particular, we are often interested in some small subsystem of a larger system, that is, a subsystem coupled to an environment. We call the equation of motion governing the matrix elements of the *reduced density operator* of the subsystem only a *master equation*. We will quantify these statements when introducing the method of master equations in Ch. 2. In particular, we apply master equations in part I of this thesis (Ch. 3) to study transport processes in nanostructures with quantum dots. The small set of basis states needed to characterize quantum dots makes it convenient to resolve the matrix elements of the reduced density matrix and describe transport processes in terms of master equations. The challenge is how to include the external environment, and we will discuss different perturbative approaches in Ch. 2.

The method of non-equilibrium Green functions develops from the evaluation of expectation values in Eq. (1.5). We introduce the methodology in Ch. 4 which is applied in part II of this thesis in chapters 5–6. In particular, in Ch. 6, we consider a tight-binding lattice system where the larger set of basis states make it more challenging to resolve the density operator, and instead non-equilibrium Green functions provide a convenient methodology to study the properties of the system. Here, in contrast to our study in part I, it is the effect of electron interactions that is treated perturbatively.

Having said so, there are many examples of applying von Neumann equations to study extended systems and non-equilibrium Green functions to study quantum dots, and we will consider an example of the latter in Sec. 5.2. To some extend, the choice of master equations versus non-equilibrium Green functions is also a matter of preference in different research groups and historical development within subgenres of research.

1.5 Thesis outline

Having set the stage, we now outline the content of the chapters in the thesis. At The Technical University of Denmark it is recommended that a thesis is based on scientific articles already published. In addition to describing results from publications I–IV (which are also attached in the format of regular articles in the end of thesis), the thesis aims to provide some additional discussions and results not part of publications I–IV, specifically:

Chapter 2 introduces the methodology of master equations, a direct application of the von Neumann equation governing a particular subsystem of interest coupled to an environment. In particular, we introduce the T-matrix master equation [31], which provides a governing equation for the diagonal components of the reduced density matrix, as well as a Markovian quantum master equation, which is valid in the case of unidirectional transport [32].

Chapter 3 presents results published in publications I, II, IV for two specific systems; thermoelectric effects in a Coulomb-coupled QD system, and transport characteristics of a Cooper pair splitter. Coulomb coupled QD systems have been designed to explore phenomena for energy harvesting and cooling. In particular, with results published in Publication I, we discuss the role of higher-order tunneling processes and energy-dependent couplings to external leads.
Cooper pair splitters have been proposed as a device to generate split pairs of entangled electrons in solid-state devices. In particular, with results published in Publication II and IV, we discuss the characteristics of the transport processes in terms of the current, noise, and electron waiting time distributions.

Chapter 4 introduces the methodology of non-equilibrium field theory and Green functions. The section aims to provide the reader with sufficient background information for the discussion presented in Chs. 5-6. In particular, we construct the path integral that leads to the non-equilibrium Green functions.

Chapter 5 sets the stage for periodically driven systems, and introduces the so-called Floquet non-equilibrium Green functions. We discuss a periodically driven level as well as a periodically driven

square lattice. For the former, we see an explicit example of how the periodically driven system may approach a dynamical non-equilibrium steady state. The latter example introduces some general properties of the periodically-driven square lattice that is needed for the discussion in Ch. 6.

Chapter 6 presents results published in Publication III for the antiferromagnetic phase of the periodically driven Hubbard model. In particular, we discuss the importance of collective mode excitations arising from the non-equilibrium drive. We find that in general a highly excited, generically non-thermal distribution of magnetic fluctuations occurs. Above a critical drive amplitude, the low-energy distribution of fluctuations diverges as the frequency tends to zero which in turn may destroy antiferromagnetism. Finally, we present analytical results for fluctuations in the periodically driven level, which we show provide valuable insight into the onset of mean-field configurations, and which may provide a route for future studies.

Chapter 7 summarizes the thesis and provides an outlook for future research, and the **appendices** contain additional details for the interested reader.

To ease the flow of reading, a few side notes and calculational details that are not essential, but may be of value to the interested reader, are provided in-text in gray boxes like this.
I thank you for reading this thesis, and hope it may be of interest to you,
Nicklas Walldorf, August 28, 2020.

2 | Master equations

The von Neumann equation (1.10) governs the time-evolution of the full density operator $\hat{\rho}$ that characterizes some system of interest S, referred to as the *system* for simplicity, and its *environment* E, which together is assumed to constitute a closed system. Specifically, consider the Hamiltonian

$$\hat{H} = \hat{H}_0 + \hat{H}_T, \qquad \hat{H}_0 = \hat{H}_S + \hat{H}_E, \tag{2.1}$$

where $\hat{H}_S$ and $\hat{H}_E$ are the Hamiltonians describing the system and the environment, respectively, which are coupled via tunneling processes[1] described by $\hat{H}_T$ (see Fig 2.1). The full state of the system and the environment is characterized in the product Hilbert space $\mathcal{H} = \mathcal{H}_S \otimes \mathcal{H}_E$. However, if we are only concerned with observables belonging to S, $\hat{\mathcal{O}} = \hat{\mathcal{O}}_S \otimes \mathbb{1}_E$, the reduced density operator $\hat{\rho}_S \equiv \mathrm{Tr}_E[\hat{\rho}]$, which acts in the Hilbert space of the system of interest only, contains all relevant information [27]

$$\langle \hat{\mathcal{O}} \rangle = \mathrm{Tr}\Big[\hat{\mathcal{O}}\hat{\rho}\Big] = \sum_{m,m',n} \langle s_m\, e_n | \hat{\mathcal{O}}_S | s_{m'} \rangle \langle s_{m'} e_n | \hat{\rho} | s_m\, e_n \rangle = \mathrm{Tr}_S\Big[\hat{\mathcal{O}}_S \hat{\rho}_S\Big], \tag{2.2}$$

where $\mathrm{Tr}_{S(E)}$ denotes the partial trace over system (environment) degrees of freedom, and we have spanned $\mathcal{H}$ by a set of product vectors $|s_m e_n\rangle = |s_m\rangle \otimes |e_n\rangle$ with $\{|s_m\rangle\}$ ($\{|e_n\rangle\}$) being a complete set of orthonormal states in S (E).

A master equation refers to the equation of motion for the reduced density matrix, and come in various forms. Examples include the T-matrix master equation [31, 33], master equations for unidirectional[2] transport by S. A. Gurvitz and Ya. S. Prager [32], the real-time diagrammatic formulation by J. König, H. Schoeller, and G. Schön [34], the works by S. Koller, M. Grifoni, M. Leijnse, and M. R. Wegewijs [35], and many more. In this thesis, we will apply the two former, the T-matrix master equation and master equations for unidirectional transport, which are introduced below.

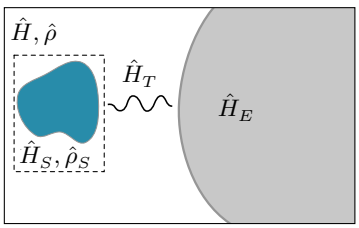

Figure 2.1: Illustration of a subsystem of interest (blue) coupled to a macroscopic environment (gray). Figure inspired by Ref. [7].

[1] We consider electron tunneling Hamiltonians which change the number of electrons in the environment, and consider cases where no energy is gained from or lost in the tunneling barriers. Specific systems are studied in Ch. 3.

[2] The meaning of 'unidirectional' is defined in Sec. 2.3.

2.1 T-matrix master equation

The T-matrix master equation is a master equation in terms of probabilities, that is, in terms of diagonal components of the reduced density matrix. Such master equations are also referred to as Pauli master equations, and we will see an example in Sec. 3.1 where a Pauli master equation is applicable. By contrast, master equations that include off-diagonal matrix elements of the reduced density operator are called generalized (quantum) master equations (we will discuss this situation further below). As for all master equations, the T-matrix approach relies on a perturbative expansion in the coupling to the environment, whereby the effect of the environment is transferred into rates of transitions between diagonal elements of the reduced density matrix. To lowest order in the tunneling Hamiltonian, the transition rates in the T-matrix master equation correspond to the rates from Fermi's golden rule [36]. However, the T matrix offers a fairly straightforward way to calculate rates of transitions from higher-order tunneling processes, and is therefore also referred to as the generalized Fermi's golden rule [31]. Hence, although the T-matrix master equation describes transitions between diagonal components of the reduced density matrix, coherent quantum processes are included as higher-order processes in the T matrix. For this reason, the T-matrix approach is widely applied in the literature [31, 33], and we will apply it in Sec. 3.1.

The T-matrix master equation can be derived from Eq. (1.11) for a time-independent $\hat{H}_0$, and with $\hat{H}_T$ turned on adiabatically [31, 33]. A detailed derivation is provided in Appendix A.1. However, highlighting some key points in the derivation, we note that the full system and environment is assumed to be in a product state at some initial time t_0 with S described by a diagonal reduced density operator, and the large environment is assumed to remain in thermal equilibrium. Since the T-matrix approach is a master equation for the diagonal components of the reduced density operator, it is conveniently derived by projecting the density operator onto a diagonal form using the projectors [33]

$$\mathcal{P}[\,\bullet\,] \equiv \left[\sum_m |m\rangle\langle m|\mathrm{Tr}_E[\,\bullet\,]|m\rangle\langle m|\right] \otimes \hat{\rho}_E^{\mathrm{eq}}, \qquad \mathcal{Q} \equiv \mathbb{1} - \mathcal{P}, \tag{2.3}$$

where $|m\rangle$ are eigenstates of the uncoupled system S, and $\hat{\rho}_E^{\mathrm{eq}}$ describes the environment. Projecting onto the time-evolved density operator, one obtains

$$\frac{d}{dt}\mathcal{P}\hat{\rho}(t) = \mathcal{R}(t,t_0)\mathcal{P}\hat{\rho}(t_0), \tag{2.4}$$

where the kernel $\mathcal{R}(t,t_0)$ is given by Eq. (A.6) in App. A.1. Notice that the right-hand side in Eq. (2.4) involves the density operator evaluated at time t_0. Importantly, however, to derive the T-matrix master equation [31], one defines the transition rate from an initial state $|i\rangle$ to the final state $|f\rangle$ as[3] [33]

$$\tilde{\Gamma}_{if} \equiv \langle f|\{\mathcal{R}(t,t_0)[|i\rangle\langle i|]\}|f\rangle, \tag{2.5}$$

and assumes that the rate of transition from $|i\rangle$ is at the present time t. This is a central approximation in the T-matrix approach [33], and as a consequence one has to apply a regularization procedure for tunneling rates above first order as first proposed by Turek and Matveev[4] [37]. We detail the Turek-Matveev regularization scheme [37, 38] for higher-order cotunneling processes in Sec. 3.1.1. Expressed in terms of the so-called T matrix we obtain the Fermi's generalized golden rule [31]

$$\tilde{\Gamma}_{if} = \frac{2\pi}{\hbar}|\langle f|\hat{T}|i\rangle|^2\delta(E_i - E_f), \quad \hat{T} = \hat{H}_T + \hat{H}_T[E_i - \hat{H}_0 + i\eta]^{-1}\hat{T}, \quad \eta \to 0^+, \tag{2.6}$$

[3] Notice that we use subscript if for the transition rate from state $|i\rangle$ to $|f\rangle$ in Eq. (2.5) (the reverse ordering is also often found in the literature).

[4] The Turek-Matveev regularization scheme has become a standard regularization scheme in the T-matrix approach. We apply the scheme in Sec. 3.1.1, but in future work it would be useful to discuss other regularization schemes, and the relation to the more recently identified approximation mentioned below Eq. (2.5), as discussed in e.g. Ref. [33].

where $(E_i|f\rangle, E_f|f\rangle) = \hat{H}_0(|i\rangle, |f\rangle)$, and the T matrix is written in a compact iterative form. Upon expressing the initial and final states in the product basis of eigenstates of the uncoupled system $|m\rangle$ and the environment $|j\rangle$, and summing over the environment states, we can write the transition rate from state $|m\rangle$ to $|n\rangle$ as [31, 33]

$$\tilde{\Gamma}_{mn} = \frac{2\pi}{\hbar} \sum_{jj'} |\langle j'|\langle n|\hat{T}|m\rangle|j\rangle|^2 \rho_j \delta(E_{S,m} + E_{E,j} - E_{S,n} - E_{E,j'}), \tag{2.7}$$

where $E_{S,m}$ ($E_{E,j}$) are eigenenergies of system S (environment E), and ρ_j is the thermal probability of finding the environment in the initial state $|j\rangle$. We can then write a master equation in terms of transition rates as[5]

$$\frac{d}{dt}p_m = \sum_{n(\neq m)} \Gamma_{nm}\, p_n - \sum_{n(\neq m)} \Gamma_{mn}\, p_m, \qquad \sum_m p_m = 1, \tag{2.8}$$

where we denote the regularized rates without a tilde (see section 3.1.1). For a given physical problem, one identifies the relevant basis states, the possible transitions between the states as described by the T matrix (to a given order), and calculates the transition rates from Eq. (2.7). An explicit example is considered in Sec. 3.1.

2.2 Generalized quantum master equation

The T-matrix master equation resembles a classical master equation in terms of probabilities, where quantum aspects reside in the transition rates. Let us, however, return to the von Neumann equation in Eq. (1.10) that governs the dynamics of the *full* density matrix. Still, one can reformulate the full von Neumann equation as a master equation for the reduced density matrix, the so-called Nakajima-Zwanzig equation [39, 40]. To this end, we project the von Neumann equation onto the system of interest with the projectors [7, 33]

$$\mathcal{P}[\,\bullet\,] \equiv \mathrm{Tr}_E[\,\bullet\,] \otimes \hat{\rho}_E^{\mathrm{eq}}, \qquad \mathcal{Q} \equiv \mathbb{1} - \mathcal{P}. \tag{2.9}$$

We can then split the von Neumann equation into two parts

$$\frac{d}{dt}\mathcal{P}\hat{\rho}(t) = \mathcal{P}\mathcal{L}(t)\mathcal{P}\hat{\rho}(t) + \mathcal{P}\mathcal{L}(t)\mathcal{Q}\hat{\rho}(t), \tag{2.10}$$

$$\frac{d}{dt}\mathcal{Q}\hat{\rho}(t) = \mathcal{Q}\mathcal{L}(t)\mathcal{P}\hat{\rho}(t) + \mathcal{Q}\mathcal{L}(t)\mathcal{Q}\hat{\rho}(t). \tag{2.11}$$

Upon inserting the solution to Eq. (2.11) into Eq. (2.10), and employing the projection operator we obtain (suppressing the time-variable in the arguments) [7]

$$\frac{d}{dt}\hat{\rho}_S = \mathcal{L}_S\hat{\rho}_S + \mathcal{D}\hat{\rho}_S, \tag{2.12}$$

where $\mathcal{L}_S\hat{\rho}_S = -i\hbar^{-1}[\hat{H}_S(t), \hat{\rho}_S(t)]$, and

$$\mathcal{D}\hat{\rho}_S = \int_{t_0}^{t} dt' \left\langle \mathcal{L}_T(t) T e^{\mathcal{Q}\int_{t'}^{t} dt'' \mathcal{L}(t'')} \mathcal{Q}\mathcal{L}_T(t') \right\rangle_E \hat{\rho}_S(t'), \tag{2.13}$$

where $\langle\,\bullet\,\rangle_E = \mathrm{Tr}_E[\,\bullet\,\hat{\rho}_E^{\mathrm{eq}}]$, $\mathcal{L}_T(t)[\,\bullet\,] = -i\hbar^{-1}[\hat{H}_T(t),\,\bullet\,]$, and we have used that $\mathrm{Tr}_E[\hat{H}_T\hat{\rho}_E^{\mathrm{eq}}] = 0$, and assumed that the system and environment have no correlations at some initial time t_0, $\hat{\rho}(t_0) =$

[5] To simplify the notation, we do not write subscript S on the probabilities, p, but emphasize that these are diagonal components of the reduced density matrix $\hat{\rho}_S$.

$\hat{\rho}_S(t_0) \otimes \hat{\rho}_E^{\text{eq}}$. The form in Eq. (2.12) may seem encouraging: It is an equation of motion for the reduced density matrix of the system, where the first term is the von Neumann equation for system S if isolated, and the latter term incorporates the effect of the environment. However, we are no closer in solving problems in practice due to the complicated form of $\mathcal{D}\hat{\rho}_S$ in Eq. (2.13), which includes an integral over the history, or a memory, of the system in the time interval $[t_0, t]$. Indeed, much work is invested into deriving more manageable master equations under various assumptions. In the following, we will consider a particular example, a Gurvitz-Prager-like master equation for unidirectional transport, where $\mathcal{D}\hat{\rho}_S$ acquires a time-local (Markovian) form.

2.3 Unidirectional transport

This section is based on Publication IV, Physical Review B 101, 205422 (2020) by N. Walldorf, F. Brange, C. Padurariu, and C. Flindt.

A particularly convenient form for the term $\mathcal{D}\hat{\rho}_S$ in Eq. (2.12) is obtained in the limit of unidirectional electron transport where external electron reservoirs are either completely full or completely empty (in the energy range relevant for transport). An example of the simple case of a central level coupled to a full left electron reservoir and an empty right reservoir is illustrated in Fig. 2.2 (see also the info-box in the end of this section). The original derivation of a master equation by S. A. Gurvitz and Ya. S. Prager [32] starts from the Schrödinger equation and an occupation number representation of the many-body wave function. However, as argued in the introduction, for an open out-of-equilibrium quantum system the density matrix governed by the von Neumann equation is the natural quantity to consider. There exists a large literature that applies the results by Gurvitz and Prager[6], but derivations of the results starting from the von Neumann equation are sparse. An expansion to second order in the coupling to external reservoirs is given in Refs. [44, 45]. For completeness[7], and to elaborate on the contribution from higher-order terms which Gurvitz and Prager show vanish, we give the key elements of a derivation starting from the von Neumann equation (which is derived in collaboration with F. Brange and follows similar arguments as in Ref. [45]).

For a time-independent Hamiltonian, it is convenient to Laplace-transform the density operator [46]

$$\hat{\rho}(E) = \int_{t_0}^{\infty} dt\, \hat{\rho}(t) e^{\frac{i}{\hbar}(E+i\eta)(t-t_0)}, \tag{2.14}$$

whereby the von Neumann equation becomes

$$(E + i\eta)\hat{\rho}(E) - i\hbar\hat{\rho}(t_0) = L_0\hat{\rho}(E) + L_T\hat{\rho}(E), \quad L_{0/T/S/E}[\,\cdot\,] \equiv [\hat{H}_{0/T/S/E},\, \cdot\,], \tag{2.15}$$

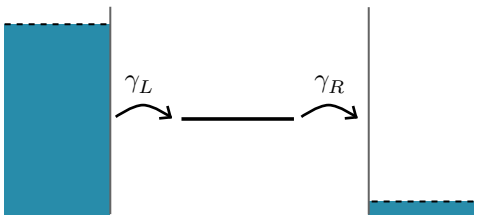

Figure 2.2: Unidirectional transport. Energy diagram illustrated for the example considered in the end of Sec. 2.3 where a central level is coupled to a full left electron reservoir and an empty right electron reservoir. The coupling is governed by the rates γ_L and γ_R (see main text).

[6] See e.g. examples in Refs. [41, 42, 43].

[7] The hope is that this may be of value to other students within the subject.

with solution

$$\begin{aligned}\hat{\rho}(E) &= [E+i\eta-L_0-L_T]^{-1}i\hbar\hat{\rho}(t_0)\\ &= (W_0(E)+W_0(E)L_TW_0(E)+W_0(E)L_TW_0(E)L_TW_0(E)+\cdots)\,i\hbar\hat{\rho}(t_0),\end{aligned} \tag{2.16}$$

where $W_0(E)=[E+i\eta-L_0]^{-1}$, and we have used a geometric series to express the result in terms of an expansion in L_T [46]. We could also have obtained the solution by iterating Eq. (2.15)

$$\begin{aligned}(E+i\eta-L_0)\hat{\rho}(E) &= L_T\hat{\rho}(E)+i\hbar\hat{\rho}(t_0)\\ &= L_T\left(W_0(E)L_T\hat{\rho}(E)+W_0(E)i\hbar\hat{\rho}(t_0)\right)+i\hbar\hat{\rho}(t_0)\\ &= L_T\left(W_0(E)L_T\left(W_0(E)L_T\hat{\rho}(E)+W_0(E)i\hbar\hat{\rho}(t_0)\right)+W_0(E)i\hbar\hat{\rho}(t_0)\right)+i\hbar\hat{\rho}(t_0)\\ &= \cdots,\end{aligned} \tag{2.17}$$

which produces the same series as above.

Consider a tunneling Hamiltonian of the form $\hat{H}_T=\sum_{\ell\delta}(t_{\ell\delta}\hat{c}_\ell^\dagger\hat{d}_\delta+\text{h.c.})=\sum_{\xi=\pm,\ell\delta}\xi t_{\ell\delta}^\xi\hat{c}_\ell^\xi\hat{d}_\delta^\xi$, where $\hat{c}_\ell^+=\hat{c}_\ell^\dagger$ ($\hat{c}_\ell^-=\hat{c}_\ell$) creates (annihilates) a reservoir electron with vector-index ℓ (e.g. reservoir index, momentum, and spin), $\hat{d}_\delta^+=\hat{d}_\delta$ ($\hat{d}_\delta^-=\hat{d}_\delta^\dagger$) annihilates (creates) an electron in the system with vector-index δ, and $t_{\ell\delta}^+=t_{\ell\delta}$, $t_{\ell\delta}^-=t_{\ell\delta}^*$. Furthermore, we express [45] $L_T=\sum_{\xi,\theta=\pm,\ell\delta}\xi t_{\ell\delta}^\xi C_\ell^{\xi\theta}D_\delta^{\xi\theta}$, where $\theta=\pm$ determines if the operators $\hat{c}_\ell^\xi$ and $\hat{d}_\delta^\xi$ act to the left (+) or to the right (−), e.g. $C_\ell^{\xi+}\hat{\rho}(E)=\hat{c}_\ell^\xi\hat{\rho}(E)$ and $C_\ell^{\xi-}\hat{\rho}(E)=\hat{\rho}(E)\hat{c}_\ell^\xi$. Consider the term[8] $L_TW_0(E)L_T\hat{\rho}(E)$ that appears after the first iteration in Eq. (2.17). In particular, we have

$$\begin{aligned}L_TW_0(E)L_T &= \sum_{\xi\theta\ell\delta}\sum_{\xi'\theta'\ell'\delta'}\xi\xi' t_{\ell\delta}^\xi t_{\ell'\delta'}^{\xi'}C_{\ell'}^{\xi'\theta'}D_{\delta'}^{\xi'\theta'}W_0(E)C_\ell^{\xi\theta}D_\delta^{\xi\theta}\\ &= \sum_{\xi\theta\ell\delta}\sum_{\xi'\theta'\ell'\delta'}\xi\xi' t_{\ell\delta}^\xi t_{\ell'\delta'}^{\xi'}D_{\delta'}^{\xi'\theta'}C_{\ell'}^{\xi'\theta'}W_0(E)D_\delta^{\xi\theta}C_\ell^{\xi\theta},\end{aligned} \tag{2.18}$$

where we have used the commutation relation $C_\ell^{\xi\theta}D_\delta^{\xi'\theta'}=-\theta\theta' D_\delta^{\xi'\theta'}C_\ell^{\xi\theta}$. Furthermore, using that for a non-interacting fermionic reservoir $C_\ell^{\xi\theta}L_0=[L_0-\xi\epsilon_\ell]C_\ell^{\xi\theta}$, where ϵ_ℓ is the eigenenergy of the reservoir electron with index ℓ, we get

$$\begin{aligned}L_TW_0(E)L_T &= \sum_{\xi\theta\ell\delta}\sum_{\xi'\theta'\ell'\delta'}\xi\xi' t_{\ell\delta}^\xi t_{\ell'\delta'}^{\xi'}D_{\delta'}^{\xi'\theta'}W_0(E+\xi'\epsilon_{\ell'})C_{\ell'}^{\xi'\theta'}D_\delta^{\xi\theta}C_\ell^{\xi\theta}\\ &= -\sum_{\xi\theta\ell\delta}\sum_{\xi'\theta'\ell'\delta'}\xi\xi'\theta\theta' t_{\ell\delta}^\xi t_{\ell'\delta'}^{\xi'}D_{\delta'}^{\xi'\theta'}W_0(E+\xi'\epsilon_{\ell'})D_\delta^{\xi\theta}C_{\ell'}^{\xi'\theta'}C_\ell^{\xi\theta}.\end{aligned} \tag{2.19}$$

We approximate $\hat{\rho}(E)\simeq\hat{\rho}_S(E)\otimes\hat{\rho}_E^{\text{eq}}$, assuming that the macroscopic environment is largely unaffected by the system, and trace out the environment

$$\begin{aligned}\text{Tr}_E\left[L_TW_0(E)L_T\hat{\rho}(E)\right] &= -\sum_{\xi\theta\ell\delta}\sum_{\xi'\theta'\ell'\delta'}\xi\xi'\theta\theta' t_{\ell\delta}^\xi t_{\ell'\delta'}^{\xi'}D_{\delta'}^{\xi'\theta'}W_S(E+\xi'\epsilon_{\ell'})D_\delta^{\xi\theta}\hat{\rho}_S(E)\text{Tr}_E\left[C_{\ell'}^{\xi'\theta'}C_\ell^{\xi\theta}\hat{\rho}_E^{\text{eq}}\right]\\ &= \sum_{\xi\theta\ell\delta}\sum_{\theta'\delta'}\theta\theta' t_{\ell\delta}^\xi t_{\ell\delta'}^{-\xi}D_{\delta'}^{(-\xi)\theta'}W_S(E-\xi\epsilon_\ell)D_\delta^{\xi\theta}\hat{\rho}_S(E)n_{F,\ell}^{(-\xi\theta)},\end{aligned} \tag{2.20}$$

where we have used that $\text{Tr}_E[C_{\ell'}^{\xi'\theta'}C_\ell^{\xi\theta}\hat{\rho}_E^{\text{eq}}]=\delta_{\ell\ell'}\delta_{\xi,-\xi'}n_{F,\ell}^{(-\xi\theta)}$, where $n_{F,\ell}^+=n_{F,\ell}$ is the Fermi-Dirac distribution evaluated at the energy corresponding to index ℓ, and $n_{F,\ell}^-=1-n_{F,\ell}(\equiv\bar{n}_{F,\ell})$, and we have expressed W_0 as a geometric series in L_E whereby the contribution from L_E to W_0 vanishes

[8] Terms with an odd number of L_T vanish upon tracing over the environment degrees of freedom.

upon taking the trace. Next, we formally insert completeness relations in terms of eigenstates of $\hat{H}_S$, $\sum_a |a\rangle\langle a|$ with energy ϵ_a,

$$\begin{aligned}\mathrm{Tr}_E\left[L_T W_0(E) L_T \hat{\rho}(E)\right] &= \sum_{\xi\theta\theta'\ell\delta\delta'} \sum_{aa'} \theta\theta' t^{\xi}_{\ell\delta} t^{-\xi}_{\ell\delta'} D^{(-\xi)\theta'}_{\delta'} W_S(E-\xi\epsilon_\ell)|a\rangle\langle a|(D^{\xi\theta}_{\delta}\hat{\rho}_S(E))|a'\rangle\langle a'|n^{(-\xi\theta)}_{F,\ell} \\ &= \sum_{\xi\theta\theta'\delta\delta'} \sum_{aa'} \theta\theta' D^{(-\xi)\theta'}_{\delta'} |a\rangle\langle a|(D^{\xi\theta}_{\delta}\hat{\rho}_S(E))|a'\rangle\langle a'| I_{\delta\delta'\xi\theta aa'}, \end{aligned} \tag{2.21}$$

where

$$I_{\delta\delta'\xi\theta aa'} = \sum_{\ell} \frac{t^{\xi}_{\ell\delta} t^{-\xi}_{\ell\delta'} n^{(-\xi\theta)}_{F,\ell}}{E - \xi\epsilon_\ell + i\eta - (\epsilon_a - \epsilon_{a'})}. \tag{2.22}$$

Letting the reservoir vector-index $\ell = (R, k, \sigma)$ denote an electron with momentum k and spin σ in reservoir R, we have

$$I_{\delta\delta'\xi\theta aa'} = \sum_{R\sigma} \int d\epsilon \frac{\nu_R(\epsilon) t^{\xi}_{R\sigma k\delta} t^{-\xi}_{R\sigma k\delta'} n^{(-\xi\theta)}_{F,R}(\epsilon)}{E - \xi\epsilon + i\eta - (\epsilon_a - \epsilon_{a'})}, \tag{2.23}$$

where ν_R is the reservoir density of states. Considering the situation where the tunneling coefficients and density of states are assumed to be constant, and $n^{+(-)}_{F,R}$ is assumed to be either 0 or 1, i.e. the reservoirs are either completely empty or completely full (unidirectional transport), we get

$$\begin{aligned} I_{\delta\delta'\xi\theta aa'} &= \sum_{R\sigma} \nu_R t^{\xi}_{R\sigma\delta} t^{-\xi}_{R\sigma\delta'} \delta_{-\xi\theta,s_R} \int d\epsilon \frac{1}{E - \xi\epsilon - (\epsilon_a - \epsilon_{a'}) + i\eta} \\ &= -i\pi \sum_{R\sigma} \nu_R t^{\xi}_{R\sigma\delta} t^{-\xi}_{R\sigma\delta'} \delta_{-\xi\theta,s_R} \end{aligned} \tag{2.24}$$

where $s_R = +(-)$ corresponds to a full (empty) reservoir and the latter equality follows from the Cauchy principal relation [26, p. 217] in the wide-band approximation where the integral is extended from minus to plus infinity. Hence, in this limit, $I_{\delta\delta'\xi\theta aa'}$ does not depend on a and a', and we get

$$\mathrm{Tr}_E\left[L_T W_0(E) L_T \hat{\rho}(E)\right] = -\frac{i\hbar}{2} \sum_{\xi\theta\theta'\delta\delta'} \theta\theta' D^{(-\xi)\theta'}_{\delta'} D^{\xi\theta}_{\delta} \hat{\rho}_S(E) I_{\delta\delta'\xi\theta}, \quad I_{\delta\delta'\xi\theta} \equiv \frac{2\pi}{\hbar} \sum_{R\sigma} \nu_R t^{\xi}_{R\sigma\delta} t^{-\xi}_{R\sigma\delta'} \delta_{-\xi\theta,s_R}. \tag{2.25}$$

For higher-order terms in (2.17), upon commuting all the C's to the right (as above), the leftmost C will give rise to the substitution, $E \to E + \xi\epsilon$ in all the W_0's, and hence lead to an integral where the integrand is a product of simple fractions with poles on the same complex half-plane. Indeed, Gurvitz and Prager showed that all such higher-order contributions vanish in the limit of unidirectional transport and wideband reservoirs [32]. Hence, the iteration loop in Eq. (2.17) closes, and we obtain

$$(E + i\eta - L_S)\hat{\rho}_S(E) = i\hbar\mathcal{D}\hat{\rho}_S(E) + i\hbar\hat{\rho}_S(t_0), \quad \mathcal{D} = -\frac{1}{2} \sum_{\xi\theta\theta'\delta\delta'} \theta\theta' D^{(-\xi)\theta'}_{\delta'} D^{\xi\theta}_{\delta} I_{\delta\delta'\xi\theta}, \tag{2.26}$$

where we have traced out the environment. Upon transforming back to time-space Eq. (2.26) gives the form in Eq. (2.12) with the specific dissipator $\mathcal{D}$ in Eq. (2.26). At this stage, the dissipator might still have a rather formal appearance; however, it will take a more familiar form for the specific situation considered in Sec. 3.2 (see also the info-box below).

Consider the case of unidirectional electron transport illustrated in Fig. 2.2, where (spinless) electrons enter from a full left reservoir, into a single level which can be either empty or occupied by an electron, and tunnel out to an empty right reservoir (see e.g. the experiment in Ref. [47]). The tunneling Hamiltonian

reads, $\hat{H}_T = \sum_k ((t_L \hat{c}^\dagger_{L,k} + t_R \hat{c}^\dagger_{R,k})\hat{d} + \text{h.c.})$, and the dissipator becomes

$$\mathcal{D} = -\frac{1}{2} \sum_{\xi\theta\theta'} D^{(-\xi)\theta'} D^{\xi\theta} \left(\gamma_L \delta_{-\xi\theta,+} + \gamma_R \delta_{-\xi\theta,-} \right), \quad \gamma_{L,R} \equiv \frac{2\pi}{\hbar} \nu_{L,R} |t_{L,R}|^2. \tag{2.27}$$

Upon acting on the reduced density matrix, we find

$$\mathcal{D}\hat{\rho}_S = \gamma_L \left(\hat{d}^\dagger \hat{\rho}_S \hat{d} - \frac{1}{2} \{ \hat{\rho}_S, \hat{d}\hat{d}^\dagger \} \right) + \gamma_R \left(\hat{d} \hat{\rho}_S \hat{d}^\dagger - \frac{1}{2} \{ \hat{\rho}_S, \hat{d}^\dagger \hat{d} \} \right). \tag{2.28}$$

Hence, the dissipator takes the so-called *Lindblad* form [27]. The dissipator governs the incoherent evolution of the level due to the coupling to the reservoirs. In particular, the terms $\hat{d}^\dagger \hat{\rho}_S \hat{d}$ and $\hat{d} \hat{\rho}_S \hat{d}^\dagger$ describe incoherent jump processes that change the electron number in the system, and the anti-commutators ensure conservation of probability. The reduced density operator has only two diagonal matrix elements, which are the probabilities of being in the empty state, $\rho_{S,00} \equiv p_0$, or occupied state, $\rho_{S,11} \equiv p_1$, respectively. From Eq. (2.28), we obtain (the coherent contribution vanishes)

$$\frac{d}{dt} \begin{pmatrix} p_0 \\ p_1 \end{pmatrix} = \begin{pmatrix} -\gamma_L & \gamma_R \\ \gamma_L & -\gamma_R \end{pmatrix} \begin{pmatrix} p_0 \\ p_1 \end{pmatrix}. \tag{2.29}$$

From this, and from normalization of the probabilities, we obtain the steady-state occupations $d(p_0^{(S)}, p_1^{(S)})/dt = (0,0)$ as $p_0^{(S)} = \gamma_R/(\gamma_L + \gamma_R)$ and $p_1^{(S)} = \gamma_L/(\gamma_L + \gamma_R)$, and the expression for the particle current as $I \equiv \gamma_R p_1^{(S)} = \gamma_L p_0^{(S)} = \gamma_L \gamma_R/(\gamma_L + \gamma_R)$. In Sec. 3.1.2 we consider the current through a non-interacting level as obtained by the standard Landauer-Büttiker formula (see Eq. (3.24)), and we note that the result above indeed coincides with the Landauer-Büttiker formula when the difference in the two reservoir distribution functions approaches one.

3 | Transport in nanostructures

In section 1.2 we introduced an important example of a nanostructure where electrons are confined in a region of size in the order of nanometers to a few microns: quantum dots[1]. Such structures can be fabricated by structure fabrication or by depletion gates, e.g. by creating a confining potential in the two-dimensional electron gas formed at the interface between two semiconductor materials such as AlGaAs/InGaAs [48]. Upon coupling a quantum dot to metallic leads, the electrons can tunnel between the QD and the leads which thereby act as drain and source electron reservoirs (we considered a particular example in the end of the previous chapter). Hence, the number of electrons on the QD can fluctuate and cause a broadening of the discrete energy levels in the QDs. However, for small enough coupling to the leads the broadening can be much smaller than the spacing between the levels. With a back gate the energy levels can be tuned relative to the electrochemical potentials in the reservoirs, and hence the dot can act as a filter for transport between the reservoirs. However, due to Coulomb-repulsion between electrons, it costs a charging energy to add an electron to the QD, and if no reservoir electrons have sufficient energy, transport is Coulomb-blockaded. These governing mechanisms have enabled control of transport on the level of single electrons [49].

In this chapter we describe the works in publications I, II, IV studying transport properties of two particular setups involving quantum dots: 1) Thermoelectric effects in a system of Coulomb-coupled quantum dots (publication I), and 2) non-local splitting characteristics of a Cooper pair splitter (publication II, IV). The two systems are introduced in Secs. 3.1 and 3.2, respectively.

3.1 Thermoelectric effects: Coulomb-coupled quantum dots

This section is based on Publication I, Physical Review B 96, 115415 (2017) by N. Walldorf, A.-P. Jauho, and K. Kaasbjerg, and N. Walldorf's master's thesis [50].

A characteristic of a stationary non-equilibrium steady state is the existence of stationary non-equilibrium (mean) currents [52], such as the electron flow from a region of high to low electrochemical potential or the heat flow between hot and cold parts of a system, together referred to as thermoelectric currents.

In nanostructures, non-equilibrium conditions can be established from differences in the distribution of electrons in two or more reservoirs, whereby currents are generated in response to reestablish equilibrium. However, if the electrochemical potentials and temperatures in the reservoirs are kept fixed, stationary non-equilibrium currents can flow persistently. Since quantum dots can 'filter' out the particular electrons that contribute to the transport currents between source and drain reservoirs, such structures are ideal for studying thermoelectric effects. In particular, the selective tunneling of thermally excited electrons enables the Peltier effect where a heat current develops between source-drain reservoirs in response to an electric bias [53], or the reverse Seebeck effect, where an electric current develops in response to a temperature difference between the source and drain reservoirs (which in turn may develop a thermovoltage) [54]. In such source-QD-drain setups (e.g. System 1

[1] One may distinguish between metallic dots with a continuum of density of states and non-metallic dots with discrete states [31]. We consider the latter only in this thesis.

in Fig. 3.1a), however, the heat and charge currents are intimately linked: The Peltier effect can cool down one part of the conductor circuit (one of the reservoirs), but only at the cost of heating up the other part of the conductor circuit (the other reservoir). However, the presence of Coulomb interaction provides an extra handle to engineer systems with tailored thermoelectric properties [51]. In particular, R. Sánchez and M. Büttiker proposed a three-terminal setup with Coulomb-coupled quantum dots (CCQD) [14], as illustrated in Fig. 3.1a, where a heat reservoir (reservoir C in System 2 in Fig. 3.1a) is spatially separated from the conductor circuit (System 1), and the direction of heat and charge flow becomes decoupled [15]. A picture of an experimental realization of such a setup, fabricated from a GaAs/AlGaAs wafer, can be found in Figure 1 in the supplementary information to Ref. [15].

The three-terminal configuration has been realized for energy harvesting, where a thermal gradient is converted into an electric current [15], as well as for demonstrating so-called "Maxwell's demon" cooling [16] (in the latter experiment for metallic dots). The two effects are a consequence of the same underlying mechanism. Specifically, the cooling mechanism can be understood from the cycle of processes illustrated in Fig. 3.1b: If QD2 is occupied (top left panel), and reservoir C is sufficiently cold such that the probability that the electron tunnels into lead C is small, a hot electron above the electrochemical potential in lead A can overcome the Coulomb-interaction barrier (illustrated by dashed line) and tunnel into QD1 and thereby cool lead A[2]. This increases the effective potential in QD2, whereby the occupying electron can tunnel into lead C (top right panel). The electron in QD1 can then tunnel into lead B below the electrochemical potential (bottom right panel), and thereby cool the lead [16]. If the rate of tunneling from lead C is larger than the tunneling rates from leads A or B, an electron can then tunnel into QD2 to return to the initial configuration. Hence, as a result, the current carrying System 1 is cooled from the Coulomb-mediated energy exchange to System 2, in spite of the fact that no electrons are exchanged between the two systems.

While such systems indeed invite for many interesting ideas to explore[3], in the following we are interested in studying the underlying electron transport processes. The qualitative picture given above

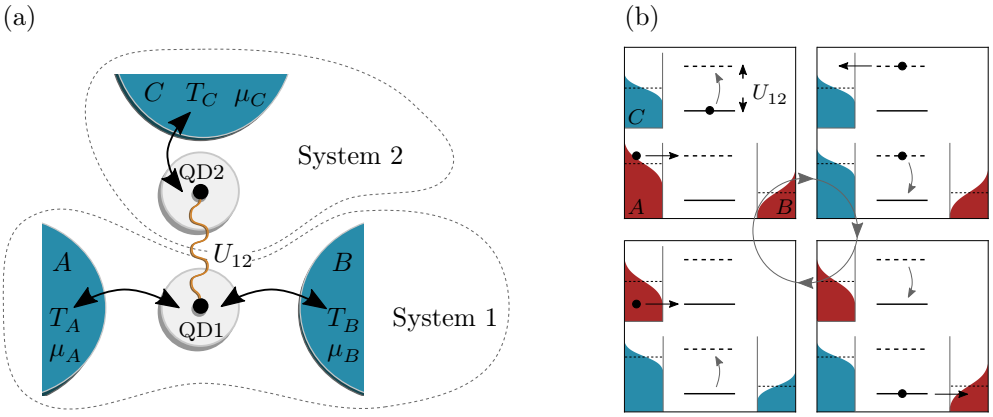

Figure 3.1: (a) Spatial illustration of the CCQD system studied in Sec. 3.1.3 consisting of two Coulomb-coupled QDs (QDδ, $\delta \in \{1, 2\}$) with inter-dot Coulomb interaction U_{12}, tunnel-coupled in a three-terminal configuration to leads $\ell \in \{A, B, C\}$ (no tunneling allowed between the QDs) with temperatures T_ℓ and electrochemical potentials μ_ℓ. (b) Energy diagrams showing the sequence of sequential tunneling processes that cool System 1. The positions of the dot levels when the other dot is empty (occupied) is illustrated with solid (dotted) lines. Adapted from Refs. [1, 50, 51, 16].

[2] In the figure we illustrate this as a sharpening of the sketched distribution function in lead A and a change of color from red to blue when going from the top left panel to the top right panel.

[3] As an open question we may, for example, ask: Can we utilize the cooling mechanism of the conductor circuit and develop a self-cooling diode by tuning the particular coupling to the leads in System 1?

describes the thermoelectric effect in terms of tunneling events of electrons, and master equations provide an ideal method for exploring and characterizing such systems. While the effect may be explained qualitatively in terms of single-electron transitions, we will in the following apply the T-matrix approach introduced in Sec. 2.1, which allows us to go beyond sequential tunneling and also study the effect of higher-order tunneling (cotunneling) processes. These inevitable coherent processes are examples of the underlying quantum properties that govern the non-equilibrium transport. Importantly, in contrast to the often applied wide-band approximation, we include energy-dependent couplings to the reservoirs in the formalism to discuss important aspects of the particular coupling.

3.1.1 Master equation and transport currents

To study systems like the one illustrated in Fig. 3.1a, we consider the Hamiltonian

$$\hat{H} = \hat{H}_0 + \hat{H}_T, \qquad \hat{H}_0 = \hat{H}_{\text{dots}} + \hat{H}_{\text{leads}}, \tag{3.1}$$

which describes a system of CCQDs with Hamiltonian $\hat{H}_{\text{dots}}$ that is coupled to external leads with Hamiltonian $\hat{H}_{\text{leads}}$ by tunnel couplings described by $\hat{H}_T$. In particular, we consider a spinless model of Coulomb-coupled single-level QDs described by the Hamiltonian

$$\hat{H}_{\text{dots}} = \sum_{\delta} \epsilon_\delta \hat{c}_\delta^\dagger \hat{c}_\delta + \sum_{\langle \delta,\delta' \rangle} U_{\delta\delta'} \hat{n}_\delta \, \hat{n}_{\delta'}. \tag{3.2}$$

The first term describes electrons in the individual QDs (QDδ), created (annihilated) by $\hat{c}_\delta^\dagger$ ($\hat{c}_\delta$) with energy ϵ_δ. If the intradot Coulomb-interaction between electrons occupying the same QD is sufficiently strong (it is typically an order of magnitude larger than the level spacing [14]), the excess electron occupancy of the quantum dot fluctuates between zero and one. In this case, a spinless model is sufficient to study the thermoelectric effects described above[4] [14]. The energy levels can be controlled by gate voltages $\epsilon_\delta = -eV_\delta$, where V_δ is the gate potential on QDδ. Importantly, *inter*dot Coulomb-interaction between electrons occupying different quantum dots, as described by the second term in Eq. (3.2), is crucial for the thermoelectric properties of the system. In this term, $\hat{n}_\delta = \hat{c}_\delta^\dagger \hat{c}_\delta$ is the occupation number operator, $U_{\delta\delta'}$ is the interdot Coulomb interaction, and the summation is over all QD pairs (we consider the specific configuration in Fig. 3.1a in Sec. 3.1.3). The interdot Coulomb-interaction depends on the particular experimental setup, but typical values are ~ 0.1 meV [55], although values order of magnitudes larger are also reported in the literature [56].

We describe the leads by non-interacting electron reservoirs, $\hat{H}_{\text{leads}} = \sum_{\ell k} \epsilon_{\ell k} \hat{c}_{\ell k}^\dagger \hat{c}_{\ell k}$, where $\hat{c}_{\ell k}^\dagger$ ($\hat{c}_{\ell k}$) creates (annihilates) an electron with momentum k and energy $\epsilon_{\ell k}$ in lead ℓ. The leads are assumed to be in local equilibrium with temperature T_ℓ and electrochemical potential $\mu_\ell = \mu_0 - eV_\ell$, where μ_0 is the equilibrium chemical potential and V_ℓ is the voltage applied to lead ℓ. We define the tunneling Hamiltonian that couples the QD system to the leads as $\hat{H}_T = \sum_{\ell k \delta} (t_{\ell k \delta} \hat{c}_\delta^\dagger \hat{c}_{\ell k} + \text{h.c.})$, where the tunneling amplitude $t_{\ell k \delta}$ is allowed to be energy-dependent, and we consider the case where each lead couples to one QD only.

As introduced in Sec. 2.1, the T-matrix approach calculates tunneling rates between diagonal components of the reduced density operator which describes probabilities for being in particular states. Hence, we can write a master equation governing the non-equilibrium occupation probabilities p_m as in Eq. (2.8), where m index eigenstates of the number operator for the QD system in the absence of tunneling, and Γ_{mn} denotes the (regularized) tunneling-induced transition rate from QD state $|m\rangle$ to $|n\rangle$ obtained from Eq. (2.7)

$$\tilde{\Gamma}_{mn} = \frac{2\pi}{\hbar} \sum_{jj'} |\langle j'|\langle n|\hat{T}|m\rangle|j\rangle|^2 \rho_j \delta(\Delta_{mn} + E_{\text{leads},j'} - E_{\text{leads},j}), \tag{3.3}$$

[4] We consider a system in Sec. 3.2 where the electron spin is paramount.

where $E_{\text{dots},m} = \langle m|\hat{H}_{\text{dots}}|m\rangle$, $\Delta_{mn} \equiv E_{\text{dots},n} - E_{\text{dots},m}$, ρ_j is the thermal probability of finding the leads in the initial state, the sum is over initial and final states of the leads, and the T matrix obeys Eq. (2.6) with $E_i = E_{\text{dots},m} + E_{\text{leads},j}$, for leads in state $|j\rangle$ with energy $E_{\text{leads},j} = \langle j|\hat{H}_{\text{leads}}|j\rangle$. As mentioned in Sec. 2.1, a regularization procedure is required for tunneling rates above first order (discussed below), and we denote the regularized rates without a tilde.

We are interested in the stationary non-equilibrium steady-state occupation probabilities, hence we solve the master equation for $\dot{p}_m = 0$ and denote the stationary solution by $p^{(S)}$. The steady-state transport currents can then be obtained from the occupation probabilities. The electric current going into lead ℓ is defined as

$$I_\ell \equiv -e\left\langle \sum_k \frac{d\hat{n}_{\ell k}}{dt}\right\rangle = -e\sum_{mn} p_m^{(S)}\Big(\Gamma_{mn}^{\ell\leftarrow} - \Gamma_{mn}^{\ell\rightarrow}\Big), \tag{3.4}$$

where we have expressed the electric current in terms of the total rate of electrons tunneling (between states in an occupation representation) into lead ℓ, minus the total rate of electrons tunneling out of lead ℓ. We define the heat current going into lead ℓ as [57]

$$J_\ell \equiv \left\langle \sum_k (\epsilon_{\ell k} - \mu_\ell)\frac{d\hat{n}_{\ell k}}{dt}\right\rangle = \sum_{mn} p_m^{(S)}\Big(W_{mn}^{\ell\leftarrow} - W_{mn}^{\ell\rightarrow}\Big), \tag{3.5}$$

where we have expressed the heat current in terms of heat transfer rates W which we define below.

Transition and heat transfer rates

We consider the first- (sequential processes) and second- (cotunneling processes) order contributions to the T-matrix master equation. Effects such as tunneling-induced level broadening and level shifts [58, 59, 60] are not captured by this approach, which is only valid in the weak-coupling regime where the coupling to the leads is smaller than the temperature and the interdot Coulomb interaction.

The transition rates for lowest-order single-electron sequential tunneling processes between the QD system and the leads become

$$\Gamma_{mn}^{\overrightarrow{\ell}} = \hbar^{-1}\tilde{\gamma}^\ell(\Delta_{mn})n_{F,\ell}(\Delta_{mn}), \tag{3.6}$$

$$\Gamma_{mn}^{\overleftarrow{\ell}} = \hbar^{-1}\tilde{\gamma}^\ell(\Delta_{nm})\bar{n}_{F,\ell}(\Delta_{nm}), \tag{3.7}$$

where Eq. (3.6) (Eq. (3.7)) is the sequential rate of tunneling out of, $\rightarrow$, (into, $\leftarrow$,) lead ℓ, thereby changing the state of the QD system from m to n (see e.g. the example in Fig. 3.2a), $\tilde{\gamma}^\ell(\epsilon) \equiv 2\pi\nu_\ell(\epsilon)|t_\ell(\epsilon)|^2$ is the lead coupling[5] with $\nu_\ell(\epsilon)$ being the lead density of states, $\bar{n}_{F,\ell}(\epsilon) = 1 - n_{F,\ell}(\epsilon)$ with $n_{F,\ell}(\epsilon) = [\exp(\beta_\ell(\epsilon-\mu_\ell))+1]^{-1}$ being the Fermi-Dirac distribution in lead ℓ, and $\beta_\ell = 1/(k_B T_\ell)$. The macroscopic leads are assumed to remain in equilibrium.

Consider e.g. the rate $\Gamma_{mn}^{\overrightarrow{\ell}}$ governing the process $|f\rangle = \hat{c}_\delta^\dagger\hat{c}_{\ell k}|i\rangle$, $|i\rangle = |i_\ell i_\delta\rangle$. From Eq. (3.3) we have

$$\begin{aligned}\Gamma_{mn}^{\overrightarrow{\ell}} &= \frac{2\pi}{\hbar}\sum_{k i_\ell} |\langle i|\hat{c}_{\ell k}^\dagger\hat{c}_\delta t_{\ell k\delta}\hat{c}_\delta^\dagger\hat{c}_{\ell k}|i\rangle|^2\rho_{i_\ell}\delta(\Delta_{mn}-\epsilon_{\ell k})\\ &= \frac{2\pi}{\hbar}\sum_{k i_\ell} |t_{\ell k\delta}|^2\langle i_\ell|\hat{c}_{\ell k}^\dagger\hat{c}_{\ell k}|i_\ell\rangle\rho_{i_\ell}\delta(\Delta_{mn}-\epsilon_{\ell k}),\end{aligned} \tag{3.8}$$

where we have used that the fermionic occupancies are either zero or one to omit the absolute squares, and that QDδ is initially empty (the other case is trivially zero due to Pauli exclusion). Upon summing

[5] In contrast to the info-box in Sec. 2.3, the lead couplings are here defined in units of energy, and are expressed with a tilde as a reminder.

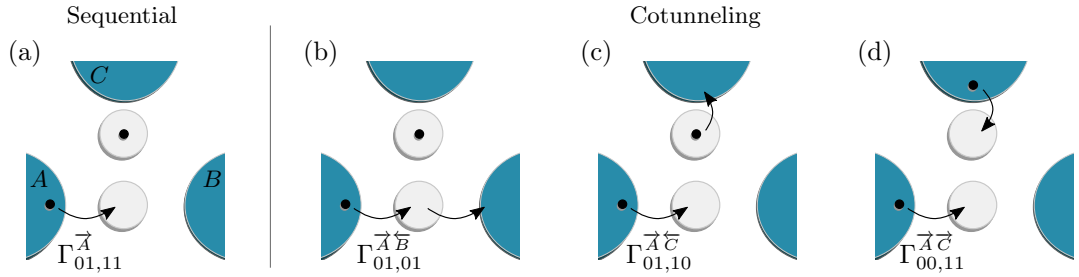

Figure 3.2: Examples of tunneling processes for the particular setup in Fig. 3.1a, see also Sec. 3.1.3. Figure adapted from Ref. [50].

over the initial lead states we obtain

$$\begin{aligned}\Gamma^{\vec{\ell}}_{mn} &= \frac{2\pi}{\hbar}\sum_k |t_{\ell\delta}(\epsilon_{\ell k})|^2 n_{F,\ell}(\epsilon_{\ell k})\delta(\Delta_{mn}-\epsilon_{\ell k}) \\ &= \hbar^{-1}\int \mathrm{d}\epsilon\, \tilde{\gamma}^{\ell}(\epsilon) n_{F,\ell}(\epsilon)\delta(\Delta_{mn}-\epsilon) \\ &= \hbar^{-1}\tilde{\gamma}^{\ell}(\Delta_{mn}) n_{F,\ell}(\Delta_{mn}).\end{aligned} \tag{3.9}$$

The sequential-tunneling heat transfer rate in lead ℓ is calculated as the tunneling rate multiplied by the energy of the tunneling electron relative to the electrochemical potential in the lead,

$$\begin{aligned}W^{\vec{\ell}}_{\ell,mn} &= (\Delta_{mn}-\mu_\ell)\Gamma^{\vec{\ell}}_{mn}, \\ W^{\overleftarrow{\ell}}_{\ell,mn} &= (\Delta_{nm}-\mu_\ell)\Gamma^{\overleftarrow{\ell}}_{mn},\end{aligned} \tag{3.10}$$

where the indices follow the notation of the tunneling rates, however, the additional first subscript ℓ refers to the lead in which the heat transfer rate is calculated.

Next, we consider the rates for second-order cotunneling processes. In addition to local cotunneling processes where a net electron is transferred between two leads attached to the same QD (see e.g. the example in Fig. 3.2b), we also consider nonlocal cotunneling processes [61, 62] in which a net electron is transferred between leads attached to different QDs (example in Fig. 3.2c), as well as pair-cotunneling processes where two electrons tunnel into, or out of, the CCQD system in one coherent process [63, 64] (example in Fig. 3.2d). In particular, the more unconventional process of nonlocal cotunneling becomes important for the configuration in Fig. 3.1. The (unregularized) rate reads

$$\tilde{\Gamma}^{\vec{\ell}\,\overleftarrow{\ell'}}_{mn} = \int \frac{d\epsilon}{2\pi\hbar}\tilde{\gamma}^{\ell}(\epsilon)\tilde{\gamma}^{\ell'}(\epsilon-\Delta_{mn}) n_{F,\ell}(\epsilon)\bar{n}_{F,\ell'}(\epsilon-\Delta_{mn})\left|\frac{1}{\Delta_{vm}+\epsilon+i\eta}+\frac{1}{\Delta_{v'n}-\epsilon+i\eta}\right|^2, \tag{3.11}$$

and gives the rate of net transfer of an electron out of lead ℓ and into lead ℓ', and v (v') refers to the virtually occupied intermediate state in the process where an electron initially tunnels from lead ℓ and into the QD system (from the QD system and into lead ℓ')[6].

Consider the cotunneling rate in Eq. (3.11) leading to the final state $|f\rangle = \hat{c}^\dagger_{\ell' k}\hat{c}_{\delta'}\hat{c}^\dagger_{\delta}\hat{c}_{\ell k}|i\rangle$, $\ell\neq\ell'$, $\delta\neq\delta'$.

[6] For example, for the process illustrated in Fig. 3.2c, v (v') refers to the intermediate state where both dots are occupied (empty).

From Eq. (3.3) we have

$$\tilde{\Gamma}^{\vec{\ell}\,\vec{\ell'}}_{mn} = \frac{2\pi}{\hbar}\sum_{k_\ell k_{\ell'} i_\ell i_{\ell'}} \Big|\langle i|\hat{c}^\dagger_{\ell k}\,\hat{c}_\delta\,\hat{c}^\dagger_{\delta'}\hat{c}_{\ell' k}\Big[t^*_{\ell' k\delta'}\hat{c}^\dagger_{\ell' k}\hat{c}_{\delta'}(\Delta_{vm}+\epsilon_{\ell k}+i\eta)^{-1}t_{\ell k\delta}\hat{c}^\dagger_\delta\hat{c}_{\ell k} \\ +t_{\ell k\delta}\hat{c}^\dagger_\delta\hat{c}_{\ell k}(\Delta_{v'm}-\epsilon_{\ell' k}+i\eta)^{-1}t^*_{\ell' k\delta'}\hat{c}^\dagger_{\ell' k}\hat{c}_{\delta'}\Big]|i\rangle\Big|^2 \rho_{i_\ell}\rho_{i_{\ell'}}\delta(\Delta_{mn}+\epsilon_{\ell' k}-\epsilon_{\ell k}), \tag{3.12}$$

where v, v' is defined above. Upon performing the sum over initial lead states we obtain

$$\begin{aligned}\tilde{\Gamma}^{\vec{\ell}\,\vec{\ell'}}_{mn} &= \frac{1}{2\pi\hbar}\int d\epsilon \int d\epsilon' \tilde{\gamma}^{\ell}(\epsilon)\tilde{\gamma}^{\ell'}(\epsilon') n_{F,\ell}(\epsilon)\bar{n}_{F,\ell'}(\epsilon')\left|\frac{1}{\Delta_{vm}+\epsilon+i\eta}+\frac{1}{\Delta_{v'm}-\epsilon'+i\eta}\right|^2 \delta(\Delta_{mn}+\epsilon'-\epsilon) \\ &= \int \frac{d\epsilon}{2\pi\hbar}\tilde{\gamma}^{\ell}(\epsilon)\tilde{\gamma}^{\ell'}(\epsilon-\Delta_{mn}) n_{F,\ell}(\epsilon)\bar{n}_{F,\ell'}(\epsilon-\Delta_{mn})\left|\frac{1}{\Delta_{vm}+\epsilon+i\eta}+\frac{1}{\Delta_{v'n}-\epsilon+i\eta}\right|^2 .\end{aligned} \tag{3.13}$$

The remaining cotunneling rates relevant for this study are provided in Appendix A.2.1.

Analogously, the cotunneling heat transfer rates into, or out of, the leads are calculated a posteriori by multiplying the integrand in the cotunneling rate by the energy of the tunneling electron relative to the electrochemical potential in the lead. For example, for the nonlocal cotunneling process between lead l and l', the heat transfer rate in lead ℓ reads

$$\tilde{W}^{\vec{\ell}\,\vec{\ell'}}_{\ell,mn} = \int \frac{d\epsilon}{2\pi\hbar}(\epsilon-\mu_\ell)\tilde{\gamma}^{\ell}(\epsilon)\tilde{\gamma}^{\ell'}(\epsilon-\Delta_{mn}) n_{F,\ell}(\epsilon)\bar{n}_{F,\ell'}(\epsilon-\Delta_{mn})\left|\frac{1}{\Delta_{vm}+\epsilon+i\eta}+\frac{1}{\Delta_{v'n}-\epsilon+i\eta}\right|^2, \tag{3.14}$$

with the heat transfer rate in lead ℓ', $\tilde{W}^{\vec{\ell}\,\vec{\ell'}}_{\ell',mn}$, given as above but with $(\epsilon-\mu_\ell)$ replaced by $(\epsilon-\Delta_{mn}-\mu_{\ell'})$. The remaining cotunneling heat transfer rates follow analogously.

In summary, we consider the processes

$$\Gamma_{mn} \equiv \sum_\ell(\Gamma^{\ell\leftarrow}_{mn}+\Gamma^{\ell\rightarrow}_{mn}), \quad \Gamma^{\ell\leftarrow}_{mn} \equiv \Gamma^{\leftarrow}_{\ell mn} + \sum_{\ell'}(\Gamma^{\leftarrow\rightarrow}_{\ell\,\ell' mn}+\Gamma^{\leftarrow\leftarrow}_{\ell\,\ell' mn}), \quad \Gamma^{\ell\rightarrow}_{mn} \equiv \Gamma^{\rightarrow}_{\ell mn} + \sum_{\ell'}(\Gamma^{\rightarrow\leftarrow}_{\ell\,\ell' mn}+\Gamma^{\rightarrow\rightarrow}_{\ell\,\ell' mn}). \tag{3.15}$$

Results for transport through a single level and for the particular setup in Fig. 3.1a are discussed in Secs. 3.1.2 and 3.1.3, respectively.

Cotunneling integrals and regularization

To calculate the cotunneling rates, we need to evaluate the integral over energies. Analytically, when a cotunneling process involves reservoirs with equal temperature T, the product of energy-dependent Fermi functions which enters into the cotunneling rates can be separated by

$$n_{F,\ell}(\epsilon+\Delta)\bar{n}_{F,\ell'}(\epsilon) = n_B\left(\frac{\Delta+\mu_{\ell'}-\mu_\ell}{k_BT}\right)\Big[n_{F,\ell'}(\epsilon)-n_{F,\ell}(\epsilon+\Delta)\Big], \tag{3.16}$$

where n_B is the Bose-Einstein function. In such cases we can express the cotunneling rates in terms of integrals of the form

$$I = \int_{-\infty}^{\infty} d\epsilon P(\epsilon)\Big[n_{F,\ell'}(\epsilon)-n_{F,\ell}(\epsilon+\Delta)\Big]\left|\frac{c_1}{\epsilon-\Delta_1+i\eta}+\frac{c_2}{\Delta_2-\epsilon+i\eta}\right|^2, \tag{3.17}$$

where $P(\epsilon)$ is a polynomial of order n, and Δ, Δ_1, Δ_2, c_1, c_2 are constants. The integral (3.17) can be evaluated analytically using Cauchy's residue theorem [65] and the result is (we refer to App. A.2.2 for details) [50]

$$\begin{aligned} I =& c_1^2 P'(\Delta_1)\mathrm{Re}\left[\psi_{\ell'}^-(\Delta_1) - \psi_{\ell}^-(\Delta_1+\Delta)\right] + \frac{c_1^2\beta}{2\pi}P(\Delta_1)\mathrm{Im}\left[\psi_{1_{\ell'}}^-(\Delta_1) - \psi_{1_\ell}^-(\Delta_1+\Delta)\right] \\ &+ c_2^2 P'(\Delta_2)\mathrm{Re}\left[\psi_{\ell'}^-(\Delta_2) - \psi_{\ell}^-(\Delta_2+\Delta)\right] + \frac{c_2^2\beta}{2\pi}P(\Delta_2)\mathrm{Im}\left[\psi_{1_{\ell'}}^-(\Delta_2) - \psi_{1_\ell}^-(\Delta_2+\Delta)\right] \\ &- \frac{2c_1c_2}{\Delta_1-\Delta_2}\Big(P(\Delta_1)\mathrm{Re}\left[\psi_{\ell'}^-(\Delta_1) - \psi_{\ell}^-(\Delta_1+\Delta)\right] - P(\Delta_2)\mathrm{Re}\left[\psi_{\ell'}^-(\Delta_2) - \psi_{\ell}^-(\Delta_2+\Delta)\right]\Big) \\ &+ R + \mathcal{O}(\eta^{-1}) + \mathcal{O}(\eta), \end{aligned} \tag{3.18}$$

where $\psi_\ell^\pm(\epsilon) \equiv \psi(1/2 \pm i\beta(\epsilon-\mu_\ell)/(2\pi))$ with ψ being the digamma function, $\psi_{1_\ell}^\pm(\epsilon)$ is defined analogously but with ψ_1 being the trigamma function, and assuming $P(\epsilon) = a_0 + a_1\epsilon + a_2\epsilon^2 + a_3\epsilon^3 + a_4\epsilon^4$,

$$R = \begin{cases} a_2(\mu_{\ell'} - \mu_\ell + \Delta)(c_1-c_2)^2, & c_1 - c_2 \neq 0, \\ a_4(\mu_{\ell'} - \mu_\ell + \Delta)c_1^2(\Delta_1-\Delta_2)^2, & c_1 - c_2 = 0. \end{cases} \tag{3.19}$$

The coefficients a_2 or a_4 corresponds to the largest order of $P(\epsilon)$ for which the integral is well-defined.

The divergent contribution in Eq. (3.18) (upon letting $\eta \to 0$) reads

$$\begin{aligned} \mathcal{O}(\eta^{-1}) =& \frac{i}{\eta}\sum_{j=1}^{2}\left[\frac{c_j^2}{2}P(\Delta_j)\left(\psi_{\ell'}^+(\Delta_j) - \psi_{\ell'}^-(\Delta_j) - \psi_\ell^+(\Delta_j+\Delta) + \psi_\ell^-(\Delta_j+\Delta)\right)\right] \\ =& \frac{\pi}{\eta}\sum_{j=1}^{2} c_j^2 P(\Delta_j)\left(n_{F,\ell'}(\Delta_j) - n_{F,\ell}(\Delta_j+\Delta)\right). \end{aligned} \tag{3.20}$$

This diverging term is a well-known artifact of the T-matrix approach. Indeed, from the T matrix in Eq. (2.7) we can identify $i\eta$ as an infinitesimal imaginary shift of the energy of the intermediate state, or equivalently $\hbar/(2\eta)$ a divergent lifetime of the intermediate state [66]. Consider e.g. the local cotunneling processes illustrated in Fig. 3.2b (with corresponding rate from Eq. (A.16)). Phenomenologically, we could think of the cotunneling process with an infinite-lifetime intermediate state as a sequence of sequential tunneling with rate given by the number of intermediates states[7], $\Gamma^{\vec{A}}_{00,10}\hbar/(2\eta)$, times the rate in which the intermediate state sequentially "tunnels out", $\Gamma^{\overleftarrow{B}}_{10,00}$. This is exactly what the expression in Eq. (3.20) gives for this process. Such energy conserving sequential processes have already been included, and to prevent overcounting, this term is omitted following the by now standard regularization scheme first proposed in Ref. [37].

In general, we can identify the divergent contribution using [37, Eq. (27)]

$$\left|\frac{1}{x+i\eta}\right|^2 \to \frac{\pi}{\eta}\delta(x) + \mathcal{P}\frac{1}{x^2}, \quad \eta \to 0^+, \tag{3.21}$$

where $\mathcal{P}$ denotes the principle value. E.g. from Eq. (3.11),

$$\tilde{\Gamma}^{\vec{\ell}\,\overleftarrow{\ell'}}_{mn} \to \frac{\hbar}{2\eta}\left(\Gamma^{\vec{\ell}}_{mv}\Gamma^{\overleftarrow{\ell'}}_{vn} + \Gamma^{\overleftarrow{\ell'}}_{mv'}\Gamma^{\vec{\ell}}_{v'n}\right) + \Gamma^{\vec{\ell}\,\overleftarrow{\ell'}}_{mn}, \tag{3.22}$$

where $\Gamma^{\vec{\ell}\,\overleftarrow{\ell'}}_{mn}$ denotes the regularized cotunneling rate, and we have used the fact that the cross-terms from the absolute squared in Eq. (3.11) do not contribute to any divergences. Similarly, for the cotunneling heat transfer rates, e.g. Eq. (3.14),

$$\tilde{W}^{\vec{\ell}\,\overleftarrow{\ell'}}_{\ell,mn} \to \frac{\hbar}{2\eta}\left[W^{\vec{\ell}}_{\ell,mv}\Gamma^{\overleftarrow{\ell'}}_{vn} + \Gamma^{\overleftarrow{\ell'}}_{mv'}W^{\vec{\ell}}_{\ell,v'n}\right] + W^{\vec{\ell}\,\overleftarrow{\ell'}}_{\ell,mn}. \tag{3.23}$$

[7] See Sec. 3.1.3 for the notation used for the basis states in this example.

In the general case of different lead temperatures as well as more general energy dependence of the lead couplings we can evaluate the cotunneling integrals numerically[8] with a small but finite η, and subsequently subtract the contributions of order η^{-1}. Agreement between analytical and numerical evaluations of the cotunneling rates is verified in previous work [50].

3.1.2 Transport through a non-interacting single level

Before turning our attention to the setup in Fig. 3.1a, let us benchmark the steady-state transport currents obtained from the T-matrix approach against the Landauer-Büttiker (LB) formalism which is exact for non-interacting systems. In particular, consider a single-level QD coupled to two leads $\ell \in \{A, B\}$ (such as the isolated System 1 in Fig. 3.1a). The Hamiltonian of the QD is $\hat{H}_{\rm dots} = \epsilon_1 \hat{c}_1^\dagger \hat{c}_1$, with states labeled by the occupancy, $|n_1\rangle \in \{|0\rangle, |1\rangle\}$.

In the LB formalism, the electric current and heat current going into lead A are given by [29, 67],

$$I_A^{\rm LB} = \frac{-e}{h}\int d\epsilon\, T(\epsilon)[n_{F,B}(\epsilon) - n_{F,A}(\epsilon)], \qquad J_A^{\rm LB} = \frac{1}{h}\int d\epsilon\,(\epsilon-\mu_A) T(\epsilon)[n_{F,B}(\epsilon) - n_{F,A}(\epsilon)], \quad (3.24)$$

respectively, where for a non-interacting single-level QD, the transmission function $T(\epsilon)$ reads

$$T(\epsilon) = \frac{\tilde{\gamma}^A \tilde{\gamma}^B}{(\epsilon-\epsilon_1)^2 + (\tilde{\gamma}/2)^2}, \quad (3.25)$$

with $\tilde{\gamma} = \tilde{\gamma}^A + \tilde{\gamma}^B$ (assuming energy-independent lead couplings in this example), and we have omitted any tunneling-induced energy shift which is not captured by the T-matrix approach.

Transport currents obtained with the two approaches for a finite bias and temperature difference ($T_B = 2T_A \equiv 2T$) between the leads are plotted in Fig. 3.3 as a function of the gate voltage for two different lead coupling strengths. To demonstrate the importance of cotunneling processes, we have included master equation (ME) results based on sequential tunneling only (black dotted curves) that do not depend on $\tilde{\gamma}^\ell$ in the units shown, as well as sequential plus cotunneling (dashed curves). The results based purely on sequential tunneling differ significantly from the LB results unless $\tilde{\gamma}^\ell \ll k_B T$, and may even in some regions of parameter-space give the wrong sign of the heat current as seen in

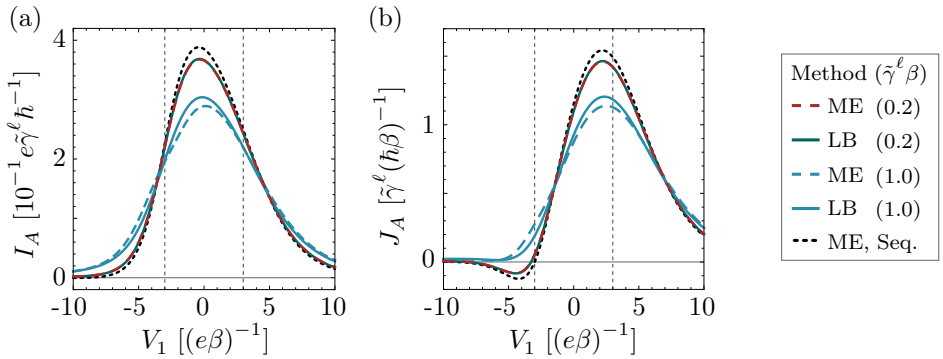

Figure 3.3: Comparison of the electric current (a) and heat current (b) calculated with the ME and LB approaches. Currents are plotted as function of gate voltage V_1 for two different lead coupling strengths $\tilde{\gamma}^A = \tilde{\gamma}^B = \tilde{\gamma}^\ell$ (energy-independent). The ME result including only sequential tunneling is shown for reference (black dotted), and the vertical dashed lines mark the alignment of the dot level with the electrochemical potentials of leads A (left) and B (right). Parameters: $T_B = 2T_A \equiv 2/(k_B\beta)$, $\mu_A = 3\,\beta^{-1}$, $\mu_B = -3\,\beta^{-1}$, and $\eta = 10^{-3}\,\beta^{-1}$. Adapted from Publication [1].

[8] Specifically, we calculate the cotunneling integrals numerically in Fig. 3.3 and 3.5c, and state the value of η in the figure captions.

Fig. 3.3b. However, for $\tilde{\gamma}^{\ell} < k_B T$, the ME results with cotunneling are in excellent agreement with the LB formalism. For $\tilde{\gamma}^{\ell} > k_B T$, which is outside the regime of validity of the ME approach, the two approaches deviate as expected.

3.1.3 Three-terminal setup: Steady-state thermoelectric currents

Consider now the setup illustrated in Fig. 3.1a with dot Hamiltonian

$$\hat{H}_{\rm dots} = \epsilon_1 \hat{c}_1^\dagger \hat{c}_1 + \epsilon_2 \hat{c}_2^\dagger \hat{c}_2 + U \hat{n}_1 \hat{n}_2, \tag{3.26}$$

where QD1 is tunnel-coupled to leads A and B, QD2 is tunnel-coupled to lead C, and U is the interdot Coulomb coupling. A potential bias is applied to leads A and B such that $\mu_A = \mu_0 + eV/2$ and $\mu_B = \mu_0 - eV/2$ with $\mu_0 = 0$ set as reference.

In the basis of the occupation states $|m\rangle = |n_1 n_2\rangle \in \{|00\rangle, |10\rangle, |01\rangle, |11\rangle\}$, we can write the master equation that governs the evolution of the diagonal components of the reduced density matrix of the QDs in a matrix form $dp/dt = \mathcal{L}p$, where $p = (p_{00}, p_{10}, p_{01}, p_{11})$, $\mathcal{L} = \mathcal{L}^s + \mathcal{L}^c$, with $\mathcal{L}^s$ describing the contribution from sequential tunneling,

$$\mathcal{L}^s = \begin{pmatrix} -\Gamma^{\vec{A}}_{00,10} - \Gamma^{\vec{B}}_{00,10} - \Gamma^{\vec{C}}_{00,01} & \Gamma^{\overleftarrow{A}}_{10,00} + \Gamma^{\overleftarrow{B}}_{10,00} & \Gamma^{\overleftarrow{C}}_{01,00} & 0 \\ \Gamma^{\vec{A}}_{00,10} + \Gamma^{\vec{B}}_{00,10} & -\Gamma^{\overleftarrow{A}}_{10,00} - \Gamma^{\overleftarrow{B}}_{10,00} - \Gamma^{\vec{C}}_{10,11} & 0 & \Gamma^{\overleftarrow{C}}_{11,10} \\ \Gamma^{\vec{C}}_{00,01} & 0 & -\Gamma^{\vec{A}}_{01,11} - \Gamma^{\vec{B}}_{01,11} - \Gamma^{\overleftarrow{C}}_{01,00} & \Gamma^{\overleftarrow{A}}_{11,01} + \Gamma^{\overleftarrow{B}}_{11,01} \\ 0 & \Gamma^{\vec{C}}_{10,11} & \Gamma^{\vec{A}}_{01,11} + \Gamma^{\vec{B}}_{01,11} & -\Gamma^{\overleftarrow{A}}_{11,01} - \Gamma^{\overleftarrow{B}}_{11,01} - \Gamma^{\overleftarrow{C}}_{11,10} \end{pmatrix}, \tag{3.27}$$

and $\mathcal{L}^c$ is the contribution from nonlocal cotunneling processes

$$\mathcal{L}^c = \begin{pmatrix} -\Gamma^{\vec{A}\,\vec{C}}_{00,11} - \Gamma^{\vec{B}\,\vec{C}}_{00,11} & 0 & 0 & \Gamma^{\overleftarrow{A}\,\overleftarrow{C}}_{11,00} + \Gamma^{\overleftarrow{B}\,\overleftarrow{C}}_{11,00} \\ 0 & -\Gamma^{\vec{C}\,\overleftarrow{A}}_{10,01} - \Gamma^{\vec{C}\,\overleftarrow{B}}_{10,01} & \Gamma^{\vec{A}\,\overleftarrow{C}}_{01,10} + \Gamma^{\vec{B}\,\overleftarrow{C}}_{01,10} & 0 \\ 0 & \Gamma^{\vec{C}\,\overleftarrow{A}}_{10,01} + \Gamma^{\vec{C}\,\overleftarrow{B}}_{10,01} & -\Gamma^{\vec{A}\,\overleftarrow{C}}_{01,10} - \Gamma^{\vec{B}\,\overleftarrow{C}}_{01,10} & 0 \\ \Gamma^{\vec{A}\,\vec{C}}_{00,11} + \Gamma^{\vec{B}\,\vec{C}}_{00,11} & 0 & 0 & -\Gamma^{\overleftarrow{A}\,\overleftarrow{C}}_{11,00} - \Gamma^{\overleftarrow{B}\,\overleftarrow{C}}_{11,00} \end{pmatrix}. \tag{3.28}$$

Notice that we include local cotunneling processes in the transport currents cf. Eq. (3.15), however, these do not change the state of the system and therefore do not enter the master equation.

The steady-state electric current in System 1, $I \equiv I_A = -I_B$, is shown in Fig. 3.4a as a function of gate detuning $V_2 - V_1$ and total gating $V_2 + V_1$ at low temperature in the vicinity of the so-called triple

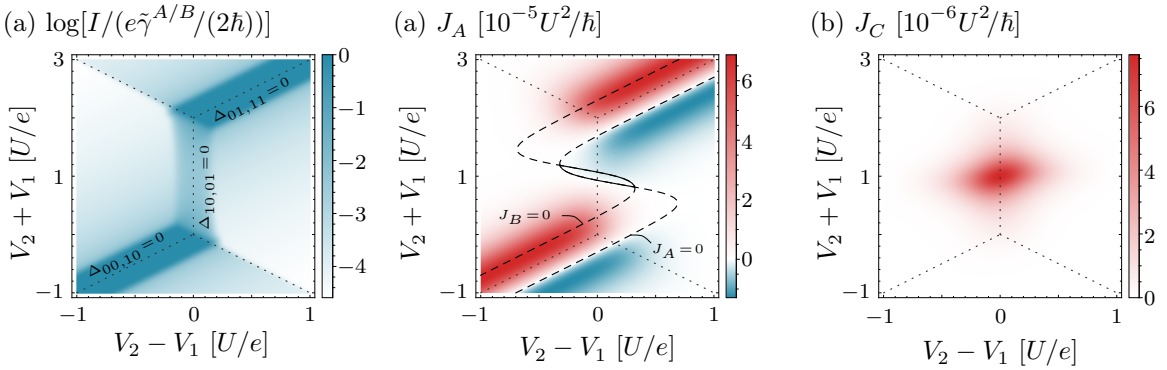

Figure 3.4: (a) Electric current in System 1 as a function of gate detuning $V_2 - V_1$ and total gating $V_2 + V_1$ at low temperature, $k_B T_\ell = 10^{-2}\,U$. The degeneracy lines of the honeycomb vertex are indicated with dotted lines. (b) Heat current in lead A, J_A, at high temperature, $k_B T_\ell = 10^{-1}\,U$ (contours indicate where J_A and J_B are zero). (c) Heat current in lead C, J_C, for $k_B T_\ell = 10^{-1}\,U$. Parameters: $\tilde{\gamma}^{A/B}(\epsilon) = 10^{-3}\,U$, $\tilde{\gamma}^{C}(\epsilon) = 10^{-2}\,U$, and $eV = 0.3\,U$. From publications [1, 50].

points at $(V_1, V_2) = (0, 0), (U, U)$. Near the degeneracy lines $\Delta_{00,10} = \Delta_{01,11} = 0$, sequential tunneling processes dominate and give rise to a strong current. However, outside the bias window around these degeneracy lines, cotunneling processes dominate over the exponentially suppressed sequential tunneling processes. In particular, nonlocal cotunneling processes give rise to the enhanced current along the $\Delta_{10,01} = 0$ degeneracy line.

The heat current J_A in lead A is shown in Fig. 3.4b as a function of gate voltages. Near the degeneracy lines where sequential tunneling processes dominate, the heat current turns from positive to negative (from heating to cooling) as the dot energy level changes from filtering out electrons tunneling from below to from above the chemical potential in lead A (similar to the behavior in Fig. 3.3b), as also confirmed experimentally in e.g. metallic QD systems [68, 16]. However, the cooling of lead A happens at the cost of heating in lead B, and the whole System 1 is heated from this Joule heating. However, in the center of the diagram both leads in System 1 are cooled (the zero-point of the heat current in lead A and B are shown with dashed lines, and as solid lines in the center of the diagram to mark the region where both heat currents become negative). From the heat current in lead C shown in Fig. 3.4c, the cooling of System 1 is seen to be at the cost of heating System 2. This occurs in spite of the fact that no electrons are exchanged between the two systems, and is caused solely by the Coulomb-mediated energy exchange between the two QD systems. The origin of the mechanism was discussed qualitatively in the beginning of Sec. 3.1, and the mechanism is the driving force behind "demon"-induced cooling [69, 16], energy harvesting [14, 70, 15, 51], as well as Coulomb drag [71, 62]. Analytically, when considering sequential tunneling processes only, one can show [14] that the total heat currents in System 1 and System 2 are[9] $J_1^s = U(\Gamma^+ - \Gamma^-)/\tau^s + (\mu_A - \mu_B)I^s/e$ and $J_2^s = U(\Gamma^- - \Gamma^+)/\tau^s$, respectively, where $\Gamma^- \equiv \Gamma_{00,01}\Gamma_{01,11}\Gamma_{11,10}\Gamma_{10,00}$, $\Gamma^+ \equiv \Gamma_{00,10}\Gamma_{10,11}\Gamma_{11,01}\Gamma_{01,00}$, and τ^s is merely a normalization factor which depends on the sequential tunneling rates. The Coulomb-mediated energy exchange is given by the term proportional to U, with Γ^- governing the cooling cycle illustrated in Fig. 3.1b, and the last term in J_1^s is the contribution from Joule heating. Upon including cotunneling processes, the expressions for the thermoelectric currents become more complicated, however, we can understand the effect from cotunneling by plotting the individual contributions from sequential tunneling processes and cotunneling processes as in Fig. 3.5a. The figure clearly shows how higher-order processes contribute to heating, similarly to the discussion in Ref. [16] for metallic dots. In particular, as we saw in Fig. 3.4b, the effect from the interaction-mediated energy-exchange is dominant in the center of the stability diagram where the system can fluctuate between the $|10\rangle$ and $|01\rangle$ state via nonlocal cotunneling processes, which can thereby transfer energy between the two systems. However, in a cotunneling process the intermediate state does not have to conserve energy, therefore these processes overall contribute to heating the system. Figure 3.5a also shows the dominating contribution from joule heating that sets in at large bias voltages.

Large lead couplings, $\tilde{\gamma}^\ell(\epsilon) \sim k_B T, U$, are desirable to maximize the achievable cooling power [72], however, this also increases the adverse contribution from higher-order tunneling processes. Denoting the minimum in J_1 as a function of bias voltage as the maximum cooling power, $J_{1,\max} \equiv \min J_1(V)$, we can show the cooling effect as a function of tunneling rates in Fig. 3.5b. As discussed qualitatively above, cooling is achieved for $\tilde{\gamma}^C > \tilde{\gamma}^{A/B}$ and increases with increasing rates until cotunneling processes start to become important and reduce the area in the lead coupling parameter space where cooling is achieved. However, as we show in Fig. 3.5c, we can enhance the effect further with energy-dependent lead couplings, similarly to the enhancement of the heat to current conversion discussed in Ref. [14]. Indeed, for small bias voltages and temperature differences compared to the energy scale at which the lead couplings vary, we can consider the expansion of the lead couplings[10] around their

[9] We define the total heat currents (from sequential and cotunneling processes) in System 1 and 2 as $J_1 = J_A + J_B$ and $J_2 = J_C$, respectively, and use superscript s and c to denote the individual contributions from sequential (e.g. J_1^s) and cotunneling (e.g. J_1^c) processes.

[10] To ensure that the lead coupling strengths are positive, a linear expansion is only appropriate when the bias window or the thermal window exponentially suppress the contribution to the cotunneling integrals at energies where the lead coupling becomes negative. In the numerical calculation we take the absolute value of the lead couplings.

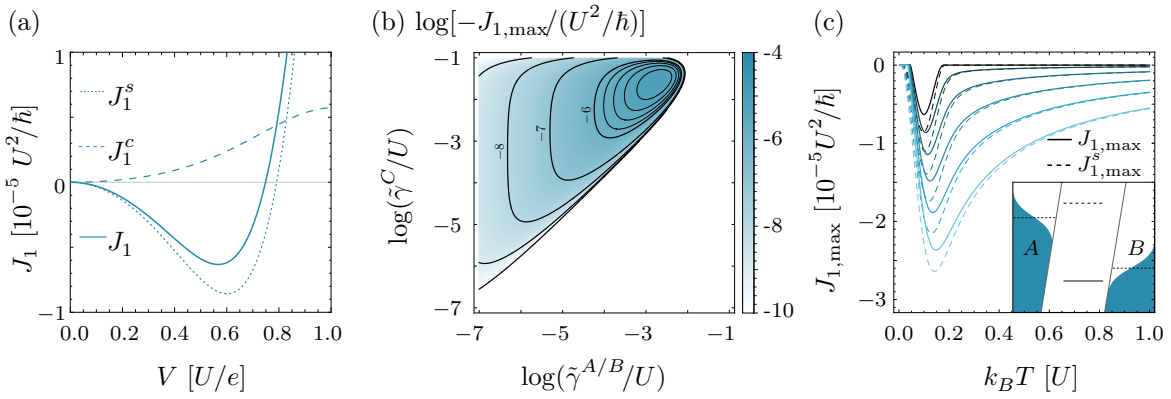

Figure 3.5: (a) Heat current J_1 as a function of bias voltage for $\tilde{\gamma}^{A/B}(\epsilon) = 10^{-3}U$ and $\tilde{\gamma}^{C}(\epsilon) = 10^{-2}U$. The individual contributions from sequential (J_1^s) and cotunneling (J_1^c) are also shown. (b) Maximum cooling power, $J_{1,\mathrm{max}}$, as a function of the lead coupling strengths for energy-independent couplings. Parameters in (a)-(b): $eV_1 = eV_2 = U/2$ and $k_BT = 0.1\,U$. (c): Performance boosting with energy-dependent lead couplings (sketched in the inset). Maximum cooling power as function of temperature for different lead coupling strengths: $\partial\tilde{\gamma}^{A} = -\partial\tilde{\gamma}^{B} = x\tilde{\gamma}_0^{A/B}/U$, with $x = 0$ (black) to $x = 1$ (light blue) in steps of 0.2. The full (dashed) lines show the result obtained with (without) cotunneling. Parameters in (c): $\tilde{\gamma}^{C}(\epsilon) = 10^{-2}\,U$, $\tilde{\gamma}_0^{A/B} = 10^{-3}\,U$, $eV_1 = eV_2 = U/2$, and $\eta = 10^{-4}\,U$. From publications [1, 50].

value at μ_0,

$$\tilde{\gamma}^{\ell}(\epsilon) = \tilde{\gamma}_0^{\ell} + (\epsilon - \mu_0)\partial\tilde{\gamma}^{\ell}, \qquad \tilde{\gamma}_0^{\ell} = \tilde{\gamma}^{\ell}(\mu_0), \qquad \partial\tilde{\gamma}^{\ell} \equiv \tfrac{\partial\tilde{\gamma}^{\ell}(\epsilon)}{\partial\epsilon}|_{\epsilon=\mu_0}. \tag{3.29}$$

For $\mu_A > \mu_B$, the configuration illustrated in the inset of Fig. 3.5c boosts Γ^-/Γ^+. This results in an enhancement of the cooling power by suppressing tunneling between leads A and B via two sequential tunneling processes, while at the same time promoting the processes of the cooling cycle in Fig. 3.1b. As seen in Fig. 3.5c, when tuning the energy-dependence of the lead couplings, a significant enhancement of the cooling power is achieved, although still reduced by cotunneling processes.

3.1.4 Short summary

In this section we encountered our first example of non-equilibrium transport processes in nanostructures induced from coupling to external reservoirs with unequal electron distributions. In particular, we studied thermoelectric effects in a system of capacitively coupled quantum dots, focusing in particular on a three-terminal configuration [14] where the interdot Coulomb-interaction mediates an energy exchange between two otherwise decoupled systems. We set up a master equation with rates calculated from the T matrix, which enabled us to discuss the contribution from coherent cotunneling processes. To benchmark the T-matrix approach, we considered a non-interacting single level coupled to source and drain leads for which the Landauer-Büttiker formalism is exact, and demonstrated excellent agreement in the regime of validity of the T-matrix approach (small tunnel couplings to the leads $\tilde{\gamma} < k_BT$) when cotunneling processes are included in the master equation.

For the three-terminal setup, we found that cotunneling processes can contribute significantly in the center of the stability diagram where the interdot mediated energy-exchange is dominant. To boost the thermoelectric cooling effect we included energy-dependent lead couplings in the formalism. In all cases, cotunneling processes reduce the cooling effect since they do not share the delicate energy selectivity inherent to sequential tunneling processes. In future work, it would be interesting to consider alternative regularization schemes for higher-order processes, as discussed in Ref. [33].

3.2 Cooper pair splitter

This section is based on Publication II, Physical Review Letters 120, 087701 (2018) by N. Walldorf, C. Padurariu, A.-P. Jauho, and C. Flindt, and Publication IV, Physical Review B 101, 205422 (2020) by N. Walldorf, F. Brange, C. Padurariu, and C. Flindt.

In the previous section, we saw an example of how to engineer a particular electron transport effect in a nanostructure composed of Coulomb-coupled quantum dots attached to electron reservoirs. In particular, we considered the inter-dot mediated energy-exchange which resulted from a cycle of tunneling processes of single electrons (to lowest order) to and from metallic source and drain reservoirs. In this section, we will discuss another setup, a so-called Cooper pair splitter (proposed by P. Recher et al. [13] and G. B. Lesovik et. al. [12]), where instead of single electrons originating from a metallic reservoir, the source of particles are entangled electron-pairs originating from a superconductor.

Entangled particle-pairs are particles whose state cannot be described independently from each other, and may share a correlated degree of freedom even when spatially separated (we will see an explicit example below). Historically, such non-local correlations of entangled particle-pairs led to the Einstein-Podolsky-Rosen (EPR) paradox, arguing that the description of reality as described by quantum mechanics was incomplete [73]. The paradox was settled by an experimental test proposed by J. S. Bell [74] which was first verified experimentally by A. Aspect et al. [75]. Today, entangled particle-pairs form a key ingredient in a range of quantum applications such as quantum information and cryptography [76], and long-range distribution of entangled photon pairs is already a reality [77] [78]. The prospect of utilizing entanglement properties in solid-state circuits has led to significant research in entangled electrons in nanostructures. Preservation of entanglement is challenged by decoherence from interactions in nanostructures, however, electron spin coherence has been shown to be maintained over distances greater than 100 μm in semiconductors [79].

Superconductors have been proposed as a natural source of mobile spin-entangled pairs in solid-state circuits. Superconductivity was discovered by Kamerlingh Onnes in 1911 as the disappearance of electrical resistance in mercury below 4.2 Kelvin[11]. Since the discovery of superconductivity, different underlying pairing mechanisms have been proposed to explain different (conventional and unconventional) superconducting states of matter. In the BCS theory of conventional superconductivity, proposed by Bardeen, Cooper, and Schrieffer in 1957 [81], the pairing mechanism is caused by lattice deformations which mediates an attractive electron interaction, which when dominating over the repulsive Coulomb-interaction can give rise to a superconducting phase where electrons are grouped into pairs (Cooper pairs) of opposite spin and momentum. The pairing is described by the BCS mean-field Hamiltonian

$$\hat{H}_{SC} = \sum_{q\sigma} \epsilon_q \hat{a}^\dagger_{q\sigma} \hat{a}_{q\sigma} - \left(\sum_q \Delta \, \hat{a}^\dagger_{q\uparrow} \hat{a}^\dagger_{-q\downarrow} + \text{h.c.} \right), \tag{3.30}$$

where the first term describes non-interacting electrons with momentum q, spin σ, and single-particle energy ϵ_q, created (annihilated) by the operators $\hat{a}^\dagger_{q\sigma}$ ($\hat{a}_{q\sigma}$), and the second term is the so-called pairing term which governs the attractive (isotropic[12]) interaction on a mean-field level. The factor $\Delta = |\Delta| e^{i\phi_S}$ is the superconducting order parameter with phase ϕ_S and amplitude $|\Delta|$, which equals the energy-gap that developes around the Fermi-level. The superconducting gap depends on the particular material and setting, but is in the order of $\sim 10^2$ μeV for the aluminium-based superconductors in Refs. [82, 83, 84]. Upon coupling a (BCS) superconductor to two spatially separated quantum dots QD_ℓ, $\ell \in \{L, R\}$ (see Fig. 3.6) with large intradot Coulomb interactions U_ℓ which prevent double-occupancy of the individual QDs ($U_\ell \sim 1$ meV in Refs. [82, 83]), in the limit of a large superconducting gap, upon tracing over the superconductor degrees of freedom the QD system coupled to the superconductor can

[11] See e.g. the review [80] on the discovery of superconductivity with references to original notebooks and publications by Kamerlingh Onnes.

[12] Anisotropic effects can be included in a momentum-dependent order parameter Δ_q.

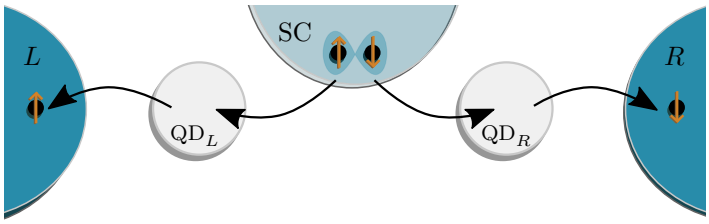

Figure 3.6: Spatial illustration of a Cooper pair splitter consisting of two QDs coupled to a superconducting (SC) source of Cooper pairs and two normal-metal drains (L, R). The figure is adapted from Publication IV, and is inspired by the original proposal in Ref. [13] Fig. 1.

be described by the effective Hamiltonian [43, 85] (we refer to App. A.3 for a derivation)

$$\hat{H}_S = \sum_{\ell\sigma} \epsilon_\ell \hat{d}^\dagger_{\ell\sigma}\hat{d}_{\ell\sigma} - \frac{\hbar\gamma_{\rm CPS}}{\sqrt{2}}\left(\hat{d}^\dagger_{L\downarrow}\hat{d}^\dagger_{R\uparrow} - \hat{d}^\dagger_{L\uparrow}\hat{d}^\dagger_{R\downarrow} + \text{h.c.}\right) - \hbar\gamma_{\rm EC}\sum_\sigma\left(\hat{d}^\dagger_{L\sigma}\hat{d}_{R\sigma} + \text{h.c.}\right). \tag{3.31}$$

Here, the operator $\hat{d}^\dagger_{\ell\sigma}$ ($\hat{d}_{\ell\sigma}$) creates (annihilates) an electron in QD$_\ell$ with spin $\sigma \in \{\uparrow,\downarrow\}$ and energy[13] ϵ_ℓ relative to the chemical potential of the superconductor, $\mu_S = 0$. The empty state couples to the singlet state with amplitude $\hbar\gamma_{\rm CPS}$, which describes the coherent coupling of the quantum dots to Cooper pairs in the superconductor. This non-local proximity effect is similar to the local proximity effect induced in a single dot (which is suppressed by the large onsite interaction) [86] [85]. The amplitude $\hbar\gamma_{\rm EC}$ governs the contribution from elastic cotunneling (EC) via the superconductor.

The Hamiltonian (3.31) reveals the spin-entangled singlet nature of Cooper pairs: even when spatially separated in the two quantum dots, the spins of the spin-entangled electrons are correlated. Upon coupling to two normal-metal leads[14] as illustrated in Fig. 3.6, and with a bias applied[15], Cooper pairs can be converted into spatially separated entangled pairs and injected into the separated normal-metal leads [13]. The strong intradot Coulomb interaction in the quantum dots ensures that Cooper pairs originating from the superconductor do not tunnel to the same lead, but are spatially separated by the two quantum dots before injected into the normal-metal drains. Such Cooper pair splitters have been realized experimentally in various architectures[16], e.g. using InAs nanowires [82] or carbon nanotube based quantum dots [83].

Conventionally, transport in Cooper pair splitters is characterized by means of electric current and zero-frequency shot noise[16]. Here we discuss the rich information available in the distribution of electron waiting times between electron tunneling events into the drains (defined in Eqs. (3.45)-(3.46) below), as well as finite-frequency shot noise (which we define in Eq. (3.39) below).

3.2.1 Master equation

Since we are interested in unidirectional transport of split Cooper pairs originating from the superconductor and injected into the normal metal leads, we use the result from Sec. 2.2 and write a master equation for the reduced density operator[17] $\hat{\rho}_S$, which reads

$$\frac{d}{dt}\hat{\rho}_S(t) = -\frac{i}{\hbar}[\hat{H}_S, \hat{\rho}_S(t)] + \mathcal{D}[\hat{\rho}_S(t)] \equiv \mathcal{L}\hat{\rho}_S(t), \tag{3.32}$$

[13] We treat the QDs as spin-degenerate single levels, i.e. the level spacing is assumed to be larger than the bias (and temperature) window.

[14] The full Hamiltonian is detailed in App. A.3.

[15] We summarize the operating conditions in Eq. (3.36) below.

[16] We refer to references in publication II and IV, attached in the end of the thesis.

[17] Where all lead degrees of freedom have been traced out. See also App. A and B in Publication IV, attached in the end of the thesis.

with dissipator $\mathcal{D}$ defined in Eq. (2.26). For the tunneling Hamiltonian $\hat{H}_T = \sum_{\ell k\sigma}\left(t_\ell \hat{c}^\dagger_{\ell k\sigma}\hat{d}_{\ell\sigma} + \text{h.c.}\right)$, where $\hat{c}^\dagger_{\ell k\sigma}$ ($\hat{c}_{\ell k\sigma}$) creates (annihilates) an electron in reservoir $\ell \in \{L, R\}$ with spin σ and momentum k, in the working regime of a unidirectional transport, the dissipator becomes

$$\mathcal{D} = -\frac{1}{2}\sum_{\sigma\ell\xi\theta\theta'} \gamma_\ell \theta\theta' D^{(-\xi)\theta'}_{\ell\sigma} D^{\xi\theta}_{\ell\sigma}\delta_{-\xi\theta,-}, \quad \gamma_\ell = \frac{2\pi}{\hbar}\nu_\ell |t_\ell|^2, \tag{3.33}$$

which, upon acting on the reduced density operator, takes the form [87, 43]

$$\mathcal{D}[\hat{\rho}_S] = \sum_{\sigma\ell}\gamma_\ell\left[\hat{d}_{\ell\sigma}\hat{\rho}_S\hat{d}^\dagger_{\ell\sigma} - \frac{1}{2}\{\hat{\rho}_S, \hat{d}^\dagger_{\ell\sigma}\hat{d}_{\ell\sigma}\}\right]. \tag{3.34}$$

As in the example in Sec. 2.3, terms of the form $\mathcal{J}_{\ell\sigma}\hat{\rho}_S \equiv \gamma_\ell \hat{d}_{\ell\sigma}\hat{\rho}_S\hat{d}^\dagger_{\ell\sigma}$ describe incoherent tunneling processes in which an electron with spin σ in QD_ℓ tunnels into lead ℓ. Only terms of the form as in the second term in Eq. (2.28) contribute in Eq. (3.34) since both normal leads act as drains.

The Liouvillian can be expressed as a matrix in terms of its action on the matrix elements of the reduced density operator [88], $\rho_{mn} \equiv \langle m|\hat{\rho}_S|n\rangle$, where $|m\rangle \in \{|0\rangle, |\ell\sigma\rangle = d^\dagger_{\ell\sigma}|0\rangle, |S\rangle = 2^{-1/2}\left(d^\dagger_{L\downarrow}d^\dagger_{R\uparrow} - d^\dagger_{L\uparrow}d^\dagger_{R\downarrow}\right)|0\rangle\}$. In the basis $\{\rho_{(0)(0)}, \rho_{(L\uparrow)(L\uparrow)}, \rho_{(L\downarrow)(L\downarrow)}, \rho_{(R\uparrow)(R\uparrow)}, \rho_{(R\downarrow)(R\downarrow)}, \rho_{(S)(S)}, \rho_{(0)(S)}, \rho_{(S)(0)}, \rho_{(L\uparrow)(R\uparrow)}, \rho_{(R\uparrow)(L\uparrow)}, \rho_{(L\downarrow)(R\downarrow)}, \rho_{(R\downarrow)(L\downarrow)}\}$, the Liouvillian becomes

$$\mathcal{L} = \begin{pmatrix}
0 & \gamma_L & \gamma_L & \gamma_R & \gamma_R & 0 & -i\gamma_{\text{CPS}} & i\gamma_{\text{CPS}} & 0 & 0 & 0 & 0 \\
0 & -\gamma_L & 0 & 0 & 0 & \frac{\gamma_R}{2} & 0 & 0 & -i\gamma_{\text{EC}} & i\gamma_{\text{EC}} & 0 & 0 \\
0 & 0 & -\gamma_L & 0 & 0 & \frac{\gamma_R}{2} & 0 & 0 & 0 & 0 & -i\gamma_{\text{EC}} & i\gamma_{\text{EC}} \\
0 & 0 & 0 & -\gamma_R & 0 & \frac{\gamma_L}{2} & 0 & 0 & i\gamma_{\text{EC}} & -i\gamma_{\text{EC}} & 0 & 0 \\
0 & 0 & 0 & 0 & -\gamma_R & \frac{\gamma_L}{2} & 0 & 0 & 0 & 0 & i\gamma_{\text{EC}} & -i\gamma_{\text{EC}} \\
0 & 0 & 0 & 0 & 0 & -(\gamma_L+\gamma_R) & i\gamma_{\text{CPS}} & -i\gamma_{\text{CPS}} & 0 & 0 & 0 & 0 \\
-i\gamma_{\text{CPS}} & 0 & 0 & 0 & 0 & i\gamma_{\text{CPS}} & i\varepsilon - \frac{\gamma_L+\gamma_R}{2} & 0 & 0 & 0 & 0 & 0 \\
i\gamma_{\text{CPS}} & 0 & 0 & 0 & 0 & -i\gamma_{\text{CPS}} & 0 & -i\varepsilon - \frac{\gamma_L+\gamma_R}{2} & 0 & 0 & 0 & 0 \\
0 & -i\gamma_{\text{EC}} & 0 & i\gamma_{\text{EC}} & 0 & 0 & 0 & 0 & -i\delta - \frac{\gamma_L+\gamma_R}{2} & 0 & 0 & 0 \\
0 & i\gamma_{\text{EC}} & 0 & -i\gamma_{\text{EC}} & 0 & 0 & 0 & 0 & 0 & i\delta - \frac{\gamma_L+\gamma_R}{2} & 0 & 0 \\
0 & 0 & -i\gamma_{\text{EC}} & 0 & i\gamma_{\text{EC}} & 0 & 0 & 0 & 0 & 0 & -i\delta - \frac{\gamma_L+\gamma_R}{2} & 0 \\
0 & 0 & i\gamma_{\text{EC}} & 0 & -i\gamma_{\text{EC}} & 0 & 0 & 0 & 0 & 0 & 0 & i\delta - \frac{\gamma_L+\gamma_R}{2}
\end{pmatrix}, \tag{3.35}$$

where $\varepsilon \equiv (\epsilon_L + \epsilon_R)/\hbar$ and $\delta \equiv (\epsilon_L - \epsilon_R)/\hbar$. We recognize terms in the off-diagonal (diagonal) of the Liouvillian and corresponding to diagonal components of the reduced density matrix as describing incoherent tunneling events (conservation of probability), and the remaining off-diagonal terms correspond to coherent CPS and EC processes.

In the following, we consider the stationary transport properties as obtained from the stationary reduced density matrix, $\hat{\rho}^{(S)}$, given as the normalized solution to $\mathcal{L}\hat{\rho}_S = 0$. Furthermore, to summarize we consider the following operating conditions

$$k_B T, \epsilon_\ell, \hbar\gamma_{\text{EC}}, \hbar\gamma_{\text{CPS}}, \hbar\gamma_\ell \ll |\mu_\ell| < |\Delta| < U_\ell, \tag{3.36}$$

where T is the temperature[18] and μ_ℓ is the negative electrochemical potential of drain electrode ℓ relative to μ_S.

3.2.2 Steady-state transport properties

Current

In the limit of large Coulomb interaction, Cooper pair splitting (CPS) is the only process injecting charge equally into each quantum dot. Possible contact asymmetries together with EC may, however, lead to unequal particle currents flowing into each collector, $I_\ell \equiv \text{Tr}[\mathcal{J}_\ell\hat{\rho}^{(S)}]$, where $\mathcal{J}_\ell = \sum_\sigma \mathcal{J}_{\ell\sigma}$, and

[18] The assumption of a small temperature is needed to satisfy the Gurvitz-Prager conditions of unidirectional transport [32]. In this regime, temperature does not enter as an explicit parameter in the rates (see Sec. 2.3).

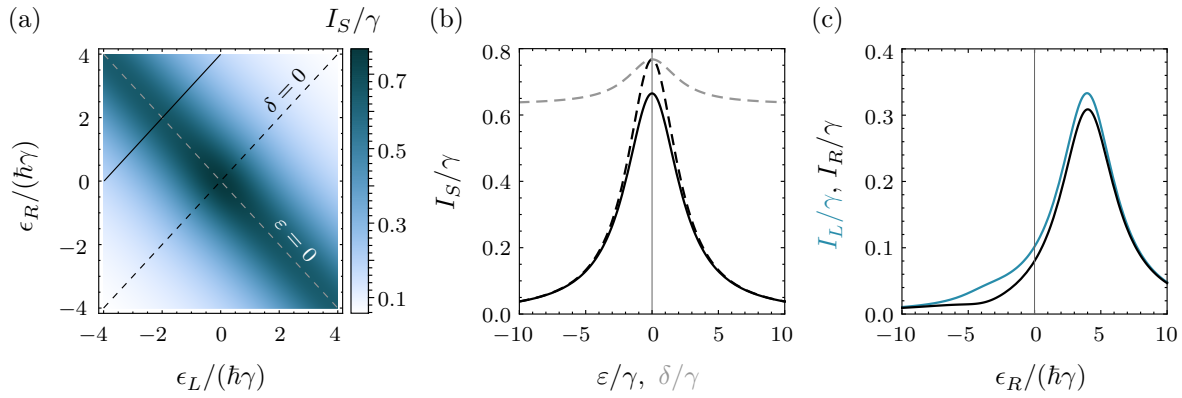

Figure 3.7: (a) Average current from the superconductor into the drain electrodes as a function of the quantum dot levels. (b) Average current as a function of the sum $\varepsilon = (\epsilon_L + \epsilon_R)/\hbar$ (black curves with corresponding ε-axis), and the detuning $\delta = (\epsilon_L - \epsilon_R)/\hbar$ (gray curve with corresponding δ-axis), of the quantum dot levels corresponding to the three cuts in the left panel. (c) Average current in the left and right lead as a function of ϵ_R for a fixed $\epsilon_L = -4\hbar\gamma$. The remaining parameters are $\gamma_{\rm CPS} = \gamma_{\rm EC} = \gamma$, $\gamma_L = 1.5\gamma$, $\gamma_R = 0.5\gamma$. (a) and (b) from Publication IV.

Tr sums over diagonal-component basis elements of the density matrix[19] [89]. The total steady-state particle current flowing from the superconductor into the two dots, $I_S \equiv I_L + I_R$, reads

$$I_S = \bar{\gamma}^2_{\rm CPS}\gamma_\Sigma, \tag{3.37}$$

where

$$\bar{\gamma}^2_{\rm CPS} \equiv \frac{(2\gamma_{\rm CPS})^2}{\varepsilon^2 + \gamma_\Sigma^2 + (2\gamma_{\rm CPS})^2/\eta}, \quad \bar{\gamma}^2_{\rm EC} \equiv \frac{(2\gamma_{\rm EC})^2}{\delta^2 + \gamma_\Sigma^2 + (2\gamma_{\rm EC})^2}, \quad \eta \equiv 1 + \left(\frac{\gamma_\Delta}{\gamma_\Sigma}\right)^2 \left[\bar{\gamma}^2_{\rm EC} - 1\right], \tag{3.38}$$

with $\gamma_\Sigma \equiv (\gamma_L + \gamma_R)/2$ and $\gamma_\Delta \equiv (\gamma_L - \gamma_R)/2$. We note that the current reduces to the expression in Ref. [43] obtained for $\gamma_{\rm EC} = 0$ and with energy renormalization absorbed into the dot-levels (as discussed in App. A.3), which again reduces to the result in Ref. [13] in the limit $\gamma_{\rm CPS} \ll \gamma_\Sigma$.

The average current from the superconductor is shown in Fig. 3.7a as a function of the energies of the quantum dots, and particular cuts are shown in Fig. 3.7b. The current presents a Lorentzian shaped resonance around $\varepsilon = 0$, where the double occupied state from Cooper pair splitting is on resonance with the empty state. The non-local nature of the governing transport processes is clearly seen in Fig. 3.7c as an increased current in both the left and right collector when ϵ_R is tuned into resonance such that $\varepsilon = 0$. The asymmetry in the two current outputs is caused by contact asymmetries together with EC, which also gives rise to the enhanced current in Fig. 3.7b when also EC is on resonance at $\delta = 0$. In the limit of symmetric normal contacts $\gamma_L = \gamma_R$ the EC process does not contribute to the average current.

Although the current already gives us some insight into the non-local nature of the transport processes in the system, in the following we discuss some alternative transport characteristics that reveal even richer and detailed information about the governing transport processes.

Current correlations

Before turning our attention to the distribution of so-called electron waiting times, let us first consider the somewhat more conventional measure of current correlations. In particular, the discrete nature

[19] For example, for the current flowing into the left collector, we express $\mathcal{J}_L$ in the same basis as the Liuovillian in Eq. (3.35), and let it act on the corresponding vector containing the matrix-elements of $\hat{\rho}^{(S)}$. Taking Tr gives $I_L = \gamma_L \left(\rho^{(S)}_{(L\uparrow)(L\uparrow)} + \rho^{(S)}_{(L\downarrow)(L\downarrow)} + \rho^{(S)}_{(S)(S)}\right)$ in agreement with Ref. [43]. See also App. A.4 for a derivation of the expression for the current in terms of full counting statistics.

of tunneling electrons give rise to fluctuations in the electrical current, referred to as shot noise, and hence measurements of shot noise may provide insight into the underlying physical processes in the system. The shot-noise power spectrum is defined as [90, 91]

$$S_{\ell\ell'}(\omega) = \frac{1}{2}\int_{-\infty}^{\infty} \mathrm{d}t e^{i\omega t}\langle\{\delta\hat{I}_\ell(t), \delta\hat{I}_{\ell'}(0)\}\rangle, \tag{3.39}$$

where $\delta\hat{I}_\ell(t) = \hat{I}_\ell(t) - I_\ell$, $\ell = L, R$ measures the deviation of the tunnel current[20] from its average value in steady state, and curly brackets denote the anti-commutator. Notice that the definition in Eq. (3.39) also includes cross correlations between different leads, $\ell \neq \ell'$ [90]. Using the so-called MacDonald's formula, we can calculate the real part of the noise power spectrum[21] from the master equation as [92, 93, 91]

$$S_{\ell\ell'}(\omega) = \delta_{\ell\ell'}\mathrm{Tr}[\mathcal{J}_\ell\hat{\rho}^{(S)}] - \mathrm{Re}\Big\{\mathrm{Tr}\left[\mathcal{J}_\ell\mathcal{R}(\omega)\mathcal{J}_{\ell'}\hat{\rho}^{(S)}\right] + (\ell \leftrightarrow \ell')\Big\}, \tag{3.40}$$

where the pseudoinverse, $\mathcal{R}(\omega)$, is defined as

$$\mathcal{R}(\omega) = \mathcal{Q}(\mathcal{L} + i\omega)^{-1}\mathcal{Q}, \tag{3.41}$$

in terms of the orthogonal projectors $\mathcal{Q} = 1 - \mathcal{P}$ and $\mathcal{P}[\,\cdot\,] = \hat{\rho}^{(S)}\mathrm{Tr}[\,\cdot\,]$. Zero-frequency noise of the Cooper pair splitter has previously been calculated numerically in e.g. Refs. [94, 95]. From Eq. (3.40) the full noise power spectrum can be calculated analytically[22]. In particular, for the symmetric configuration $\gamma_L = \gamma_R \equiv \gamma_N$, upon defining the average current $I_N \equiv I_L = I_R = I_S/2$, the Fano factor $F_{\ell\ell'}(\omega) \equiv S_{\ell\ell'}(\omega)/I_N$ takes the rather compact form[23]

$$\begin{aligned} F_{\ell\ell'}(\omega) = \delta_{\ell\ell'} - I_N\gamma_N(\gamma_N^2 + \omega_{\mathrm{CPS}}^2)\Bigg(&\frac{5\gamma_N^2 + \omega_{\mathrm{CPS}}^2 + \omega^2}{h(\omega_{\mathrm{CPS}}, \omega)} - \frac{(1 - \delta_{\ell\ell'})}{2\gamma_{\mathrm{CPS}}^2(\gamma_N^2 + \omega^2)} \\ &+ (-1)^{\delta_{\ell\ell'}}\left[\frac{\gamma_{\mathrm{EC}}}{\gamma_{\mathrm{CPS}}}\right]^2\frac{\gamma_N^2 + \omega_{\mathrm{EC}}^2 - 3\omega^2}{h(\omega_{\mathrm{EC}}, \omega)}\Bigg), \end{aligned} \tag{3.42}$$

where we have defined the characteristic frequencies $\omega_{\mathrm{CPS}} = \sqrt{4\gamma_{\mathrm{CPS}}^2 + \varepsilon^2}$ and $\omega_{\mathrm{EC}} = \sqrt{4\gamma_{\mathrm{EC}}^2 + \delta^2}$, as well as the function

$$h(\omega_0, \omega) = (\gamma_N^2 + \omega^2)^3 + 2(\gamma_N^4 - \omega^4)\omega_0^2 + (\gamma_N^2 + \omega^2)\omega_0^4. \tag{3.43}$$

The noise power spectrum (3.42) is limited to frequencies $|\omega| \ll |\mu_\ell/\hbar|$, cf. our assumptions in Eq. (3.36), however, algebraically $F_{\ell\ell'}(\omega) \to \delta_{\ell\ell'}$ as $\omega \to \infty$ as in the experiment in Ref. [96]. The zero-frequency noise equals the second cumulant of the steady-state statistics. In particular, we find for $F_{\ell\ell'} \equiv F_{\ell\ell'}(0)$,

$$F_{\ell\ell'} = 1 + \left(\delta_{\ell\ell'} - \frac{1}{2}\right)\bar{\gamma}_{\mathrm{EC}}^2 - \frac{I_N}{\gamma_N}\left(1 + \frac{2I_N\gamma_N}{\gamma_{\mathrm{CPS}}^2}\right). \tag{3.44}$$

The zero-frequency Fano factor (3.44) reveals that in the limit of large drain tunneling rates and in the absence of elastic cotunneling where only the first term dominates, fluctuations as expressed by

[20] For simplicity we consider the particle current correlations which differs from the charge current correlations by a factor e^2.

[21] The auto-correlation spectrum, $S_{\ell\ell}(\omega)$, is always real and positive. However, cross correlations, $S_{\ell\neq\ell'}(\omega)$, can take complex values at finite frequencies. As is customary in the literature, we only consider the real part, and from now on we let $S_{\ell\neq\ell'}(\omega)$ denote the real part.

[22] See Ref. [89] for details on how to evaluate the pseudoinverse.

[23] This result has been obtained independently by N. Walldorf and F. Brange. F. Brange obtained the result via the so-called $g^{(2)}$-function [4].

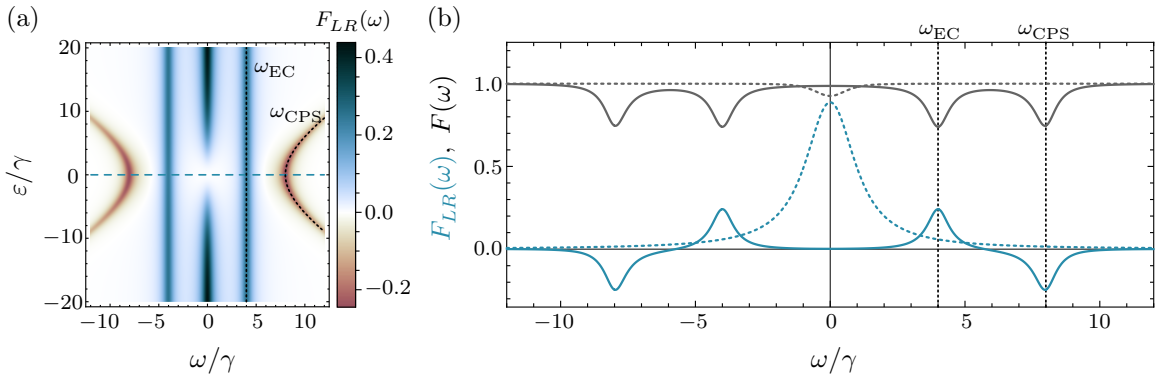

Figure 3.8: Finite-frequency noise. (a) Fano factor of the cross-correlations as a function of the frequency and the total energy of the quantum dots. The other parameters are $\gamma_L = \gamma_R \equiv 0.5\gamma$, $\gamma_{\rm CPS} = 4\gamma$, $\gamma_{\rm EC} = 2\gamma$, and $\delta = 0$. (b) Auto- (gray) and cross- (blue) correlations as functions of the frequency for $\epsilon_L = \epsilon_R = 0$ and $\gamma_L = \gamma_R \equiv 0.5\gamma$, $\gamma_{\rm CPS} = 4\gamma$, $\gamma_{\rm EC} = 2\gamma$ (solid), given by the cut in the left panel, and $\gamma_L = \gamma_R \equiv \gamma$, $\gamma_{\rm CPS} = \gamma_{\rm EC} = 0.1\gamma$ (dotted). In both panels, we indicate $\omega_{\rm CPS}$ and $\omega_{\rm EC}$. From Publication IV.

the auto Fano factor $F_{\ell\ell}$ approach unity, and transport into each drain resembles a Poisson process[24]. However, since electrons in each drain emerge from split Cooper pairs, the cross currents are highly correlated, and also the cross Fano factor that describes (cross-) correlations is positive. Indeed, positive cross-correlation noise was measured experimentally for the Cooper pair splitter in Ref. [97]. The presence of elastic cotunneling can mix the separate flows of electrons from split Cooper pairs, thereby reducing correlations and increasing fluctuations as described by the second term in Eq. (3.44). As the drain tunneling rates are reduced, and all governing processes become more intertwined, the Fano factor is complicated further by the additional contribution from the third term in Eq. (3.44).

The frequency-dependent noise spectrum provide additional insights into the transport processes. In particular, Fig. 3.8 shows the frequency-resolved Fano factor. Importantly, for small tunneling rates to the drains (solid curves), the characteristic frequencies $\omega_{\rm CPS}$ and $\omega_{\rm EC}$ in Eq. (3.42) show up as dips and peaks, respectively, in the cross Fano factor. In the regime of large drain tunneling rates (dotted curves), the frequency-resolved Fano factor develops a centralized structure with extrema characterized by the zero-frequency Fano factor. Thus, finite-frequency noise measurements may allow one to understand the relative importance of incoherent and coherent processes, and when the rate of the latter exceeds the former, it may provide additional insight into the role of Cooper pair splitting versus elastic cotunneling. We note, however, that delicate features in the finite-frequency noise spectrum may be sensitive to external decoherence and dephasing mechanisms that are not included here.

Electron waiting times

An alternative way to describe the transport characteristics of the Cooper pair splitter is in terms of so-called electron waiting time distributions (WTD), i.e. the distribution of waiting times between electron tunneling events to the metal collectors. Experimentally, there is a trade-off between separating time-scales to control the governing processes in Cooper pair splitters, and achieving large enough currents for conventional current measurements. For example, in Refs. [82, 83] the tunnel couplings are in the same order of magnitude as the superconducting gap, corresponding to rates in the order of GHz. Hence transport may not be fully limited to subgap transport, and it is commented in Ref. [82] that "there is potential for improving the efficiency of such a device by using more opaque tunnelling

[24] See, e.g., also the experimental results in Ref. [47] for Poissonian transport through an asymmetrically coupled QD.

barriers." Indeed, there has been a recent interest in studying transport in nanostructures with tunneling rates in the kHz, where real-time detection of tunneling events is feasible, and the distribution of waiting times between tunneling events can be measured. For example, real-time detection was used to study transport statistics of a single-electron transistor [96] and cross normal-state–superconductor interfaces [84], with the latter reference proposing as an outlook "experimental investigations of the statistics of entangled electron pairs" [84]. Experimental measurements of electron waiting time distributions is still a somewhat new, but growing, research field [98, 99, 100, 101, 102], which at this stage has focused mainly on analyzing dynamics in single quantum dots[25]. However, the Cooper pair splitter is a very interesting system to characterize in terms of electron waiting time distributions, and we show in the following how the WTD provides a fairly direct view into the governing transport processes, and in particular into the non-local nature of Cooper pair splitting.

Experimentally, waiting time distributions and frequency-dependent current statistics can be measured from charge detections in real-time. For example, in Ref. [96] the authors study frequency-resolved transport properties of a quantum dot coupled through tunneling barriers to source and drain electrodes (in the regime of unidirectional transport). The quantum dot is fabricated from local depletion of electrons in a two-dimensional electron gas in a GaAs/AlGaAs heterostructure. The electron occupancy of the quantum dot is measured in real time by passing a current through a nearby quantum point contact (QPC). The conductance of the QPC is highly sensitive to the electron occupancy on the QD, and hence the current shows abrupt jumps in real-time when the occupancy on the dot changes (see e.g. Fig. 1(a) in Ref. [96]). This enables the authors to fully characterize the device in terms of frequency-dependent current statistics.

We define the waiting time distribution (WTD) [103, 104]

$$\mathcal{W}_{ji}(\tau) \equiv \frac{\mathrm{Tr}[\mathcal{J}_j e^{(\mathcal{L}-\mathcal{J}_j)\tau}\mathcal{J}_i\hat{\rho}^{(S)}]}{\mathrm{Tr}[\mathcal{J}_i\hat{\rho}^{(S)}]}, \tag{3.45}$$

where $\mathcal{W}_{ji}(\tau)d\tau$ measures the probability that, given an event of type i has just occurred, an event of type j occurs in the time interval $d\tau$ that follows after a period of length τ where no events of type j has occurred, as well as the exclusive waiting time distribution [91]

$$\mathcal{W}^{\mathrm{ex}}_{ji}(\tau) \equiv \frac{\mathrm{Tr}[\mathcal{J}_j e^{\mathcal{L}^{\mathrm{ex}}\tau}\mathcal{J}_i\hat{\rho}^{(S)}]}{\mathrm{Tr}[\mathcal{J}_i\hat{\rho}^{(S)}]}, \tag{3.46}$$

where $\mathcal{L}^{\mathrm{ex}} = \mathcal{L} - \sum_k \mathcal{J}_k$ removes all possible incoherent transitions from the full time evolution given by $\mathcal{L}$. Using that $\int_0^T d\tau e^{(\mathcal{L}-\mathcal{J}_j)\tau} \xrightarrow{T\to\infty} -[\mathcal{L}-\mathcal{J}_j]^{-1}$, one has

$$\int_0^\infty d\tau \mathcal{W}_{ji}(\tau) = -\frac{\mathrm{Tr}[\mathcal{J}_j[\mathcal{L}-\mathcal{J}_j]^{-1}\mathcal{J}_i\hat{\rho}^{(S)}]}{\mathrm{Tr}[\mathcal{J}_i\hat{\rho}^{(S)}]} = \frac{\mathrm{Tr}[[\mathcal{L}-\mathcal{J}_j][\mathcal{L}-\mathcal{J}_j]^{-1}\mathcal{J}_i\hat{\rho}^{(S)}]}{\mathrm{Tr}[\mathcal{J}_i\hat{\rho}^{(S)}]} = 1, \tag{3.47}$$

where we have used that $\mathrm{Tr}[\mathcal{L}[\,\bullet\,]] = 0$ due to conservation of probability (can e.g. be seen by acting with $\mathcal{L}$ in Eq. (3.35) on a general vector). By contrast, the exclusive WTD is only normalised upon integrating over all waiting times *and* summing over all types of final events.

The definition of the waiting time distribution can be motivated in various ways. Here we are inspired by the discussion in Ref. [105]. Expanding the exponential of the Liouville operator, $\mathcal{L} = \mathcal{L}_0 + \sum_{l=1}^M \mathcal{J}_l$,

[25] See, however, Ref. [101] for an experiment on double quantum dots.

we can unravel the master equation as [91] [105, Eq. (7.17)]

$$\hat{\rho}_S(t) = \sum_{n=0}^{\infty} \sum_{l_1=1,\cdots l_n=1}^{M} \int_0^t dt_n \cdots \int_0^{t_2} dt_1 \left\{ S_{t-t_n} \mathcal{J}_{l_n} S_{t_n-t_{n-1}} \mathcal{J}_{l_{n-1}} \cdots \mathcal{J}_{l_1} S_{t_1} \hat{\rho}_{S,0} \right\} \equiv \sum_{n=0}^{\infty} \hat{\rho}_S(n,t), \tag{3.48}$$

where $S_t = \exp[\mathcal{L}_0 t]$ and the quantity inside $\{ \bullet \}$ is the unnormalized conditioned density operator describing the time-evolution of an initial density operator $\hat{\rho}_{S,0}$, interrupted by n jumps of type l_i at times t_i with $i = 1, \ldots n$ [91]. We can understand Eq. (3.48) as a generalized sum over all the possible event trajectories that the system can follow during its evolution. Each trajectory may involve any number of different events, from $n = 0$ to $n = \infty$, and the times of the events can be any ordered sequence of n times in the interval $[0, t]$ [105]. We can define a conditioned density operator by taking a particular trajectory, normalize it, and give it a physical interpretation in terms of an evolution without events interrupted by collapses at the times of the events [105]. Consider the subset of trajectories with two types of jump processes, i and j, where the final jump only is of type j, and let us furthermore reduce to the subset where the stationary density matrix $\hat{\rho}^{(S)}$ evolves after an event of type i to the last event j at $t_l = \tau$

$$\begin{aligned} \hat{\rho}_{S,\mathrm{c}}(\tau) &\equiv \mathcal{J}_j S_\tau \mathcal{J}_i \hat{\rho}^{(S)} + \int_0^\tau dt_1 \mathcal{J}_j S_{\tau-t_1} \mathcal{J}_i S_{t_1} \mathcal{J}_i \hat{\rho}^{(S)} + \int_0^\tau dt_2 \int_0^{t_2} dt_1 \mathcal{J}_j S_{\tau-t_2} \mathcal{J}_i S_{t_2-t_1} \mathcal{J}_i S_{t_1} \mathcal{J}_i \hat{\rho}^{(S)} + \cdots \\ &= \mathcal{J}_j e^{(\mathcal{L}_0+\mathcal{J}_i)\tau} \mathcal{J}_i \hat{\rho}^{(S)} = \mathcal{J}_j e^{(\mathcal{L}-\mathcal{J}_j)\tau} \mathcal{J}_i \hat{\rho}^{(S)}. \end{aligned} \tag{3.49}$$

The trace of this unnormalized conditional density matrix can be interpreted as the probability of these trajectories to occur, and upon dividing by the rate of events of type i we obtain the normalized waiting time distribution in Eq. (3.45).

Figures 3.9a and 3.9b show the spin-resolved waiting time distributions[26] (solid lines) for transitions into the same lead (local WTD) and different leads (non-local WTD), respectively, with levels detuned so that only CPS processes are on resonance and $\gamma_L, \gamma_R \gg \gamma_{\mathrm{CPS}}, \gamma_{\mathrm{EC}}$. Since the QDs cannot be doubly occupied, the distribution of waiting times between transitions into the left lead (Fig. 3.9a) is strongly suppressed at short times, and vanishes completely at $\tau = 0$. At long times, the local WTD is governed by the slow refilling of the left QD and the subsequent tunneling of an electron into the left lead. This local WTD resembles what one would expect for single-electron tunneling through a single QD without any Cooper pair splitting (see e.g. the experimental paper [100], and in particular Fig. 3(a)). By contrast, the non-local distribution of waiting times between transitions into different leads (Fig. 3.9b) shows an entirely different short-time behavior for opposite spins. The tunneling of a spin-up electron into the left lead is likely followed by the tunneling of a spin-down electron into the right lead, signaled by a large peak in the non-local WTD at short times. This is a clear signature of the splitting of Cooper pairs, and reflects the non-local nature of the CPS processes. At long times, the non-local WTD is governed by the slow refilling of the right QD by an electron from a new Cooper pair and the subsequent tunneling of the electron into the right lead. Thus, the non-local waiting time distribution carries information about the short waiting times between electrons from the same Cooper pair and the long waiting times between electrons originating from different Cooper pairs. For opposite spins, the local intermediate-time WTD in Fig. 3.9a shows a small enhancement due to elastic cotunneling. This effect is enhanced in Fig. 3.9c where both CPS and EC processes are tuned into resonance.

To gain further insights, we can evaluate the exclusive WTD analytically. For example, with

[26] We apply the matrix exponential in Eqs. (3.45)-(3.46) using the function "MatrixExp" in Mathematica (see also Ref. [91]).

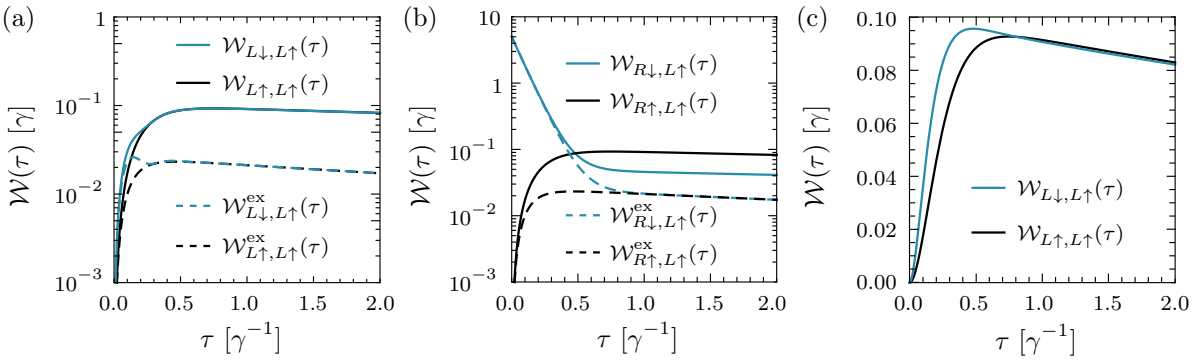

Figure 3.9: (a) Spin-resolved WTDs for tunneling into the same lead. (b) Spin-resolved WTDs for tunneling into different leads. In (a) and (b), the parameters are $\gamma_L = \gamma_R \equiv 10\gamma$, $\gamma_{\rm CPS} = \gamma_{\rm EC} = \gamma$, and $\epsilon_L = -\epsilon_R = 10\hbar\gamma$. (c) Spin-resolved WTDs for tunneling into the same lead with same parameters except that $\epsilon_L = \epsilon_R = 0$. From Publication II.

$\gamma_L = \gamma_R = \gamma_N$ and $\epsilon_L = -\epsilon_R = \epsilon\hbar$, we find

$$\begin{aligned}
\mathcal{W}^{\rm ex}_{\ell\sigma,\ell'\sigma}(\tau) =& \frac{\gamma_N}{2} e^{-\gamma_N\tau}\alpha^2_{\rm CPS}[1-\cos(\bar{\omega}_{\rm CPS}\tau)]\,,\\
\mathcal{W}^{\rm ex}_{\ell\sigma,\ell\bar{\sigma}}(\tau) =& \gamma_N e^{-\gamma_N\tau}\alpha^2_{\rm EC}[1-\cos(\bar{\omega}_{\rm EC}\tau)] + \mathcal{W}^{\rm ex}_{\ell\sigma,\ell\sigma}(\tau),\\
\mathcal{W}^{\rm ex}_{\ell\sigma,\bar{\ell}\bar{\sigma}}(\tau) =& \frac{\gamma_N}{2} e^{-\gamma_N\tau} + 2\mathcal{W}^{\rm ex}_{\ell\sigma,\ell\sigma}(\tau) - \mathcal{W}^{\rm ex}_{\ell\sigma,\ell\bar{\sigma}}(\tau),
\end{aligned} \tag{3.50}$$

with $\bar{L} = R$ and $\bar{\uparrow} = \downarrow$ and vice versa, and we have identified the frequencies $\bar{\omega}_{\rm CPS} = 2\sqrt{\gamma^2_{\rm CPS} - (\gamma_N/2)^2}$ and $\bar{\omega}_{\rm EC} = 2\sqrt{\gamma^2_{\rm EC} + \epsilon^2}$ associated with the coherent CPS and EC processes, and introduced the ratios $\alpha_{\rm CPS} = \gamma_{\rm CPS}/\bar{\omega}_{\rm CPS}$ and $\alpha_{\rm EC} = \gamma_{\rm EC}/\bar{\omega}_{\rm EC}$. Exclusive WTDs are plotted with dashed lines in Figs. 3.9a-b. If $\gamma_{\rm CPS} \gg \gamma_L, \gamma_R$, the WTD exhibits oscillations with frequency $\bar{\omega}_{\rm CPS} \simeq 2\gamma_{\rm CPS}$ (discussed below). By contrast, for $\gamma_{\rm CPS} \ll \gamma_L, \gamma_R$, the frequency becomes imaginary and now rather corresponds to an exponential decay.

Experimentally, one might measure spin-resolved WTDs using ferromagnetic detectors [106, 107, 108, 109], which, however, is indeed more challenging than measuring charge states [110, 111, 112, 84]. However, from the non-local spin-resolved waiting time distribution, we can define a branching ratio as

$$\mathcal{R}_{R\downarrow,L\uparrow}(\tau) \equiv \frac{\mathcal{W}_{R\downarrow,L\uparrow}(\tau)}{\mathcal{W}_{R\downarrow,L\uparrow}(\tau) + \mathcal{W}_{R\uparrow,L\uparrow}(\tau)}. \tag{3.51}$$

The branching ratio is shown in Fig. 3.10a and shows that it is highly probable that electrons separated by a short non-local waiting time have opposite spins and they likely originate from the same Cooper pair. Hence, the non-local nature of Cooper pair splitting may also conveniently be identified in the charge-resolved WTDs shown in Fig. 3.10b-c and, experimentally, a measurement of these WTDs (in particular, observing the difference in the short-time characteristics of the local and non-local WTD in panel b and c, respectively) would constitute a strong evidence of efficient Cooper pair splitting. In Fig. 3.10b-c, we also show the exclusive WTDs $\mathcal{W}^{\rm ex}_{\ell\ell'}(\tau) = \sum_{\sigma,\sigma'}\mathcal{W}^{\rm ex}_{\ell\sigma,\ell'\sigma'}(\tau)/2$. For short times, we have $\mathcal{W}^{\rm ex}_{LL}(\tau) \simeq (\bar{\omega}_{\rm CPS}\tau)^2$. By contrast, for the WTD in Fig. 3.10c the short-time behavior $\mathcal{W}^{\rm ex}_{RL}(\tau) \simeq e^{-\gamma_N\tau}$ is governed by the escape rate, while the long-time decay $\mathcal{W}^{\rm ex}_{RL}(\tau) \simeq e^{-2\tau\gamma^2_{\rm CPS}/\gamma_N}$ is governed by the rate of Cooper pair splitting and emission.

Until now we have discussed the case where $\gamma_{\rm CPS}, \gamma_{\rm EC} \ll \gamma_L, \gamma_R$. While this regime may be most attractive for efficient Cooper pair splitting, since the split pair is quickly transferred to the drains, the opposite regime, $\gamma_{\rm CPS}, \gamma_{\rm EC} \gg \gamma_L, \gamma_R$, is also interesting. WTDs in this regime are plotted in

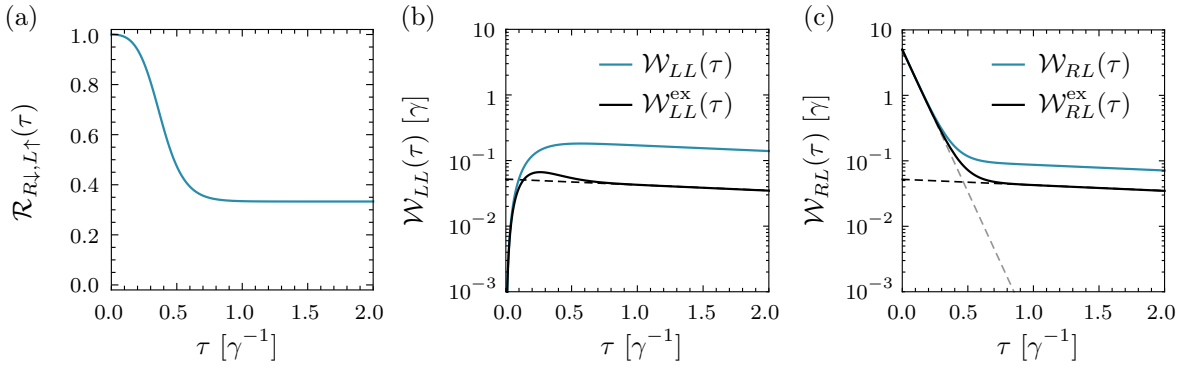

Figure 3.10: (a) The branching ratio in Eq. (3.51) corresponding to the WTDs in Fig. 3.9b. (b)–(c): Charge-resolved WTDs for tunneling into the same (b) and different (c) leads. Parameters are $\gamma_L = \gamma_R \equiv \gamma_N = 10\gamma$, $\gamma_{\rm CPS} = \gamma_{\rm EC} = \gamma$, and $\epsilon_L = \epsilon_R = 0$. Dashed lines are exponentials with decay rates γ_N (grey) and $2\gamma^2_{\rm CPS}/\gamma_N$ (black). From Publication II.

Fig. 3.11, where the rate of escape to the drains is so slow that several coherent oscillations (similar to the oscillations discussed in Refs. [91, 113]), with frequency $\bar{\omega}_{\rm CPS} \simeq 2\gamma_{\rm CPS}$, between the QDs and the superconductor may occur. Such oscillations may, however, be sensitive to decoherence (see however the discussion in Ref. [113]).

3.2.3 Short summary

In this section we discussed some transport characteristics of a Cooper pair splitter. In the regime of unidirectional transport, large superconducting gap, and large intradot Coulomb-interactions which prevent double-occupancy of the individual QDs, we described the Cooper pair splitter by a Markovian master equation for the dynamics of electrons in the quantum dots, from which we obtained the steady-state transport characteristics. For the current we recovered well-known results in certain limits. Furthermore, we showed how the competing processes of Cooper pair splitting and elastic cotunneling may be manifested in the low-frequency fluctuations of the currents and their cross correlations. In the limit of small couplings to the normal-state leads, the two types of processes showed up as dips and peaks in the finite-frequency noise spectrum of the cross correlations. We furthermore characterized the Cooper pair splitter in terms of the distribution of electron waiting times, which provides a fairly direct view into the governing transport processes and the non-local nature of Cooper pair splitting.

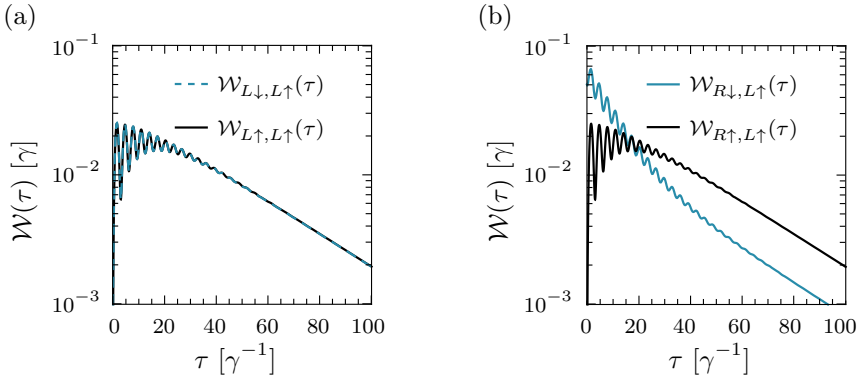

Figure 3.11: (a) Spin-resolved WTDs for tunneling into the same lead. (b) Spin-resolved WTDs for tunneling into different leads. In both panels, the parameters are $\gamma_L = \gamma_R \equiv 0.1\gamma$, $\gamma_{\rm CPS} = \gamma_{\rm EC} = \gamma$, and $\epsilon_L = -\epsilon_R = 10\hbar\gamma$. From Publication II.

Specifically, the splitting of Cooper pairs is associated with a large peak at short times in the WTD for tunneling into different drains. When the couplings to the collector leads are larger than the amplitudes for Cooper pair splitting, a short waiting time between electrons tunneling into different leads is associated with a fast emission of a split Cooper pair, while long waiting times are governed by the slow coherent injection of Cooper pairs from a superconductor.

Although the simple model considered here allowed us to obtain some analytical results, in future work, it would be useful to relax the assumptions of the ideal operating conditions, such as including finite Coulomb-interactions, superconducting gap, bias voltages, and possible measurement back-action mechanisms in order to obtain an even more realistic model relevant for comparison with experiments. In this case, the master equation becomes non-Markovian in general. Recently, a real-time diagrammatic theory of electron waiting times for non-Markovian dynamics has been discussed in Ref. [114].

In perspective to our study of thermoelectric effects in Sec. 3.1, we also highlight some recent studies, and indeed an interesting route of research, of thermoelectric effects in Cooper pair splitters in Refs. [115, 116]. Furthermore, as introduced in Ch. 1, in the second part of the thesis we will study a selection of periodically driven low-dimensional systems, and another interesting route could indeed be to perturb the Cooper pair splitter periodically in time. Let us briefly discuss such a dynamically controlled Cooper pair splitter as an outlook for future research.

3.2.4 Outlook: Dynamically controlled Cooper pair splitting

Quoting Ref. [117]: "The ability to create non-local entangled electron pairs—known as Einstein-Podolsky-Rosen pairs—on demand has long been a dream." Let us discuss how we might dynamically control the Cooper pair splitter (discussions in collaboration with Christian Flindt).

When not resolving the spin-degree of freedom, it is convenient to write the Liouvillian in Eq. (3.35) in the simpler charge state basis $\{\rho_{(0)(0)}, \rho_{(L)(L)}, \rho_{(R)(R)}, \rho_{(S)(S)}, \rho_{(0)(S)}, \rho_{(S)(0)}, \rho_{(L)(R)}, \rho_{(R)(L)}\}$, where $\rho_{(\ell)(\ell')} = \sum_\sigma \rho_{(\ell\sigma)(\ell'\sigma)}$, $\ell, \ell' \in \{L, R\}$. We could then propose a time-dependent evolution governed by

$$\mathcal{L}(t) = \begin{pmatrix} 0 & \gamma_L & \gamma_R & 0 & -i\gamma_{\rm CPS} & i\gamma_{\rm CPS} & 0 & 0 \\ 0 & -\gamma_L & 0 & \gamma_R & 0 & 0 & -i\gamma_{\rm EC} & i\gamma_{\rm EC} \\ 0 & 0 & -\gamma_R & \gamma_L & 0 & 0 & i\gamma_{\rm EC} & -i\gamma_{\rm EC} \\ 0 & 0 & 0 & -(\gamma_L+\gamma_R) & i\gamma_{\rm CPS} & -i\gamma_{\rm CPS} & 0 & 0 \\ -i\gamma_{\rm CPS} & 0 & 0 & i\gamma_{\rm CPS} & i\varepsilon(t)-\frac{\gamma_L+\gamma_R}{2} & 0 & 0 & 0 \\ i\gamma_{\rm CPS} & 0 & 0 & -i\gamma_{\rm CPS} & 0 & -i\varepsilon(t)-\frac{\gamma_L+\gamma_R}{2} & 0 & 0 \\ 0 & -i\gamma_{\rm EC} & i\gamma_{\rm EC} & 0 & 0 & 0 & -i\delta(t)-\frac{\gamma_L+\gamma_R}{2} & 0 \\ 0 & i\gamma_{\rm EC} & -i\gamma_{\rm EC} & 0 & 0 & 0 & 0 & i\delta(t)-\frac{\gamma_L+\gamma_R}{2} \end{pmatrix}, \tag{3.52}$$

where now $\varepsilon(t) = (\epsilon_L(t) + \epsilon_R(t))/\hbar$ and $\delta(t) = (\epsilon_L(t) - \epsilon_R(t))\hbar$ are time-dependent. At this stage, Eq. (3.52) is not justified, but let us see what kind of behavior it can give rise to. For a periodic drive, $\mathcal{L}(t+T) = \mathcal{L}(t)$, the Liouville equation has a periodic solution with the same period [118], $\hat{\rho}(t+T) = \hat{\rho}(t)$. Hence,

$$\hat{\rho}(t) = A_{t+T,t}\hat{\rho}(t), \tag{3.53}$$

and we can find a cyclic solution, $\hat{\rho}^{(C)}(t)$, from the eigenvector of $A_{t+T,t}$ corresponding to the eigenvalue one. Consider e.g. the drive scheme illustrated in Fig. 3.12a

$$\epsilon_L(t) = \epsilon_L, \quad \epsilon_R(t) = \epsilon_R + V_g\theta[\sin(2\pi(t-T_1)/T)], \tag{3.54}$$

where θ is the Heaviside step function, T is the drive period, and T_1 controls the time where the QD levels changes as in (1) and (2) in Fig. 3.12a. In Fig. 3.12b, we show the cyclic current $I_S(t) = I_L(t) + I_R(t)$, $I_\ell(t) \equiv \mathrm{Tr}[\mathcal{J}_\ell\hat{\rho}^{(C)}(t)]$ for one drive period. Here T_1 is tuned to the frequency of Cooper pair splitting such that the QDs are likely occupied by a Cooper pair at the moment where the level of the right QD is shifted, whereafter the split Cooper pair can tunnel into the normal leads. The current during one drive period is integrated to 1.98, hence, approximately one Cooper pair is split

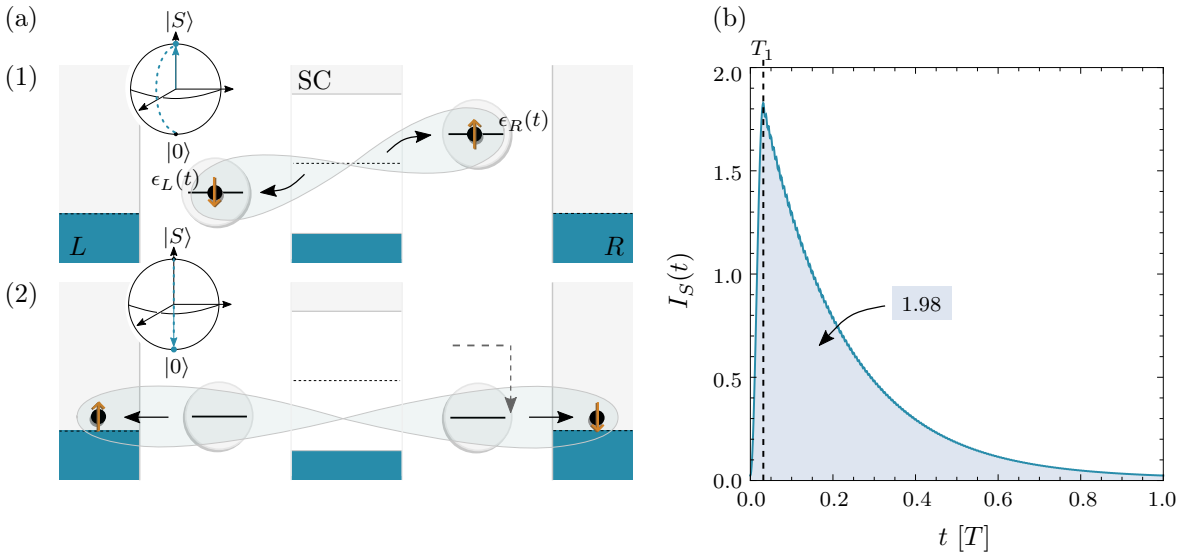

Figure 3.12: (a) Two quantum dots with time-dependent energy-levels coupled to a superconducting source and two normal-metal drains. (1) To load the dots, the energy-levels are tuned into resonance for a duration in which the state coherently evolves from the empty state to the singlet state. (2) Tuning the levels off-resonance, the Cooper pair can unload into the normal-state drains before repeating the cycle. (b) Current from the Cooper pair splitter as a function of time for $\gamma_L = \gamma_R = \gamma_N = 1$, $\gamma_{\rm CPS} = 10\gamma_N$, $\gamma_{\rm EC} = 0$, $\epsilon_R = -\epsilon_L = 100\gamma_N$, $V_G = -200\gamma_N$, $T = 5$, and $T_1 = \pi/(2\gamma_{\rm CPS}[1-(\gamma_N/(2\gamma_{\rm CPS}))^2]^{1/2})$. The current integrated over one drive period is indicated in the blue box.

in each drive cycle. The unload time $T - T_1$ needs to be sufficiently large to allow the Cooper pair to escape to the leads, therefore the integrated current deviates slightly from 2. The integrated current could similarly be slightly larger than 2 due to the finite lead-coupling. In another drive scheme one could dynamically control the lead-coupling instead of the QD levels to reduce this deviation. Upon justification of Eq. (3.52), for further analysis it would be interesting to study the waiting time distribution in such a dynamically driven system, similar to the recent experiment in Ref. [102] where they measure waiting time distributions of a dynamically driven single-electron transistor. We note that in work-in-progress in collaboration with C. O. Taberner, we have set up a description of the periodically driven Cooper pair splitter in terms of non-equilibrium Green functions which in the un-driven case reduces to the results in Ref. [95]. The challenge is how to include the effect of Coulomb-interactions which becomes challenging even in the un-driven case [119].

4 | Non-equilibrium field theory

In the previous chapter we set up master equations to study transport processes in a few nano-structured systems out-of-equilibrium. Transport through 'small' systems of interest resulted from electron tunneling processes to and from large external reservoirs, caused by differences in the (locally equilibrated) distribution of electrons in the reservoirs. However, an external drive may also 'de-equilibrate' larger lattice systems and induce interesting macroscopic material properties, such as the light-induced superconductivity mentioned in Sec. 1.1. We will discuss some consequences of a periodic drive of a tight-binding lattice and the Hubbard model in the following chapters. The 'non-equilibrium Green function' (NEGF) formalism is an important technique for studying out-of-equilibrium quantum systems[1], and is well suited for this study. Non-equilibrium Green functions, however, have broad applicability, and we will also apply the formalism to discuss some properties of a harmonically driven single level in Secs. 5.2 and 6.7.1.

The following introduction to non-equilibrium Green functions is based on the formulation by Kamenev [121] and Altland and Simons [7], referred to as non-equilibrium field theory, which build on the works by Schwinger [122], Kadanoff and Baym [123], and Keldysh [124]. Although the formalism is introduced many places[2], the chapter serves to introduce the particular notation used in the following chapters as well as provide readers with sufficient background information for the discussions in the following chapters. For a more in-depth introduction we refer to Refs. [121, 7].

4.1 Time contour

The starting point for constructing the non-equilibrium field theory and the non-equilibrium Green functions is the time-evolution of expectation values of observables (1.5) [121]

$$\langle\hat{\mathcal{O}}\rangle(t) = \mathrm{Tr}\Big[\hat{U}_{t_0,t}\hat{\mathcal{O}}\hat{U}_{t,t_0}\hat{\rho}_0\Big] = \mathrm{Tr}\Big[\hat{U}_{t_0,t_f}\hat{U}_{t_f,t}\hat{\mathcal{O}}\hat{U}_{t,t_0}\hat{\rho}_0\Big]\,, \tag{4.1}$$

where we have used the property in Eq. (1.7). The right-hand-side of (4.1) describes an evolution along the contour $\mathcal{C} = \mathcal{C}_+ \cup \mathcal{C}_-$ illustrated in Fig. 4.1, from the initial density operator $\hat{\rho}_0$ at time t_0 to time t where the operator $\hat{\mathcal{O}}$ is evaluated, then continuing the evolution to time $t_f > t$ and back again to the initial time t_0. Due to the property of the evolution operator in Eq. (1.7), the expectation value does not depend on t_f, and it may be convenient to send $t_f \to \infty$. Thus, the calculation in (4.1) involves evolution *forward* and *backward* in time, and the resulting contour is denoted the *Schwinger-Keldysh contour* [26].

The contour in Fig. 4.1 is central to the following formulation of the non-equilibrium theory. The corresponding key operator is the time evolution operator along the contour, $\hat{U}_{\mathcal{C}} \equiv \hat{U}_{t_0,t_f}\hat{U}_{t_f,t_0}$, which is simply the identity, and hence we may define

$$\mathcal{Z} \equiv \mathrm{Tr}\Big[\hat{U}_{\mathcal{C}}\hat{\rho}_0\Big] = 1. \tag{4.2}$$

[1] Some remarks of the use of master equations versus non-equilibrium Greens function were provided in Sec. 1.4, however, see also Ref. [120].

[2] Besides the above-mentioned references, the author has also benefitted from excellent references such as by Aoki et al. [125] and Jakobs [126].

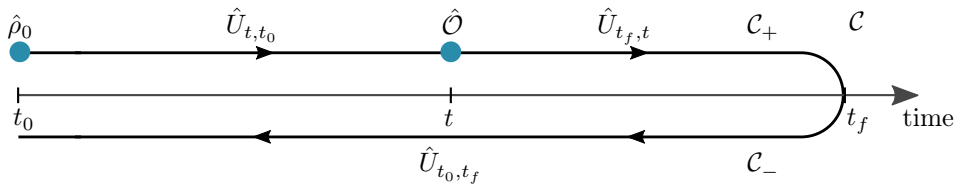

Figure 4.1: Contour $\mathcal{C} = \mathcal{C}_+ \cup \mathcal{C}_-$. Both the forward and backward branches coincide with the real time axis and are only drawn with a shift from the real axis for illustrational convenience.

The function $\mathcal{Z}$, which is referred to as the partition function, is nothing but (what will be proven to be) a very useful construction of unity. Indeed, we will see in the following how correlation functions are naturally derived from $\mathcal{Z}$.

4.2 Path integral representation

Since the path illustrated in Fig. 4.1 is central to the non-equilibrium theory, this seems to suggest that the path integral formalism could provide a convenient way to formulate the theory. Alternatively, one could also use the operator formalism [29]. To construct the path integral formulation of the theory, we discretize the contour in Fig. 4.1 in infinitesimal time steps, and introduce resolutions of identities which allow us to describe the infinitesimal time-evolution in each discrete time step. The eigenstates in terms of which we formulate resolutions of identities are eigenstates of the annihilation operators, the so-called *coherent states* [7]

$$\hat{a}_\lambda |\psi\rangle = \psi_\lambda |\psi\rangle, \tag{4.3}$$

where $\hat{a}_\lambda$ ($\hat{a}^\dagger_\lambda$) is the annihilation (creation) operator corresponding to the states, indexed by λ, which span the single-particle Hilbert-space of the problem. We will see an explicit construction of such a coherent state below. For bosons, $\{\psi_\lambda\}$ is a set of complex numbers, however, due to the anti-commuting property of fermionic operators, fermionic coherent states have a different mathematical structure from the bosonic coherent states; for fermions $\{\psi_\lambda\}$ is a set of so-called Grassmann numbers which anti-commute

$$\psi_\nu \psi_\lambda = -\psi_\lambda \psi_\nu \qquad \text{(fermions)}. \tag{4.4}$$

In the following we list some properties of coherent states which we will use to construct the path integral representation of the partition function. For a more detailed introduction to coherent states, Grassmann numbers, and for proofs of the following properties, we refer to Ref. [7] (see also Refs. [127, 128]). One can show that the following construction satisfies Eq. (4.3),

$$|\psi\rangle \equiv e^{\zeta \sum_\lambda \psi_\lambda \hat{a}^\dagger_\lambda} |0\rangle, \tag{4.5}$$

where $\zeta = +$ for bosons and $\zeta = -$ for fermions. The overlap between two coherent states is

$$\langle \psi | \psi' \rangle = e^{\sum_\lambda \bar{\psi}_\lambda \psi'_\lambda}, \tag{4.6}$$

where $\bar{\psi}_\lambda$ corresponds to the left eigenvalue of the left eigenstate, $\langle \psi | \hat{a}^\dagger_\lambda = \langle \psi | \bar{\psi}_\lambda$. Resolutions of identity in the Fock space can be represented by coherent states as

$$\mathbb{1} = \int d(\bar{\psi}, \psi)\, e^{-\sum_\lambda \bar{\psi}_\lambda \psi_\lambda} |\psi\rangle\langle\psi|, \tag{4.7}$$

where $d(\bar{\psi}, \psi) \equiv \Pi_\lambda d(\mathrm{Re}\,\psi_\lambda) d(\mathrm{Im}\,\psi_\lambda)/\pi$ for bosons and $d(\bar{\psi}, \psi) \equiv \Pi_\lambda d\bar{\psi}_\lambda\, d\psi_\lambda$ for fermions.

4.2.1 Partition function

We are now ready to construct the path integral representation of the partition function. From Eq. (4.2) we have

$$\begin{aligned}\mathcal{Z} &= \sum_n \langle n|\hat{U}_{\mathcal{C}}\hat{\rho}_0|n\rangle = \int d(\bar{\psi},\psi) e^{-\sum_\lambda \bar{\psi}_\lambda \psi_\lambda} \sum_n \langle n|\psi\rangle\langle\psi|\hat{U}_{\mathcal{C}}\hat{\rho}_0|n\rangle \\ &= \int d(\bar{\psi},\psi) e^{-\sum_\lambda \bar{\psi}_\lambda \psi_\lambda} \sum_n \langle\psi|\hat{U}_{\mathcal{C}}\hat{\rho}_0|n\rangle\langle n|\zeta\psi\rangle = \int d(\bar{\psi},\psi) e^{-\sum_\lambda \bar{\psi}_\lambda \psi_\lambda} \langle\psi|\hat{U}_{\mathcal{C}}\hat{\rho}_0|\zeta\psi\rangle,\end{aligned} \tag{4.8}$$

where $\{|n\rangle\}$ is a complete set of Fock space states, and we have inserted a coherent state resolution of identity and commuted left and right coherent states whereby in the fermionic case the coherent state picks up a minus sign $|-\psi\rangle = \exp\left(\sum_\lambda \psi_\lambda \hat{a}_\lambda^\dagger\right)|0\rangle$ [7]. To formulate the path integral representation of the partition function, we discretize the contour $\mathcal{C}$ in (4.8) into $2(N_{\mathcal{C}}-1)$ time-slices of length $\delta \to 0$ as $N_{\mathcal{C}} \to \infty$, while keeping $t_f - t_0 = \delta(N_{\mathcal{C}}-1)$ constant (see Fig. 4.2). Using Eq. (1.6) we can write the partition function as

$$\mathcal{Z} = \lim_{N_{\mathcal{C}}\to\infty} \int d(\bar{\psi},\psi) e^{-\sum_\lambda \bar{\psi}_\lambda \psi_\lambda} \langle\psi| e^{\frac{i}{\hbar}\hat{H}(t_0)\delta} \cdots e^{\frac{i}{\hbar}\hat{H}(t_0+(N_{\mathcal{C}}-2)\delta)\delta} e^{-\frac{i}{\hbar}\hat{H}(t_0+(N_{\mathcal{C}}-2)\delta)\delta} \cdots e^{-\frac{i}{\hbar}\hat{H}(t_0)\delta} \hat{\rho}_0|\zeta\psi\rangle, \tag{4.9}$$

which upon inserting $2N_{\mathcal{C}}-1$ coherent state resolutions of unity becomes

$$\begin{aligned}\mathcal{Z} = \int \mathcal{D}(\bar{\psi},\psi) & e^{-\sum_\lambda \bar{\psi}^-_{1\lambda}\psi^-_{1\lambda}} \langle\psi^-_1|\hat{U}_{\delta_1^-} e^{-\sum_\lambda \bar{\psi}^-_{2\lambda}\psi^-_{2\lambda}} |\psi^-_2\rangle\langle\psi^-_2| \cdots \hat{U}_{\delta^-_{N_{\mathcal{C}}-1}} e^{-\sum_\lambda \bar{\psi}^-_{N_{\mathcal{C}}\lambda}\psi^-_{N_{\mathcal{C}}\lambda}} |\psi^-_{N_{\mathcal{C}}}\rangle\langle\psi^-_{N_{\mathcal{C}}}|\mathbb{1} \\ & \times e^{-\sum_\lambda \bar{\psi}^+_{N_{\mathcal{C}}\lambda}\psi^+_{N_{\mathcal{C}}\lambda}} |\psi^+_{N_{\mathcal{C}}}\rangle\langle\psi^+_{N_{\mathcal{C}}}|\hat{U}_{\delta^+_{N_{\mathcal{C}}-1}} e^{-\sum_\lambda \bar{\psi}^+_{N_{\mathcal{C}}-1,\lambda}\psi^+_{N_{\mathcal{C}}-1,\lambda}} |\psi^+_{N_{\mathcal{C}}-1}\rangle\langle\psi^+_{N_{\mathcal{C}}-1}| \cdots \hat{U}_{\delta_1^+} e^{-\sum_\lambda \bar{\psi}^+_{1\lambda}\psi^+_{1\lambda}} |\psi^+_1\rangle \\ & \times \langle\psi^+_1|\hat{\rho}_0|\zeta\psi^-_1\rangle,\end{aligned} \tag{4.10}$$

where $\int\mathcal{D}(\bar{\psi},\psi) = \lim_{N_{\mathcal{C}}\to\infty}\int\Pi_{\tau=\pm}\Pi_{t=1}^{N_{\mathcal{C}}}\Pi_\lambda d(\bar{\psi}^\tau_{t,\lambda},\psi^\tau_{t,\lambda})$, t is a discrete time index, and $\hat{U}_{\delta_t^\pm}$ governs the time-evolution along the infinitesimal contour $\delta_t^\pm$ cf. Fig. 4.2,

$$\hat{U}_{\delta_t^\pm} = 1 \mp \frac{i}{\hbar}\hat{H}(t_0+(t-1)\delta)\delta + O(\delta^2). \tag{4.11}$$

The matrix elements of the infinitesimal time evolution operators are obtained for the normal-ordered Hamiltonian as

$$\langle\psi^+_t|\hat{U}_{\delta^+_{t-1}}|\psi^+_{t-1}\rangle = e^{\sum_\lambda \bar{\psi}^+_{t\lambda}\psi^+_{t-1,\lambda}} e^{-\frac{i\delta}{\hbar}H(t_0+(t-2)\delta)[\bar{\psi}^+_t,\psi^+_{t-1}]} + O(\delta^2), \tag{4.12a}$$

$$\langle\psi^-_t|\hat{U}_{\delta^-_t}|\psi^-_{t+1}\rangle = e^{\sum_\lambda \bar{\psi}^-_{t\lambda}\psi^-_{t+1,\lambda}} e^{\frac{i\delta}{\hbar}H(t_0+(t-1)\delta)[\bar{\psi}^-_t,\psi^-_{t+1}]} + O(\delta^2), \tag{4.12b}$$

where we have used that $\langle\psi|\hat{H}[\hat{a}^\dagger,\hat{a}\,]|\psi'\rangle = \langle\psi|\psi'\rangle\hat{H}[\hat{a}^\dagger\to\bar{\psi},\hat{a}\,\to\psi']$ for $\hat{H}$ containing linear combinations of products of creation and annihilation operators. Hence, we can write the partition function as

$$\mathcal{Z} = \int\mathcal{D}(\bar{\psi},\psi)\exp\left(\frac{i}{\hbar}S(\bar{\psi},\psi)\right), \tag{4.13}$$

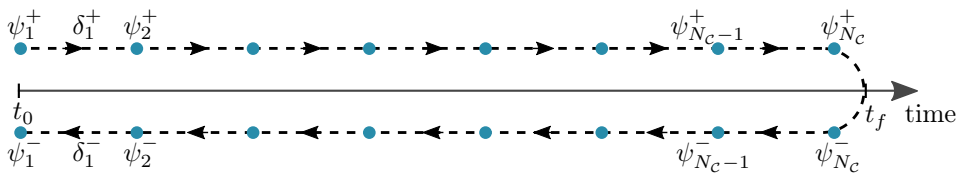

Figure 4.2: Discretized contour $\mathcal{C}$.

where we have defined the action

$$\begin{aligned} S(\bar{\psi},\psi) \equiv \sum_{\tau=\pm}\sum_{t=2-\delta_{\tau,-}}^{N_{\mathcal{C}}-\delta_{\tau,-}}(\tau\delta)\left[i\hbar\sum_{\lambda}\bar{\psi}^{\tau}_{t\lambda}\frac{\psi^{\tau}_{t+\delta_{\tau-},\lambda}-\psi^{\tau}_{t-\delta_{\tau+},\lambda}}{\delta}-H^{\tau}_{t}[\bar{\psi}^{\tau}_{t},\psi^{\tau}_{t-\tau}]\right] \\ +i\hbar\sum_{\lambda}\left[\bar{\psi}^{+}_{1\lambda}\psi^{+}_{1\lambda}+\bar{\psi}^{-}_{N_{\mathcal{C}}\lambda}(\psi^{-}_{N_{\mathcal{C}}\lambda}-\psi^{+}_{N_{\mathcal{C}}\lambda})\right]-i\hbar\mathcal{B}(\bar{\psi}^{+}_{1},\psi^{-}_{1}), \end{aligned} \tag{4.14}$$

where $H^{\tau}_{t}\equiv H(t-\delta_{\tau+})$, and we have used the notation $t-\tau=t\mp 1$ for $\tau=\pm$, and defined

$$\mathcal{B}(\bar{\psi}^{+}_{1},\psi^{-}_{1})\equiv\ln\langle\psi^{+}_{1}|\hat{\rho}_{0}|\zeta\psi^{-}_{1}\rangle. \tag{4.15}$$

Equation (4.14) is the general discrete-time form of the non-equilibrium action. In the following we consider a particular useful limit of Eq. (4.14).

4.2.2 Non-interacting Green functions

Consider a diagonal Hamiltonian with the initial state operator being the thermal equilibrium Gibbs distribution

$$\hat{H}_{0}(t)=\sum_{\lambda}\epsilon_{\lambda}(t)\hat{a}^{\dagger}_{\lambda}\hat{a}_{\lambda},\qquad \hat{\rho}_{0}=\mathcal{Z}_{0}^{-1}e^{-\beta\sum_{\lambda}(\epsilon_{\lambda}(t_{0})-\mu)\hat{a}^{\dagger}_{\lambda}\hat{a}_{\lambda}}, \tag{4.16}$$

where μ is the chemical potential, $\beta=1/(k_{B}T)$ with T being the temperature, and $\mathcal{Z}_{0}=\Pi_{\lambda}(1-\zeta\kappa_{\lambda})^{-\zeta}$ with $\kappa_{\lambda}=\exp(-\beta(\epsilon_{\lambda}(t_{0})-\mu))$. In this case[3]

$$\langle\psi^{+}_{1}|\hat{\rho}_{0}|\zeta\psi^{-}_{1}\rangle=\mathcal{Z}_{0}^{-1}e^{\zeta\sum_{\lambda}\bar{\psi}^{+}_{1,\lambda}\psi^{-}_{1,\lambda}\kappa_{\lambda}}. \tag{4.17}$$

The action in (4.14) takes a quadratic form of the fermionic fields, and may be written as (see also Sec. 4.3 below) [121]

$$S_{0}(\bar{\psi},\psi)=\int_{\mathcal{C}}d\tau\sum_{\lambda}\bar{\psi}_{\lambda}(\tau)G^{-1}_{0,\lambda}(\tau)\psi_{\lambda}(\tau), \tag{4.18}$$

which is a continuum representation of the discrete-time action[4]

$$S_{0}(\bar{\psi},\psi)=\sum_{\lambda}\bar{\boldsymbol{\psi}}_{\lambda}\boldsymbol{G}^{-1}_{0,\lambda}\boldsymbol{\psi}_{\lambda}, \tag{4.19}$$

where $\boldsymbol{\psi}_{\lambda}=(\boldsymbol{\psi}^{+}_{\lambda},\boldsymbol{\psi}^{-}_{\lambda})^{T}$ with $\boldsymbol{\psi}^{\pm}_{\lambda}=(\psi^{\pm}_{1\lambda},\cdots,\psi^{\pm}_{N_{\mathcal{C}}\lambda})^{T}$, and

$$\boldsymbol{G}^{-1}_{0,\lambda}=i\hbar\left[\begin{array}{cccc|cccc} 1 & & & & -\zeta\kappa_{\lambda} & & & \\ -u^{+}_{1\lambda} & 1 & & & & & & \\ & \ddots & \ddots & & & & & \\ & & -u^{+}_{N_{\mathcal{C}}-1,\lambda} & 1 & & & & \\ \hline & & & & 1 & -u^{-}_{1\lambda} & & \\ & & & & & \ddots & \ddots & \\ & & & & & & 1 & -u^{-}_{N_{\mathcal{C}}-1,\lambda} \\ & & & -1 & & & & 1 \end{array}\right]\equiv\left[\begin{array}{c|c} \boldsymbol{G}^{-1,++}_{0,\lambda} & \boldsymbol{G}^{-1,+-}_{0,\lambda} \\ \hline \boldsymbol{G}^{-1,-+}_{0,\lambda} & \boldsymbol{G}^{-1,--}_{0,\lambda} \end{array}\right], \tag{4.20}$$

[3] For bosons the expression is derived using the identity [129] $e^{c\hat{a}^{\dagger}\hat{a}}=:\exp[(e^{c}-1)\hat{a}^{\dagger}\hat{a}]:$, where $:\cdots:$ (normal-) orders all creation operators to the left of all the annihilation operators. For fermions, a proof is provided in e.g. Ref. [130].

[4] We absorb $\mathcal{Z}_{0}^{-1}$ into the measure $\mathcal{D}$ in Eq. (4.13). See e.g. Refs. [7, 126] for a proof of the normalization of $\mathcal{Z}$ from the discrete-time action.

with

$$G^{-1,++}_{0,\lambda,tt'} = i\hbar(\delta_{tt'} - u^{+}_{t'\lambda}\delta_{t,t'+1}), \tag{4.21a}$$

$$G^{-1,--}_{0,\lambda,tt'} = i\hbar(\delta_{tt'} - u^{-}_{t\lambda}\delta_{t,t'-1}), \tag{4.21b}$$

$$G^{-1,+-}_{0,\lambda,tt'} = -\zeta i\hbar\kappa_\lambda \delta_{t1}\delta_{t'1}, \tag{4.21c}$$

$$G^{-1,-+}_{0,\lambda,tt'} = -i\hbar\delta_{tN_\mathcal{C}}\delta_{t'N_\mathcal{C}}, \tag{4.21d}$$

and $u^{\pm}_{t\lambda} \equiv 1 \mp i\epsilon_\lambda(t_0 + (t-1)\delta)\delta/\hbar = \exp(\mp i\epsilon_\lambda(t_0 + (t-1)\delta)\delta/\hbar)$ $(\delta \to 0)$.

The usefulness of constructing the partition function now becomes clear[5]: According to the property of Gaussian integration (Eqs. (A.69), (A.71)), the quadratic action in the partition function expresses the inverse propagator, that is, we obtain the correlation function of two fields as

$$\left[\begin{array}{c|c} \left\langle \psi^{+}_{t\lambda}\bar{\psi}^{+}_{t'\lambda}\right\rangle & \left\langle \psi^{+}_{t\lambda}\bar{\psi}^{-}_{t'\lambda}\right\rangle \\ \hline \left\langle \psi^{-}_{t\lambda}\bar{\psi}^{+}_{t'\lambda}\right\rangle & \left\langle \psi^{-}_{t\lambda}\bar{\psi}^{-}_{t'\lambda}\right\rangle \end{array}\right] = i\hbar \left[\begin{array}{c|c} G^{++}_{0,\lambda,tt'} & G^{+-}_{0,\lambda,tt'} \\ \hline G^{-+}_{0,\lambda,tt'} & G^{--}_{0,\lambda,tt'} \end{array}\right] = i\hbar \boldsymbol{G}_{0,\lambda,tt'}. \tag{4.22}$$

These are referred to as the single-particle Green functions, and because of the forward and backward contour we encounter four kinds, which are denoted the time-ordered ($G^{++} = G^{T}$), anti time-ordered ($G^{--} = G^{\tilde{T}}$), lesser- ($G^{+-} = G^{<}$), and greater- ($G^{-+} = G^{>}$) Green functions, respectively. The four Green functions are in fact interrelated, and we will benefit from this below. However, first, let us actually calculate the Green functions. To obtain $\boldsymbol{G}_{0,\lambda,tt'}$, we first note from Eq. (4.21) that

$$[\boldsymbol{G}^{-1,++}_{0,\lambda}]^{-1}_{tt'} = -\frac{i}{\hbar}\theta(t-t')u^{+}_{t'\lambda}\cdots u^{+}_{t-1,\lambda}, \quad [\boldsymbol{G}^{-1,--}_{0,\lambda}]^{-1}_{tt'} = -\frac{i}{\hbar}\theta(t'-t)u^{-}_{t\lambda}\cdots u^{-}_{t'-1,\lambda}, \tag{4.23}$$

which can be verified from requiring $\sum_{t'}[\boldsymbol{G}^{-1,++}_{0,\lambda}]^{-1}_{tt'}[\boldsymbol{G}^{-1,++}_{0,\lambda}]_{t't''} = \delta_{tt''}$, and we have $\theta(n) = 1$ if $n \geq 0$ and zero otherwise. Using Eq. (A.73) for inversion of block matrices, we find after some algebra (to linear order in δ)

$$G^{+-}_{0,\lambda,tt'} = -\zeta\frac{i}{\hbar}u_{t1,\lambda}u_{1t',\lambda}\, n_\zeta(\epsilon_\lambda(t_0)), \tag{4.24a}$$

$$G^{-+}_{0,\lambda,tt'} = -\frac{i}{\hbar}u_{Nt',\lambda}u_{tN,\lambda}\,(1 + \zeta n_\zeta(\epsilon_\lambda(t_0))), \tag{4.24b}$$

$$G^{++}_{0,\lambda,tt'} = \begin{cases} G^{-+}_{0,\lambda,tt'}, & t \geq t', \\ G^{+-}_{0,\lambda,tt'}, & t < t', \end{cases} \tag{4.24c}$$

$$G^{--}_{0,\lambda,tt'} = \begin{cases} G^{-+}_{0,\lambda,tt'}, & t' \geq t, \\ G^{+-}_{0,\lambda,tt'}, & t' < t, \end{cases} \tag{4.24d}$$

where $n_\zeta(\epsilon_\lambda) = [e^{\beta(\epsilon_\lambda - \mu)} - \zeta 1]^{-1}$ is the Bose-Einstein and Fermi-Dirac distribution for $\zeta = +$ and $\zeta = -$, respectively, and

$$u_{tt'\lambda} = \begin{cases} u^{+}_{t-1,\lambda}\cdots u^{+}_{t',\lambda}, & t > t', \\ 1, \quad t = t', & \\ u^{-}_{t,\lambda}\cdots u^{-}_{t'-1,\lambda}, & t < t', \end{cases} \tag{4.25}$$

describes the discretized time-evolution from t' to t. Upon taking the continuous time limit $N_\mathcal{C} \to \infty$ while keeping $N_\mathcal{C}\delta$ constant, the time index becomes a continuous time variable, $(t-1)\delta \to t - t_0$,

[5] See also Sec. 4.3 for additional motivations.

and the Green functions (4.24) become

$$G^{+-}_{0,\lambda}(t,t') = -\zeta\frac{i}{\hbar}e^{-\frac{i}{\hbar}\int_{t'}^{t}d\tilde{t}\epsilon_\lambda(\tilde{t})}n_\zeta(\epsilon_\lambda(t_0)), \tag{4.26a}$$

$$G^{-+}_{0,\lambda}(t,t') = -\frac{i}{\hbar}e^{-\frac{i}{\hbar}\int_{t'}^{t}d\tilde{t}\epsilon_\lambda(\tilde{t})}(1+\zeta n_\zeta(\epsilon_\lambda(t_0))), \tag{4.26b}$$

$$G^{++}_{0,\lambda}(t,t') = \theta(t-t')G^{-+}_{0,\lambda}(t,t') + \theta(t'-t)G^{+-}_{0,\lambda}(t,t'), \tag{4.26c}$$

$$G^{--}_{0,\lambda}(t,t') = \theta(t'-t)G^{-+}_{0,\lambda}(t,t') + \theta(t-t')G^{+-}_{0,\lambda}(t,t'). \tag{4.26d}$$

These may indeed be more familiar expressions, see e.g. Ref. [29, Eq. (13.1)], and we note for instance that the equal-time lesser Green function gives the occupation of the states which for the closed system remains given by the initial equilibrium distribution function. Another important observation is that the Green functions are interrelated. In particular, we may realize that[6]

$$G^{++}_{tt'} + G^{--}_{tt'} = G^{+-}_{tt'} + G^{-+}_{tt'}, \quad t \neq t'. \tag{4.27}$$

This suggests that we may benefit from performing a rotation of the Green functions, the so-called Keldysh rotation, as described in the following.

4.3 Continuum theory and Keldysh rotation

We have expressed the non-equilibrium theory as a path integral representation of the partition function governed by the action in (4.14), and we saw above how the formalism produced well-known expressions for continuous-time Green functions. However, why this endavior of constructing a path-integral? As in equilibrium [7], the path-integral formulation may benefit from methods such as Hubbard–Stratonovich transformations to handle interactions (discussed further below), and may guide our analysis of the Hubbard model in Ch. 6 in terms of fluctuations around saddle-point configurations, in close resemblance with the equilibrium theory presented in e.g. Refs. [131, 132] (see also the works by J. A. Hertz [133] and A. J. Millis [134]). This is our particular motivation, however, methods such as the functional renormalization group, see e.g. Ref. [135], and the iterative path integral summation [136], are also conveniently expressed in this formalism. When studying transient effects, the discrete representation in Eq. (4.14) (and (4.20)) may be useful [137]. However, such numerical time-dependent simulations come with a cost: they can be computationally very time-consuming. In our case, we are interested in steady-state phenomena, and benefit explicitly from a continuum representation of the action[7]. However, whereas the forward and backward branches of the contour appear to be decoupled in Eq. (4.18), it is important to remember that the Green functions are not independent. How to handle this in the continuum theory is assisted by the Keldysh rotation [121]. To this end, we define the transformation matrix[8]

$$\hat{L} \equiv \frac{1}{\sqrt{2}}\begin{bmatrix} 1 & 1 \\ 1 & -1 \end{bmatrix} = \hat{L}^{-1}. \tag{4.28}$$

By convention, the transformation is different for bosons and fermions [121]. In the following we consider the case for fermions and refer to the info-box in the end of this section for the bosonic case. For fermions, the independent fields ψ and $\bar{\psi}$ transform as

$$\hat{\Psi} \equiv \begin{pmatrix} \psi_1 \\ \psi_2 \end{pmatrix} \equiv \hat{L}\begin{pmatrix} \psi^+ \\ \psi^- \end{pmatrix} = \frac{1}{\sqrt{2}}\begin{pmatrix} \psi^+ + \psi^- \\ \psi^+ - \psi^- \end{pmatrix}, \tag{4.29a}$$

$$\hat{\bar{\Psi}} \equiv \begin{pmatrix} \bar{\psi}_1 & \bar{\psi}_2 \end{pmatrix} \equiv \begin{pmatrix} \bar{\psi}^+ & \bar{\psi}^- \end{pmatrix}\hat{\tau}_3\hat{L} = \frac{1}{\sqrt{2}}\begin{pmatrix} \bar{\psi}^+ - \bar{\psi}^- & \bar{\psi}^+ + \bar{\psi}^- \end{pmatrix}, \tag{4.29b}$$

[6] The relation (4.27) is a general property of non-equilibrium Green functions G [124]. It can be verified for the non-interacting Green functions G_0 from direct inspection of Eq. (4.24).

[7] From now on we take $t_0 \to -\infty$ and $t_f \to \infty$.

[8] Linear transformations of fields are discussed in e.g. Ref. [126].

where $\hat{\tau}_3$ is the third Pauli matrix[9]. The transformation leads to the transformed Green function[10]

$$\hat{G} \equiv \hat{L}\begin{bmatrix} G^{++} & G^{+-} \\ G^{-+} & G^{--} \end{bmatrix}\hat{\tau}_3\hat{L} = \frac{1}{2}\begin{bmatrix} G^{++} - G^{+-} + G^{-+} - G^{--} & G^{++} + G^{+-} + G^{-+} + G^{--} \\ G^{++} - G^{+-} - G^{-+} + G^{--} & G^{++} + G^{+-} - G^{-+} - G^{--} \end{bmatrix}. \quad (4.30)$$

In the continuum representation this reduces to [121]

$$\hat{G} \to \begin{bmatrix} G^R & G^K \\ 0 & G^A \end{bmatrix}, \quad (4.31)$$

where we have defined the retarded Green function, G^R, the advanced Green function, G^A, and the Keldysh Green function, G^K. The particular transformation in (4.29) is the so-called Larkin-Ovchinnikov choice which ensures that the fermionic Green function $\hat{G}$ and its inverse $\hat{G}^{-1}$ have the same triangular structure according to the rule (A.73) for inversion of block matrices. For the fermionic non-interacting Green functions in Eq. (4.26) in the continuous time representation we obtain

$$\begin{bmatrix} G^R_{0,\lambda}(t,t') & G^K_{0,\lambda}(t,t') \\ 0 & G^A_{0,\lambda}(t,t') \end{bmatrix} = -\frac{i}{\hbar}e^{-\frac{i}{\hbar}\int_{t'}^{t} d\tilde{t}\epsilon_\lambda(\tilde{t})}\begin{bmatrix} \theta(t-t') & 1-2n_F(\epsilon_\lambda(t_0)) \\ 0 & -\theta(t'-t) \end{bmatrix}. \quad (4.32)$$

The triangular form of the Keldysh-rotated non-equilibrium Green functions was first introduced by Keldysh [124], and is an integrated part of non-equilibrium field theory [138, 121]. We note, however, that there is an ambiguity at equal times (from (4.27)), which is not fully settled in the literature. The subtlety is discussed to a limited degree in Ref. [121], where it is commented that "[...] since the $t = t'$ line is a manifold of measure zero, the violation of [Eq. (4.27)] for most purposes is inconsequential" [121]. A particular example of this is given in Sec. 5.2 where we compare time-dependent results obtained from the continuous time-formulation and from inversion of the discrete-time inverse Green function. We also refer to more recent discussions of the subtlety of the continuous-time limit in e.g. Refs. [139, 140].

For a time-independent Hamiltonian it is useful to consider the Fourier-transformed Green function[11]. In particular, the Fourier-transformation of Eq. (4.32) for a time-independent $\epsilon_\lambda(t) = \epsilon_\lambda$ becomes

$$\hat{G}_{0,\lambda}(\omega) = \begin{bmatrix} (\hbar\omega - \epsilon_\lambda + i0^+)^{-1} & -2\pi i F(\epsilon_\lambda))\delta(\hbar\omega - \epsilon_\lambda) \\ 0 & (\hbar\omega - \epsilon_\lambda - i0^+)^{-1} \end{bmatrix}, \quad \hat{G}^{-1}_{0,\lambda}(\omega) = \begin{bmatrix} \hbar\omega - \epsilon_\lambda + i0^+ & 2i0^+F(\epsilon_\lambda) \\ 0 & \hbar\omega - \epsilon_\lambda - i0^+ \end{bmatrix}, \quad (4.33)$$

where the latter is verified upon taking the inverse and using the decomposition $(x \pm i0^+)^{-1} = \mathcal{P}x^{-1} \mp i\pi\delta(x)$, and $F(\epsilon) \equiv 1 - 2n_F(\epsilon)$. The apparently unnecessary $\pm i0^+$-term becomes meaningful in the algebraic form to ensure the correct algebraic inversion of the matrix, and furthermore, we will see later how interactions will make the infinitesimal 0^+ finite. We notice that the retarded and advanced Green functions carry information about the spectrum, whereas information about occupations is contained in the Keldysh Green function. In this equilibrium situation, however, the Keldysh component is related to the retarded and advanced components via the so-called fluctuation-dissipation relation, $G^K_{0,\lambda}(\omega) = F(\epsilon_\lambda)(G^R_{0,\lambda}(\omega) - G^A_{0,\lambda}(\omega))$.

In general, according to the property of Gaussian integration, the non-equilibrium Green function (4.31) is obtained from a quadratic action containing the inverse Green function. Upon separating

$$\hat{H} = \hat{H}_0 + \hat{H}_\Sigma, \quad \hat{H}_0 = \sum_{\lambda\lambda'} h_{\lambda\lambda'}(t)\hat{a}^\dagger_\lambda \hat{a}_{\lambda'} \quad (4.34)$$

[9] The zeroth, first (x), second (y), and third (z) Pauli matrices are $\begin{pmatrix} 1 & 0 \\ 0 & 1 \end{pmatrix}$, $\begin{pmatrix} 0 & 1 \\ 1 & 0 \end{pmatrix}$, $\begin{pmatrix} 0 & -i \\ i & 0 \end{pmatrix}$, and $\begin{pmatrix} 1 & 0 \\ 0 & -1 \end{pmatrix}$, respectively.

[10] We denote these with a hat (not to be confused with the hat over creation/annihilation operators).

[11] We use the definition of the Fourier transformation from Ref. [31, App. A]: $f(\omega) = \int_{-\infty}^{\infty} dt f(t)e^{i\omega t}$. We define the Fourier transform of "bar"-fields with opposite sign in the exponential.

where $\hat{H}_0$ describes some single-particle Hamiltonian and all possible remaining terms of the full Hamiltonian $\hat{H}$ is collected in $\hat{H}_\Sigma$ (we will see explicit examples in the following), and inverting Eq. (4.31), we may write the full continuum Keldysh action as[12] [121]

$$S = S_0 + S_\Sigma, \quad S_0 = \int dt dt' \sum_{\lambda\lambda'} \hat{\bar{\Psi}}_\lambda(t) \hat{G}^{-1}_{0,\lambda\lambda'}(t,t') \hat{\Psi}_{\lambda'}(t'), \quad \hat{G}^{-1}_{0,\lambda\lambda'}(t,t') = \begin{bmatrix} G^{-1,R}_{0,\lambda\lambda'}(t,t') & G^{-1,K}_{0,\lambda\lambda'}(t,t') \\ 0 & G^{-1,A}_{0,\lambda\lambda'}(t,t') \end{bmatrix}, \tag{4.35}$$

where $\hat{\bar{\Psi}}_\lambda(t) = (\bar{\psi}_{1,\lambda}(t), \bar{\psi}_{2,\lambda}(t))$, $\hat{\Psi}_{\lambda'}(t') = (\psi_{1,\lambda'}(t'), \psi_{2,\lambda'}(t'))^T$, and the inverse retarded/advanced non-interacting Green function reads[13] [7, 126]

$$G^{-1,R/A}_{0,\lambda\lambda'}(t,t') = \delta(t-t')(i[\hbar\partial_{t'} \pm 0^+]\delta_{\lambda\lambda'} - h_{\lambda\lambda'}(t)). \tag{4.36}$$

For bosons, we define the transformed fields as

$$\hat{\Psi} \equiv \begin{pmatrix} \psi^c \\ \psi^q \end{pmatrix} \equiv \hat{L} \begin{pmatrix} \psi^+ \\ \psi^- \end{pmatrix} = \frac{1}{\sqrt{2}} \begin{pmatrix} \psi^+ + \psi^- \\ \psi^+ - \psi^- \end{pmatrix}, \tag{4.37}$$

where the subscripts c and q refer to so-called *classical* and *quantum* components of the fields [121]. Transforming the Green function, we obtain

$$\begin{aligned} \hat{G} \equiv \hat{L} \begin{bmatrix} G^{++} & G^{+-} \\ G^{-+} & G^{--} \end{bmatrix} \hat{L} &= \frac{1}{2} \begin{bmatrix} G^{++} + G^{+-} + G^{-+} + G^{--} & G^{++} - G^{+-} + G^{-+} - G^{--} \\ G^{++} + G^{+-} - G^{-+} - G^{--} & G^{++} - G^{+-} - G^{-+} + G^{--} \end{bmatrix} \\ &\to \begin{bmatrix} G^K & G^R \\ G^A & 0 \end{bmatrix}, \end{aligned} \tag{4.38}$$

where the latter expression is the continuous time representation. For the bosonic non-interacting Green functions in Eq. (4.26) we obtain

$$\begin{bmatrix} G^K_{0,\lambda}(t,t') & G^R_{0,\lambda}(t,t') \\ G^A_{0,\lambda}(t,t') & 0 \end{bmatrix} = -\frac{i}{\hbar} e^{-\frac{i}{\hbar}\int_{t'}^{t} d\tilde{t}\epsilon_\lambda(\tilde{t})} \begin{bmatrix} 1 + 2n_B(\epsilon_\lambda(t_0)) & \theta(t-t') \\ -\theta(t'-t) & 0 \end{bmatrix}. \tag{4.39}$$

4.3.1 Dyson equation

If the contribution from S_Σ to the full action S in Eq. (4.35) is expressed in a quadratic form of the fields, we see that the problem may be expressed as

$$(\hat{G}_0^{-1} - \hat{\Sigma}) \circ \hat{G} = \mathbb{1} \qquad \Leftrightarrow \qquad \hat{G} = \hat{G}_0 + \hat{G}_0 \circ \hat{\Sigma} \circ \hat{G}, \tag{4.40}$$

where the latter expression is the so-called Dyson series, $\hat{\Sigma}$ is a *self-energy* matrix from S_Σ, and " $\circ$ " refers to the (generalized) matrix structure [121], e.g. (it is helpful to think of the fields as vectors in time-space)

$$[\hat{G}_0 \circ \hat{\Sigma} \circ \hat{G}]^{\alpha\beta}_{\lambda\lambda'}(t,t') = \int dt_1 \int dt_2 \sum_{\lambda_1\lambda_2} \sum_{\gamma\delta} G^{\alpha\gamma}_{0,\lambda\lambda_1}(t,t_1) \Sigma^{\gamma\delta}_{\lambda_1\lambda_2}(t_1,t_2) G^{\delta\beta}_{\lambda_2\lambda'}(t_2,t'), \tag{4.41}$$

where α, β refer to the Keldysh matrix structure ($\alpha \in \{1,2\}$ for fermions and $\alpha \in \{c,q\}$ for bosons). Considering the case for fermions where

$$\begin{bmatrix} G_0^{-1\,R} - \Sigma^R & G_0^{-1\,K} - \Sigma^K \\ 0 & G_0^{-1\,A} - \Sigma^A \end{bmatrix} \circ \begin{bmatrix} G^R & G^K \\ 0 & G^A \end{bmatrix} = \mathbb{1}, \tag{4.42}$$

[12] It is assumed that the initial density matrix is uncorrelated. See, however, the discussion in Sec. 4.3.1.

[13] See Sec. 4.3.1 for a discussion of the Keldysh component.

this results in the equations

$$\mathbb{1} = \left(G_0^{-1\,R} - \Sigma^R\right) \circ G^R, \tag{4.43}$$

$$\mathbb{1} = \left(G_0^{-1\,A} - \Sigma^A\right) \circ G^A, \tag{4.44}$$

$$G^K = G^R \circ \Sigma^K \circ G^A - G^R \circ G_0^{-1\,K} \circ G^A. \tag{4.45}$$

But how do we deal with Eq. (4.45), and in particular the last term? An operationally safe way is to stay in time-space, keep everything, and obtain the full non-equilibrium evolution from some initial configuration. This is indeed insightful! But what if we are interested in studying the properties of a non-equilibrium steady state that the system may reach in the long-time limit where a time-dependent simulation may be computationally very demanding, or maybe even impossible in some cases with the available resources[14]? According to Kamenev [121, p. 82]: "... $[G_0^{-1\,K}]$ may be omitted in the presence of a non-zero self-energy component Σ^K." Well, indeed, we found an infinitesimal contribution from the Keldysh component of the inverse Green function in Eq. (4.33), but is this general? In a dissipative system [125, p. 791]: "Although the independence on the initial state is assumed to be true in general, it is extremely hard to prove this fact rigorously for a given model... ". To shine light on this, we complement our steady-state analyses (where the latter term in Eq. (4.45) is omitted) of the systems studied in the following chapters with explicit time-dependent simulations[15].

4.3.2 Interactions

Finally, for later referencing, we note that the two-particle interaction Hamiltonian [7]

$$\hat{H}_{\text{int}} = \sum_{ii'jj'} \sum_{\sigma\sigma'} U_{ii'jj'} \hat{a}^\dagger_{i\sigma} \hat{a}^\dagger_{i'\sigma'} \hat{a}_{j'\sigma'} \hat{a}_{j\sigma}\,, \tag{4.46}$$

contributes to the action as (suppressing time arguments)

$$S_{\text{int}} = -\int_{\mathcal{C}} d\tau \sum_{ii'jj'} \sum_{\sigma\sigma'} U_{ii'jj'} \bar{\psi}_{i\sigma} \bar{\psi}_{i'\sigma'} \psi_{j'\sigma'} \psi_{j\sigma}\,. \tag{4.47}$$

In Ch. 6 we deal with the interaction in terms of a Hubbard–Stratonovich transformation [141, 142], which re-express the two-particle interaction in terms of a weighted average over a fluctuating interaction-mediating bosonic field (see specifically Eq. (6.5)). In such transformations, or upon coupling fermionic fields to an external source field $V(t)$, we encounter terms in the action of the form (the summation over Hilbert space states is left implicit, and we suppress the time arguments)

$$S_V = \int_{\mathcal{C}} d\tau V \bar{\psi}\psi = \int dt \left[V^+ \bar{\psi}^+ \psi^+ - V^- \bar{\psi}^- \psi^-\right], \tag{4.48}$$

which upon Keldysh rotating can be expressed as

$$S_V = \int dt \hat{\bar{\Psi}} \hat{V} \hat{\Psi}, \qquad \hat{V} = V^c \hat{\tau}_0 + V^q \hat{\tau}_1 = \begin{pmatrix} V^c & V^q \\ V^q & V^c \end{pmatrix}, \tag{4.49}$$

where we have defined $V^{c(q)} = (V^+ \pm V^-)/2$ [121] .

Having introduced the formalism, let us now apply it to study a selection of systems driven out of equilibrium with a periodic drive.

[14] This is indeed the case in our study of fluctuations around the antiferromagnetic saddle point in the periodically driven Hubbard model in Ch. 6.

[15] In Ch. 5, the time-dependent simulation is performed by R. S. Souto, and in Ch. 6, the time-dependent simulation is performed by D. M. Kennes.

5 | Periodically driven systems

A key avenue in condensed-matter physics is to tailor the behavior of materials by modifying their properties by external perturbation that drives the system out of equilibrium. In particular, a periodic drive provides an interesting route to induce and engineer novel and exotic phenomena, and has spurred significant interest in the field that is commonly referred to as *Floquet* engineering[1]. This is supported by the enhanced experimental control of time-periodic modulations that now provides the tools for exploring this interesting physics [6].

The physics of periodically driven quantum systems is due to two effects caused by the drive field: a change of the Hamiltonian, and the creation of excitations. The former spurred the initial interest in periodically driven systems, as it provides a means of engineering interesting phases by constructing a particular time-dependence of the Hamiltonian. An example is the theoretical prediction [144] and experimental verification [145, 146, 147] of dynamical localization[2], where delocalized electrons are localized by a harmonic drive field when the ratio of the field amplitude and frequency becomes a root of the zeroth Bessel function. The effect of dynamical localization can be understood from a simple tight-binding model of non-interacting electrons. Indeed, most studies in the field of Floquet-engineering have dealt with non-interacting systems, however, more recently, interacting Floquet-systems have gained increasing attention. Experimental breakthroughs include the possibility to induce and control superconductivity [22, 148] and magnetism [149]. Whereas the change of the Hamiltonian caused by the drive field has received most attention, the change of the distribution of quasiparticles become utmost important in interacting systems. In particular, it is believed that closed interacting Floquet systems reach an infinite temperature state at long times [150]. Furthermore, the effects from the change of the Hamiltonian and change of the distribution of quasiparticles become even more intertwined in interacting systems, as the distribution may in turn affect the preferred response of the non-interacting system towards interactions[3].

In this chapter we introduce non-equilibrium Floquet Green functions used to study quantum systems driven out of equilibrium with a time-periodic drive. We furthermore discuss the important examples of a periodically driven single level and a periodically driven two-dimensional square lattice. These examples will give us some preliminary insights into periodically driven systems and constitute the starting point for discussing the role of Coulomb interactions in the next chapter.

5.1 Non-equilibrium Floquet Green functions

We consider systems which can be described by a time-periodic Hamiltonian

$$\hat{H}(t+T) = \hat{H}(t), \tag{5.1}$$

where T is the period of the periodic perturbation. Being inherently a non-equilibrium situation, non-equilibrium field theory provides a natural framework to study the physics of periodically driven

[1] Named after G. Floquet who studied the solutions to periodic linear differential equations [143].

[2] We will see an example of dynamical localization in Sec. 5.3.

[3] As in, for example, the case of itinerant magnetism.

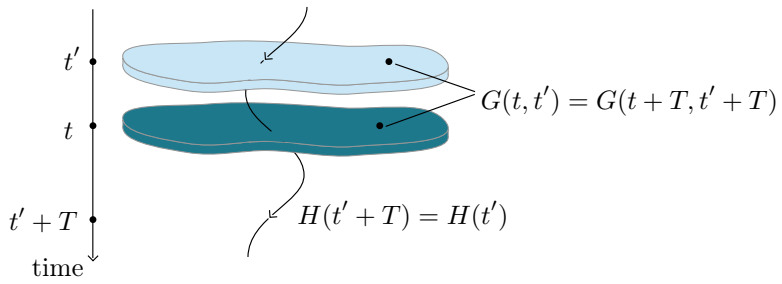

Figure 5.1: Sketch of a periodically driven quantum system, in which correlations between a configuration of the quantum system at time t' and time t satisfies the NESS condition (5.2).

quantum systems. In particular, a continuously driven system may end up in a nonequilibrium steady state (NESS) in which [125]

$$G(t+T,t'+T) = G(t,t'), \tag{5.2}$$

as illustrated in Fig. 5.1. Albeit difficult to prove in general, a nonequilibrium steady state is usually reached for dissipative systems in which a reservoir can absorb the energy from the drive [125], and we will see explicit examples of this in Sec. 5.2 and 6.4.1.

When the NESS condition is satisfied, it is convenient to transform the time-dependent Green functions to the so-called Floquet Green functions[4]. First, we define [153]

$$G(t,\omega) = \int_{-\infty}^{\infty} dt' e^{i\omega(t-t')} G(t,t'), \tag{5.3}$$

with the inverse transform

$$G(t,t') = \int_{-\infty}^{\infty} \frac{d\omega}{2\pi} e^{-i\omega(t-t')} G(t,\omega). \tag{5.4}$$

Due to the NESS condition, the transformed object is periodic in T

$$G(t+T,\omega) = \int_{-\infty}^{\infty} dt' e^{i\omega(t+T-t')} G(t+T,t') = \int_{-\infty}^{\infty} dt' e^{i\omega(t-t')} G(t+T,t'+T) = G(t,\omega), \tag{5.5}$$

and can therefore be expanded as a Fourier series

$$G(t,\omega) = \sum_{m=-\infty}^{\infty} e^{-im\Omega t} G_m(\omega), \tag{5.6}$$

with Fourier coefficients

$$G_m(\omega) = \frac{1}{T} \int_{-T/2}^{T/2} dt e^{im\Omega t} G(t,\omega), \tag{5.7}$$

where $\Omega = 2\pi/T$ is the drive frequency. From Eq. (5.7) we define the Floquet Green function $\hat{G}_{mn}(\omega) \equiv \hat{G}_{m-n}(\omega + n\Omega)$ which in full reads

$$G_{mn}(\omega) = \frac{1}{T} \int_{-T/2}^{T/2} dt \int_{-\infty}^{\infty} dt' e^{i(\omega+m\Omega)t - i(\omega+n\Omega)t'} G(t,t'), \tag{5.8}$$

$$G(t,t') = \sum_m \int_{-\infty}^{\infty} \frac{d\omega}{2\pi} e^{-i\omega(t-t') - im\Omega t} G_{m0}(\omega). \tag{5.9}$$

[4] We adopt the convention used in e.g. Refs. [151, 152, 153].

Using the definition of the Floquet Green function, we may also write the latter as

$$G(t,t') = \sum_{mn} \int_{-\Omega/2}^{\Omega/2} \frac{d\omega}{2\pi} e^{-i(\omega+m\Omega)t + i(\omega+n\Omega)t'} G_{mn}(\omega). \tag{5.10}$$

In the following, we will often refer to the transformation to non-equilibrium Floquet Green functions simply as 'transforming to Floquet space'.

Consider a quadratic action of the form (suppressing all indices but time)

$$\begin{aligned} S &= \int_{-\infty}^{\infty} dt dt' \hat{\bar{\Psi}}(t) \hat{G}^{-1}(t,t') \hat{\Psi}(t') \\ &= \int_{-\infty}^{\infty} \frac{d\omega}{2\pi} \frac{d\omega'}{2\pi} \hat{\bar{\Psi}}(\omega) \left[\int_{-\infty}^{\infty} dt\, \hat{G}^{-1}(t,\omega') e^{i(\omega-\omega')t} \right] \hat{\Psi}(\omega'), \end{aligned} \tag{5.11}$$

where we have Fourier-transformed the fields. We rewrite

$$\int_{-\infty}^{\infty} dt\, \hat{G}^{-1}(t,\omega') e^{i(\omega-\omega')t} = \sum_m \int_{-T/2}^{T/2} dt\, \hat{G}^{-1}(t,\omega') e^{i(\omega-\omega')(t+mT)}, \tag{5.12}$$

where we have used the NESS condition (for a periodic Hamiltonian, the inverse Green function satisfies the NESS condition if the self-energy contribution to the non-interacting Green function satisfies the NESS condition). Using the property of the Dirac comb [154, Eq. (3.94)] $\frac{1}{\Omega}\sum_m e^{2\pi i m \frac{\omega-\omega'}{\Omega}} = \sum_m \delta(\omega - \omega' - m\Omega)$, we find upon performing the ω-integral

$$\begin{aligned} S &= \sum_m \int_{-\infty}^{\infty} \frac{d\omega'}{2\pi} \hat{\bar{\Psi}}(\omega' + m\Omega) \left[\frac{1}{T} \int_{-T/2}^{T/2} dt\, \hat{G}^{-1}(t,\omega') e^{im\Omega t} \right] \hat{\Psi}(\omega') \\ &= \sum_m \int_{-\infty}^{\infty} \frac{d\omega'}{2\pi} \hat{\bar{\Psi}}(\omega' + m\Omega) \hat{G}_m^{-1}(\omega') \hat{\Psi}(\omega'). \end{aligned} \tag{5.13}$$

Rewriting the remaining frequency-integral

$$S = \sum_{mn} \int_{-\Omega/2}^{\Omega/2} \frac{d\omega'}{2\pi} \hat{\bar{\Psi}}(\omega' + (m+n)\Omega) \hat{G}_m^{-1}(\omega' + n\Omega) \hat{\Psi}(\omega' + n\Omega), \tag{5.14}$$

and changing the dummy variable $m \to m-n$, and defining $\hat{\bar{\Psi}}_m(\omega) \equiv \hat{\bar{\Psi}}(\omega + m\Omega)$ and $\hat{\Psi}_n(\omega) \equiv \hat{\Psi}(\omega + n\Omega)$, we can write the action in the form

$$S = \sum_{mn} \int_{-\Omega/2}^{\Omega/2} \frac{d\omega}{2\pi} \hat{\bar{\Psi}}_m(\omega) \hat{G}_{mn}^{-1}(\omega) \hat{\Psi}_n(\omega). \tag{5.15}$$

One of the main advantages of the Floquet Green functions is the matrix multiplication structure: in the time-representation of the Dyson equation we encountered convolutions of the form (see e.g. Eq. (4.41))

$$C(t,t') = \int dt'' A(t,t'') B(t'',t'). \tag{5.16}$$

However, for A and B satisfying the condition (5.2), time-convolutions become simple matrix multiplications in Floquet space

$$C_{mn}(\omega) = \sum_{m'} A_{mm'}(\omega) B_{m'n}(\omega). \tag{5.17}$$

5.1.1 Non-interacting Green functions

Upon transforming Eq. (4.36) to Floquet Green functions, we get

$$\begin{aligned} G^{-1,R/A}_{0,\lambda\lambda',mn}(\omega) &= \hbar[\omega + n\Omega \pm i0^+]\delta_{\lambda\lambda'}\delta_{mn} - h_{\lambda\lambda',m-n} \\ &= \hbar[\omega \pm i0^+]\delta_{\lambda\lambda'}\delta_{mn} - \mathcal{H}_{\lambda\lambda',m-n}, \end{aligned} \tag{5.18}$$

where we have defined the Floquet Hamiltonian (see e.g. Ref. [155])

$$\mathcal{H}_{\lambda\lambda',m-n} = h_{\lambda\lambda',m-n} - n\hbar\Omega\delta_{\lambda\lambda'}\delta_{mn}, \qquad h_{\lambda\lambda',m} = \frac{1}{T}\int_{-T/2}^{T/2} dt\; h_{\lambda\lambda'}(t)e^{im\Omega t}. \tag{5.19}$$

5.2 Periodically driven level

To gain some preliminary insights into periodically driven systems, we first consider the situation of a (spinless) driven level coupled to an electronic reservoir as illustrated in Fig. 5.2a on page 56. The situation was originally studied within the framework on non-equilibrium Green functions by Jauho, Wingreen, and Meir [156][5], however, in addition to providing some insights into the effect of a periodic drive, the results in this section also constitute the starting point for our discussion of the periodically driven Anderson model in Sec. 6.7.1.

The harmonically driven level is described by the Hamiltonian

$$\hat{H}_0(t) = \epsilon_0(t)\hat{d}^\dagger\hat{d}, \qquad \epsilon_0(t) = \epsilon_0 + E\cos(\Omega t), \tag{5.20}$$

and is coupled to the electronic reservoir, $\hat{H}_\mathcal{E} = \sum_k \epsilon_k \hat{c}_k^\dagger \hat{c}_k$, with temperature T and chemical potential μ, via the tunneling Hamiltonian $\hat{H}_\mathcal{T} = \sum_k (t\hat{c}_k^\dagger\hat{d} + \text{h.c.})$. From Eq. (5.18), the retarded/advanced inverse Floquet Green function including the self-energy from coupling to the reservoir (see info-box below) reads[6]

$$G^{-1,R/A}_{mn}(\omega) = (\omega + n\Omega - \epsilon_0 \pm i\Gamma)\delta_{mn} - \frac{E}{2}\left(\delta_{m,n+1} + \delta_{m,n-1}\right). \tag{5.21}$$

Upon inversion we obtain the retarded/advanced Green function[7]

$$G^{R/A}_{mn}(\omega) = \sum_l \frac{J_{m+l}(\frac{E}{\Omega})J_{n+l}(\frac{E}{\Omega})}{\omega - (\epsilon_0 + l\Omega) \pm i\Gamma}, \tag{5.22}$$

where $J_l(x)$ is the Bessel function of the first kind of order l. At first sight, the appearance of Bessel functions might seem surprising. Hence, to understand the origin, let us consider the 00-component of the retarded function in more detail (writing $\tilde{\omega} = \omega - \epsilon_0 + i\Gamma$ for brevity)

$$\begin{aligned} G^R_{00}(\omega) &= \sum_l \frac{J_l^2(\frac{E}{\Omega})}{\tilde{\omega} - l\Omega} \\ &= J_0^2(E/\Omega)\frac{1}{\tilde{\omega}} + J_1^2(E/\Omega)\left(\frac{1}{\tilde{\omega}+\Omega} + \frac{1}{\tilde{\omega}-\Omega}\right) + J_2^2(E/\Omega)\left(\frac{1}{\tilde{\omega}+2\Omega} + \frac{1}{\tilde{\omega}-2\Omega}\right) + \cdots, \end{aligned} \tag{5.23}$$

[5] See also more recent references such as Refs. [151, 157, 158].

[6] We set $\hbar = 1$ in the following.

[7] To obtain Eq. (5.22), we first transform the retarded/advanced component in Eq. (4.32) to Floquet space and use the generating function $e^{x(t-1/t)/2} = \sum_{l=-\infty}^{\infty} J_l(x)t^l$ [159, Eq. 27.16]. When including a finite Γ, we may then verify Eq. (5.22) from Eq. (5.21) using the recurrence relation of the Bessel functions $2lJ_l(x) = xJ_{l+1}(x) + xJ_{l-1}(x)$ [159] and $\sum_l J_{m+l}(x)J_{l+n}(x) = \delta_{mn}$ [160].

where we have used that $J_{-l}(x) = (-1)^l J_l(x)$. Upon expanding the Bessel functions and collecting terms in powers of (E/Ω) we get

$$\begin{aligned} G^R_{00}(\omega) = \frac{1}{\tilde{\omega}} &+ (E/\Omega)^2 \left(-\frac{1}{2}\frac{1}{\tilde{\omega}} + \frac{1}{4}\left(\frac{1}{\tilde{\omega}+\Omega} + \frac{1}{\tilde{\omega}-\Omega} \right) \right) \\ &+ (E/\Omega)^4 \left(\frac{3}{32}\frac{1}{\tilde{\omega}} - \frac{1}{16}\left(\frac{1}{\tilde{\omega}+\Omega} + \frac{1}{\tilde{\omega}-\Omega} \right) + \frac{1}{64}\left(\frac{1}{\tilde{\omega}+2\Omega} + \frac{1}{\tilde{\omega}-2\Omega} \right) \right) + \cdots . \end{aligned} \tag{5.24}$$

The first term of order $(E/\Omega)^0$ describes the free electron propagator (dressed by the reservoir) as illustrated by the Feynman diagram

$$g_0 \equiv \tfrac{1}{\omega-\epsilon_0+i\Gamma} = \quad \underset{\omega}{\longleftarrow} . \tag{5.25}$$

The second term of order $(E/\Omega)^2$ can be written as

$$\begin{aligned} g_2 &\equiv \left(\tfrac{E}{\Omega}\right)^2 \left(-\tfrac{1}{2}\tfrac{1}{\tilde{\omega}} + \tfrac{1}{4}\left(\tfrac{1}{\tilde{\omega}+\Omega} + \tfrac{1}{\tilde{\omega}-\Omega} \right) \right) = \tfrac{1}{\tilde{\omega}}\tfrac{E}{2}\tfrac{1}{\tilde{\omega}-\Omega}\tfrac{E}{2}\tfrac{1}{\tilde{\omega}} + \tfrac{1}{\tilde{\omega}}\tfrac{E}{2}\tfrac{1}{\tilde{\omega}+\Omega}\tfrac{E}{2}\tfrac{1}{\tilde{\omega}} \\ &= \quad \underset{\omega \quad \omega-\Omega \quad \omega}{\overset{\Omega \quad \Omega}{\longleftarrow}} + \underset{\omega \quad \omega+\Omega \quad \omega}{\overset{\Omega \quad \Omega}{\longleftarrow}} , \end{aligned} \tag{5.26}$$

where we have represented the incremental change in frequency of the electron propagator by a curly line, which is interpreted as a photon with frequency Ω which interacts with the electron with interaction vertex $E/2$. Similarly, we find

$$\begin{aligned} g_4 &\equiv \left(\tfrac{E}{\Omega}\right)^4 \left(\tfrac{3}{32}\tfrac{1}{\tilde{\omega}} - \tfrac{1}{16}\left(\tfrac{1}{\tilde{\omega}+\Omega} + \tfrac{1}{\tilde{\omega}-\Omega} \right) + \tfrac{1}{64}\left(\tfrac{1}{\tilde{\omega}+2\Omega} + \tfrac{1}{\tilde{\omega}-2\Omega} \right) \right) \\ &= \quad \longleftarrow + \longleftarrow + \longleftarrow + \longleftarrow + \longleftarrow + \longleftarrow , \end{aligned} \tag{5.27}$$

where we have suppressed the frequency labels. Hence, $G^R_{00}(\omega)$ may be interpreted as composed of amplitudes where the electron has emitted and absorbed an equal amount of photons[8]. Since this is only possible through an even number of interactions, only even powers of (E/Ω) appear in Eq. (5.24), and the Bessel functions keep track of the number of ways that these processes can occur. Similarly, we could consider

$$\begin{aligned} G^R_{10}(\omega) &= \quad \longleftarrow + \longleftarrow + \longleftarrow + \longleftarrow + \cdots \\ &\equiv \quad \omega+\Omega \Longleftarrow \omega, \end{aligned} \tag{5.28}$$

which is composed of amplitudes where the electron has absorbed one photon in excess. Notice from Eq. (5.9) how the net absorbed or emitted photons contributes to the time-dependence of the Green functions (consider e.g. the equal-time Green function), i.e., how dynamics is induced by photons.

The coupling between the level and the fermionic environment is modeled by the action $S_{\text{res}} = S_{\mathcal{T}} + S_{\mathcal{E}}$, where $S_{\mathcal{E}}$ describes the non-interacting reservoir, and

$$\begin{aligned} S_{\mathcal{T}} &= -\int_{\mathcal{C}} d\tau \sum_k \left(t\bar{\psi}_k(\tau)\psi_0(\tau) + t^*\bar{\psi}_0(\tau)\psi_k(\tau) \right) \\ &= -\int_{-\infty}^{\infty} dt \sum_k \left(t(\bar{\psi}^+_k(t), \psi^-_k(t))\hat{\tau}_3 \begin{pmatrix} \psi^+_0(t) \\ \psi^-_0(t) \end{pmatrix} + t^*(\bar{\psi}^+_0(t), \psi^-_0(t))\hat{\tau}_3 \begin{pmatrix} \psi^+_k(t) \\ \psi^-_k(t) \end{pmatrix} \right), \end{aligned} \tag{5.29}$$

[8] See e.g. Ref. [158] for a similar interpretation.

where $\bar{\psi}_0$ and $\bar{\psi}_k$ denote level and reservoir fields, respectively. Using Eq. (A.70) we integrate out the environment to obtain an effective contribution to the action. Upon Keldysh rotating we find

$$S_{\rm res} = -\int dt dt' \hat{\bar{\Psi}}_0(t)\hat{\Sigma}(t,t')\hat{\Psi}_0(t'), \quad \hat{\Sigma}(t,t') = t^2 \sum_k \hat{G}_{0,k}(t,t'). \tag{5.30}$$

Upon transforming to Floquet space (notice that the free reservoirs also satisfies the NESS condition), and using Eq. (5.18) for time-independent reservoirs, the retarded and advanced components of the self energy from the reservoir become

$$\Sigma^{R/A}_{mn}(\omega) = t^2 \sum_k G^{R/A}_{0,k,mn}(\omega) = t^2\nu \int d\epsilon \frac{1}{\omega + n\Omega - \epsilon \pm i0^+}\delta_{mn} = \mp i\frac{\gamma}{2}\delta_{mn}, \tag{5.31}$$

where we have taken the wide-band limit and assumed that $\gamma = 2\pi t^2\nu$, with ν being the reservoir density of states, is independent of energy. We furthermore define $\Gamma = \gamma/2$. Since the reservoirs are in thermal equilibrium, the Keldysh component is governed by the fluctuation-dissipation theorem, thus[a],

$$\begin{aligned}
\Sigma^K_{mn}(\omega) &= t^2 \sum_k G^K_{0,k,mn}(\omega) \\
&= t^2 \sum_k F(\epsilon_k)\left[G^R_{0,k,mn}(\omega) - G^A_{0,k,mn}(\omega)\right] \\
&= t^2\nu \int d\epsilon F(\epsilon)\left[\frac{1}{\omega + n\Omega - \epsilon + i0^+} - \frac{1}{\omega + n\Omega - \epsilon - i0^+}\right]\delta_{mn} \\
&= -i\gamma F(\omega + n\Omega)\delta_{mn},
\end{aligned} \tag{5.32}$$

in agreement with [125, Eq. (192)], and where F was defined below Eq. (4.33). We note that one may similarly obtain a lesser self-energy as [125] $\Sigma^<_{mn}(\omega) = i\gamma n_F(\omega + n\Omega)\delta_{mn}$.

[a] One may also immediately transform Eq. (4.32) to Floquet space.

Now, let us turn to the time-dependent level occupation [161] $n(t) = (1 - iG^K(t,t))/2 = -iG^<(t,t)$. We obtain the same result using G^K obtained from the (first term in the) Dyson equation (4.45) in Floquet-space with Keldysh self-energy given by Eq. (5.32) or from an equivalent Dyson equation for the lesser Green function with lesser self-energy [125] $\Sigma^<_{mn}(\omega) = 2i\Gamma n_F(\omega + n\Omega)\delta_{mn}$. Let us just consider the latter,

$$\begin{aligned}
G^<_{mn}(\omega) &= \sum_{st} G^R_{ms}(\omega)\Sigma^<_{st}(\omega)G^A_{tn}(\omega) \\
&= 2i\Gamma \sum_{kls} J_{m-k}\left(\frac{E}{\Omega}\right)J_{s-k}\left(\frac{E}{\Omega}\right)J_{s-l}\left(\frac{E}{\Omega}\right)J_{n-l}\left(\frac{E}{\Omega}\right)\frac{n_F(\omega + s\Omega)}{(\omega + k\Omega - \epsilon_0 + i\Gamma)(\omega + l\Omega - \epsilon_0 - i\Gamma)}.
\end{aligned} \tag{5.33}$$

Upon transforming back to time, we get the time-dependent level occupation (see derivation in the info-box below)

$$n(t) = \frac{1}{2} - \Gamma \sum_{klms} e^{-im\Omega t} J_{m-k}\left(\frac{E}{\Omega}\right)J_{s-k}\left(\frac{E}{\Omega}\right)J_{s-l}\left(\frac{E}{\Omega}\right)J_{-l}\left(\frac{E}{\Omega}\right)\frac{1}{(l-k)\Omega - 2i\Gamma}\left(I^-_{ls} - I^+_{ks}\right), \tag{5.34}$$

where

$$I^\pm_{st} = \frac{1}{\pi}\psi\left(\frac{1}{2} \pm \frac{i\beta}{2\pi}(\epsilon_0 + (t-s)\Omega - \mu \mp i\Gamma)\right), \tag{5.35}$$

with ψ the digamma function. In the un-driven limit, Eq. (5.34) reduces to

$$n = \frac{1}{2} + \frac{1}{\pi}\,\mathrm{Im}\,\psi\left(\frac{1}{2} - \frac{i\beta}{2\pi}(\epsilon_0 - \mu + i\Gamma)\right). \tag{5.36}$$

To derive Eq. (5.34) we first use $n_F(\omega) = (1 - \tanh(\beta(\omega - \mu))/2)/2$ to divide $G^<_{mn}(\omega)$ into two parts: a temperature-independent part $G^<_{1,mn}(\omega)$ (from the "1") and a temperature-dependent part $G^<_{2,mn}(\omega)$ (from tanh). Consider first the temperature-independent contribution to $G^<(t,t)$

$$\begin{aligned} G^<_1(t,t) &\equiv \sum_m e^{-im\Omega t} \int_{-\infty}^{\infty} \frac{d\omega}{2\pi} G^<_{1,m0}(\omega) \\ &= \sum_{mkls} J_{m-k}\left(\frac{E}{\Omega}\right) J_{s-k}\left(\frac{E}{\Omega}\right) J_{s-l}\left(\frac{E}{\Omega}\right) J_{-l}\left(\frac{E}{\Omega}\right) \frac{-\Gamma}{(k-l)\Omega + 2i\Gamma} \\ &= \frac{i}{2}, \end{aligned} \tag{5.37}$$

where we have used $\sum_s J_{s-k}(x)J_{s-l}(x) = \delta_{kl}$. This gives the first term in Eq. (5.34). For the second term we should evaluate the integral

$$I_{2,kls} \equiv \int_{-\infty}^{\infty} \frac{d\omega}{2\pi} \tanh\left(\frac{\beta}{2}(\omega + s\Omega - \mu)\right) \left[\frac{1}{\omega + k\Omega - \epsilon_0 + i\Gamma} - \frac{1}{\omega + l\Omega - \epsilon_0 - i\Gamma}\right]. \tag{5.38}$$

To this end, we write $\tanh(\beta(\omega+s\Omega-\mu)/2) = i(\psi^-(\omega+s\Omega)-\psi^+(\omega+s\Omega))/\pi$ where $\psi^\pm(x) \equiv \psi(\frac{1}{2} \pm i\beta(x-\mu)/(2\pi))$ with ψ being the digamma function. Using that $\psi^{+/-}$ has poles in the upper/lower complex half-planes only, and that the contribution to the contour-integral from the semi-circle arcs vanishes, we get

$$I_{2,kls} = I^-_{ls} - I^+_{ks}, \quad I^\pm_{ks} \equiv \frac{1}{\pi}\psi^\pm(\epsilon_0 + (s-k)\Omega \mp i\Gamma), \tag{5.39}$$

which gives the second term in Eq. (5.34).

The time-dependent level occupation is shown in Fig. 5.2b. The figure shows the non-equilibrium steady-state result obtained from Eq. (5.34) together with a numerical time-dependent simulation by R. S. Souto which is obtained from inverting the discrete-time inverse Green function including a self-energy from the leads. In the time-dependent simulation, the initially unoccupied (black curve) and occupied (red curve) level is first brought into contact with the fermionic reservoir, whereafter follows a period of thermalization where the two initial configurations thermalizes with the bath. At time zero, the drive is turned on, giving rise to a transient behavior until the level occupation reaches a non-equilibrium steady state in agreement with the result from Eq. (5.34)[9]. Here we see an explicit example of the independence on the initial state in the steady-state long-time limit, as discussed in Sec. 4.3.1.

Clearly, the level occupation has a richer structure than would have been anticipated by simply substituting $\epsilon_0 \to \epsilon_0(t)$ in Eq. (5.36) (dashed line). In other words, the non-equilibrium steady state does not simply follow the drive signal adiabatically, as was also concluded in Ref. [156]. To get further insight into the dynamical behavior, we show the Floquet-components of the Floquet Green functions $\boldsymbol{A}(\omega) \equiv -2\mathrm{Im}\,\boldsymbol{G}^R(\omega)$ (black curves) and the real (blue) and imaginary (red) part of $\boldsymbol{n}(\omega) \equiv -i\,\boldsymbol{G}^<(\omega)$ in Fig. 5.2c. Consider the 00-component of $\boldsymbol{A}(\omega)$, often referred to as the time-averaged spectral function [162] [10]. In the limit $E, \Gamma \to 0$ in Eq. (5.22), $A_0(\omega) \equiv -2\mathrm{Im}G^R_{00}(\omega) \to 2\pi\delta(\omega - \epsilon_0)$ gives the spectrum of the level, a delta-function peak at the frequency of the level, which is normalized as $\int d\omega A_0(\omega)/(2\pi) = 1$. For a finite Γ, $A_0(\omega) \to 2\Gamma/((\omega - \epsilon_0)^2 + \Gamma^2)$, i.e. the finite life-time causes the level to broaden in the spectrum. For a finite Γ and drive amplitude E,

$$A_0(\omega) = \sum_l J_l^2\left(\frac{E}{\Omega}\right) \frac{2\Gamma}{(\omega - (\epsilon_0 + l\Omega))^2 + \Gamma^2}, \tag{5.40}$$

[9] The analytical results in Fig. 5.2b are shifted in time by $T/4$ since the time-dependent simulation uses $\epsilon_0(t) = \epsilon_0 + E\sin(\Omega t)\theta(t)$ such that $\epsilon_0(0) = \epsilon_0$.

[10] 'Period-averaged' component would be a slightly better terminology cf. Eq. (5.7). Performing the frequency-integral over this component gives the period-averaged equal-time properties.

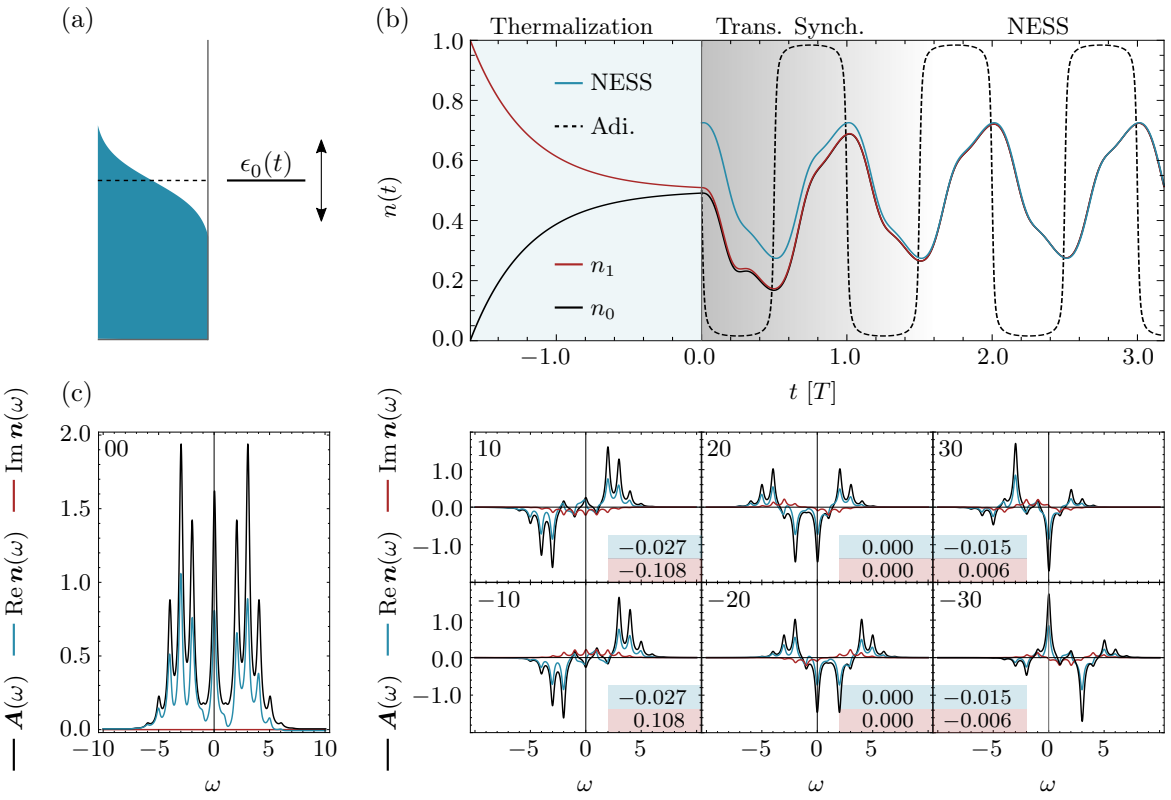

Figure 5.2: Harmonically driven level. (a) Illustration of a harmonically driven single level coupled to a fermionic reservoir. (b) Time-dependence of the level occupation $n(t)$ showing the NESS result from Eq. (5.34) (blue line) together with time-dependent results by R. S. Souto where an occupied (red curve) and unoccupied (black curve) level is initially brought to contact with the reservoir, whereafter follows a regime of thermalization, before the drive is turned on at time $t = 0$ (see footnote 9 on p. 55). The adiabatic result from substituting the time-dependent dot-level into Eq. (5.36) is shown with a dashed line. (c) Floquet matrix components (as written in the top left corner of the subfigures) of $\boldsymbol{A}(\omega) = -2\mathrm{Im}\,\boldsymbol{G}^R(\omega)$ (black) and real (blue) and imaginary (red) part of $\boldsymbol{n}(\omega) = -i\boldsymbol{G}^<(\omega)$ as a function of frequency. The blue and red boxes in the right panels show the frequency-integrated blue and red curves (divided by 2π) corresponding to the Fourier coefficients that gives the behavior in (b) (higher order contributions does not change the behavior noticeable). The parameters are $\Omega = 1$, $E = 4$, $\Gamma = 0.2$, $\epsilon_0 = \mu = 0$, $k_BT = 0.1$. The figure is made by N. Walldorf for a working paper in collaboration with R. S. Souto and J. Paaske.

hence, as seen in Fig. 5.2c, spectral weight is moved from the single peak to sidebands[11] at $\epsilon_0 + l\Omega$ with spectral weight $J_l^2(E/\Omega)$ such that $\int d\omega A_0(\omega)/(2\pi) = \sum_l J_l^2(E/\Omega) = 1$. From the diagrams above, we can interpret $A_0(\omega)$ as probing the density of states at frequency ω, revealing, however, that an electron can have interacted with an integer number of photons.

What can we say about the other components of the Floquet Green function matrices? We note from Eq. (5.9) that $G(t,t) = \sum_m e^{-im\Omega t}\int_{-\infty}^{\infty}\frac{d\omega}{2\pi}G_{m0}(\omega)$, hence, the frequency-integrated $\boldsymbol{n}(\omega)$-curves gives the Fourier coefficients (times 2π) which builds up the dynamical behavior in Fig. 5.2b. Although we may take simple limits (such as high drive frequency or large coupling to the reservoir) where the frequency-integrated results become simple (not shown), in general, we see that the dynamic content emerges from a rich underlying structure, caused by the complex interplay between drive and dissipation. We will discuss some aspects of the periodically driven level further in Sec. 6.7.1, but

[11] For the particular parameters in Fig. 5.2c, $J_1^2(E/\Omega) = 0.004$, and hence the first sideband is highly suppressed.

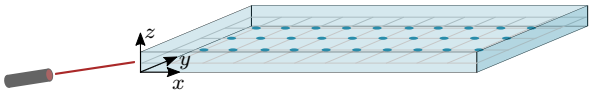

Figure 5.3: Sketch of a two-dimensional square lattice driven by a periodic electric field. Adapted from Publication III.

aim in future work to get even more insights into periodically driven systems from this fairly simple model.

5.3 Periodically driven square lattice

Next, we consider a two-dimensional square lattice, as sketched in Fig. 5.3, in a uniform[12] but time-dependent classical electric field. The system is described by a tight-binding Hamiltonian with nearest neighbor coupling $-\tilde{t}$. In momentum space and in the temporal gauge [125] the lattice Hamiltonian reads

$$\hat{H} = \sum_{\boldsymbol{k}\sigma} \epsilon_{\boldsymbol{k}}(t) \hat{c}^{\dagger}_{\boldsymbol{k}\sigma} \hat{c}_{\boldsymbol{k}\sigma}, \qquad \epsilon_{\boldsymbol{k}}(t) = -2\tilde{t} \sum_{l=x,y} \cos\left(k_l a_l + \frac{e a_l}{\hbar} A_l(t)\right), \tag{5.41}$$

where a_l is the lattice spacing, $A_l(t)$ is the time-dependent vector potential in direction l, and we have defined $\hat{c}_{\boldsymbol{k}\sigma} = N^{-1/2} \sum_j \hat{c}_{j\sigma} e^{-i\boldsymbol{k}\cdot\boldsymbol{r}_j}$, with j a lattice site index, and N is the number of lattice sites. The equilibrium electron dispersion in the absence of an electric field is shown in Fig. 5.4 and is bounded by $\epsilon_{\boldsymbol{k}} \in [-4\tilde{t}, 4\tilde{t}]$ (a maximum of $2\tilde{t}$ added from each spatial dimension). At half filling, the Fermi surface has the nesting property that there exists a single vector $\boldsymbol{Q} = (\pi, \pi)$ (in units of the inverse lattice spacing) which connects opposite sides of the Fermi surface. In the interacting system, which we consider in the next chapter, this will have some important consequences.

For different periodic drive protocols, the task is to calculate the Fourier coefficients $\epsilon_{\boldsymbol{k},m}$ cf. Eq.

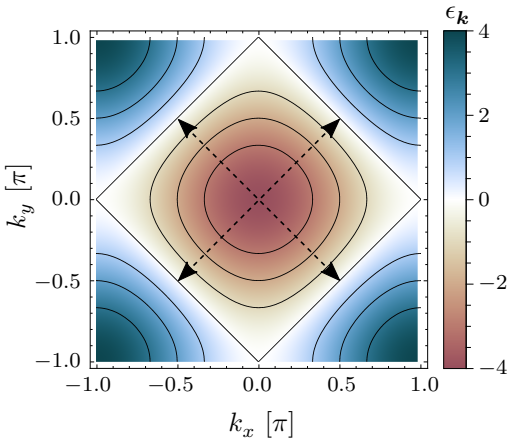

Figure 5.4: Un-driven electron dispersion (in units of $\tilde{t}$) in the Brillouin zone of the square lattice (in units of the inverse lattice spacing). Nesting vectors are shown with dashed arrows.

[12] Although a typical starting point for making theoretical progress, see e.g. the review [125], we note that the experimental setup required to satisfy this assumption is not trivial. See, however, the discussion in Sec. 6.5.2.

(5.18)-(5.19). Hence, it is convenient to write $\epsilon_{\boldsymbol{k}}(t)$ in the form

$$\epsilon_{\boldsymbol{k}}(t) = -\tilde{t} \sum_{l=x,y} \left[e^{ik_l a_l} e^{i\frac{ea_l}{\hbar}A_l(t)} + e^{-ik_l a_l} e^{-i\frac{ea_l}{\hbar}A_l(t)} \right], \tag{5.42}$$

whereby

$$\epsilon_{\boldsymbol{k},m} = -\tilde{t} \sum_{l=x,y} \left[e^{ik_l a_l} \alpha_{l,+,m} + e^{-ik_l a_l} \alpha_{l,-,m} \right], \quad \alpha_{l,\pm,m} \equiv \int_{-\pi}^{\pi} \frac{dz}{2\pi} e^{imz \pm i\frac{ea_l}{\hbar}A_l(z/\Omega)}. \tag{5.43}$$

For a harmonically oscillating electric field with vector potential

$$A_l(t) = \frac{\hbar E_l \sin(\Omega t)}{-ea_l \Omega}, \tag{5.44}$$

we find

$$\alpha_{l,\pm,m} = \int_{-\pi}^{\pi} \frac{dz}{2\pi} e^{imz \mp i\frac{E_l}{\Omega}\sin(z)} = J_m\left(\pm\frac{E_l}{\Omega}\right), \tag{5.45}$$

where we have used the integral representation of the Bessel function [163]. To allow the system to dissipate energy, we couple it to a fermionic reservoir. The coupling is achieved in a similar way as above for the harmonically driven level (however, is also detailed in App. A.7).

From Eq. (5.18) we can calculate the time-averaged and momentum-summed spectral function $A_0(\omega) \equiv -2/N \sum_{\boldsymbol{k}} \mathrm{Im} G^R_{\boldsymbol{k},00}(\omega)$ as shown in Fig. 5.5 (for $E_x = E_y = E$). The result for zero drive

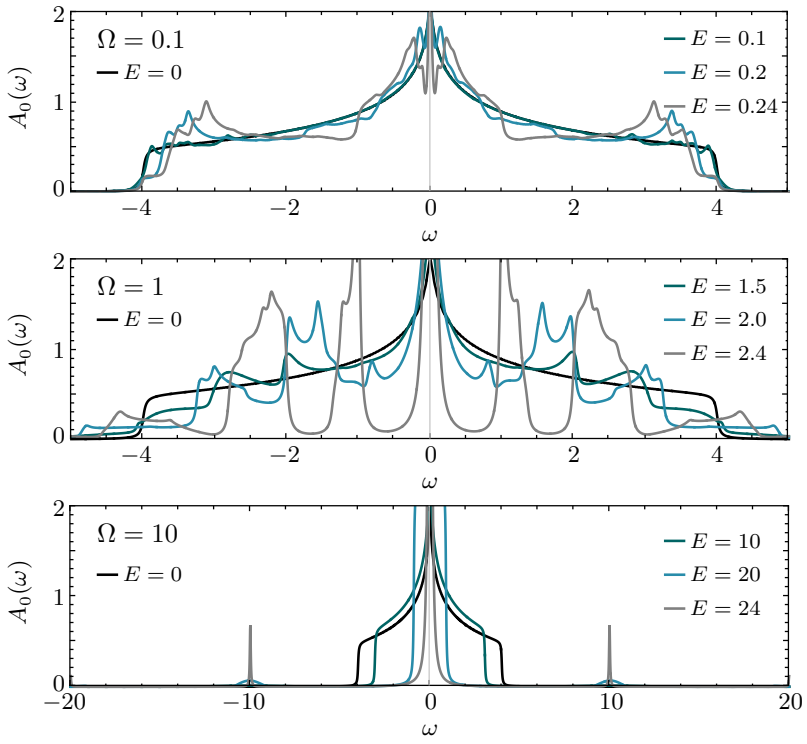

Figure 5.5: Spectral function for the driven two-dimensional lattice ($\int_{-\infty}^{\infty} d\omega A_0(\omega)/(2\pi) = 1$). Parameters: $\tilde{t} = a_x = a_y = 1$, $\Gamma = 0.03$ (see App. A.7), $k_B T = 0.01$, and Floquet-matrices of size 9×9.

amplitude is plotted with a black line, and shows the well-known equilibrium spectral function for the two-dimensional tight-binding square lattice: the spectral function is bounded in frequency by the dispersion band edges, and shows a Van Hove singularity at the center. As we turn on the periodic drive, the time-averaged spectrum shows Floquet sidebands centered at integer multiples of the drive-frequency, similarly to the harmonically driven level discussed above. Recent experimental progress has opened for the possibility to image such so-called Floquet band structures [164, 165]. As the drive frequency increases, the argument of the Bessel-functions in Eq. (5.45) decreases (for a fixed drive amplitude) whereby the contribution from higher-order Bessel functions decreases. This has the dramatic consequence that as the amplitude is increased sufficiently, the zeroth Bessel function in Eq. (5.45) approaches its first root, i.e. from Eq. (5.43) $\epsilon_{\boldsymbol{k},0} \to 0$ or the effective hopping in the time-averaged energy goes to zero. This is most easily seen in the lower panel in Fig. 5.5 as a narrowing of the central spectral weight. This phenomenon is known as dynamical localization, first studied by Dunlap et. al. [144]. Intuitively, the oscillating field moves the otherwise delocalized electrons back and forth until they effectively appear localized. Such vanishing hopping from dynamical localization has been observed experimentally in related experiments on Bose-Einstein condensates in an optical lattice. However, in condensed-matter materials where a typical nearest-neighbor coupling $\tilde{t} \sim 1$ eV, which corresponds to a frequency in the order of 10^{14} Hz or a light-wave wavelength in the order of 1 μm, the electric field magnitude required for dynamical localization is in the order of 10^9 V/m (for a lattice constant in the order of 1 Å), and as pointed out in Ref. [144], it is indeed experimentally challenging to apply such field magnitudes without destroying the sample. Yet, it is an interesting example of how a periodic drive may affect a condensed-matter system, even in this simple non-interacting case. But what happens when including electron-electron interactions? This is the subject of the next chapter, where we will study the periodically driven Hubbard model.

6 | Periodically driven Hubbard model

This chapter is based on Publication III, Physical Review B 100, 121110(R) (2019) by N. Walldorf, D. M. Kennes, J. Paaske, and A. J. Millis.

We have already seen examples of interesting effects caused by interactions between electrons: from the Coulomb-mediated energy-transfer between two otherwise decoupled systems in Sec. 3.1 to the underlying prerequisite for splitting Cooper pairs in Sec. 3.2. The origin of Cooper pairs in the first place is an example of the paramount effect that interactions can have in 'strongly correlated' materials (in the case of conventional superconductivity caused by interactions between electrons and ions[1]). Other fascinating phenomena such as magnetism and high-temperature superconductivity arise in strongly correlated materials. Originating from the complex interplay between the motion of individual particles (kinetic energy) and their interactions (Coulomb energy), the nature of these effects depend on the degree of localization of the electrons. This is reflected in the diagram in Fig. 6.1 where d- and f-electron compounds are listed according to the degree of electronic localization [131]: higher principle quantum numbers (moving downwards in the table) have more delocalized orbitals, whereas more protons in the nucleus (moving to the right in the table, and from d to f) pull electrons towards the nucleus. Elements in the delocalized part of the table have highly itinerant electrons that can perturb the ion lattice as they move through the material, giving rise to conventional superconductivity. By contrast, elements with highly localized electrons are strongly interacting with each other and form magnetic moments. Near the boundary between delocalization

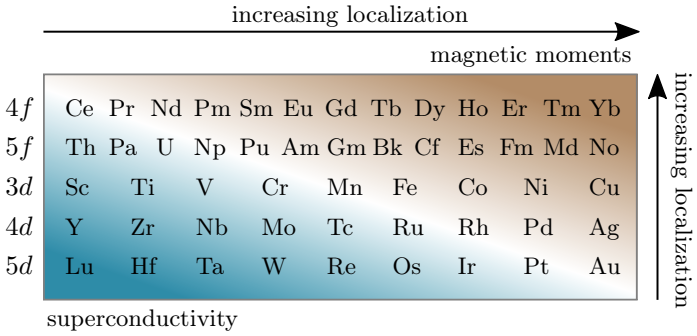

Figure 6.1: Kmetko-Smith diagram showing the trend of electronic localization and the corresponding trend towards formation of superconductivity and magnetic moments. Adapted from Ref. [131].

[1] Often 'strongly-correlated' refers to strong direct electron-electron interaction, however, for conventional superconductivity the correlation is caused by the electron-ion interaction [166].

(itineracy) and localization (magnetic moments) we find some fascinating materials such as Ce-based superconductors [131] where superconductivity emerges at the limit where magnetic order is suppressed [167]. Whereas the mechanisms behind these phenomena are still poorly understood, it seems to suggest that one interesting route of study is the magnetic effect caused by itinerant electrons, called itinerant magnetism, and to ask, what physics emerges when driven out of equilibrium[2]?

Due to its apparent simplicity yet capability of describing a plethora of many-body phenomena, the *Hubbard model* [169] has become a standard starting point for theories of strongly correlated electron systems, and is central in describing itinerant magnetism [132]. The Hubbard model describes a lattice system where electrons are almost localized in atomic orbitals at each site in the lattice and interact through an *on-site* Coulomb interaction. The Hamiltonian reads

$$\hat{H} = \sum_{ij\sigma} h_{ij}(t)\hat{c}^\dagger_{i\sigma}\hat{c}_{j\sigma} + U(t)\sum_i \hat{n}_{i\uparrow}\hat{n}_{i\downarrow} + \hat{H}_{\mathrm{res}}, \tag{6.1}$$

where $\hat{n}_{i\sigma} = \hat{c}^\dagger_{i\sigma}\hat{c}_{i\sigma}$, and $\hat{c}^\dagger_{i\sigma}$ ($\hat{c}_{i\sigma}$) creates (annihilates) an electron with spin $\sigma \in \{\uparrow,\downarrow\}$ on lattice site i. The (possibly time-dependent) matrix element $h_{ij}(t)$ describes electron hopping from lattice site j to i with lattice site coordinates $\boldsymbol{r}_j$ and $\boldsymbol{r}_i$, respectively, and $U(t)$ is the on-site Coulomb or *Hubbard interaction* which dominates when the atoms are well separated and the overlap between neighboring orbitals is weak[3]. A time-dependent kinetic energy term can be introduced by a time-dependent electromagnetic field, and a time-dependent interaction could effectively arise from e.g. a parametric drive of the lattice [172] as e.g. realized in cold-atom experiments (however, this will not be our main focus in the discussions to follow). The system can dissipate energy to an electron reservoir in thermal equilibrium via $\hat{H}_{\mathrm{res}}$ (which includes the non-interacting reservoir and its coupling to the two-dimensional square-lattice, as detailed in App. A.7).

The (single-band) Hubbard-model refers to the approximation in which hopping is restricted to nearest neighbor sites. As in Sec. 5.3 we consider a two-dimensional square lattice in a uniform but time-dependent electric field where the non-interacting part of the Hamiltonian is diagonalized in momentum space as

$$\hat{H}_0 = \sum_{\boldsymbol{k}\sigma} \epsilon_{\boldsymbol{k}}(t)\hat{c}^\dagger_{\boldsymbol{k}\sigma}\hat{c}_{\boldsymbol{k}\sigma}. \tag{6.2}$$

where $\epsilon_{\boldsymbol{k}}(t) = -2\tilde{t}\sum_{l=x,y}\cos(k_l a_l + e a_l A_l(t)/\hbar)$, with $\boldsymbol{k} = (k_x, k_y)$ (see Fig. 6.2), and nearest neighbour hopping element $-\tilde{t}$.

The equilibrium properties of the half-filled Hubbard model in the square lattice with nearest neighbor hopping are reasonably well understood[4] [168, 173, 174]. At half filling in the two-dimensional square lattice, the nesting vector $\boldsymbol{Q} = (\pi, \pi)$ (in units of the inverse lattice spacing) gives rise to

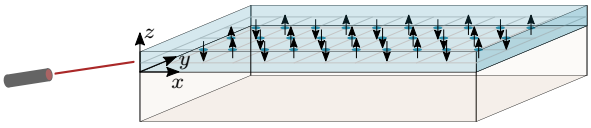

Figure 6.2: Sketch of a driven, antiferromagnetically ordered, strongly correlated film coupled to an electron reservoir. From Publication III.

[2]We focus solely on itinerant antiferromagnetism in this study. See, however, Ref. [168] for a proposed theory of high-temperature superconductivity in itinerant antiferromagnetism.

[3]The ratio $U/\tilde{t}$, where the nearest neighbour hopping element $-\tilde{t}$ is defined below Eq. (6.2), depends on the particular material, but $U/\tilde{t} \sim 20$ for ET-F_2TCNQ in Ref. [170], and first-principles calculations for e.g. herbertsmithite suggest $U/\tilde{t}$ up to 40 [171].

[4]The understanding of itinerant magnetism is a product of contributions from many great physicists. A historical perspective, including some milestone references, is provided in Ref. [131].

antiferromagnetic ordering[5]. Hence, for any $U > 0$ the ground state is antiferromagnetically (Néel) ordered, has a gap to charge and electronic excitations and supports gapless magnons (discussed further below). As the temperature is raised, magnetic excitations are thermally excited, leading to the destruction of long-ranged order above a temperature T_N (which equals zero in dimensions 1 and 2 cf. the Hohenberg-Mermim-Wagner theorem [177, 24, 178]). A crossover occurring around a temperature T_{MI} leads to filling in of the charge gap and restoration of conducting behavior; at large U, $T_{MI} \gg T_N$. These features are revealed by an appropriate interpretation of the results of a mean field plus fluctuation analysis [168, 173, 132] which is known to provide a qualitatively correct description of the equilibrium properties of the model. We are here interested in how these properties are changed when driven out of equilibrium by a periodic drive.

6.1 Non-equilibrium action

In Ch. 4, we introduced the formalism of non-equilibrium field theory and Green functions. Let us now formulate the non-equilibrium action of the Hubbard model. To deal with the Hubbard interaction[6] we transform the interaction by a so-called *Hubbard–Stratonovich transformation.* As a first step we rewrite

$$\bar{\psi}_{i\uparrow}\psi_{i\uparrow}\bar{\psi}_{i\downarrow}\psi_{i\downarrow} = -\frac{1}{2}(\bar{\psi}_{i\uparrow}\psi_{i\uparrow} - \bar{\psi}_{i\downarrow}\psi_{i\downarrow})^2 = -\frac{1}{6}\boldsymbol{s}_i^2, \quad \boldsymbol{s}_i \equiv \sum_{\sigma\sigma'} \bar{\psi}_{i\sigma}\,\boldsymbol{\sigma}_{\sigma\sigma'}\psi_{i\sigma'}, \tag{6.3}$$

where we have used that $\psi_{i\sigma}\psi_{i\sigma} = \bar{\psi}_{i\sigma}\bar{\psi}_{i\sigma} = 0$ for Grassmann fields [127], and $\boldsymbol{\sigma} = (\sigma_x, \sigma_y, \sigma_z)$ with σ_μ a Pauli matrix. Thus, we can write the interaction contribution to the action in real space as

$$S_{\text{int}}[\bar{\psi}, \psi] = \frac{1}{2}\int_{\mathcal{C}} d\tau \sum_i I\boldsymbol{s}_i^2, \tag{6.4}$$

where $I = U/3$ [131], and we have suppressed the time-argument. We introduce a *magnetization* field, $\boldsymbol{m}_i$, to transform the interaction term by a Hubbard–Stratonovich transformation, i.e. we use the Gaussian identity [121, Eq. (9.73)][7]

$$e^{iS_{\text{int}}[\bar{\psi},\psi]} = \int \mathcal{D}[m] e^{iS_{\text{int}}[\bar{\psi},\psi,m]}, \quad S_{\text{int}}[\bar{\psi},\psi,m] = \int_{\mathcal{C}} d\tau \sum_i \left[-\frac{\boldsymbol{m}_i\cdot\boldsymbol{m}_i}{2I} + \boldsymbol{m}_i\cdot\boldsymbol{s}_i\right]. \tag{6.5}$$

There is a degree of freedom in how one can pair the fields as in (6.3), referred to as a choice of decoupling 'channel', and therefore a degree of freedom in the form of the decoupling Hubbard–Stratonovich field. A part of the difficulty of describing strongly correlated systems is linked to the competition between physics described by different channels. The ambiguity in the choice of Hubbard–Stratonovich transformation is referred to as Fierz ambiguity [179]. In this work, we are interested in studying itinerant antiferromagnetism and adopt the convention for decoupling the interaction as in Ref. [131] and [132], where the Hubbard–Stratonovich field couples to the fermionic fields in the same way as an external Zeeman magnetic field [121]. Upon transforming to momentum space[8], the action

[5] Two-dimensional itinerant antiferromagnetism is e.g. discussed in relation to La_2CuO_4 in Ref. [173], however, itinerant antiferromagnetism is indeed also found in some materials that lie in the cross-over region in Fig. 6.1 such as Cr [175] and Ce compounds [176].

[6] The Hubbard-interaction follows from the two-particle interaction in Eq. (4.47) in the case $U_{ii'jj'} = U_{iiii}\delta_{ii'}\delta_{ij}\,\delta_{ij'}$ upon defining $U \equiv 2U_{iiii}$.

[7] Notice that one may choose $\boldsymbol{m} \to -\boldsymbol{m}$.

[8] Notice that although ψ and $\bar{\psi}$ are independent fields, we define their Fourier transforms as if they were related by complex conjugation, i.e. analogously to the definition of the Fourier transform of the creation/annihilation operators (see Sec. 5.3). We define the Fourier transform of the Hubbard–Stratonovich field as $\boldsymbol{m}_{\boldsymbol{k}} = \frac{1}{N}\sum_i \boldsymbol{m}_i e^{-i\boldsymbol{k}\cdot\boldsymbol{r}_i}$.

reads in the continuous time representation

$$\begin{aligned} S_0[\bar{\psi},\psi]+S_{\mathrm{int}}[\bar{\psi},\psi,m] = -N\int_{\mathcal{C}} d\tau \sum_{\boldsymbol{k}} \frac{\boldsymbol{m}_{\boldsymbol{k}}(\tau)\cdot\boldsymbol{m}_{-\boldsymbol{k}}(\tau)}{2I(\tau)} \\ + \int_{\mathcal{C}} d\tau \sum_{\boldsymbol{k}\boldsymbol{k}'\sigma\sigma'} \bar{\psi}_{\boldsymbol{k}\sigma}(\tau)\left[G^{-1}_{0,\boldsymbol{k}}(\tau)\delta_{\boldsymbol{k}\boldsymbol{k}'}\delta_{\sigma\sigma'} + \boldsymbol{m}_{\boldsymbol{k}-\boldsymbol{k}'}(\tau)\cdot\boldsymbol{\sigma}_{\sigma\sigma'}\right]\psi_{\boldsymbol{k}'\sigma'}(\tau), \end{aligned} \tag{6.6}$$

where $G_{0,\boldsymbol{k}}$ is the non-interacting Green function from the non-interacting part of the Hamiltonian Eq. (6.2). The action (6.6) is the non-equilibrium analogue of the equilibrium action (13.14) in Ref. [131].

6.1.1 Keldysh rotation and effective action

To Keldysh rotate the action, we define the transformed classical and quantum[9] Hubbard–Stratonovich fields $\boldsymbol{m}^{c(q)}(t) = (\boldsymbol{m}^{+}(t) \pm \boldsymbol{m}^{-}(t))/2$ [25] (see also Sec. 4.3.2). Hence, in the continuous time representation, the free Hubbard–Stratonovich component of the action transforms as

$$\begin{aligned} S_{m,0} &\equiv -N\int_{\mathcal{C}} d\tau \sum_{\boldsymbol{k}} \frac{\boldsymbol{m}_{\boldsymbol{k}}(\tau)\cdot\boldsymbol{m}_{-\boldsymbol{k}}(\tau)}{2I(\tau)} = -N\int dt \frac{1}{2I(t)} \sum_{\boldsymbol{k}} \left[\boldsymbol{m}^{+}_{\boldsymbol{k}}(t)\cdot\boldsymbol{m}^{+}_{-\boldsymbol{k}}(t) - \boldsymbol{m}^{-}_{\boldsymbol{k}}(t)\cdot\boldsymbol{m}^{-}_{-\boldsymbol{k}}(t)\right] \\ &= -2N\int dt \frac{1}{I(t)} \sum_{\boldsymbol{k}} \left[\boldsymbol{m}^{c}_{\boldsymbol{k}}(t)\cdot\boldsymbol{m}^{q}_{-\boldsymbol{k}}(t)\right], \end{aligned} \tag{6.7}$$

and the component which couples the magnetization field to the fermionic degree of freedom becomes (suppressing time-arguments)

$$S_{m,1} \equiv \int_{\mathcal{C}} d\tau \sum_{\boldsymbol{k}\boldsymbol{k}'\sigma\sigma'} \bar{\psi}_{\boldsymbol{k}\sigma}\,\boldsymbol{m}_{\boldsymbol{k}-\boldsymbol{k}'}\cdot\boldsymbol{\sigma}_{\sigma\sigma'}\psi_{\boldsymbol{k}'\sigma'} = -\int dt \sum_{\boldsymbol{k}\boldsymbol{k}'\sigma\sigma'} \hat{\bar{\Psi}}_{\boldsymbol{k}\sigma}\,\hat{M}_{\boldsymbol{k}\boldsymbol{k}',\sigma\sigma'}\hat{\Psi}_{\boldsymbol{k}'\sigma'}, \tag{6.8}$$

where

$$\hat{M}_{\boldsymbol{k}\boldsymbol{k}',\sigma\sigma'}(t) = -\hat{\boldsymbol{m}}_{\boldsymbol{k}-\boldsymbol{k}'}(t)\cdot\boldsymbol{\sigma}_{\sigma\sigma'}, \quad \hat{\boldsymbol{m}}_{\boldsymbol{k}}(t) = \boldsymbol{m}^{c}_{\boldsymbol{k}}(t)\hat{\tau}_0 + \boldsymbol{m}^{q}_{\boldsymbol{k}}(t)\hat{\tau}_1, \tag{6.9}$$

and we have used Eq. (4.49) to transform to Keldysh-rotated fields defined in Eq. (4.29).

As for the systems considered in the previous chapter, in order to stabilize the driven system in a non-equilibrium steady state (we will see an example of the dynamical evolution towards a non-equilibrium steady state in Sec. (6.4.1)), we couple the system to an external fermionic reservoir (as detailed in App. A.7). Hence, we obtain the full Keldysh-rotated action

$$S[\bar{\psi},\psi,m] = -2N\int dt \frac{1}{I(t)} \sum_{\boldsymbol{k}} \left[\boldsymbol{m}^{c}_{\boldsymbol{k}}(t)\cdot\boldsymbol{m}^{q}_{-\boldsymbol{k}}(t)\right] + \int dt dt' \sum_{\boldsymbol{k}\boldsymbol{k}'\sigma\sigma'} \hat{\bar{\Psi}}_{\boldsymbol{k}\sigma}(t)(\hat{G}^{-1})_{\boldsymbol{k}\boldsymbol{k}',\sigma\sigma'}(t,t')\hat{\Psi}_{\boldsymbol{k}'\sigma'}(t'), \tag{6.10}$$

where

$$(\hat{G}^{-1})_{\boldsymbol{k}\boldsymbol{k}',\sigma\sigma'}(t,t') \equiv (\hat{\tilde{G}}^{-1}_{0})_{\boldsymbol{k}\boldsymbol{k}',\sigma\sigma'}(t,t') - \hat{M}_{\boldsymbol{k}\boldsymbol{k}',\sigma\sigma'}(t)\delta(t-t'), \tag{6.11}$$

with $\hat{\tilde{G}}^{-1}_{0}$ being the free-electron inverse Green function dressed by the reservoir

$$(\hat{\tilde{G}}^{-1}_{0})_{\boldsymbol{k}\boldsymbol{k}',\sigma\sigma'}(t,t') = \hat{G}^{-1}_{0,\boldsymbol{k}}(t)\delta_{\boldsymbol{k}\boldsymbol{k}'}\delta_{\sigma\sigma'}\delta(t-t') - \hat{R}_{\boldsymbol{k}}(t,t')\delta_{\boldsymbol{k}\boldsymbol{k}'}\delta_{\sigma\sigma'}, \tag{6.12}$$

where $\hat{R}$ is given in Eq. (A.76).

[9] We will comment on the classical and quantum nomenclature in Sec. 6.2.

To obtain an effective action governing the magnetization field, we may carry out the Gaussian integral over the fermionic degree of freedom. Using the identity [132, Eq. (3.111)] $\ln\det \boldsymbol{A} = \mathrm{Tr}\ln \boldsymbol{A}$ we obtain the effective action

$$S[m] = -2N\int dt \frac{1}{I(t)} \sum_{\boldsymbol{k}} \left[\boldsymbol{m}^c_{\boldsymbol{k}}(t)\cdot \boldsymbol{m}^q_{-\boldsymbol{k}}(t)\right] - i\hbar \mathrm{Tr}\ln\left[\mathbb{1} - \hat{\tilde{G}}_0\hat{M}\right], \tag{6.13}$$

where the trace should be taken over time, momentum, spin, and the Keldysh structure. The expansion of the logarithm can be presented as the infinite sum of diagrams

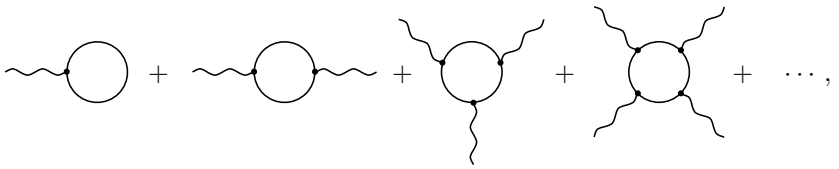

where curly lines represent the magnetization field (matrices) and solid lines represent fermionic propagators. The Hubbard model describes electrons propagating in the system and fluctuatingly experiencing an interaction, or exchanging an interaction-mediating bosonic field, when occupying the same lattice site. Equivalently, we can think of the model and the diagrams that appear in the effective action (6.13) as an interaction-mediating bosonic field which fluctuatingly disappears from electron propagation, and adds as a magnetization field to the fermionic action.

6.2 Saddle point

Up to this point, everything has been formal manipulations of the action, however, the effective action (6.13) is a convenient starting point for expanding around the "classical physics". Noticing that the effective action enters as the integrand $\exp(iS[m]/\hbar)$ in the path integral, for semiclassical paths where $S[m] \gg \hbar$ (i.e. $\hbar$ is a small scale, which is the meaning of "semiclassical"), the integrand is a highly oscillating functional of the paths m^c, m^q [180]. Hence, contributions to the path integral from m^c, m^q are canceled by contributions from $m^c + \delta m^c, m^q + \delta m^q$, except when [7]

$$\frac{\partial S[m^c, m^q]}{\partial m^q} = \frac{\partial S[m^c, m^q]}{\partial m^c} = 0, \tag{6.14}$$

that is, when the action does not vary (to linear order) with m^c, m^q. These configurations will therefore dominate to the semiclassical paths. Furthermore, since the Hubbard–Stratonovich field enters in Eq. (6.6) similarly to a classical external Zeeman field, which would be equal on the forward and backward branch on the contour, we explore an expansion around a classical magnetization field by considering the *classical saddle-point* equation defined by[10] [7, 181]

$$\left.\frac{\partial S[m^c, m^q]}{\partial m^q}\right|_{m^q=0} = 0. \tag{6.15}$$

It is, however, interesting to note the possible existence of non–classical saddle-point solutions which have non-zero quantum components, an idea which is still poorly developed [181].

As is customary, we hereafter set $\hbar = 1$. From Eq. (6.13) we find

$$\left.\frac{\partial S[m^c, m^q]}{\partial \boldsymbol{m}^q_{-\boldsymbol{k}}(t)}\right|_{m^q=0} = -2N\frac{\boldsymbol{m}^c_{\boldsymbol{k}}(t)}{I(t)} - i\mathrm{Tr}\left[[\hat{\tilde{G}}_0^{-1} - \hat{M}^c]^{-1}\frac{\partial}{\partial \boldsymbol{m}^q_{-\boldsymbol{k}}(t)}(-\hat{M}^q)|_{m^q=0}\right] = 0, \tag{6.16}$$

[10] Note that $\partial S[m^c, m^q]/\partial m^c|_{m^q=0} = 0$ is solved trivially.

where $\hat{M}^c_{\boldsymbol{k}\boldsymbol{k}'\sigma\sigma'}(t,t') = -\hat{\tau}_0 \boldsymbol{m}^c_{\boldsymbol{k}-\boldsymbol{k}'}(t)\cdot\boldsymbol{\sigma}_{\sigma\sigma'}\delta(t-t')$ and $\hat{M}^q_{\boldsymbol{k}\boldsymbol{k}'\sigma\sigma'}(t,t') = -\hat{\tau}_1 \boldsymbol{m}^q_{\boldsymbol{k}-\boldsymbol{k}'}(t)\cdot\boldsymbol{\sigma}_{\sigma\sigma'}\delta(t-t')$, and we have used that $(\boldsymbol{AB})^{-1} = \boldsymbol{B}^{-1}\boldsymbol{A}^{-1}$. Performing the partial trace over time, momentum, and spin, and defining the reservoir and (classical) mean-field dressed Green function $\hat{\tilde{G}} \equiv \left[\hat{\tilde{G}}_0^{-1} - \hat{M}^c\right]^{-1}$, we find the saddle-point equation

$$\begin{aligned}\boldsymbol{m}^c_{\boldsymbol{k}}(t) &= -i\frac{I(t)}{2N}\int dt'dt''\sum_{\boldsymbol{k}'\boldsymbol{k}''\sigma\sigma'}\mathrm{Tr}\left[\hat{\tilde{G}}_{\boldsymbol{k}'\boldsymbol{k}''\sigma\sigma'}(t',t'')\hat{\tau}_1\frac{\partial}{\partial \boldsymbol{m}^q_{-\boldsymbol{k}}(t)}\boldsymbol{m}^q_{\boldsymbol{k}''-\boldsymbol{k}'}(t'')\cdot\boldsymbol{\sigma}_{\sigma'\sigma}\delta(t''-t')\right] \\ &= -i\frac{I(t)}{2N}\sum_{\boldsymbol{k}'\sigma\sigma'}\mathrm{Tr}\left[\hat{\tilde{G}}_{\boldsymbol{k}',\boldsymbol{k}'-\boldsymbol{k},\sigma\sigma'}(t,t)\hat{\tau}_1\boldsymbol{\sigma}_{\sigma'\sigma}\right].\end{aligned} \tag{6.17}$$

The saddle-point equation can have multiple solutions and is, in general, solved by making a physically motivated ansatz. Indeed, interesting physics could hide in "un-guessed" ansätze, and all the more so when driven out of equilibrium. However, a possible starting point is to get inspired from our knowledge in equilibrium and see how the physics changes as we increase the non-equilibrium drive.

6.3 The Néel antiferromagnetic state

The repulsive Coulomb interaction between electrons can affect their movement in a lattice significantly. Whereas free electrons tend to delocalize (as described by the finite hopping matrix element between different sites in the tight-binding Hamiltonian), the repulsive Coulomb interaction may act oppositely and localize electrons in the lattice. Indeed, in the limit of infinite on-site repulsion, no two electrons would prefer to occupy the same site, and if the total number of electrons equals the number of lattice sites (half-filling) the electrons would localize with one electron on each site. For finite interactions, however, the tendency to delocalize may lead an electron to tunnel to its neighbouring site, which, however, due to Pauli exclusion is only possible if the two electrons have opposite spin [182]. Therefore, at half filling the system may order antiferromagnetically resulting in an antiferromagnetic magnetization mean field,

$$\boldsymbol{m}^c_{\boldsymbol{k}}(t) = \boldsymbol{m}_0(t)\delta_{\boldsymbol{k}\boldsymbol{Q}}, \tag{6.18}$$

where $\boldsymbol{Q} = (\pi,\pi)$. The above motivates the antiferromagnetic behavior on a qualitative level. On a quantitative level, one may look at the governing fluctuations in magnetization around the disordered state, that is, ask how the system would like to order in response to an infinitesimal external field. In equilibrium the answer is antiferromagnetically for the square lattice at half-filling as we will see in Sec. 6.5.1, and numerical evidence indicates that a Néel state is the ground state at half-filling except in one-dimensional systems [132] (see also the experiment in Ref. [183]). Yet, if one focus on the antiferromagnetic saddle point, still an infinite number of solutions exists, i.e. any direction in spin space. This rotational symmetry will give rise to a Goldstone-mode as we will discuss in Sec. 6.5.

To study the Néel state, it is convenient to express the action in terms of the spinors (suppressing time index) $\bar{\Phi}_{\boldsymbol{k}} = (\bar{\psi}_{1,\boldsymbol{k}\uparrow}\ \bar{\psi}_{1,\boldsymbol{k}\downarrow}\ \bar{\psi}_{1,\boldsymbol{k}+\boldsymbol{Q},\uparrow}\ \bar{\psi}_{1,\boldsymbol{k}+\boldsymbol{Q},\downarrow}\ \bar{\psi}_{2,\boldsymbol{k}\uparrow}\ \bar{\psi}_{2,\boldsymbol{k}\downarrow}\ \bar{\psi}_{2,\boldsymbol{k}+\boldsymbol{Q},\uparrow}\ \bar{\psi}_{2,\boldsymbol{k}+\boldsymbol{Q},\downarrow})$, and $\Phi_{\boldsymbol{k}} = (\psi_{1,\boldsymbol{k}\uparrow}\ \psi_{1,\boldsymbol{k}\downarrow}\ \psi_{1,\boldsymbol{k}+\boldsymbol{Q},\uparrow}\ \psi_{1,\boldsymbol{k}+\boldsymbol{Q},\downarrow}\ \psi_{2,\boldsymbol{k}\uparrow}\ \psi_{2,\boldsymbol{k}\downarrow}\ \psi_{2,\boldsymbol{k}+\boldsymbol{Q},\uparrow}\ \psi_{2,\boldsymbol{k}+\boldsymbol{Q},\downarrow})^T$, where the subscripts 1 and 2 refer to the components of the Keldysh-rotated fields cf. Eq. (4.29). Hence,

$$S[\bar{\psi},\psi,m] = -2N\int dt\frac{1}{I(t)}\sum_{\boldsymbol{k}}\left[\boldsymbol{m}^c_{\boldsymbol{k}}(t)\cdot\boldsymbol{m}^q_{-\boldsymbol{k}}(t)\right] + \int dtdt'\sum_{\boldsymbol{k}\boldsymbol{k}'}{}'\hat{\bar{\Phi}}_{\boldsymbol{k}}(t)(\hat{\mathcal{G}}^{-1})_{\boldsymbol{k}\boldsymbol{k}'}(t,t')\hat{\Phi}_{\boldsymbol{k}'}(t'), \tag{6.19}$$

where we have defined the Green function

$$(\hat{\mathcal{G}}^{-1})_{\boldsymbol{k}\boldsymbol{k}'}(t,t') = \hat{\mathcal{G}}^{-1}_{0\boldsymbol{k}}(t)\delta_{\boldsymbol{k}\boldsymbol{k}'}\delta(t-t') - \hat{\mathcal{R}}_{\boldsymbol{k}}(t,t')\delta_{\boldsymbol{k}\boldsymbol{k}'} - \hat{\mathcal{M}}_{\boldsymbol{k}\boldsymbol{k}'}(t)\delta(t-t'), \tag{6.20}$$

with

$$\hat{\mathcal{G}}^{-1}_{0\boldsymbol{k}}(t)=\begin{pmatrix} \mathcal{G}^{-1R}_{0\boldsymbol{k}}(t) & \mathcal{G}^{-1K}_{0\boldsymbol{k}}(t) \\ 0 & \mathcal{G}^{-1A}_{0\boldsymbol{k}}(t) \end{pmatrix},\ \mathcal{G}^{-1R/A/K}_{0\boldsymbol{k}}(t)=\begin{pmatrix} G^{-1R/A/K}_{0\boldsymbol{k}}(t) & 0 \\ 0 & G^{-1R/A/K}_{0\boldsymbol{k}+\boldsymbol{Q}}(t) \end{pmatrix}\otimes\sigma_0,$$
$$\hat{\mathcal{M}}_{\boldsymbol{k}\boldsymbol{k}'}(t)=\begin{pmatrix} \mathcal{M}^{c}_{\boldsymbol{k}\boldsymbol{k}'}(t) & \mathcal{M}^{q}_{\boldsymbol{k}\boldsymbol{k}'}(t) \\ \mathcal{M}^{q}_{\boldsymbol{k}\boldsymbol{k}'}(t) & \mathcal{M}^{c}_{\boldsymbol{k}\boldsymbol{k}'}(t) \end{pmatrix},\ \mathcal{M}^{c/q}_{\boldsymbol{k}\boldsymbol{k}'}(t)=-\begin{pmatrix} \boldsymbol{m}^{c/q}_{\boldsymbol{k}-\boldsymbol{k}'}(t)\cdot & \boldsymbol{m}^{c/q}_{\boldsymbol{k}-(\boldsymbol{k}'+\boldsymbol{Q})}(t)\cdot \\ \boldsymbol{m}^{c/q}_{(\boldsymbol{k}+\boldsymbol{Q})-\boldsymbol{k}'}(t)\cdot & \boldsymbol{m}^{c/q}_{(\boldsymbol{k}+\boldsymbol{Q})-(\boldsymbol{k}'+\boldsymbol{Q})}(t)\cdot \end{pmatrix}\otimes\boldsymbol{\sigma}, \tag{6.21}$$
$$\hat{\mathcal{R}}_{\boldsymbol{k}}(t,t')=\sum_{\ell} t_\ell^2 \sum_{k_z}\begin{pmatrix} \mathcal{G}^{R}_{0\ell\boldsymbol{k}k_z}(t,t') & \mathcal{G}^{K}_{0\ell\boldsymbol{k}k_z}(t,t') \\ 0 & \mathcal{G}^{A}_{0\ell\boldsymbol{k}k_z}(t,t') \end{pmatrix},$$
$$\mathcal{G}^{R/A/K}_{0\ell\boldsymbol{k}k_z}(t,t')=\begin{pmatrix} G^{R/A/K}_{0\ell\boldsymbol{k}k_z}(t,t') & 0 \\ 0 & G^{R/A/K}_{0\ell,\boldsymbol{k}+\boldsymbol{Q},k_z}(t,t') \end{pmatrix}\otimes\sigma_0,$$

and the primed momentum summation in Eq. (6.19) means that momentum runs over half the Brillouin zone (the magnetic Brillouin zone[11]). In terms of $\mathcal{G}$, the saddle-point equation reads

$$\boldsymbol{m}_0(t)=\frac{I(t)}{2N}{\sum_{\boldsymbol{k}}}'\mathrm{Tr}\left\{(-i\hat{\tilde{\mathcal{G}}}_{\boldsymbol{k}}(t,t))\,\hat{\tau}_1\otimes\tau_1\otimes\boldsymbol{\sigma}\right\}, \tag{6.22}$$

where $\hat{\tilde{\mathcal{G}}}$ is the reservoir and (classical) mean-field dressed Green function (as in Sec. 6.2), $\hat{\tau},\tau$, σ are Pauli matrices in Keldysh, momentum and spin space, respectively (cf. the spinor structure defined above), the trace refers to the full matrix structure of $\hat{\tilde{\mathcal{G}}}_{\boldsymbol{k}}(t,t)$.

6.3.1 Time-independent limit

If we consider the limit where the system is not perturbed by a periodic drive (but possibly still driven out of equilibrium from coupling to reservoirs with different chemical potentials), the mean-field equation reduces to

$$\boldsymbol{m}_0=\frac{I}{2N}{\sum_{\boldsymbol{k}}}'\int_{-\infty}^{\infty}\frac{d\omega}{2\pi}\mathrm{Tr}\Big\{(-i\hat{\tilde{\mathcal{G}}}_{\boldsymbol{k}}(\omega))\,\hat{\tau}_1\otimes\tau_1\otimes\boldsymbol{\sigma}\Big\}, \tag{6.23}$$

where $\hat{\tilde{\mathcal{G}}}_{\boldsymbol{k}}(\omega)$ is the Fourier transformed dressed Green function with

$$\tilde{\mathcal{G}}^{R/A}_{\boldsymbol{k}}(\omega)=\frac{1}{(\omega\pm i\Gamma)^2-E_{\boldsymbol{k}}^2}\begin{pmatrix} (\omega\pm i\Gamma+\epsilon_{\boldsymbol{k}})\sigma_0 & -\boldsymbol{m}_0\cdot\boldsymbol{\sigma} \\ -\boldsymbol{m}_0\cdot\boldsymbol{\sigma} & (\omega\pm i\Gamma-\epsilon_{\boldsymbol{k}})\sigma_0 \end{pmatrix}, \tag{6.24}$$

where $E_{\boldsymbol{k}}=\sqrt{\epsilon_{\boldsymbol{k}}^2+|\boldsymbol{m}_0|^2}$, and the Keldysh self energy is governed by the Keldysh component of $\hat{\mathcal{R}}$ from Eq. (6.21) (see also App. A.7). From Eq. (6.6), we see that for an antiferromagnetic mean field (say in the z-direction) $-m_0\sigma_3$ scatters an electron with momentum $\boldsymbol{k}$ and spin σ into an electron with momentum $\boldsymbol{k}+\boldsymbol{Q}$ and spin σ'. Two such processes scatters an electron back to itself (momentum is conserved modulus a reciprocal lattice vector), and we can understand the diagonal component in Eq. (6.24) as the amplitude for all such processes, and similarly, the off-diagonal component results from an odd number of scattering events. The integral over frequencies in Eq. (6.23) can be carried out analytically (see e.g. Sec. 6.4.1), and we find the non-equilibrium saddle-point equation

$$\frac{1}{I}=\frac{1}{2\pi\Gamma N}\sum_{\boldsymbol{k},\ell,p=\pm}\frac{\gamma_\ell}{E_{\boldsymbol{k}}}\mathrm{Im}\,\psi\Big(\frac{1}{2}+\frac{i\beta_\ell}{2\pi}(E_{\boldsymbol{k}}-p\mu_\ell-i\Gamma)\Big), \tag{6.25}$$

[11] The magnetic Brillouin zone can be chosen as convenient. We use the upper half-plane in Fig. 5.4 as in Ref. [132], with an 80×40 momentum grid used in the numerical simulations in Secs. 6.4–6.5.

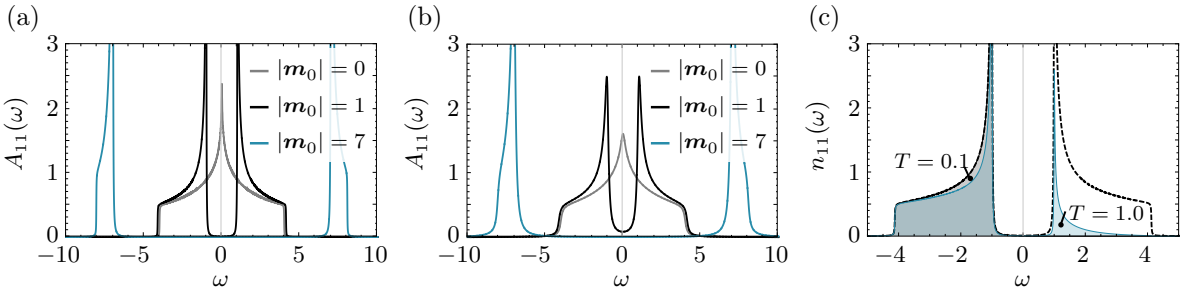

Figure 6.3: Spectral functions and occupations. (a) & (b): Spectral function as function of frequency for varying $|\boldsymbol{m}_0|$ with $T = 0.01$ and (a) $\Gamma = 0.01$ and (b) $\Gamma = 0.1$. (c) Occupation as function of frequency for varying temperature and $|\boldsymbol{m}_0| = 1$, $\Gamma = 0.01$, $\mu = 0$ (dashed line shows the spectral function).

where ψ is the digamma function and $\beta_\ell = 1/k_B T_\ell$ is the inverse temperature of reservoir ℓ. Equation (6.25) is the antiferromagnetic analogue of the bias-driven itinerant ferromagnet studied in Ref. [25] (see also the info-box below). In the case when coupling to a single reservoir with inverse temperature β and chemical potential μ, the saddle-point equation reads

$$\frac{1}{I} = \frac{1}{\pi N} \sum_{\boldsymbol{k},p} \frac{1}{E_{\boldsymbol{k}}} \mathrm{Im}\, \psi\left(\frac{1}{2} + \frac{i\beta}{2\pi}(E_{\boldsymbol{k}} - p\mu - i\Gamma)\right), \tag{6.26}$$

which in turn, in the limit of vanishing coupling to reservoirs, reduces to the equilibrium result in Ref. [131]

$$\frac{1}{I} = \frac{1}{2N} \sum_{\boldsymbol{k},p} \frac{1}{E_{\boldsymbol{k}}} \tanh(\beta(E_{\boldsymbol{k}} - p\mu)/2), \tag{6.27}$$

where we have used the relation $\mathrm{Im}\, \psi(1/2 + iy) = \pi \tanh(\pi y)/2$ [184]. The saddle-point equations determine the antiferromagnetic saddle-point magnetization field as a function of the electron interaction, electron dispersion, and possible couplings to wide-band reservoirs with particular coupling strengths, chemical potentials, and temperatures. Figure 6.3a shows the imaginary part of the upper diagonal component[12] of the Green function $A_{11}(\omega) \equiv -2\mathrm{Im} \sum_{\boldsymbol{k}}' \bar{\mathcal{G}}^R_{\boldsymbol{k},11}(\omega)$ for varying magnetization field (corresponding to varying interaction, I). In the non-interacting limit, $I = |\boldsymbol{m}_0| = 0$, we find the usual 2D square-lattice tight-binding spectrum as discussed in Sec. 5.3. However, as the interaction, and therefore $|\boldsymbol{m}_0|$ increases, a gap opens in the spectrum, which for $I \gg \tilde{t}, T, \mu$ is $2|\boldsymbol{m}_0| \approx 2I$ (from Eq. (6.27)). Indeed, also on a qualitative level we expect an insulating gap in the antiferromagnetic phase since electron tunneling to next-nearest neighbors are suppressed by Pauli exclusion. The effect of an enhanced coupling to a reservoir is seen as a smoothening of the spectral structures in Fig. 6.3b, and increasing the reservoir temperature excites particles into the upper band as shown from the quasiparticle occupation $n_{11}(\omega) \equiv -i \sum_{\boldsymbol{k}}' \bar{\mathcal{G}}^<_{\boldsymbol{k},11}(\omega)$ at half-filling in Fig. 6.3c (colored filling).

For the *ferromagnetic* case, we employ the ansatz $\boldsymbol{m}^c_{\boldsymbol{k}} = m_0 \hat{\boldsymbol{z}} \delta_{\boldsymbol{k},\boldsymbol{0}}$. From Eq. (6.6), we see that this ansatz simply shifts the energy in the non-interacting Green function $\epsilon_{\boldsymbol{k}} \to \epsilon_{\boldsymbol{k}} - \sigma m_0$, and hence from Eq. (4.33) the mean-field retarded, advanced, and Keldysh Green functions read

$$G^{R/A}_{\boldsymbol{k}\sigma}(\omega) = \frac{1}{\omega - \epsilon_{\boldsymbol{k}} + \sigma m_0 \pm i\Gamma}, \qquad G^K_{\boldsymbol{k}\sigma}(\omega) = \bar{F}(\omega)(G^R_{\boldsymbol{k}\sigma}(\omega) - G^A_{\boldsymbol{k}\sigma}(\omega)), \tag{6.28}$$

where $\bar{F}(\omega) = \sum_\ell \gamma_\ell F_\ell(\omega)/(2\Gamma)$ and $\Gamma = \sum_\ell \gamma_\ell/2$. The frequency integral over the Keldysh Green

[12] The lower diagonal component is identical.

function can be performed analytically, and we obtain the mean-field equation

$$m_0 = -I\sum_{\ell \boldsymbol{k}\sigma} \frac{\sigma\gamma_\ell}{2\pi\Gamma}\mathrm{Im}\left[\psi\left(\frac{1}{2}+i\frac{\beta_\ell}{2\pi}(\epsilon_{\boldsymbol{k}}-\sigma m_0-\mu_\ell-i\Gamma)\right)\right]. \tag{6.29}$$

Using that $\mathrm{Im}\{\psi(1/2+iy)\} = \pi\tanh(\pi y)/2$ [184] we find in the limit when decoupling from reservoirs with $\mu = 0$ the mean-field equation reduces to $m_0 = I\sum_{\boldsymbol{k}\sigma}\sigma n_F(\epsilon_{\boldsymbol{k}}-\sigma m_0)$. Upon rewriting $\sum_{\boldsymbol{k}} \to \int d\epsilon\nu(\epsilon)/2$, where $\nu(\epsilon)$ is the density of states [131, Eq. (13.34)], we find

$$m_0 = \frac{I}{2}\sum_{\sigma=\pm}\sigma\int d\epsilon\nu(\epsilon)n_F(\epsilon-\sigma m_0), \tag{6.30}$$

in agreement with Ref. [131, Eq. (13.36)]. Around the phase transition $m_0 \to 0$, we can expand $n_F(\epsilon-\sigma m_0) \approx n_F(\epsilon) - \sigma m_0 n_F'(\epsilon)$ to obtain the transition temperature T_c [131, p. 471]

$$1 = I\chi_0(T_c), \qquad \chi_0(T_c) = \int d\epsilon\nu(\epsilon)\left(-\frac{dn_F(\epsilon)}{d\epsilon}\right)\Big|_{T=T_c}, \tag{6.31}$$

which is the *finite-T Stoner criterion*. In the zero-temperature limit, we can approximate the derivative of the Fermi-Dirac distribution by a delta-function and find the *zero-T Stoner criterion* $1 = I\nu(\mu)$ (see the discussion of I versus U in Ref. [131, p. 474]).

In Ref. [25, 185, 186], the effect of a voltage bias is studied. We note that in the ferromagnetic case, when coupled to left and right reservoirs, we can write the mean-field equation in the form (not evaluating the frequency-integral for easier comparison)

$$m_0 = -\frac{I}{2}\int\frac{d\omega}{2\pi}\sum_{\boldsymbol{k}\sigma\ell}\sigma\frac{\gamma_\ell F_\ell(\omega)}{(\omega-\epsilon_{\boldsymbol{k}}+\sigma m_0)^2+\Gamma^2} = \frac{I}{2}\int\frac{d\omega}{2\pi}\sum_{\boldsymbol{k}\sigma\ell}\frac{2\sigma\gamma_\ell n_{F,\ell}(\omega)}{(\omega-\epsilon_{\boldsymbol{k}}+\sigma m_0)^2+\Gamma^2}, \tag{6.32}$$

where $\Gamma = (\gamma_L+\gamma_R)/2$. This is in agreement with Ref. [185, Eq. (6.48)] upon letting $I \to U$ (due to [131, (13.7)]), $\frac{2}{U}m_0 \to m_0$, and $\gamma_\ell \to 2\gamma_\ell$ (coupling strength defined with a factor 2).

6.4 Periodic drive

Let us return to our main interest; the periodically driven Hubbard model. The exciting route towards Floquet-engineering novel non-equilibrium phases becomes no less exciting in strongly-correlated materials. For example, in Ref. [22] the authors were able to induce superconductivity in a strongly-correlated material by application of a radiation field. The microscopic pathway that leads to superconductivity in the experiment is not fully understood, however, from our introductory discussion to this chapter we might anticipate that interesting physics could emerge. Indeed, we argued that materials that lie in the crossover between delocalized and localized electrons appear to be particularly interesting. Since a periodic drive affects the localization of electrons, ultimately in the form of dynamical localization[13] as discussed in Sec. 5.3, it seems plausible that a periodic drive might probe interesting physics in this crossover region where materials are on the brink of magnetism. One example is the optical melting of antiferromagnetism in $La_{0.5}Sr_{1.5}MnO_4$ [23].

While this serves to motivate our interest, needless to say, the general physics is highly challenging to describe. To make some initial progress, we will focus solely on periodically driven itinerant antiferromagnetism. In particular, we will see how a periodic drive may induce dynamics in the system on a mean-field level and affect the collective modes, both in terms of the dispersive properties (Floquet-engineering) as well as the distribution.

[13] The meaning of this 'localization' is the suppression of the nearest neighbour hopping element.

6.4.1 Saddle-point results

To study the periodically driven system, it is convenient to work with the Floquet Green functions described in Ch. 5. In a non-equilibrium steady state where the mean field is synchronized to the drive (see discussion below), we can expand $\boldsymbol{m}_0(t) = \sum_n \boldsymbol{m}_0^{(n)} e^{-in\Omega t}$ and transform Eq. (6.22) to the Floquet representation

$$\boldsymbol{m}_0^{(m)} = \frac{1}{2N} \sum_n \sum_{\boldsymbol{k}}{}' \int_{-\infty}^{\infty} \frac{d\omega}{2\pi} \mathrm{Tr}\Big\{ (-i\hat{\bar{\mathcal{G}}}_{\boldsymbol{k},mn}(\omega))\, \hat{\tau}_1 \otimes \tau_1 \otimes \boldsymbol{\sigma} \Big\} I_n, \tag{6.33}$$

where we have also expanded $I(t) = \sum_n I_n e^{-in\Omega t}$. In the following, however, we only consider a time-dependent interaction in Fig. 6.5b below, and in all other cases the interaction is assumed constant. We set the chemical potential corresponding to half-filling and couple to an oscillating electric field, represented as a vector potential $A_{x,y}(t) = -E\sin(\Omega t)/\Omega$. We set $\hbar = k_B = e = a_{x,y} = 1$, and choose the magnetization field direction along the z-direction, $\boldsymbol{m}_0(t) = m_0(t)\hat{\boldsymbol{z}}$. In the following, all energies will be given in units of $\tilde{t}$. The retarded/advanced component of the inverse electron Green function dressed by the reservoir is given by

$$\bar{\mathcal{G}}^{-1\,R/A}_{\boldsymbol{k},mn}(\omega) = (\omega + n\Omega \pm i\Gamma)\delta_{mn}\tau_0 \otimes \sigma_0 - h_{\boldsymbol{k},mn}, \tag{6.34}$$

where $h_{\boldsymbol{k},mn} = \epsilon_{\boldsymbol{k},m-n}\tau_3 \otimes \sigma_0 - m_0^{(m-n)}\tau_1 \otimes \sigma_3$, with $\epsilon_{\boldsymbol{k},m}$ given by Eq. (5.43). The Keldysh Green function is $\bar{\mathcal{G}}^K_{\boldsymbol{k},mn}(\omega) = \sum_{m'n'} \bar{\mathcal{G}}^R_{\boldsymbol{k},mm'}(\omega)\mathcal{R}^K_{m'n'}(\omega)\bar{\mathcal{G}}^A_{\boldsymbol{k},n'n}(\omega)$, where $\mathcal{R}^K_{mn}(\omega) = -2i\Gamma\tanh((\omega + n\Omega)/2T)\delta_{mn}\tau_0 \otimes \sigma_0$ is the self-energy from coupling to the reservoir (see App. A.7.1). We solve Eq. (6.33) numerically with a Floquet cutoff $|n| \leq n_{\max}$ set large enough to ensure convergence (specified in the figure captions) where n is the Floquet index. We iterate from an initial guess $m_0^{(n)} = 10^{-2}\theta(n_{\max} - |n|)$, and use converged solutions as new starting points to explore multistability.

From a practical point of view, we note that the integral over frequency for the reservoir- and mean-field dressed Keldysh and Lesser Green functions can be evaluated analytically. E.g. for the Keldysh Green function

$$\begin{aligned}
\int_{-\infty}^{\infty} \frac{d\omega}{2\pi} \bar{\mathcal{G}}^K_{\boldsymbol{k},mn}(\omega) &= \sum_{m'n'} \int \frac{d\omega}{2\pi} \bar{\mathcal{G}}^R_{\boldsymbol{k},mm'}(\omega)\mathcal{R}^K_{m'n'}(\omega)\bar{\mathcal{G}}^A_{\boldsymbol{k},n'n}(\omega) \\
&= \sum_{ijm'n'} \mathcal{U}_{\boldsymbol{k},mi}\mathcal{U}^{-1}_{\boldsymbol{k},im'} \left[\int \frac{d\omega}{2\pi} \mathcal{D}^R_{\boldsymbol{k},i}(\omega)\mathcal{R}^K_{m'n'}(\omega)\mathcal{D}^A_{\boldsymbol{k},j}(\omega) \right] \mathcal{U}_{\boldsymbol{k},n'j}\mathcal{U}^{-1}_{\boldsymbol{k},jn} \\
&= -i\sum_{\ell} \gamma_\ell \sum_{ijm'} \mathcal{U}_{\boldsymbol{k},mi}\mathcal{U}^{-1}_{\boldsymbol{k},im'} \left[\int \frac{d\omega}{2\pi} \mathcal{D}^R_{\boldsymbol{k},i}(\omega)F_\ell(\hbar\omega + L[m']\hbar\Omega)\mathcal{D}^A_{\boldsymbol{k},j}(\omega) \right] \mathcal{U}_{\boldsymbol{k},m'j}\mathcal{U}^{-1}_{\boldsymbol{k},jn},
\end{aligned} \tag{6.35}$$

where the indices refer to the full matrix structure, the matrices $\mathcal{U}$ diagonalize the retarded/advanced Green functions, $\mathcal{D}^{R/A}_{\boldsymbol{k},i}(\omega) = 1/(\omega \pm i\Gamma + \alpha_{\boldsymbol{k},i})$, and $L[m']$ assigns the Floquet-space index. Evaluating the integral we find

$$\int \frac{d\omega}{2\pi} \bar{\mathcal{G}}^K_{\boldsymbol{k},mn}(\omega) = -i\sum_{\ell} \gamma_\ell \sum_{ijm'} \mathcal{U}_{\boldsymbol{k},mi}\mathcal{U}^{-1}_{\boldsymbol{k},im'}\mathcal{M}_{\boldsymbol{k}ijm'}\mathcal{U}_{\boldsymbol{k},m'j}\mathcal{U}^{-1}_{\boldsymbol{k},jn}, \tag{6.36}$$

where

$$\begin{aligned}
\mathcal{M}_{\boldsymbol{k}ijm'} = \frac{1}{\pi}\frac{1}{\alpha_{\boldsymbol{k},i} - \alpha_{\boldsymbol{k},j} + 2i\Gamma} \Bigg[&\psi\left(\frac{1}{2} + \frac{i\beta_\ell}{2\pi}(-\alpha_{\boldsymbol{k},i} + L[m']\Omega - \mu_\ell - i\Gamma) \right) \\
&- \psi\left(\frac{1}{2} - \frac{i\beta_\ell}{2\pi}(-\alpha_{\boldsymbol{k},j} + L[m']\Omega - \mu_\ell + i\Gamma) \right) \Bigg],
\end{aligned} \tag{6.37}$$

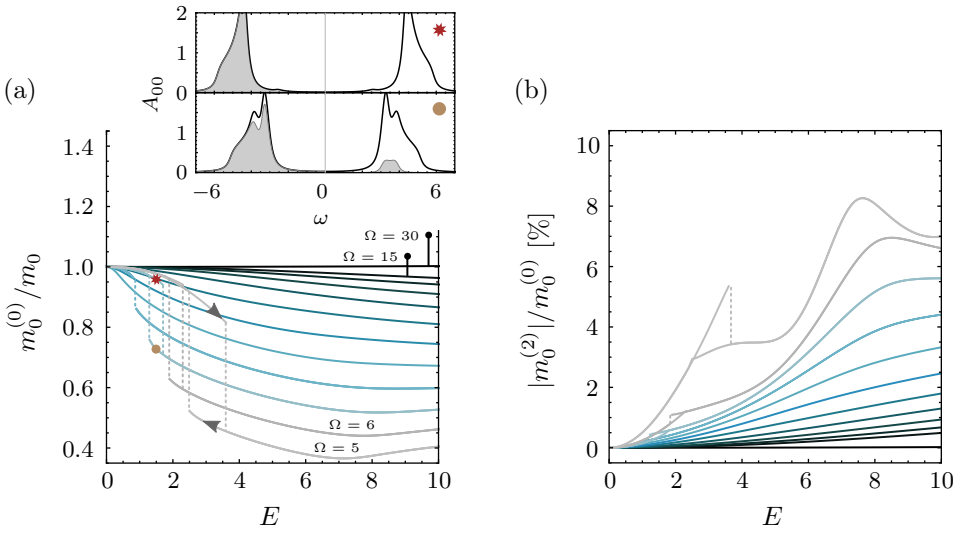

Figure 6.4: Mean field solutions for varying drive frequencies $\Omega = 5 - 15$ in steps of 1 and $\Omega = 30$. (a) Time-averaged mean field as a function of field amplitude, and (inset) diagonal-component of the time-averaged spectral functions (solid lines) and occupation functions (shaded areas) for the mean field solutions marked in (a). (b) Second mean field Floquet component as a function of field amplitude. The parameters are $I = 5$, $T = 0.01$, $\Gamma = 0.2$ and $n_{\max} = 10$. All energies are in units of $\tilde{t}$. From Publication III.

with ψ being the digamma function. We note that when integrating over frequency in a product of Keldysh Green functions, the identity $\tanh(a)\tanh(b) = 1 + \coth(a-b)[\tanh(b) - \tanh(a)]$ [121] is useful.

In Fig. 6.4a we show results for the time-averaged component of the mean field relative to its value at zero drive amplitude $m_0 \equiv m_0^{(0)}(E = 0)$. In the limit of drive frequencies much larger than the charge gap, i.e. $2m_0^{(0)} \ll \Omega$, the main features of the saddle-point solution remain similar to equilibrium, albeit with a small increase in the average staggered magnetization as a function of drive amplitude[14]. This behavior is expected from the renormalization of the hopping parameter in this Magnus limit [187, 188]. In contrast, as the drive frequency is decreased towards the sub-gap regime, the saddle-point results deviate from equilibrium-like and show a rich behavior as a function of drive amplitude and frequency which for still lower drive frequency shows discontinuous transitions (within a regime of bistability) to a state of lower gap amplitude and significant occupation of the upper band (Fig. 6.4a inset).

Our main focus in this study, is on the fluctuations in the high-frequency regime (in the following section), where the saddle-point behavior is more equilibrium-like. However, an analysis of the behavior when the drive frequency is tuned towards the sub-gap regime is an important route for future work. As a preliminary analysis, Fig. 6.5a shows a comparison of the mean-field result from Eq. (6.33) (black) and from a time-dependent simulation by D. M. Kennes[15] (blue) (panel b shows a comparison for a time-dependent interaction). Indeed, we see that after an initial transient behavior, the time-dependent solution reaches a periodic non-equilibrium steady state in good agreement with the Floquet result. This also justifies our expansion of the saddle-point magnetization as a Fourier-series in anticipation of synchronization. The non-equilibrium steady state shows rich dynamical behavior

[14] This is barely visible in the $\Omega = 30$ trace in Fig. 6.4a.

[15] For computational details on the time-dependent simulation see [189, 190].

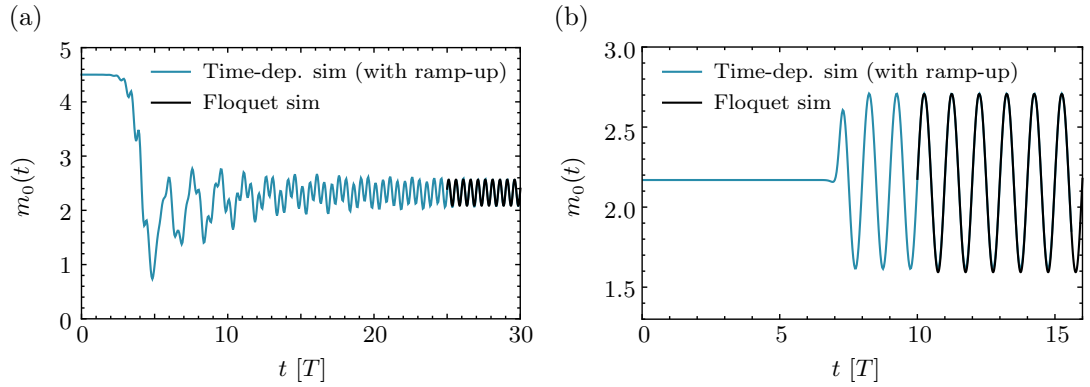

Figure 6.5: Synchronization of the mean field. An explicit time-dependent mean field solution (by D. M. Kennes) ramped from the un-driven state to the driven state synchronized to the time-transformed Floquet mean field solution (by N. Walldorf) for (a) the drive discussed in Sec. 6.4.1 with parameters $I = 5$, $T = 0.01$, $\Omega = 7$, $E = 8$, $\Gamma = 0.2$, and (b) for a time-dependent interaction with parameters $I_0 = 5$, $I_{\pm 1} = \pm i/2$, $\Gamma = 0.1$, $T = 0.01$, $\Omega = 1/50$ ($E = 0$). The time-dependent simulations have initial ramp-ups. See Refs. [189, 190] for computational details. (a) from Publication III.

in this regime. This is also reflected in Fig. 6.4b which shows the second Floquet component of the order parameter (the first Floquet component is vanishing). The resulting 2Ω oscillation in the order parameter implies moderate amplitude oscillations in the gap and order parameter amplitudes. Whether an analysis beyond mean-field theory, such as non-equilibrium DMFT as in Ref. [191], would lead to a Mott or gapless state is an interesting open question.

6.5 Fluctuations

The path-integral formulation of the theory provides a natural setting to explore higher-order corrections to the saddle-point theory, that is, *fluctuations* around the saddle point. From the previous analysis we found that the system can break its spin rotational symmetry to an antiferromagnetic ordering as illustrated in Fig. 6.6 (left panel). However, we can easily imagine that the system will have fluctuations, $\delta \boldsymbol{m} = (\delta m^x, \delta m^y, \delta m^z)$, around this ordering as illustrated in Fig. 6.6 (right panel). In particular, since any spatial rotation of the saddle-point solution is still a solution to the saddle-point equation, one could expect configurations of $\delta \boldsymbol{m}$ with infinitesimal contribution to the action, i.e. gapless fluctuations [132]. Indeed, we will see this so-called Goldstone mode emerging from the following analysis. To this end, we expand the magnetization field around the antiferromagnetic

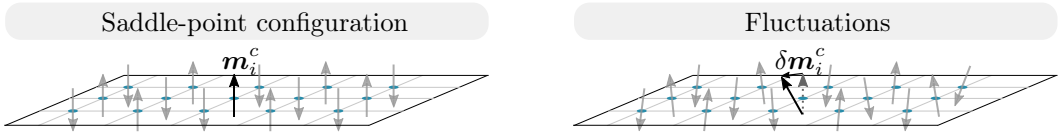

Figure 6.6: Antiferromagnetic mean-field theory (left) and fluctuations about the mean-field theory (right). The broken symmetry is illustrated to be out of plane.

sadlde-point mean field

$$\boldsymbol{m}^c_{\boldsymbol{k}}(t) = \boldsymbol{m}_0(t)\delta_{\boldsymbol{kQ}} + \delta\boldsymbol{m}^c_{\boldsymbol{k}}(t), \tag{6.38}$$
$$\boldsymbol{m}^q_{\boldsymbol{k}}(t) = \delta\boldsymbol{m}^q_{\boldsymbol{k}}(t), \tag{6.39}$$

where $\delta\boldsymbol{m}^c$ and $\delta\boldsymbol{m}^q$ describe classical and quantum components, respectively, of fluctuations around the saddle-point configuration. Notice that the saddle-point solution in Sec. 6.2 described a classical antiferromagnetic configuration, that is, where the field entered the action as a classical field. Hence, in addition to identifying corrections to the magnetization configuration, we also consider quantum corrections to the classical saddle-point theory. Upon performing the Gaussian integral over the fermionic degree of freedom in Eq. (6.20) as in Eq. (6.13), and expanding the logarithm to second order, we obtain the quadratic action governing the fluctuations[16]

$$S[\delta\boldsymbol{m}^c, \delta\boldsymbol{m}^q] = -2N\int dt \sum_{\boldsymbol{k}} \frac{\delta\boldsymbol{m}^c_{\boldsymbol{k}}(t)\cdot\delta\boldsymbol{m}^q_{-\boldsymbol{k}}(t)}{I(t)} + \frac{i}{2}\mathrm{Tr}\left\{((\delta\hat{\mathcal{M}})\hat{\bar{\mathcal{G}}})^2\right\}, \tag{6.40}$$

where $\hat{\bar{\mathcal{G}}}$ is the reservoir- and mean-field dressed Green function, and $(\delta\hat{\mathcal{M}})$ is given as in Eq. (6.21), but now in terms of the fluctuation fields, replacing $\boldsymbol{m}^{c/q} \to \delta\boldsymbol{m}^{c/q}$. Performing the partial trace over momentum, time, and the Keldysh structure gives

$$\mathrm{Tr}\left\{((\delta\hat{\mathcal{M}})\hat{\bar{\mathcal{G}}})^2\right\} = \int dtdt' \sum_{\boldsymbol{kk}'}{}' \sum_{\mu\nu} \mathrm{Tr}\left\{X^{\mu\nu,R}_{\boldsymbol{kk}'}(t,t') + X^{\mu\nu,A}_{\boldsymbol{kk}'}(t,t') + X^{\mu\nu,K}_{\boldsymbol{kk}'}(t,t')\right\}, \tag{6.41}$$

where

$$X^{\mu\nu,R}_{\boldsymbol{kk}'}(t,t') = \delta\mathcal{M}^{\mu,q}_{\boldsymbol{kk}'}(t)\bar{\mathcal{G}}^R_{\boldsymbol{k}'}(t,t')\delta\mathcal{M}^{\nu,c}_{\boldsymbol{k}'\boldsymbol{k}}(t')\bar{\mathcal{G}}^K_{\boldsymbol{k}}(t',t) + \delta\mathcal{M}^{\mu,q}_{\boldsymbol{kk}'}(t)\bar{\mathcal{G}}^K_{\boldsymbol{k}'}(t,t')\delta\mathcal{M}^{\nu,c}_{\boldsymbol{k}'\boldsymbol{k}}(t')\bar{\mathcal{G}}^A_{\boldsymbol{k}}(t',t), \tag{6.42}$$
$$X^{\mu\nu,A}_{\boldsymbol{kk}'}(t,t') = \delta\mathcal{M}^{\mu,c}_{\boldsymbol{kk}'}(t)\bar{\mathcal{G}}^K_{\boldsymbol{k}'}(t,t')\delta\mathcal{M}^{\nu,q}_{\boldsymbol{k}'\boldsymbol{k}}(t')\bar{\mathcal{G}}^R_{\boldsymbol{k}}(t',t) + \delta\mathcal{M}^{\mu,c}_{\boldsymbol{kk}'}(t)\bar{\mathcal{G}}^A_{\boldsymbol{k}'}(t,t')\delta\mathcal{M}^{\nu,q}_{\boldsymbol{k}'\boldsymbol{k}}(t')\bar{\mathcal{G}}^K_{\boldsymbol{k}}(t',t), \tag{6.43}$$
$$\begin{aligned} X^{\mu\nu,K}_{\boldsymbol{kk}'}(t,t') = {}& \delta\mathcal{M}^{\mu,q}_{\boldsymbol{kk}'}(t)\bar{\mathcal{G}}^A_{\boldsymbol{k}'}(t,t')\delta\mathcal{M}^{\nu,q}_{\boldsymbol{k}'\boldsymbol{k}}(t')\bar{\mathcal{G}}^R_{\boldsymbol{k}}(t',t) + \delta\mathcal{M}^{\mu,q}_{\boldsymbol{kk}'}(t)\bar{\mathcal{G}}^R_{\boldsymbol{k}'}(t,t')\delta\mathcal{M}^{\nu,q}_{\boldsymbol{k}'\boldsymbol{k}}(t')\bar{\mathcal{G}}^A_{\boldsymbol{k}}(t',t) \\ & + \delta\mathcal{M}^{\mu,q}_{\boldsymbol{kk}'}(t)\bar{\mathcal{G}}^K_{\boldsymbol{k}'}(t,t')\delta\mathcal{M}^{\nu,q}_{\boldsymbol{k}'\boldsymbol{k}}(t')\bar{\mathcal{G}}^K_{\boldsymbol{k}}(t',t), \end{aligned} \tag{6.44}$$

with index $\mu,\nu \in \{x,y,z\}$ referring to the directional component of the magnetization field. Reorganizing terms, we can write the Gaussian action in the form

$$S[\delta\boldsymbol{m}^c, \delta\boldsymbol{m}^q] = -N\int dt\int dt' \sum_{\boldsymbol{q}}{}' \sum_{\mu\nu} \begin{pmatrix}\delta\boldsymbol{m}^{\mu,c}_{\boldsymbol{q}}(t) & \delta\boldsymbol{m}^{\mu,q}_{\boldsymbol{q}}(t)\end{pmatrix} \left(\frac{1}{I(t)}\delta_{\mu\nu}\delta(t-t')\hat{\tau}_1\otimes\mathbb{1} - \hat{\Pi}^{\mu\nu}_{\boldsymbol{q}}(t,t')\right) \begin{pmatrix}\delta\boldsymbol{m}^{\nu,c}_{-\boldsymbol{q}}(t') \\ \delta\boldsymbol{m}^{\nu,q}_{-\boldsymbol{q}}(t')\end{pmatrix}, \tag{6.45}$$

where $\delta\boldsymbol{m}^{\mu,i}_{\boldsymbol{q}}(t) = (\delta m^{\mu,i}_{\boldsymbol{q}}(t), \delta m^{\mu,i}_{\boldsymbol{q}+\boldsymbol{Q}}(t))$[17], and

$$\hat{\Pi}^{\mu\nu}_{\boldsymbol{q}}(t,t') = \begin{pmatrix} 0 & \boldsymbol{\Pi}^{\mu\nu,A}_{\boldsymbol{q}}(t,t') \\ \boldsymbol{\Pi}^{\mu\nu,R}_{\boldsymbol{q}}(t,t') & \boldsymbol{\Pi}^{\mu\nu,K}_{\boldsymbol{q}}(t,t')\end{pmatrix}, \quad \boldsymbol{\Pi}_{\boldsymbol{q}} = \begin{pmatrix} \Pi_{0,\boldsymbol{q}} & \Pi_{Q,\boldsymbol{q}} \\ \Pi_{Q,\boldsymbol{q}} & \Pi_{0,\boldsymbol{q}+\boldsymbol{Q}}\end{pmatrix}, \tag{6.46}$$

with

$$\Pi^{\mu\nu,ij}_{0/Q,\boldsymbol{q}}(t,t') = \frac{i}{2N}\sum_{\boldsymbol{k}}{}' \mathrm{Tr}\left[(\hat{\gamma}_i\otimes\tau_0\otimes\sigma_\mu)\hat{\bar{\mathcal{G}}}_{\boldsymbol{k}}(t,t')(\hat{\gamma}_j\otimes\tau_{0/1}\otimes\sigma_\nu)\hat{\bar{\mathcal{G}}}_{\boldsymbol{k}+\boldsymbol{q}}(t',t)\right], \tag{6.47}$$

where the Keldysh indices $i,j \in \{c,q\}$ are encoded in the matrices $\hat{\gamma}_{c/q} = \hat{\tau}_{0/1}$. Notice that the action governing the fluctuation fields has the bosonic Keldysh structure. Choosing the z-component in spin

[16] The first-order term in the expansion vanishes from the saddle-point requirement.

[17] Notice that the additional superscript μ reminds us that bold-symbol in $\delta\boldsymbol{m}^{\mu,i}_{\boldsymbol{q}}(t)$ refers to the vector $(\delta m^{\mu,i}_{\boldsymbol{q}}(t), \delta m^{\mu,i}_{\boldsymbol{q}+\boldsymbol{Q}}(t))$, and not a vector of the directional components of the magnetization field.

space to align with the mean field, the z-component decouples from the xy-components. To decouple the xy-components, i.e. to find the propagators of the fluctuation fields, we transform the transverse components as $\delta m^{\pm} \equiv \delta m^x \pm i\delta m^y$ [131], whereby the remaining non-zero terms in the action can be written in the form

$$\begin{aligned} S[\delta\boldsymbol{m}^c,\delta\boldsymbol{m}^q] = -N\int dt\int dt' {\sum_{\boldsymbol{q}}}' \Bigg[& \left(\delta\boldsymbol{m}^{z,c}_{\boldsymbol{q}}(t)\ \ \delta\boldsymbol{m}^{z,q}_{\boldsymbol{q}}(t)\right)\left(\frac{1}{I(t)}\delta(t-t')\hat{\tau}_1\otimes\mathbb{1}-\hat{\Pi}^{zz}_{\boldsymbol{q}}(t,t')\right)\begin{pmatrix}\delta\boldsymbol{m}^{z,c}_{-\boldsymbol{q}}(t')\\ \delta\boldsymbol{m}^{z,q}_{-\boldsymbol{q}}(t')\end{pmatrix} \\ & + \left(\delta\boldsymbol{m}^{+,c}_{\boldsymbol{q}}(t)\ \ \delta\boldsymbol{m}^{+,q}_{\boldsymbol{q}}(t)\right)\left(\frac{1}{2I(t)}\delta(t-t')\hat{\tau}_1\otimes\mathbb{1}-\hat{\Pi}^{-+}_{\boldsymbol{q}}(t,t')\right)\begin{pmatrix}\delta\boldsymbol{m}^{-,c}_{-\boldsymbol{q}}(t')\\ \delta\boldsymbol{m}^{-,q}_{-\boldsymbol{q}}(t')\end{pmatrix} \\ & + \left(\delta\boldsymbol{m}^{-,c}_{\boldsymbol{q}}(t)\ \ \delta\boldsymbol{m}^{-,q}_{\boldsymbol{q}}(t)\right)\left(\frac{1}{2I(t)}\delta(t-t')\hat{\tau}_1\otimes\mathbb{1}-\hat{\Pi}^{+-}_{\boldsymbol{q}}(t,t')\right)\begin{pmatrix}\delta\boldsymbol{m}^{+,c}_{-\boldsymbol{q}}(t')\\ \delta\boldsymbol{m}^{+,q}_{-\boldsymbol{q}}(t')\end{pmatrix}\Bigg], \end{aligned} \tag{6.48}$$

where now $\mu,\nu\in\{+,-,z\}$ in Eq. (6.47) with $\sigma_{\pm}=(\sigma_x\pm i\sigma_y)/2$. For a periodic drive, we transform the action to the Floquet representation cf. Ch. 5

$$\begin{aligned} S[\delta\boldsymbol{m}^c,\delta\boldsymbol{m}^q] = -N\int_{-\Omega/2}^{\Omega/2}\frac{d\omega}{2\pi}\sum_{mn}{\sum_{\boldsymbol{q}}}' \Bigg[& \left(\delta\boldsymbol{m}^{z,c}_{-qm}\ \ \delta\boldsymbol{m}^{z,q}_{-qm}\right)\left(\frac{\delta_{mn}\hat{\tau}_1\otimes\mathbb{1}}{I}-\hat{\Pi}^{zz}_{\boldsymbol{q}mn}(\omega)\right)\begin{pmatrix}\delta\boldsymbol{m}^{z,c}_{qn}\\ \delta\boldsymbol{m}^{z,q}_{qn}\end{pmatrix} \\ & + 2\left(\delta\boldsymbol{m}^{+,c^*}_{qm}\ \ \delta\boldsymbol{m}^{+,q^*}_{qm}\right)\left(\frac{\delta_{mn}\hat{\tau}_1\otimes\mathbb{1}}{2I}-\hat{\Pi}^{+-}_{\boldsymbol{q}mn}(\omega)\right)\begin{pmatrix}\delta\boldsymbol{m}^{+,c}_{qn}\\ \delta\boldsymbol{m}^{+,q}_{qn}\end{pmatrix}\Bigg], \end{aligned} \tag{6.49}$$

where $q=(\omega,-\boldsymbol{q})$, $\delta\boldsymbol{m}_m(-\omega)=\delta\boldsymbol{m}(-\omega-m\Omega)$, $\delta\boldsymbol{m}_n(\omega)=\delta\boldsymbol{m}(\omega+n\Omega)$, $\delta\boldsymbol{m}^{-,c/q}_{-qm}=\delta\boldsymbol{m}^{+,c/q^*}_{qm}$, and we have used that $\mathrm{Tr}X^{-+R}_{\boldsymbol{k}\boldsymbol{k}'}(t,t')=\mathrm{Tr}X^{+-A}_{\boldsymbol{k}'\boldsymbol{k}}(t',t)$ and $\mathrm{Tr}X^{-+K}_{\boldsymbol{k}\boldsymbol{k}'}(t,t')=\mathrm{Tr}X^{+-K}_{\boldsymbol{k}'\boldsymbol{k}}(t',t)$. To transform Eq. (6.47), we use that $C(t,t')=A(t,t')B(t',t)$ transforms to $C_{mn}(\omega)=\sum_{m'}\int_{-\infty}^{\infty}\frac{d\omega'}{2\pi}A_{mm'}(\omega')B_{m'n}(\omega'-(\omega+n\Omega))$. Since the action is quadratic in the fluctuation fields, we can write down their correlation functions, and we are in particular interested in the transverse components which read

$$\boldsymbol{\chi}^{\perp R}_{\boldsymbol{q},mn}(\omega)\equiv\left[\frac{1}{2I}\mathbb{1}-\boldsymbol{\Pi}^{+-R}_{\boldsymbol{q}}(\omega)\right]^{-1}_{mn}, \tag{6.50}$$

$$\boldsymbol{\chi}^{\perp K}_{\boldsymbol{q},mn}(\omega)\equiv\left(\left[\frac{1}{2I}\mathbb{1}-\boldsymbol{\Pi}^{+-R}_{\boldsymbol{q}}(\omega)\right]^{-1}\boldsymbol{\Pi}^{+-K}_{\boldsymbol{q}}(\omega)\left[\frac{1}{2I}\mathbb{1}-\boldsymbol{\Pi}^{+-A}_{\boldsymbol{q}}(\omega)\right]^{-1}\right)_{mn}. \tag{6.51}$$

Before analyzing these correlations functions in the periodically driven case, let us consider the time-independent limit where we can derive analytical results to get some preliminary insights.

6.5.1 Time-independent limit

In the time-independent case, it is convenient to transform the action to frequency space whereby the retarded contribution reads

$$\begin{aligned} S^R = -N\int_{-\infty}^{\infty}\frac{d\omega}{2\pi}{\sum_{\boldsymbol{q}}}'\Bigg[& \delta\boldsymbol{m}^{z,q}_{-q}\frac{1}{I}\left(\mathbb{1}-I\boldsymbol{\Pi}^{zz,R}_{\boldsymbol{q}}(\omega)\right)\delta\boldsymbol{m}^{z,c}_{q}+\delta\boldsymbol{m}^{+,q}_{-q}\frac{1}{2I}\left(\mathbb{1}-2I\boldsymbol{\Pi}^{-+,R}_{\boldsymbol{q}}(\omega)\right)\delta\boldsymbol{m}^{-,c}_{q} \\ & +\delta\boldsymbol{m}^{-,q}_{-q}\frac{1}{2I}\left(\mathbb{1}-2I\boldsymbol{\Pi}^{+-,R}_{\boldsymbol{q}}(\omega)\right)\delta\boldsymbol{m}^{+,c}_{q}\Bigg], \end{aligned} \tag{6.52}$$

where

$$\boldsymbol{\Pi}^{\mu\nu,R}_{\boldsymbol{q}}(\omega)=\begin{pmatrix}\Pi^{\mu\nu,R}_{0,\boldsymbol{q}}(\omega) & \Pi^{\mu\nu,R}_{Q,\boldsymbol{q}}(\omega)\\ \Pi^{\mu\nu,R}_{Q,\boldsymbol{q}}(\omega) & \Pi^{\mu\nu,R}_{0,\boldsymbol{q}+\boldsymbol{Q}}(\omega)\end{pmatrix}, \tag{6.53}$$

and

$$\Pi^{\mu\nu,R}_{0,\boldsymbol{q}}(\omega) = \frac{i}{2}\int\frac{d\omega'}{2\pi}\frac{1}{N}\sum_{\boldsymbol{k}}{}' \mathrm{Tr}\Big[(\sigma_0\otimes\sigma_\mu)\bar{\mathcal{G}}^R_{\boldsymbol{k}}(\omega')(\sigma_0\otimes\sigma_\nu)\bar{\mathcal{G}}^K_{\boldsymbol{k}+\boldsymbol{q}}(\omega'-\omega) \tag{6.54}$$
$$+(\sigma_0\otimes\sigma_\mu)\bar{\mathcal{G}}^K_{\boldsymbol{k}}(\omega')(\sigma_0\otimes\sigma_\nu)\bar{\mathcal{G}}^A_{\boldsymbol{k}+\boldsymbol{q}}(\omega'-\omega)\Big],$$
$$\Pi^{\mu\nu,R}_{Q,\boldsymbol{q}}(\omega) = \frac{i}{2}\int\frac{d\omega'}{2\pi}\frac{1}{N}\sum_{\boldsymbol{k}}{}' \mathrm{Tr}\Big[(\sigma_0\otimes\sigma_\mu)\bar{\mathcal{G}}^R_{\boldsymbol{k}}(\omega')(\sigma_1\otimes\sigma_\nu)\bar{\mathcal{G}}^K_{\boldsymbol{k}+\boldsymbol{q}}(\omega'-\omega) \tag{6.55}$$
$$+(\sigma_0\otimes\sigma_\mu)\bar{\mathcal{G}}^K_{\boldsymbol{k}}(\omega')(\sigma_1\otimes\sigma_\nu)\bar{\mathcal{G}}^A_{\boldsymbol{k}+\boldsymbol{q}}(\omega'-\omega)\Big].$$

Upon performing the frequency integral we find $\Pi^{zz,R}_{Q,\boldsymbol{q}}(\omega)=0$, and

$$\Pi^{zz,R}_{0,\boldsymbol{q}}(\omega) = \frac{1}{2\pi i N}\sum_{\boldsymbol{k}}{}'\left[\frac{\epsilon_{\boldsymbol{k}}\epsilon_{\boldsymbol{k}+\boldsymbol{q}}+m_0^2}{E_{\boldsymbol{k}}E_{\boldsymbol{k}+\boldsymbol{q}}}(M^{++}_{\boldsymbol{k}\boldsymbol{q}}(\omega)+M^{--}_{\boldsymbol{k}\boldsymbol{q}}(\omega)-M^{+-}_{\boldsymbol{k}\boldsymbol{q}}(\omega)-M^{-+}_{\boldsymbol{k}\boldsymbol{q}}(\omega)) \tag{6.56}$$
$$+M^{++}_{\boldsymbol{k}\boldsymbol{q}}(\omega)+M^{--}_{\boldsymbol{k}\boldsymbol{q}}(\omega)+M^{+-}_{\boldsymbol{k}\boldsymbol{q}}(\omega)+M^{-+}_{\boldsymbol{k}\boldsymbol{q}}(\omega)\Big],$$
$$\Pi^{+-,R}_{0,\boldsymbol{q}}(\omega) = \frac{1}{4\pi i N}\sum_{\boldsymbol{k}}{}'\left[\frac{\epsilon_{\boldsymbol{k}}\epsilon_{\boldsymbol{k}+\boldsymbol{q}}-m_0^2}{E_{\boldsymbol{k}}E_{\boldsymbol{k}+\boldsymbol{q}}}(M^{++}_{\boldsymbol{k}\boldsymbol{q}}(\omega)+M^{--}_{\boldsymbol{k}\boldsymbol{q}}(\omega)-M^{+-}_{\boldsymbol{k}\boldsymbol{q}}(\omega)-M^{-+}_{\boldsymbol{k}\boldsymbol{q}}(\omega)) \tag{6.57}$$
$$+M^{++}_{\boldsymbol{k}\boldsymbol{q}}(\omega)+M^{--}_{\boldsymbol{k}\boldsymbol{q}}(\omega)+M^{+-}_{\boldsymbol{k}\boldsymbol{q}}(\omega)+M^{-+}_{\boldsymbol{k}\boldsymbol{q}}(\omega)\Big],$$

$$\Pi^{+-,R}_{Q,\boldsymbol{q}}(\omega) = \frac{m_0}{4\pi i N}\sum_{\boldsymbol{k}}{}'\left[\frac{M^{++}_{\boldsymbol{k}\boldsymbol{q}}(\omega)-M^{--}_{\boldsymbol{k}\boldsymbol{q}}(\omega)-M^{+-}_{\boldsymbol{k}\boldsymbol{q}}(\omega)+M^{-+}_{\boldsymbol{k}\boldsymbol{q}}(\omega)}{E_{\boldsymbol{k}+\boldsymbol{q}}}\right. \tag{6.58}$$
$$\left.-\frac{M^{++}_{\boldsymbol{k}\boldsymbol{q}}(\omega)-M^{--}_{\boldsymbol{k}\boldsymbol{q}}(\omega)+M^{+-}_{\boldsymbol{k}\boldsymbol{q}}(\omega)-M^{-+}_{\boldsymbol{k}\boldsymbol{q}}(\omega)}{E_{\boldsymbol{k}}}\right],$$

where upon coupling to a single reservoir at zero chemical potential

$$M^{m'n'}_{\boldsymbol{k}\boldsymbol{q}}(\omega) = \frac{\psi^-(i\Gamma+n'E_{\boldsymbol{k}+\boldsymbol{q}})-\psi^-(\omega+i\Gamma+m'E_{\boldsymbol{k}})+\psi^-(i\Gamma-m'E_{\boldsymbol{k}})-\psi^-(\omega+i\Gamma-n'E_{\boldsymbol{k}+\boldsymbol{q}})}{\omega+m'E_{\boldsymbol{k}}-n'E_{\boldsymbol{k}+\boldsymbol{q}}}$$
$$-\frac{\psi^-(i\Gamma-n'E_{\boldsymbol{k}+\boldsymbol{q}})-\psi^-(\omega+i\Gamma+m'E_{\boldsymbol{k}})+\psi^-(i\Gamma+m'E_{\boldsymbol{k}})-\psi^-(\omega+i\Gamma-n'E_{\boldsymbol{k}+\boldsymbol{q}})}{\omega+m'E_{\boldsymbol{k}}-n'E_{\boldsymbol{k}+\boldsymbol{q}}+2i\Gamma}, \tag{6.59}$$

with $\psi^-(z)=\psi(\frac{1}{2}-\frac{i\beta}{2\pi}z)$ and ψ being the digamma function. In the limit $\omega\to 0$, $\boldsymbol{q}\to\boldsymbol{Q}$ we find $\Pi^{+-,R}_{Q,\boldsymbol{Q}}(0)=0$, and

$$\Pi^{+-,R}_{0,\boldsymbol{Q}}(0) = \frac{1}{\pi N}\sum_{\boldsymbol{k}}\frac{1}{E_{\boldsymbol{k}}}\mathrm{Im}\,\psi\left(\frac{1}{2}+\frac{i\beta}{2\pi}(E_{\boldsymbol{k}}-i\Gamma)\right)=\frac{1}{2I}, \tag{6.60}$$

where the last equality follows from the saddle-point equation (6.26). This appearance of the saddle-point equation in the fluctuation analysis has some importance consequences which we will discuss below (and is indeed a non-trivial check of the theory). In the limit $T,\Gamma\to 0$, $M^{m'n'}_{\boldsymbol{k}\boldsymbol{q}}(\omega)$ reduces to

$$M^{m'n'}_{\boldsymbol{k}\boldsymbol{q}}(\omega) = \frac{i\pi(\mathrm{sgn}(m')-\mathrm{sgn}(n'))}{\omega+m'E_{\boldsymbol{k}}-n'E_{\boldsymbol{k}+\boldsymbol{q}}},\quad \mathrm{sgn}(\pm)=\pm 1, \tag{6.61}$$

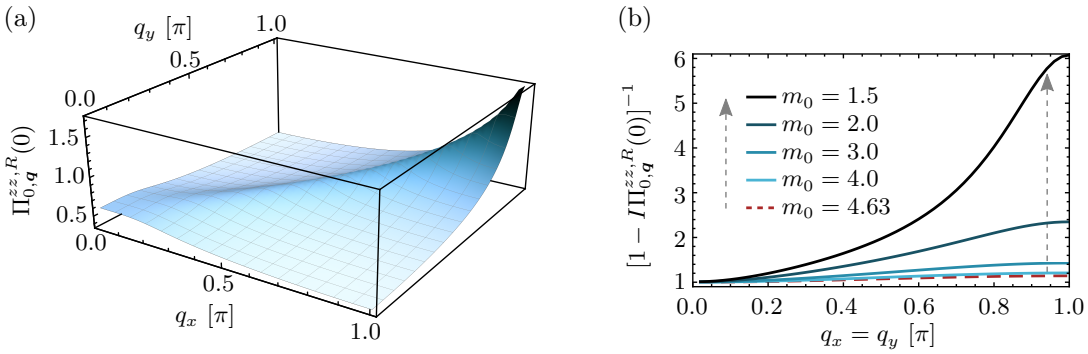

Figure 6.7: (a) $\Pi^{zz,R}_{0,\boldsymbol{q}}(0)$ as a function of momentum for $m_0 = 0$, $T = 0.05$, $\Gamma = 0.001$ (in good agreement with Ref. [179] Fig. 6.3, where, however the particular dissipation is unspecified). (b) $[1 - I\Pi^{zz,R}_{0,\boldsymbol{q}}(0)]^{-1}$ along the diagonal $q_x = q_y$ for $I = 5$, $T = 0.001$, $\Gamma = 0.01$ for varying m_0 with $m_0 = 4.63$ (red dashed) given by the saddle-point solution.

whereby Eqs. (6.56)-(6.58) become

$$\Pi^{zz,R}_{0,\boldsymbol{q}}(\omega) = -\frac{1}{N}\sum_{\boldsymbol{k}}{}' \left[\left(1 - \frac{\epsilon_{\boldsymbol{k}}\epsilon_{\boldsymbol{k}+\boldsymbol{q}} + m_0^2}{E_{\boldsymbol{k}}E_{\boldsymbol{k}+\boldsymbol{q}}}\right)\left(\frac{1}{\omega - E_{\boldsymbol{k}} - E_{\boldsymbol{k}+\boldsymbol{q}}} + \frac{1}{-\omega - E_{\boldsymbol{k}} - E_{\boldsymbol{k}+\boldsymbol{q}}}\right)\right], \tag{6.62}$$

$$\Pi^{+-,R}_{0,\boldsymbol{q}}(\omega) = -\frac{1}{2N}\sum_{\boldsymbol{k}}{}' \left[\left(1 - \frac{\epsilon_{\boldsymbol{k}}\epsilon_{\boldsymbol{k}+\boldsymbol{q}} - m_0^2}{E_{\boldsymbol{k}}E_{\boldsymbol{k}+\boldsymbol{q}}}\right)\left(\frac{1}{\omega - E_{\boldsymbol{k}} - E_{\boldsymbol{k}+\boldsymbol{q}}} + \frac{1}{-\omega - E_{\boldsymbol{k}} - E_{\boldsymbol{k}+\boldsymbol{q}}}\right)\right], \tag{6.63}$$

$$\Pi^{+-,R}_{Q,\boldsymbol{q}}(\omega) = -\frac{m_0}{2N}\sum_{\boldsymbol{k}}{}' \left[\left(\frac{1}{E_{\boldsymbol{k}}} + \frac{1}{E_{\boldsymbol{k}+\boldsymbol{q}}}\right)\left(\frac{1}{\omega - E_{\boldsymbol{k}} - E_{\boldsymbol{k}+\boldsymbol{q}}} - \frac{1}{-\omega - E_{\boldsymbol{k}} - E_{\boldsymbol{k}+\boldsymbol{q}}}\right)\right]. \tag{6.64}$$

Figure 6.7a shows $\Pi^{zz,R}_{0,\boldsymbol{q}}(0)$ from Eq. (6.56) at half filling in the limit of vanishing m_0, i.e. it shows the magnetic response around the disordered state. We see that antiferromagnetic fluctuations dominate and hence the disordered system has a largest response towards building up antiferromagnetic order. Thus, considering fluctuations around the antiferromagnetic saddle point, the red dashed curve in Fig. 6.7b shows $[1 - I\Pi^{zz,R}_{0,\boldsymbol{q}}(0)]^{-1}$ for a finite interaction and the corresponding magnetization field determined from the saddle-point equation (6.26). If we now, by hand, decrease the magnetization field for a constant interaction, i.e. if the system for some reason reduced its magnetization field, we see that fluctuations along the z-direction increases, i.e. the system has a larger response towards increasing the magnetization field again. The settled field strength is determined by the saddle-point equation, which in turn is bounded by the interaction strength. However, since the magnetic symmetry breaking could occur in all directions, one would expect the existence of transverse fluctuations with infinitesimal contribution to the action. Referring to the action in Eq. (6.52), this is indeed what Eq. (6.60) tells us, and it is again the saddle-point equation that ensures this. The vanishing of the transverse contribution to the action gives a pole in the propagator (the pole structure is visualized in Sec. (6.5.2)), corresponding to a collective magnetic mode, or a magnon. Notice that by coupling the spin-density field to a source field and integrating out the fermions one finds a generating functional for spin-spin correlation functions. For the retarded transverse susceptibility matrix we have [121]

$$\boldsymbol{\Pi}^{+-,R}_{\mathrm{RPA},\boldsymbol{q}}(\omega) = \boldsymbol{\Pi}^{+-,R}_{\boldsymbol{q}}(\omega)[\mathbb{1} - 2I\boldsymbol{\Pi}^{+-,R}_{\boldsymbol{q}}(\omega)]^{-1}. \tag{6.65}$$

The pole-structure of $[\mathbb{1} - 2I\boldsymbol{\Pi}^{+-,R}_{\boldsymbol{q}}(\omega)]^{-1}$ in (6.65) picks out $\omega = \omega_q$ in the first factor, which is then just a constant $(2I)^{-1}$. To consider the spectrum for transverse excitations we expand the determinant

of the matrix inverted in Eq. (6.65) around $\omega = 0$ and $\boldsymbol{q} = \boldsymbol{Q}$ in the zero-temperature limit

$$\begin{aligned} D_{\boldsymbol{q}}(\omega) &= (1 - 2I\Pi^{+-R}_{0,\boldsymbol{q}}(\omega))(1 - 2I\Pi^{+-R}_{0,\boldsymbol{Q}+\boldsymbol{q}}(\omega)) - 4I^2(\Pi^{+-R}_{Q,\boldsymbol{q}}(\omega))^2 \\ &\approx -4I^2\left[i\omega\gamma + (m_0\omega x_1)^2 + \omega^2(x_2x_3 + x_4^2) - \delta q^2 x_2 x_5\right], \end{aligned} \tag{6.66}$$

where $\delta q = |\boldsymbol{q} - \boldsymbol{Q}|$, and

$$\begin{aligned} &x_0 = \frac{1}{\pi N}\sum_{\mathbf{k}}{}' \frac{1}{E_{\boldsymbol{k}}^3}\tan^{-1}\left(\frac{E_{\boldsymbol{k}}}{\Gamma}\right),\ x_1 = x_0 + \frac{\Gamma}{\pi N}\sum_{\mathbf{k}}{}' \frac{1}{E_{\boldsymbol{k}}^2}\frac{E_{\boldsymbol{k}}^2 - \Gamma^2}{(E_{\boldsymbol{k}}^2 + \Gamma^2)^2},\ x_2 = \frac{1}{\pi N}\sum_{\mathbf{k}}{}' \frac{\epsilon_{\boldsymbol{k}}^2}{E_{\boldsymbol{k}}^3}\tan^{-1}\left(\frac{E_{\boldsymbol{k}}}{\Gamma}\right), \\ &x_3 = x_1 + \frac{\Gamma}{\pi N}\sum_{\mathbf{k}}{}' \left(\frac{\Gamma}{E_{\boldsymbol{k}}}\frac{3E_{\boldsymbol{k}}^2 - \Gamma^2}{(E_{\boldsymbol{k}}^2 + \Gamma^2)^3} + \frac{E_{\boldsymbol{k}}^2 - 3\Gamma^2}{(E_{\boldsymbol{k}}^2 + \Gamma^2)^3}\right),\ x_4 = \frac{2}{\pi N}\sum_{\mathbf{k}}{}' \left(\frac{\Gamma}{E_{\boldsymbol{k}}^2 + \Gamma^2}\right)^2, \\ &x_5 = -\left(\frac{\partial^2\Pi^{+-,R}_{0,\boldsymbol{Q}+\delta\boldsymbol{q}}(0)}{\partial\delta\boldsymbol{q}^2}\right)|_{\delta\boldsymbol{q}=0},\ \gamma = 2x_2x_4. \end{aligned} \tag{6.67}$$

In the limit $I \gg \tilde{t}, \Gamma$ we find upon expanding in $x = \tilde{t}/m_0$, $y = \Gamma/m_0$

$$x_0 \approx \frac{6\pi - 36\pi x^2 + 405\pi x^4 - 12y + 96x^2y - 1296x^4y + 4y^3 - 48x^2y^3}{24\pi m_0^3}, \tag{6.68}$$

$$x_1 \approx \frac{6\pi - 36\pi x^2 + 405\pi x^4 - 32y^3 + 384x^2y^3 + 60y^5}{24\pi m_0^3}, \tag{6.69}$$

$$x_2 \approx -\frac{x^2(-6\pi + 81\pi x^2 + 12y - 216x^2y - 4y^3)}{6\pi m_0}, \tag{6.70}$$

$$\begin{aligned} x_3 \approx (&6\pi - 36\pi x^2 + 405\pi x^4 + 12y - 96x^2y + 1296x^4y + 36y^2 - 360x^2y^2 + 5670x^4y^2 \\ &- 104y^3 + 1248x^2y^3 - 120y^4 + 1680x^2y^4 + 240y^5 + 252y^6)/(24\pi m_0^3), \end{aligned} \tag{6.71}$$

$$x_4 \approx \frac{y^2(1 - 8x^2 + 108x^4 - 2y^2 + 24x^2y^2 + 3y^4)}{\pi m_0^2}, \tag{6.72}$$

$$x_5 \approx -\frac{x^2(-6\pi + 27\pi x^2 + 24y - 144x^2y - 16y^3)}{12\pi m_0}, \tag{6.73}$$

$$\gamma \approx -\frac{x^2y^2(-2\pi + 43\pi x^2 + 4y + 4\pi y^2)}{\pi^2 m_0^3}. \tag{6.74}$$

Upon solving $D_{\boldsymbol{q}}(\omega) = 0$, the dispersion exhibits the well-known linear dispersion at lowest energies for antiferromagnetic magnons, $\omega = v\delta q$, with velocity $v = (2\sqrt{2}\tilde{t}^2/m_0)(1 - 5\tilde{t}^2/m_0^2 - 3\Gamma/(\pi m_0) - \Gamma^2/(2m_0^2)) + O\left(\tilde{t}^{2+n}\Gamma^{3-n}/m_0^5\right)$ for $n = 0, 1, 2, 3$, in agreement with Ref. [174] for $\Gamma = 0$. We see that the coupling to the resevoir reduces the magnon velocity.

6.5.2 Periodic drive

Let us now return to the periodically driven system, focusing in particular on the high drive frequency regime. Consider the time-averaged[18] transverse fluctuation spectral component $\mathrm{Im}\chi^{\perp,R}_{0,\boldsymbol{q},00}(\omega)$ which is shown in Fig. 6.8a. The low-lying excitations show a sharp peak, corresponding to magnons, with a small but non-zero broadening from the coupling to the reservoir. At energies below the charge gap and for not too large Γ, $\mathrm{Im}\chi^{\perp R}_{0,\boldsymbol{q},00}(\omega) \approx Z_q\delta(|\omega| - \omega_q)$. The peak amplitude grows as $\boldsymbol{q} \to \boldsymbol{Q}$, and upon integrating over the peaks in Fig. 6.8a we obtain the inverse spectral weight Z_q^{-1}, which is shown in the inset in Fig. 6.8a (blue points). The inverse spectral weight shows a linear δq dependence which is in excellent agreement with the expanded equilibrium result (solid line), which we obtain as $Z_q^{-1} \approx \alpha\delta q,\ \alpha = 1/(8\sqrt{2}\pi m_0^2)[2 + t^2/m_0^2 + O(t^4/m_0^4)]$.

[18] Referring to the 00-Floquet component, see Sec 5.2.

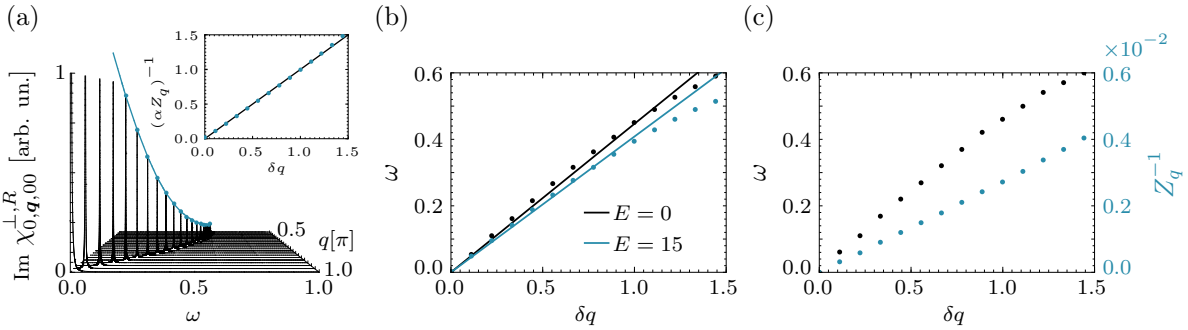

Figure 6.8: Transverse magnons. (a) Spectrum showing the magnon pole for $E = 15$ as a function of frequency and momentum $q_x = q_y = q$ for $\Gamma = 0.2$. Inset: Inverse spectral weight of the peaks in (a). (b) Location of the spin wave pole (points) as a function of frequency and δq together with the equilibrium linear dispersion $\omega = v\delta q$) (solid lines) with $\tilde{t} \to \tilde{t}J_0(E/\Omega)$ and $\Gamma = 0.2$. (c) Location of magnon pole (black, left axis) and inverse spectral weight (blue, right axis) for $E = 3.0$ and $\Gamma = 0.02$ (parameters relevant for Fig. 6.9). The remaining parameters are $I = 5$, $\Omega = 30$, $T = 0.01$, and $n_{\max} = 3$. (a) and (b) from publication III.

From the peak positions we identify ω_q, which gives the dispersion presented in Fig. 6.8b (blue points). The dispersion is seen to be similar to the equilibrium result (black points), with a linear momentum dependence at lowest energies, $\omega = v\delta q$. However, we see that the periodic drive slows down the linear magnon dispersion, similar to reduction of the effective velocity of electrons in an oscillating field studied by Dunlap et. al [144]. The approximated dissipative equilibrium result for the magnon velocity obtained in the previous section is shown with a black line together with the same result where, however, the hopping amplitude $\tilde{t}$ is replaced by the Magnus-renormalized value $\tilde{t}J_0(E/\Omega)$ [188, 144] (blue line). We see that the slowing down of the magnon in this high-frequency limit can be assigned to the renormalization of the hopping parameter. Such high-frequency renormalization by the Bessel function has been verified experimentally in cold-atoms experiments [192]. One may view this Bessel-function reduction of magnon velocity as a particularly simple example of "Floquet engineering".

The Keldysh component of the transverse propagator contains information about the non-equilibrium distribution of excitations. For low-lying magnons with $\omega_q \ll \Omega$, this information resides in the zeroth Floquet component, from which we define a time-averaged distribution function, F, by the ansatz

$$\chi^{\perp K}_{0,\boldsymbol{q},00}(\omega) = 2i\,\mathrm{Im}\Big[\chi^{\perp R}_{0,\boldsymbol{q},00}(\omega)\Big]F(\boldsymbol{q},\omega) \approx 2iZ_q\delta(|\omega| - \omega_q)F_q. \tag{6.75}$$

The pole approximation to $\mathrm{Im}\chi^R$ allows for a quasiclassical description in terms of an on-shell distribution function, $F_q = F(\boldsymbol{q}, \omega_q)$, referring only to the mode energy ω_q. In equilibrium, the fluctuation-dissipation theorem (FDT) ensures that $F_q = \coth(\omega_q/2T)$, which tends to unity at $\omega_q \gg T$ and diverges as ω_q^{-1} for $\omega_q \to 0$.

Figure 6.9a shows the inverse distribution function, F_q^{-1}, as a function of the mode energy, ω_q, at different drive amplitudes for a low reservoir temperature, $T = 0.01$. We plot the reciprocal to fit all data on the same panel. Because the reservoir temperature is substantially lower than the lowest ω_q included in our numerics, the equilibrium F_q is indistinguishable from unity on this plot[19]. We see that increasing the drive amplitude increases F_q (decreases F_q^{-1}) at all ω_q, with a larger increase for lower ω_q. Increasing either the drive frequency, Ω, or the reservoir coupling, Γ, for fixed drive amplitude reduces F_q (open symbols, left panel Fig. 6.9). For higher ω_q, F_q initially increases rapidly as the drive

[19] We note that the non-trivial part of F_q in the high-temperature case shown with dashed line is fully resolved with our numerics.

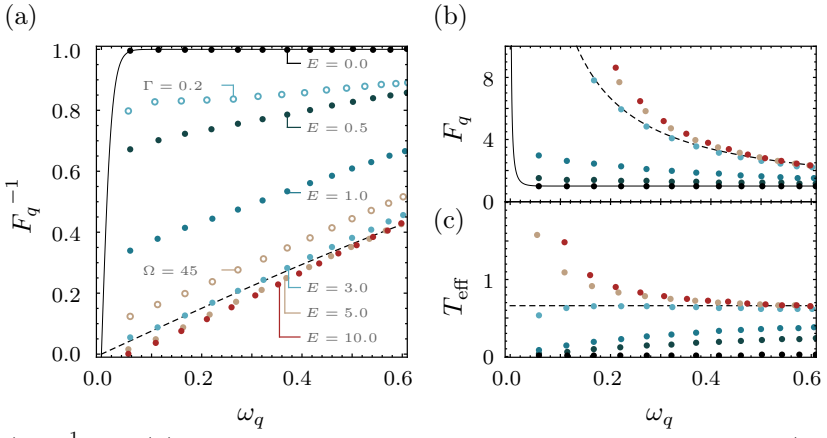

Figure 6.9: (a) F_q^{-1} and (b) F_q as function of ω_q for increasing drive amplitude (colored points, as marked in the figure) with $\Gamma = 0.02$ and $\Omega = 30$ together with the equilibrium curves for $T = 0.01$ (solid curve) and $T = 0.66$ (dashed curve). In (a) is also shown the result for $\Omega = 45$, $E = 5.0$, $\Gamma = 0.02$ (brown rings) and $\Gamma = 0.2$, $E = 3.0$, $\Omega = 30$ (blue rings). (c) $T_{\rm eff}$ corresponding to the curves in (b) together with the equilibrium $T = 0.66$ line (dashed). The remaining parameters are $I = 5$, $T = 0.01$, $q_{x,y} = q$, and $n_{\rm max} = 3$. From Publication III.

amplitude increases, but then saturates as the amplitude becomes large. This behavior is more clearly revealed in Fig. 6.9b. For small ω_q, the situation is different. For the two weakest drive amplitudes, F_q appears to approach a finite, non-zero value as ω_q approaches zero; for the intermediate drive amplitude F_q^{-1} vanishes linearly as $\omega_q \to 0$ while for the two highest drive frequencies, F_q^{-1} vanishes faster than linearly as $\omega_q \to 0$.

Apart from the intermediate drive amplitude ($E = 3$), these distribution functions depart markedly from the equilibrium distribution. To illustrate this more clearly, Fig. 6.9c shows the effective temperature $T_{\rm eff}$ as defined by $F_q = \coth(\omega_q/2T_{\rm eff}(q))$. We see that the results fall into two groups. For the two smallest drive amplitudes, $T_{\rm eff}$ is larger at high ω_q (very substantial excitation of high q magnons above the equilibrium value), but decreases to a value consistent with the reservoir temperature as $\omega_q \to 0$. For the intermediate drive amplitude, $T_{\rm eff} \approx 0.66$ is essentially momentum-independent, much larger than the reservoir temperatures (i.e. F_q fits well to the equilibrium form). For the two larger drive amplitudes, $T_{\rm eff}$ increases rapidly for small ω_q, indicating a super-thermal occupancy of the low-lying magnons, in other words F_q diverging faster than $1/\omega_q$.

The site- and period-averaged local mean squared fluctuation of the classical component of the order parameter is given by

$$\langle|\delta m^{+,c}|^2\rangle = \frac{1}{N}\sum_{\boldsymbol{q}}\int\frac{d\omega}{4\pi i}\chi^{\perp K}_{0,\boldsymbol{q},00}(\omega) \sim \int\frac{d^2q}{(2\pi)^2}Z_qF_q, \tag{6.76}$$

where in the latter expression we have used the δ-function pole approximation. In thermal equilibrium at any non-zero temperature, both F_q and Z_q diverge as $1/\delta q$ (the same is found for Z_q for all parameters in Fig. 6.9 [20]), and $\langle|\delta m^{+,c}|^2\rangle$ therefore diverges logarithmically with system size in two dimensions. This is the expression in the one-loop calculation of the well-known result [177, 24, 25] that thermal fluctuations destabilize long-ranged magnetic order in continuous-symmetry systems of dimension $d \leq 2$. Our results indicate that the generalization of the Hohenberg-Mermim-Wagner

[20] For the curves in Fig. 6.9 (see explicitly Fig. 6.8c), due to the small Γ, Z_q^{-1} is determined from the Kramers-Kronig relations as the slope of the linear interpolation of $\pi/{\rm Re}\chi^{\perp R}_{\boldsymbol{0},\boldsymbol{q},00}(\omega)$ near ω_q, consistent with the δ-function approximation for the peaks in ${\rm Im}\chi^{\perp R}_{\boldsymbol{0},\boldsymbol{q},00}(\omega)$

result to non-equilibrium is richer than expected from previous work. Unlike the dc current-driven ferromagnetic case, [25, 193] a weak non-equilibrium drive would not destabilize the ordered state in two dimensions, but larger drive amplitudes lead to a superthermal occupancy that may destabilize the order even in $d > 2$. The result highlights the delicate, yet arguably intuitive, balance in engineering material properties by means of a periodic drive: the periodic drive may destabilize the phase of (or 'melt') the material on the route towards Floquet engineering its properties.

6.6 Short summary

In this chapter, we studied the Hubbard model in a two-dimensional square lattice driven by a uniform time-periodic electric field. In particular, guided by our knowledge in equilibrium, we focused on the antiferromagnetic saddle point, and studied fluctuations around the antiferromagnetic phase. In general, we found that the antiferromagnetic mean field showed rich dynamics, which, however, approached a static behavior in the high-frequency limit. In this regime, we studied fluctuations around the antiferromagnetic saddle point, and saw a simple example of "Floquet-engineering", i.e. how the magnon dispersion could be tuned with the electric field. More importantly, we found a highly non-thermal distribution of collective mode excitations, which highlights the importance of how a radiation field may change the distribution of excitations, and not only the Hamiltonian (which the above "Floquet-engineering" is an example of). The distribution of collective mode excitations can develop a (sub-)linear behavior as momentum tends towards the ordering wave vector, which may destabilize the order. This apparent dynamical phase transition as a function of drive amplitude requires further study. However, this also opens up for many other interesting questions to explore further, such as if anisotropic effects may stabilize order as in equilibrium [182], how different drive schemes affect the system, and if destabilization of antiferromagnetism signals stabilization of other types of ordering (see also the outlook in Sec. 6.7).

The assumption of a uniform electric field is a starting point which eases the theoretical analysis. How a spatially varying electric field would affect the system is an interesting and experimentally relevant question. A typical nearest-neighbor coupling $\tilde{t} \sim 1$ eV [194] corresponds to a light-wave frequency in the order of 10^{14} Hz or a wavelength in the order of 1 μm. Indeed, in the experiment in Ref. [23] the strongly correlated material $La_{0.5}Sr_{1.5}MnO_4$ were perturbed with laser pulses with frequency in this order of magnitude, and electric field amplitudes reach up to the order of $10^8 - 10^9$ V/m [23] [195][21]. Having a vanishing spatial gradient of the electric field produced by a light-field would require that the length scale of the sample should be in the order of $10 - 10^2$ nm corresponding to $\sim 10^4 - 10^6$ lattice sites. In cold-atom experiments, collective emergent phenomena are observed in two-dimensional square lattices with as little as 80 sites [183]. Recently, there has also been quite an experimental progress in fabricating large arrays of quantum dots in InAs which makes up an artificial Fermi-Hubbard lattice with lattice spacing in the order of 50 nm. Here, system parameters such as the nearest-neighbor coupling can be more easily tuned with the fabrication to match relevant energy scales of, e.g., the homogeneous fields produced in parallel plate capacitors, and it could be an interesting platform to study the effect of a periodic drive.

6.7 Outlook: Phases induced by a periodic drive

Guided by our knowledge in equilibrium, we have focused on the antiferromagnetic saddle-point configuration and studied some of its properties when driven out of equilibrium by a periodic drive. However, as formulated by Aoki et. al. an interesting step would be to "stabilize otherwise unstable

[21] It is interesting to note that assuming a lattice spacing of $a \sim 1$ Å [196], the breakdown of antiferromagnetism reported in Ref. [23] occurs at $eEa/(\hbar\omega) \sim 0.1$ (estimated), i.e. the same ratio as where the inverse distribution in Fig. 6.8a becomes linear. This is merely a remark on magnitudes of the fields, and any connection of mechanisms would require much further analysis.

many-body states by a continuous driving and thus design material properties by external modulations" [125]. A static non-equilibrium drive was found to induce exotic magnetic (in the sense not ferro- or antiferromagnetic) phases in a 1D Hubbard chain driven out of equilibrium by coupling the endpoints to metallic reservoirs at different electrochemical potentials [186]. Furthermore, an intense electric field pulse was found to drive a transient change from antiferromagnetic to anisotropic ferromagnetic correlations [197].

In general, it is no easy task to identify novel stable phases of strongly correlated materials brought out of equilibrium. However, one approach is to study the dominating fluctuations around the disordered state, similar to the discussion in Sec. 6.5.1 for the two-dimensional square lattice in the non-driven limit.

6.7.1 Bare fluctuations in the periodically driven level

To sketch the idea, we will consider the simple (yet non-trivial) model of a periodically driven level discussed in Sec. 5.2, which when including Coulomb-interactions, is the famous Anderson model. Indeed, the Anderson model is of major importance in condensed-matter physics for describing magnetic impurities in metals and the Kondo effect. Also on a methodological level, the Anderson model constitutes a key element in dynamical mean field theory (DMFT).

In equilibrium, it is well-known that saddle-point theory for the Anderson impurity can give a magnetic solution. This is physically meaningful for the situation with many magnetic impurities in a metal, but not for a single impurity [31]. Nevertheless, since we can actually obtain some analytical results (which are scarce in the non-equilibrium world), let us continue with a discussion of fluctuations in the driven Anderson model as a precursor for future work beyond the single level (where mean-field theory become more applicable). In particular, we are interested in the fluctuations around the disordered state, i.e. how the system would like to respond to a small perturbation. In analogy with our discussion in Sec. 6.5.1, we consider the retarded bare bubble

$$\Xi^R(t,t') = \frac{i}{2}\Big(G^R(t,t')G^K(t',t) + G^K(t,t')G^A(t',t)\Big), \tag{6.77}$$

where the bare Green functions are given as in Sec. 5.2, and we have traced out the spin-degree of freedom. Transforming to Floquet Green functions, we get

$$\Xi^R_{mn}(\omega) = \frac{i}{2}\sum_{m'}\int_{-\infty}^{\infty}\frac{d\omega'}{2\pi}\Big(G^R_{mm'}(\omega')G^K_{m'n}(\omega'-(\omega+n\Omega)) + G^K_{mm'}(\omega')G^A_{m'n}(\omega'-(\omega+n\Omega))\Big), \tag{6.78}$$

where the retarded and advanced Green functions are given by Eq. (5.22), and the Keldysh Green function is given similar to Eq. (5.33) but with Keldysh self-energy from Eq. (5.32). Hence, inserting the retarded, advanced, and Keldysh Green functions we obtain

$$\Xi^R_{mn}(\omega) = \Gamma\sum_{abc} J_{m+a}\left(\frac{E}{\Omega}\right)J_{a+b}\left(\frac{E}{\Omega}\right)J_{b+c}\left(\frac{E}{\Omega}\right)J_{c+n}\left(\frac{E}{\Omega}\right)g_{abc}(\omega+n\Omega), \tag{6.79}$$

where

$$\begin{aligned} g_{abc}(\omega) = \int\frac{d\omega'}{2\pi}\Bigg(&\frac{\tanh\left(\frac{\beta}{2}(\omega'-\omega+b\Omega-\mu)\right)}{(\omega'-\omega-(\epsilon_0+a\Omega)+i\Gamma)(\omega'-\omega-(\epsilon_0+c\Omega)-i\Gamma)(\omega'-(\epsilon_0+a\Omega)+i\Gamma)} \\ &+\frac{\tanh\left(\frac{\beta}{2}(\omega'+b\Omega-\mu)\right)}{(\omega'-(\epsilon_0+a\Omega)+i\Gamma)(\omega'-(\epsilon_0+c\Omega)-i\Gamma)(\omega'-\omega-(\epsilon_0+c\Omega)-i\Gamma)}\Bigg). \end{aligned} \tag{6.80}$$

Upon changing the integration variable, we get

$$g_{abc}(\omega) = \int \frac{d\omega'}{2\pi} \tanh\left(\frac{\beta}{2}(\omega'-\mu)\right) \frac{1}{(\omega' - (\epsilon_0 + (a+b)\Omega) + i\Gamma)(\omega' - (\epsilon_0 + (b+c)\Omega) - i\Gamma)} \times \left(\frac{1}{\omega' + \omega - (\epsilon_0 + (a+b)\Omega) + i\Gamma} + \frac{1}{\omega' - \omega - (\epsilon_0 + (b+c)\Omega) - i\Gamma}\right). \tag{6.81}$$

Writing $\tanh(x) = i(\psi^-(x) - \psi^+(x))/\pi$, $\psi^\pm(x) = \psi(1/2 \pm ix/\pi)$ where ψ is the digamma function, and using that $\psi^\pm$ has poles in the upper/lower complex half-plane, we can evaluate the integral using the residue theorem. With vanishing contribution from the semi-circle arcs, we obtain

$$\begin{aligned}\Xi^R_{mn}(\omega) = -\frac{\Gamma}{\pi}\sum_{abc} J_{m+a}\left(\frac{E}{\Omega}\right) J_{a+b}\left(\frac{E}{\Omega}\right) J_{b+c}\left(\frac{E}{\Omega}\right) J_{c+n}\left(\frac{E}{\Omega}\right) \frac{1}{(\omega + n\Omega)(\omega + (n+c-a)\Omega + 2i\Gamma)} \\ \times \left\{\psi^+\left(\frac{\beta}{2}\left(-i\Gamma + \epsilon_0 - \mu - \omega + (a+b-n)\Omega\right)\right) + \psi^-\left(\frac{\beta}{2}\left(i\Gamma + \epsilon_0 - \mu + \omega + (b+c+n)\Omega\right)\right)\right. \\ \left. -\psi^-\left(\frac{\beta}{2}\left(i\Gamma + \epsilon_0 - \mu + (b+c)\Omega\right)\right) - \psi^+\left(\frac{\beta}{2}\left(-i\Gamma + \epsilon_0 - \mu + (a+b)\Omega\right)\right)\right\}.\end{aligned} \tag{6.82}$$

In general, to study the dominating fluctuations we should consider the determinant of the inverse fluctuation propagator, similar to Sec. 6.5.1. However, as a first approximation for small interactions and drive amplitude, we approximate the critical interaction as

$$I_c^{-1} \simeq 2\Xi^R_{00}(0). \tag{6.83}$$

From Eq. (6.82), we obtain

$$\begin{aligned}\Xi^R_{00}(0) = \frac{i\beta\Gamma}{2\pi^2}\sum_{abc} J_a\left(\frac{E}{\Omega}\right) J_{a+b}\left(\frac{E}{\Omega}\right) J_{b+c}\left(\frac{E}{\Omega}\right) J_c\left(\frac{E}{\Omega}\right) \\ \times \frac{\psi_1^+\left(\frac{\beta}{2}\left(-i\Gamma + \epsilon_0 - \mu + (a+b)\Omega\right)\right) + \psi_1^-\left(\frac{\beta}{2}\left(i\Gamma + \epsilon_0 - \mu + (b+c)\Omega\right)\right)}{(c-a)\Omega + 2i\Gamma},\end{aligned} \tag{6.84}$$

where we have used that $\psi'(z) = \psi_1(z)$, with ψ_1 being the trigamma function, and have defined $\psi_1^\pm(x) = \psi_1(1/2 \pm ix/\pi)$. Using that $\psi_1(z) \to 1/z$ for $z \to \infty$ in $|\arg z| < \pi$ [184], we find in the zero-temperature limit

$$\Xi^R_{00}(0) \to \frac{\Gamma}{\pi}\sum_{abc} \frac{J_a\left(\frac{E}{\Omega}\right) J_{a+b}\left(\frac{E}{\Omega}\right) J_{b+c}\left(\frac{E}{\Omega}\right) J_c\left(\frac{E}{\Omega}\right)}{(\epsilon_0 - \mu + (a+b)\Omega - i\Gamma)(\epsilon_0 - \mu + (b+c)\Omega + i\Gamma)}. \tag{6.85}$$

The critical interaction from Eq. (6.83) with the zero-temperature limit of $\Xi^R_{00}(0)$ from Eq. (6.85) is shown in Fig. 6.10 as a function of drive amplitude (black solid line). For comparison, we also show the corresponding time-averaged mean-field solution as a density-plot. Furthermore, upon expanding $\Xi^R_{00}(0)$ from Eq. (6.85) to fourth order in E/Ω, we get

$$\begin{aligned}\Xi^R_{00}(0) \approx \frac{\Gamma}{\pi((\epsilon_0-\mu)^2 + \Gamma^2)} + \frac{\Gamma}{4\pi}\left(-\frac{2}{(\epsilon_0-\mu)^2+\Gamma^2} + \sum_{p=\pm}\frac{1}{(\epsilon_0 - \mu + p\Omega)^2 + \Gamma^2}\right)\left(\frac{E}{\Omega}\right)^2 \\ + \frac{\Gamma}{64\pi}\left(\frac{6}{(\epsilon_0-\mu)^2+\Gamma^2} - \sum_{p=\pm}\frac{4}{(\epsilon_0-\mu+p\Omega)^2+\Gamma^2} + \sum_{p=\pm}\frac{1}{(\epsilon_0-\mu+2p\Omega)^2+\Gamma^2}\right)\left(\frac{E}{\Omega}\right)^4.\end{aligned} \tag{6.86}$$

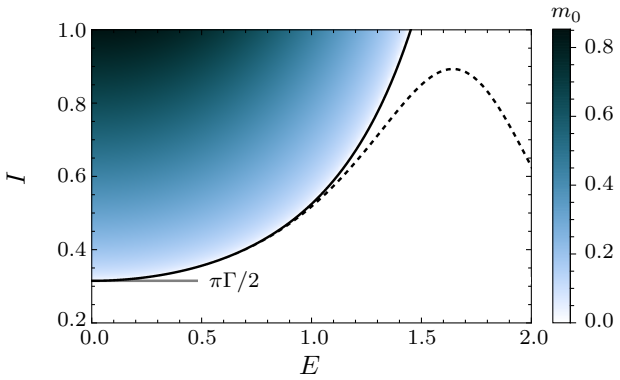

Figure 6.10: The critical interaction from Eq. (6.83) with the zero-temperature limit of $\Xi^R_{00}(0)$ from Eq. (6.85) (Eq. (6.86)) as a function of drive amplitude is shown with black solid (dashed) line. For comparison, the corresponding time-averaged saddle-point solution is shown on top in a density-plot. Parameters: $\Omega = 1.0$, $\Gamma = 0.2$, $\epsilon_0 = \mu = 0$.

The corresponding approximate critical interaction is shown in Fig. 6.10 (dashed curve), and is seen to agree well with the solid curve for sufficiently small drive amplitude. In particular, the first term in Eq. (6.86) gives the equilibrium critical interaction, which is marked in Fig. 6.10 with a gray line. Importantly, as the results illustrate, an analysis of the bare fluctuations give valuable insight into the onset of non-zero saddle-point configurations also out of equilibrium, for small interactions and drive amplitudes. This becomes particularly interesting when moving beyond the single level where the order parameter may acquire novel spatial 'patterns' similar to Ref. [186]. Our preliminary work in this direction contain an analysis similar to Ref. [198] as an initial step, and we confirm that we reproduce their Fig. 7(a) with our setup. Relating this analysis to saddle-point configurations and fluctuations is an interesting problem for our future research.

7 | Conclusion and outlook

In this thesis, we have studied a selection of steady-state phenomena in interacting nanostructured and low-dimensional condensed-matter systems out of equilibrium. In particular, we considered two main lines of research; 1) transport effects in two different nanostructures (Coulomb-coupled quantum dots and a Cooper pair splitter), and 2) periodically driven low-dimensional systems, focusing in particular on the periodically driven single level and itinerant antiferromagnetism in the periodically driven two-dimensional Hubbard model.

The first part of the thesis was motivated by the enhanced control of transport processes in nanostructures, which has inspired the engineering of nanostructure devices with tailored properties. In particular, the discrete energy levels in quantum dots provide energy-selective filters which have been explored for thermoelectric applications in various setups. In our first encounter of transport effects in Sec. 3.1, which described the works in publication I, we studied thermoelectric effects in a nanostructure with Coulomb-coupled quantum dots. In particular, we considered a three-terminal configuration [14] where the inter-dot Coulomb coupling mediates an energy exchange between two otherwise decoupled systems, whereby the heat and charge transport becomes decoupled. We set up a master-equation with rates calculated from the T matrix (introduced in Ch. 2), which enabled us to discuss the contribution from higher-order cotunneling processes, and is applicable to the general case of energy-dependent lead couplings, applied biases, and temperature gradients in the system. Similarly to how energy-dependent lead couplings can be tuned to optimize heat to current conversion in the system [14], we demonstrated the strongly enhanced performance of the interdot-mediated cooling effect by tuning the energy-dependence of the lead couplings, and in particular, we discussed the limitations set by cotunneling processes in such performance optimization, which reduce the cooling effect since cotunneling processes do not share the delicate energy selectivity inherent to sequential tunneling processes.

In Sec. 3.2, which described the works in publication II and IV, we discussed transport characteristics of a Cooper pair splitter [12, 13]. The device has received significant attention in the literature as a source of split spin-entangled electron pairs relevant for electron entanglement experiments. We considered the case of unidirectional transport where Cooper pairs originating from a superconductor (in the large gap limit) are split into spatially separated quantum dots and further on collected into separate normal-metal drains. In this case we set up a Gurvitz-Prager-like master equation [43, 32] (formulated in terms of the reduced density matrix in Sec. 2.3), from which we obtained results for transport statistics such as the current (which reduced to well-known results in certain limits [13, 43]), finite-frequency noise, and the distribution of electron waiting times between tunneling events. The latter provides a fairly direct view into the governing transport processes and the non-local nature of Cooper pair splitting. This is revealed by a large peak at short times in the WTD for tunneling into different leads, in contrast to the suppressed WTD for tunneling into the same lead. When the couplings to the collector leads are larger than the amplitudes for Cooper pair splitting, a short waiting time between electrons tunneling into different leads is associated with a fast emission of a split Cooper pair, while long waiting times are governed by the slow coherent injection of Cooper pairs from a superconductor. Although the ideal working regime considered in this study allowed us to obtain analytical results, in future work it would be useful to relax the assumptions to obtain an even

more realistic model relevant for comparison with experiments. As an outlook, we also discussed how one may dynamically control the splitting of Cooper pairs. On a theoretical level, the Gurvitz-Prager master equation is a highly applied approach to study unidirectional transport in nanostructures, and for future work on dynamically driven nanostructured devices such as a dynamically driven Cooper pair splitter, it would be valuable to generalize Gurvitz and Prager's results to periodically driven systems.

In Ch. 4 we introduced the methodology of non-equilibrium Green functions, which we used to study periodically driven systems in the second part of the thesis. We introduced the Floquet non-equilibrium Green functions and gained some initial insights into periodically driven systems by considering the periodically driven single level and square-lattice in Ch. 5. In particular, for the former, we showed an explicit example of how a non-equilibrium steady state can be reached in the long-time limit after an external drive has been turned on by comparing analytical results for the non-equilibrium steady-state limit with a numerical time-dependent simulation[1].

In Ch. 6 we studied the two-dimensional square lattice Hubbard model driven by a time-periodic electric field. Guided by our knowledge in equilibrium, we performed a mean-field analysis around the antiferromagnetic saddle point as well as a study of the fluctuations in magnetization, and discussed how the equilibrium properties changed when driving the system out of equilibrium. When the drive frequency approaches the charge gap, we found that the mean-field order parameter can develop a rich dynamical behavior in the non-equilibrium steady state, and we saw examples of the evolution towards the steady-state behavior by comparing to a time-dependent simulation[1]. We focused in particular on the high-frequency regime where the mean-field behavior is more equilibrium-like, and studied the fluctuations around the antiferromagnetic saddle-point. Here, we saw a simple example of 'Floquet engineering', i.e. of how the periodic drive can tune the magnon spectrum. By comparing to results obtained in equilibrium, we could assign this behavior to a renormalization of the hopping parameter. We furthermore went beyond this ('Floquet-engineering') discussion of the change of magnon spectrum, and also discussed the distribution of magnons. We found a highly excited, generically non-thermal distribution even for drive frequencies far above the gap. At a critical drive amplitude, the low-energy distribution diverged linearly as the frequency tends to zero with a large effective temperature which may destroy antiferromagnetism in the two-dimensional lattice, similar to the Hohenberg-Mermin-Wagner result in equilibrium. This apparent dynamical phase transition as a function of drive amplitude requires further study, however, it shows the importance of collective mode excitations arising from a non-equilibrium drive, and the delicate balance in engineering material properties by a periodic drive. We highlighted many possible extensions to the analysis of this challenging problem, including a discussion of the role of a spatially varying drive field and anistropy effects. Furthermore, whereas we focused on itinerant antiferromagnetism, it is highly interesting to study the possibility of other orderings induced by a non-equilibrium drive. For instance, does the dynamical behavior in the antiferromagnetic mean-field signal a preference towards another ordering? Indeed, as an outlook, we discussed how fluctuations around the disordered state can provide valuable information into the onset of non-zero saddle-point configurations, in particular focusing on the periodically driven single level, where we could obtain analytical results. In future work, it is interesting to generalize this study to lattice systems with different drive schemes. Another interesting route for future research is to consider a Floquet-Keldysh renormalization group study of the system. We note that in such an analysis, we have to deal with a term as represented by the rightmost diagram in the sum of diagrams on p. 65. However, to make any analytical progress we have to make some significant simplications of the diagram, where justifications of spatial and temporal approximations even in the un-driven case is not trivial [121].

There is indeed many interesting routes to pursue from here, and we can only speculate about the fascinating phenomena that Nature may still reveal out of equilibrium.

[1] In Ch. 5, the time-dependent simulation was performed by R. S. Souto, and in Ch. 6, the time-dependent simulation was performed by D. M. Kennes.

A | Appendix

A.1 Derivation of the T-matrix transition rates

In this appendix, we derive the T-matrix transition rates, or the generalized Fermi's golden rule, introduced in Sec. 2.1 in the main text. The derivation can also be found, for example, in Refs. [31, 33], however, is included here for completeness. In particular, the following derivation follows similar steps as in Ref. [33]. .

To derive the T-matrix transition rates, it is convenient to consider the projection operators introduced in Eq. (2.3) in the main text. The projectors satisfy

$$\mathcal{P}^2 = \mathcal{P}, \quad \mathcal{Q}^2 = \mathcal{Q}, \quad \mathcal{P}\mathcal{Q} = \mathcal{Q}\mathcal{P} = 0, \quad [\mathcal{P}, \mathcal{L}_0] = 0, \quad \mathcal{P}\mathcal{L}_T\mathcal{P} = 0, \tag{A.1}$$

where we have defined the sub-Liouvillians,

$$\mathcal{L} = \mathcal{L}_0 + \mathcal{L}_T, \qquad \mathcal{L}_0[\,\bullet\,] = -\frac{i}{\hbar}[\hat{H}_0,\,\bullet\,], \qquad \mathcal{L}_T[\,\bullet\,] = -\frac{i}{\hbar}[\hat{H}_T,\,\bullet\,], \tag{A.2}$$

corresponding to the system defined in Ch. 2. The first three identities in (A.1) follow from $\mathrm{Tr}[\hat{A}\otimes\hat{B}] = \mathrm{Tr}[\hat{A}]\mathrm{Tr}[\hat{B}]$ and the normalization condition $\mathrm{Tr}_E[\hat{\rho}_E] = 1$, the fourth identity follows by letting $\hat{H}_0$ act on a complete set of eigenstates, and the rightmost identity follows upon taking Tr_E since we consider tunneling Hamiltonians $\hat{H}_T$ which changes the particle number in E. For a time-independent $\hat{H}_0$ it is convenient to transform to an *interaction picture*

$$\hat{\rho}^i(t) \equiv e^{-\mathcal{L}_0 t}\hat{\rho}(t) = Te^{\int_{t_0}^{t} dt' \mathcal{L}_T^i(t')}\hat{\rho}^i(t_0), \quad \mathcal{L}_T^i(t)[\,\bullet\,] \equiv -\frac{i}{\hbar}[\hat{H}_T^i(t),\,\bullet\,], \tag{A.3}$$

where $\hat{H}_T^i(t) = e^{\frac{i}{\hbar}\hat{H}_0 t}\hat{H}_T e^{-\frac{i}{\hbar}\hat{H}_0 t}$.

We assume that the system is in a product state at time t_0 with S described by a diagonal reduced density operator, and the environment in thermal equilibrium by $\hat{\rho}_E^{\mathrm{eq}}$, i.e. $\mathcal{Q}\hat{\rho}(t_0) = 0$. Hence,

$$\mathcal{P}\hat{\rho}^i(t) = \mathcal{P}Te^{\int_{t_0}^{t} dt' \mathcal{L}_T^i(t')e^{\eta t'/\hbar}}\mathcal{P}\hat{\rho}^i(t_0), \tag{A.4}$$

where have used that $[\mathcal{L}_0, \mathcal{P}] = 0$. Furthermore, we have turned on the tunneling Hamiltonian adiabatically by $\hat{H}_T \to \hat{H}_T e^{\eta t/\hbar}$, with η being small and positive. We take $\eta \to 0^+$ in the end of the derivation. Taking the time-derivative we get

$$\frac{d}{dt}\mathcal{P}\hat{\rho}^i(t) = \mathcal{P}\mathcal{L}_T^i(t)e^{\eta t/\hbar}Te^{\int_{t_0}^{t} dt' \mathcal{L}_T^i(t')e^{\eta t'/\hbar}}\mathcal{P}\hat{\rho}^i(t_0). \tag{A.5}$$

Transforming back from the interaction picture this reads

$$\frac{d}{dt}\mathcal{P}\hat{\rho}(t) = \mathcal{R}(t, t_0)\mathcal{P}\hat{\rho}(t_0), \tag{A.6}$$

where

$$\begin{aligned}\mathcal{R}(t,t_0)[\,\bullet\,] &\equiv \mathcal{P}e^{\mathcal{L}_0 t}\mathcal{L}_T^i(t)e^{\eta t/\hbar}Te^{\int_{t_0}^t dt'\mathcal{L}_T^i(t')e^{\eta t'/\hbar}}e^{-\mathcal{L}_0 t_0}\mathcal{P}[\,\bullet\,] \\ &= -\frac{i}{\hbar}\mathcal{P}\left[\hat{H}_T e^{\eta t/\hbar}, e^{\mathcal{L}_0 t}Te^{\int_{t_0}^t dt'\mathcal{L}_T^i(t')e^{\eta t'/\hbar}}e^{-\mathcal{L}_0 t_0}\mathcal{P}[\,\bullet\,]\right],\end{aligned} \tag{A.7}$$

and we have used that $[\hat{H}_0, \mathcal{P}\rho(t)] = 0$.

To construct a master equation, we consider the rate of change of the probability p_f of being in the final eigenstate $|f\rangle$ of $\hat{H}_0$, $\mathcal{P}\hat{\rho}(t) = |f\rangle\langle f|$, given that $\mathcal{P}\hat{\rho}(t_0) = |i\rangle\langle i|$ ($|i\rangle$ also being an eigenstate of $\hat{H}_0$). However, as mentioned in the main text, to derive Fermi's generalized golden rule [31] one assumes that the rate of transition from the state $|i\rangle$ is at the *present time* t [33]. As a consequence one has to apply a regularization procedure [37, 38] for tunneling rates above first order. With this in mind, we define the (unregularized) transition rates

$$\begin{aligned}\tilde{\Gamma}_{if} &\equiv \langle f|\{\mathcal{R}(t,t_0)[|i\rangle\langle i|]\}|f\rangle \\ &= -\frac{i}{\hbar}\langle f|\left[\hat{H}_T e^{\eta t/\hbar}, e^{\mathcal{L}_0 t}Te^{\int_{t_0}^t dt'\mathcal{L}_T^i(t')e^{\eta t'/\hbar}}e^{-\mathcal{L}_0 t_0}|i\rangle\langle i|\right]|f\rangle,\end{aligned} \tag{A.8}$$

where we have omitted the now unnecessary projectors (due to the choice of initial and final states). Using that $e^{-\mathcal{L}_0 t_0}|i\rangle\langle i| = |i\rangle\langle i|$, we can rewrite this as

$$\begin{aligned}\tilde{\Gamma}_{if} &= -\frac{i}{\hbar}\langle f|\left[\hat{H}_T e^{\eta t/\hbar}, e^{-\frac{i}{\hbar}\hat{H}_0 t}\left\{Te^{\int_{t_0}^t dt'\mathcal{L}_T^i(t')e^{\eta t'/\hbar}}|i\rangle\langle i|\right\}e^{\frac{i}{\hbar}\hat{H}_0 t}\right]|f\rangle \\ &= -\frac{i}{\hbar}\langle f|\left[\hat{H}_T^i e^{\eta t/\hbar}, \left\{Te^{\int_{t_0}^t dt'\mathcal{L}_T^i(t')e^{\eta t'/\hbar}}|i\rangle\langle i|\right\}\right]|f\rangle \\ &= -\frac{i}{\hbar}\langle f|\left[\hat{H}_T^i e^{\eta/\hbar t}, Te^{-\frac{i}{\hbar}\int_{t_0}^t dt'\hat{H}_T^i(t')e^{\eta/\hbar t'}}|i\rangle\langle i|\bar{T}e^{\frac{i}{\hbar}\int_{t_0}^t dt'\hat{H}_T^i(t')e^{\eta t'/\hbar}}\right]|f\rangle,\end{aligned} \tag{A.9}$$

where we have acted with $\hat{H}_0$ on the final bra and ket to rearrange terms. We may furthermore write this as [33]

$$\begin{aligned}\tilde{\Gamma}_{if} &= \frac{d}{dt}\langle f|Te^{-\frac{i}{\hbar}\int_{t_0}^t dt'\hat{H}_T^i(t')e^{\eta t'/\hbar}}|i\rangle\langle i|\bar{T}e^{\frac{i}{\hbar}\int_{t_0}^t dt'\hat{H}_T^i(t')e^{\eta t'/\hbar}}|f\rangle \\ &= \frac{d}{dt}\left|\langle f|Te^{-\frac{i}{\hbar}\int_{t_0}^t dt'\hat{H}_T^i(t')e^{\eta t'/\hbar}}|i\rangle\right|^2 \\ &= \frac{d}{dt}\left|\langle f|1 + \frac{1}{i\hbar}\int_{t_0}^t dt_1\hat{H}_T^i(t_1)e^{\eta t_1/\hbar} + \frac{1}{(i\hbar)^2}\int_{t_0}^t dt_1\int_{t_0}^{t_1}dt_2\hat{H}_T^i(t_1)e^{\eta t_1/\hbar}\hat{H}_T^i(t_2)e^{\eta t_2/\hbar} + \cdots|i\rangle\right|^2\end{aligned} \tag{A.10}$$

Letting $t_0 \to -\infty$ and changing variables $\tau_1 = t - t_1$, $\tau_\mu = t_{\mu-1} - t_\mu$, $\mu > 1$, we find

$$\begin{aligned}\tilde{\Gamma}_{if} = \frac{d}{dt}\Bigg|&\langle f|1 + \frac{1}{i\hbar}e^{\frac{i}{\hbar}\hat{H}_0 t}\int_0^\infty d\tau_1 e^{-\frac{i}{\hbar}\hat{H}_0\tau_1}\hat{H}_T e^{\eta(t-\tau_1)/\hbar}e^{-\frac{i}{\hbar}\hat{H}_0(t-\tau_1)} + \\ &\frac{1}{(i\hbar)^2}e^{\frac{i}{\hbar}\hat{H}_0 t}\int_{t_0}^t d\tau_1\int_{t_0}^{t_1}d\tau_2 e^{-\frac{i}{\hbar}\hat{H}_0\tau_1}\hat{H}_T e^{\eta(t-\tau_1)/\hbar}e^{-\frac{i}{\hbar}\hat{H}_0\tau_2}\hat{H}_T e^{-\frac{i}{\hbar}\hat{H}_0(t-\tau_1-\tau_2)}e^{\eta(t-\tau_1-\tau_2)/\hbar} + \cdots|i\rangle\Bigg|^2 \\ = \frac{d}{dt}\Bigg|&\langle f|\sum_{\mu=1}^\infty\left(\frac{1}{i\hbar}\right)^\mu e^{\frac{i}{\hbar}\hat{H}_0 t}\int_0^\infty d\tau_1\int_0^\infty d\tau_2\cdots\int_0^\infty d\tau_\mu e^{-\frac{i}{\hbar}\hat{H}_0\tau_1}\hat{H}_T e^{-\frac{i}{\hbar}\hat{H}_0\tau_2}\hat{H}_T\cdots e^{-\frac{i}{\hbar}\hat{H}_0\tau_\mu}\hat{H}_T \\ &\times e^{-\frac{i}{\hbar}\hat{H}_0(t-\tau_1-\tau_2-\cdots-\tau_\mu)}e^{\eta(\mu t-\mu\tau_1-(\mu-1)\tau_2-\cdots-\tau_\mu)/\hbar}|i\rangle\Bigg|^2,\end{aligned} \tag{A.11}$$

where we have assumed that $\langle f|i\rangle = 0$. Carrying out the integrals and taking the complex transpose inside the absolute square we find

$$\tilde{\Gamma}_{if} = \frac{d}{dt}\left|\sum_{\mu=1}^{\infty} e^{\mu\eta t/\hbar}\langle i|\hat{H}_T\frac{1}{E_i-\hat{H}_0-i\eta}\cdots\hat{H}_T\frac{1}{E_i-\hat{H}_0-i(\mu-1)\eta}\hat{H}_T\frac{1}{E_i-E_f-i\mu\eta}|f\rangle\right|^2, \quad \text{(A.12)}$$

where we have used the notation $1/\hat{O} = \hat{O}^{-1}$. Finally, taking the derivative

$$\begin{aligned}\tilde{\Gamma}_{if} = \sum_{\mu,\nu=1}^{\infty}\frac{(\mu+\nu)\frac{\eta}{\hbar}e^{(\mu+\nu)\eta t/\hbar}}{(E_i-E_f-i\mu\eta)(E_i-E_f+i\nu\eta)}\langle i|\hat{H}_T\frac{1}{E_i-\hat{H}_0-i\eta}\cdots\hat{H}_T\frac{1}{E_i-\hat{H}_0-i(\mu-1)\eta} \\ \times\hat{H}_T|f\rangle\langle f|\hat{H}_T\frac{1}{E_i-\hat{H}_0+(\nu-1)\eta}\hat{H}_T\cdots\frac{1}{E_i-\hat{H}_0+i\eta}\hat{H}_T|i\rangle,\end{aligned} \quad \text{(A.13)}$$

and using that

$$\begin{aligned}\frac{(\mu+\nu)\eta}{(E_i-E_f-i\mu\eta)(E_i-E_f+i\nu\eta)} &= -i\left(\frac{1}{E_i-E_f-i\mu\eta}-\frac{1}{E_i-E_f+i\nu\eta}\right) \\ &\to 2\pi\delta(E_i-E_f) \text{ for } \eta\to 0^+,\end{aligned} \quad \text{(A.14)}$$

we find when letting $\eta \to 0^+$ [33]

$$\tilde{\Gamma}_{if} = \frac{2\pi}{\hbar}\delta(E_i-E_F)\left|\langle f|\sum_{\mu=0}^{\infty}\hat{H}_T\left(\frac{1}{E_i-\hat{H}_0+i0^+}\hat{H}_T\right)^{\mu}|i\rangle\right|^2. \quad \text{(A.15)}$$

Expressed in terms of the so-called T matrix, we obtain the Fermi's generalized golden rule in Eq. (2.6) in the main text.

A.2 Cotunneling

In this appendix, we provide additional information on cotunneling processes relevant for the study in Sec. 3.1 in the main text.

A.2.1 Cotunneling rates

The content in this section is published in Publication I. We here list the remaining cotunneling processes (that is not written explicitly in Sec. 3.1.1) relevant for the system studied in Sec. 3.1.

The rate for elastic cotunneling through a single-level QD is given by

$$\tilde{\Gamma}^{\overrightarrow{\ell}\,\overleftarrow{\ell'}}_{mm} = \int\frac{d\epsilon}{2\pi\hbar}\tilde{\gamma}^{\ell}(\epsilon)\tilde{\gamma}^{\ell'}(\epsilon)n_{F,\ell}(\epsilon)\bar{n}_{F,\ell'}(\epsilon)\left|\frac{1}{\Delta_{vm}\pm\epsilon+i\eta}\right|^2, \quad \text{(A.16)}$$

where v refers to the virtually occupied intermediate state created in the process where an initially empty level is filled ($+\epsilon$) or an initially filled level is emptied ($-\epsilon$).

In pair-cotunneling processes, two electrons tunnel simultaneously out of (into) the QD system and into (out of) the leads ℓ and ℓ'. The rate for such processes takes the form

$$\tilde{\Gamma}^{\overleftarrow{\ell}\,\overleftarrow{\ell'}}_{mn} = \int\frac{d\epsilon}{2\pi\hbar}\tilde{\gamma}^{\ell}(\epsilon)\tilde{\gamma}^{\ell'}(\Delta_{nm}-\epsilon)\bar{n}_{F,\ell}(\epsilon)\bar{n}_{F,\ell'}(\Delta_{nm}-\epsilon)\left|\frac{1}{\Delta_{vm}-\epsilon+i\eta}+\frac{1}{\Delta_{v'n}+\epsilon+i\eta}\right|^2, \quad \text{(A.17)}$$

where v (v') refers to the virtually occupied intermediate state in a process where an electron initially tunnels from the QD system and into lead ℓ (ℓ'). Similarly,

$$\tilde{\Gamma}^{\overrightarrow{\ell}\,\overrightarrow{\ell}'}_{mn} = \int \frac{d\epsilon}{2\pi\hbar} \tilde{\gamma}^{\ell}(\epsilon)\tilde{\gamma}^{\ell'}(\Delta_{mn}-\epsilon) n_{F,\ell}(\epsilon) n_{F,\ell'}(\Delta_{mn}-\epsilon) \left| \frac{1}{\Delta_{vn}-\epsilon+i\eta} + \frac{1}{\Delta_{v'm}+\epsilon+i\eta} \right|^2, \tag{A.18}$$

where v (v') refer to the virtually occupied intermediate state in a process where an electron initially tunnels from lead ℓ' (ℓ) and into the QD system.

A.2.2 Cotunneling integrals

The content in this section is published in Ref. [50] with notation adapted to Publication I.

In this appendix, we provide analytical results for the cotunneling integrals presented in Sec. 3.1.1 in the main text for the case of uniform temperature. The derivation follows a procedure similar to Ref. [62]. We first rewrite the Fermi-Dirac functions in terms of digamma functions ψ,

$$n_{F,\ell/\ell'}(\epsilon) = \frac{1}{2}\left[1 - \tanh\left(\frac{\beta(\epsilon-\mu_{\ell/\ell'})}{2}\right)\right] = \frac{1}{2}\left[1 + \frac{i}{\pi}\left(\psi^{+}_{\ell/\ell'}(\epsilon) - \psi^{-}_{\ell/\ell'}(\epsilon)\right)\right], \tag{A.19}$$

where

$$\psi^{\pm}_{\ell/\ell'}(\epsilon) \equiv \psi\left(\frac{1}{2} \pm i\frac{\beta}{2\pi}(\epsilon-\mu_{\ell/\ell'})\right), \tag{A.20}$$

and we have used that $\mathrm{Im}\{\psi(1/2+iy)\} = \pi\tanh(\pi y)/2$, and $\psi(z)^* = \psi(z^*)$ [184]. The digamma functions $\psi^{\pm}_{\ell/\ell'}(z)$ have poles at $z^{\pm}_{\ell/\ell',n} = \mu_{\ell/\ell'} \pm i2\pi(n+1/2)/\beta$ for $n \in \mathbb{N}^+$ where $\psi^{\pm}_{\ell/\ell'}(z^{\pm}_{\ell/\ell',n}) = \psi(-n)$. Hence, $\psi^{+}_{\ell/\ell'}$ and $\psi^{-}_{\ell/\ell'}$ have poles in the upper and lower half-planes, respectively. Thus by introducing digamma functions we can choose contours which avoid the poles of these. We therefore write the integral in Eq. (3.17) as $I = I^+ - I^-$, where

$$I^{\pm} = \frac{i}{2\pi}\int_{-\infty}^{\infty} \mathrm{d}\epsilon\; P(\epsilon)\left[\psi^{\pm}_{\ell'}(\epsilon) - \psi^{\pm}_{\ell}(\epsilon+\Delta)\right]\left|\frac{c_1}{\epsilon-\Delta_1+i\eta} + \frac{c_2}{\Delta_2-\epsilon+i\eta}\right|^2. \tag{A.21}$$

Notice that in order to split up the integral into two as above, we assume that $I^{\pm}$ converges. We will check the conditions for convergence in the end, however, if they do not converge, we cannot use this trick of choosing convenient contours which avoid the poles of the digamma functions.

To evaluate the integral using the residue theorem, we consider the contour integral over the complex variable z

$$I^{\pm}_{\mathcal{C}_{\mp}} = \frac{i}{2\pi}\oint \mathrm{d}z\; P(z)\left[\psi^{\pm}_{\ell'}(z) - \psi^{\pm}_{\ell}(z+\Delta)\right] Z(z) = \mp I^{\pm} + I^{\pm}_{\mathcal{C}_{R\mp}}, \tag{A.22}$$

where the contours $\mathcal{C}_{\pm}$ are defined in Fig. A.1, $\mathcal{C}_{R\mp}$ are the contributions from the semi-circle arcs, and

$$\begin{aligned} Z(z) \equiv\; & \frac{c_1^2}{(z-\Delta_1+i\eta)(z-\Delta_1-i\eta)} - \frac{c_1c_2}{(z-\Delta_1+i\eta)(z-\Delta_2+i\eta)} \\ & - \frac{c_1c_2}{(z-\Delta_1-i\eta)(z-\Delta_2-i\eta)} + \frac{c_2^2}{(z-\Delta_2-i\eta)(z-\Delta_2+i\eta)}. \end{aligned} \tag{A.23}$$

Notice that we should write out the complex squared term in Eq. (A.21) before making the analytic continuation $\epsilon \to z$. The integral in Eq. (3.17) can then be written as

$$I = I^+ - I^- = -I^{+}_{\mathcal{C}_-} - I^{-}_{\mathcal{C}_+} + I^{+}_{\mathcal{C}_{R-}} + I^{-}_{\mathcal{C}_{R+}} = -I_{\mathcal{C}} + I^{+}_{\mathcal{C}_{R-}} + I^{-}_{\mathcal{C}_{R+}}, \tag{A.24}$$

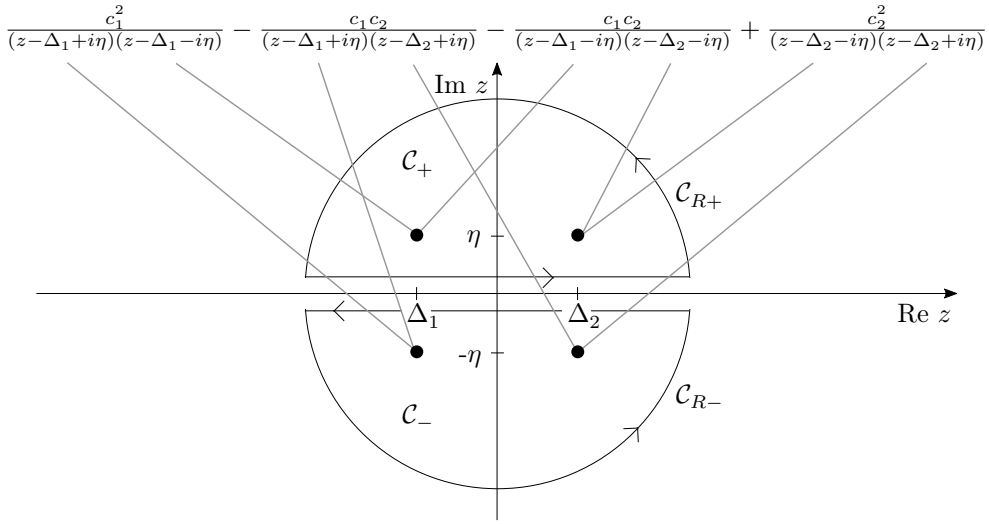

Figure A.1: Integration contours $\mathcal{C}_\pm$ for the contour integrals $I^\pm_{\mathcal{C}_\mp}$. The relevant poles to consider are illustrated as black points. Adapted from Ref. [50].

where we have defined $I_\mathcal{C} \equiv I^+_{\mathcal{C}_-} + I^-_{\mathcal{C}_+}$. We find the contribution to the integral from the residues. With the choice of contours we only have to consider the poles of $Z(z)$ cf. Fig. A.1 assuming that $P(z)$ has no poles. Since the function $Z(z)$ is already in a Laurent form, we can read off the residues, and hence when applying the residue theorem the contour integral becomes

$$\begin{aligned}
-I^\pm_{\mathcal{C}_\mp} =& P(\Delta_1 \mp i\eta)\left[\psi^\pm_{\ell'}(\Delta_1 \mp i\eta) - \psi^\pm_{\ell}(\Delta_1 \mp i\eta + \Delta)\right]\left[\frac{{c_1}^2}{\mp 2i\eta} - \frac{c_1c_2}{\Delta_1-\Delta_2}\right] \\
&+P(\Delta_2 \mp i\eta)\left[\psi^\pm_{\ell'}(\Delta_2 \mp i\eta) - \psi^\pm_{\ell}(\Delta_2 \mp i\eta + \Delta)\right]\left[\frac{{c_2}^2}{\mp 2i\eta} - \frac{c_1c_2}{\Delta_2-\Delta_1}\right].
\end{aligned} \tag{A.25}$$

Expanding in η, we find

$$\begin{aligned}
-I_\mathcal{C} =& c_1^2 P'(\Delta_1)\mathrm{Re}\left[\psi^-_{\ell'}(\Delta_1) - \psi^-_{\ell}(\Delta_1+\Delta)\right] + \frac{c_1^2\beta}{2\pi}P(\Delta_1)\mathrm{Im}\left[\psi^-_{1_{\ell'}}(\Delta_1) - \psi^-_{1_\ell}(\Delta_1+\Delta)\right] \\
&+c_2^2 P'(\Delta_2)\mathrm{Re}\left[\psi^-_{\ell'}(\Delta_2) - \psi^-_{\ell}(\Delta_2+\Delta)\right] + \frac{c_2^2\beta}{2\pi}P(\Delta_2)\mathrm{Im}\left[\psi^-_{1_{\ell'}}(\Delta_2) - \psi^-_{1_\ell}(\Delta_2+\Delta)\right] \\
&-\frac{2c_1c_2}{\Delta_1-\Delta_2}\left[P(\Delta_1)\mathrm{Re}\left[\psi^-_{\ell'}(\Delta_1) - \psi^-_{\ell}(\Delta_1+\Delta)\right] - P(\Delta_2)\mathrm{Re}\left[\psi^-_{\ell'}(\Delta_2) - \psi^-_{\ell}(\Delta_2+\Delta)\right]\right] \\
&+\mathcal{O}(\eta^{-1}) + \mathcal{O}(\eta),
\end{aligned} \tag{A.26}$$

where $\psi_1 = \mathrm{d}\psi(z)/\mathrm{d}z$ is the trigamma function, $\psi^\pm_{1_{\ell/\ell'}}(z) \equiv \psi_1(1/2 \pm i\beta(\epsilon - \mu_{\ell/\ell'})/(2\pi))$. We write the term $\mathcal{O}(\eta^{-1})$ which diverges in the limit $\eta \to 0$ explicitly below when discussing regularization, however, first we consider the contribution to the integral from the arcs by using the asymptotic expansion of the digamma function [184]

$$\lim_{|z|\to\infty}\psi(z) = \ln z - \frac{1}{2z} - \sum_{n=1}^{\infty}\frac{B_{2n}}{2nz^{2n}}, \qquad \text{for } |\arg z| < \pi, \tag{A.27}$$

where B_n are Bernoulli numbers. Hence,

$$\begin{aligned}\lim_{|z|\to\infty}\left[\psi^{\pm}_{\ell'}(z)-\psi^{\pm}_{\ell}(z+\Delta)\right] &\approx \ln\left(\frac{\frac{1}{2}\pm i\frac{\beta}{2\pi}(z-\mu_{\ell'})}{\frac{1}{2}\pm i\frac{\beta}{2\pi}(z+\Delta-\mu_{\ell})}\right)+\frac{\pm i\frac{\beta}{\pi}(\mu_{\ell}-\mu_{\ell'}-\Delta)}{[1\pm i\frac{\beta}{\pi}(z+\Delta-\mu_{\ell})][1\pm i\frac{\beta}{\pi}(z-\mu_{\ell'})]}\\ &=\ln\left(\frac{\frac{1}{2}\pm i\frac{\beta}{2\pi}(z+\Delta-\mu_{\ell})\pm i\frac{\beta}{2\pi}(\mu_{\ell}-\mu_{\ell'}-\Delta)}{\frac{1}{2}\pm i\frac{\beta}{2\pi}(z+\Delta-\mu_{\ell})}\right)\\ &\quad+\frac{\pm i\frac{\beta}{\pi}(\mu_{\ell}-\mu_{\ell'}-\Delta)}{[1\pm i\frac{\beta}{\pi}(z+\Delta-\mu_{\ell})][1\pm i\frac{\beta}{\pi}(z-\mu_{\ell'})]}\end{aligned} \tag{A.28}$$

which for large z becomes

$$\begin{aligned}\lim_{|z|\to\infty}\left[\psi^{\pm}_{\ell'}(z)-\psi^{\pm}_{\ell}(z+\Delta)\right] &\approx \ln\left(1+\frac{\mu_{\ell}-\mu_{\ell'}-\Delta}{z}\right)\mp i\frac{\pi}{\beta}\frac{\mu_{\ell}-\mu_{\ell'}-\Delta}{z^2}\\ &\approx \frac{\mu_{\ell}-\mu_{\ell'}-\Delta}{z},\qquad \mu_{\ell}-\mu_{\ell'}-\Delta\neq 0.\end{aligned} \tag{A.29}$$

When $\mu_{\ell}-\mu_{\ell'}-\Delta E=0$, the contribution decays even faster. The asymptotic expansion of Z is

$$\lim_{|z|\to\infty} Z(z)=\frac{(c_1-c_2)^2}{z^2},\quad c_1-c_2\neq 0. \tag{A.30}$$

From this we find when $z=Re^{i\theta}$, $\mathrm{d}z=iRe^{i\theta}d\theta$,

$$I_{\mathcal{C}_R}=I^{+}_{\mathcal{C}_{R-}}+I^{-}_{\mathcal{C}_{R+}}=\frac{(\mu_{\ell'}-\mu_{\ell}+\Delta)(c_1-c_2)^2}{2\pi}\int_0^{2\pi}\mathrm{d}\theta\frac{P(Re^{i\theta})}{R^2e^{2i\theta}}. \tag{A.31}$$

The integral is well-defined as long as $P(z)$ has order no higher than two for $c_1-c_2\neq 0$. Assuming that $P(z)=a_0+a_1z+a_2z^2$

$$I_{\mathcal{C}_R}=a_2(\mu_{\ell'}-\mu_{\ell}+\Delta)(c_1-c_2)^2,\quad c_1-c_2\neq 0. \tag{A.32}$$

When $c_1-c_2=0$ the asymptotic expansion of Z becomes[1]

$$\lim_{R\to\infty} Z(Re^{i\theta})=c_1^2\frac{(\Delta_1-\Delta_2)^2}{z^4},\quad z=Re^{i\theta},\quad c_1-c_2=0,\quad \Delta_1-\Delta_2\neq 0. \tag{A.33}$$

Hence, when $z=Re^{i\theta}$, $\mathrm{d}z=iRe^{i\theta}d\theta$

$$I_{\mathcal{C}_R}=\frac{(\mu_{\ell'}-\mu_{\ell}+\Delta)c_1^2(\Delta_1-\Delta_2)^2}{2\pi}\int_0^{2\pi}\mathrm{d}\theta\frac{P(Re^{i\theta})}{R^4e^{4i\theta}}. \tag{A.34}$$

Assuming that $P(z)=a_0+a_1z+a_2z^2+a_3z^3+a_4z^4$

$$I_{\mathcal{C}_R}=a_4(\mu_{\ell'}-\mu_{\ell}+\Delta)c_1^2(\Delta_1-\Delta_2)^2,\qquad c_1-c_2=0. \tag{A.35}$$

A.3 Cooper pair splitter: Effective Hamiltonian

The content in this section is published in Publication IV. In this appendix, we derive the effective Hamiltonian provided in Eq. (3.31) in the main text. We specify the full Hamiltonian of the Cooper pair splitter considered in Sec. 3.2:

$$\hat{H}=\hat{H}_{QD}+\hat{H}_{SC}+\hat{H}_{N}+\hat{H}_{T_S}+\hat{H}_{T_N}, \tag{A.36}$$

[1] We have used Mathematica to check these limits.

which describes the quantum dots, the superconductor, and the normal-metal leads, given by the first three terms, as well as the coupling between them given by the two tunneling Hamiltonians, $\hat{H}_{T_S}$ and $\hat{H}_{T_N}$, which we detail below. The superconductor is described by the BCS mean-field Hamiltonian in Eq. (3.30) in the main text. The Hamiltonian of the dots reads

$$\hat{H}_{QD} = \sum_{\ell\sigma} \epsilon_\ell \hat{d}^\dagger_{\ell\sigma} \hat{d}_{\ell\sigma} + \sum_{\ell} U_\ell \hat{n}_{\ell\uparrow} \hat{n}_{\ell\downarrow}, \tag{A.37}$$

where we have defined the operators $\hat{d}^\dagger_{\ell\sigma}$ and $\hat{d}_{\ell\sigma}$ that create and annihilate electrons with energy ϵ_ℓ and spin σ in the left or right quantum dot, $\ell = L, R$. Here, the on-site interaction on the dots is denoted by U_ℓ, and $\hat{n}_{\ell\sigma} \equiv \hat{d}^\dagger_{\ell\sigma} \hat{d}_{\ell\sigma}$ counts electrons on the dots with spin σ. The normal-state leads are described by the Hamiltonian

$$\hat{H}_N = \sum_{\ell k\sigma} \epsilon_{\ell k} \hat{c}^\dagger_{\ell k\sigma} \hat{c}_{\ell k\sigma}, \tag{A.38}$$

while the coupling between the quantum dots and the external reservoirs are given by the tunneling Hamiltonians

$$\hat{H}_{T_S} = \sum_{\ell q\sigma} \left(t_{S\ell q} \hat{a}^\dagger_{q\sigma} \hat{d}_{\ell\sigma} + \text{h.c.} \right) \tag{A.39}$$

and

$$\hat{H}_{T_N} = \sum_{\ell k\sigma} \left(t_{\ell k} \hat{c}^\dagger_{\ell k\sigma} \hat{d}_{\ell\sigma} + \text{h.c.} \right), \tag{A.40}$$

where $t_{S\ell q}$ and $t_{\ell k}$ are the tunneling amplitudes.

We consider the von Neumann equation for the density matrix $\hat{\rho}$ of the full system

$$i\hbar \frac{d}{dt} \hat{\rho}(t) = [\hat{H}, \hat{\rho}(t)]. \tag{A.41}$$

Here $\hat{H} = \hat{H}_0 + \hat{H}_{T_S}$ is the time-independent Hamiltonian, with $\hat{H}_{T_S}$ the Hamiltonian describing the tunneling between the QDs and the superconductor, and $\hat{H}_0$ is the remaining part of the Hamiltonian.

We derive the effective Hamiltonian in Eq. (3.31) in the limit of large superconducting gap and intra-dot Coulomb interaction. The latter limits the occupation of the QDs to at most one electron, whereby we can discard the interaction term in Eq. (A.37) and prevent double-occupancy in the density matrix.

By Laplace-transforming the density matrix as

$$\hat{\rho}(E) = \int_{t_0}^{\infty} dt \hat{\rho}(t) e^{\frac{i}{\hbar}(E+i\eta)(t-t_0)}, \tag{A.42}$$

we can formally rewrite the von Neumann equation as

$$(E + i\eta)\hat{\rho}(E) - i\hbar\hat{\rho}(t_0) = L_0\hat{\rho}(E) + L_{T_S}\hat{\rho}(E), \tag{A.43}$$

having defined $L_{0/T_S}[\,\cdot\,] = [\hat{H}_{0/T_S}, \,\cdot\,]$. We can write the solution as the geometric series

$$\hat{\rho}(E) = \big(W_0(E) + W_0(E)L_{T_S}W_0(E) + W_0(E)L_{T_S}W_0(E)L_{T_S}W_0(E) + \cdots\big) i\hbar\hat{\rho}(t_0), \tag{A.44}$$

where $W_0(E) = [E - L_0 + i\eta]^{-1}$. The superconductor is in thermal equilibrium, $\hat{\rho}(E) = \hat{\rho}_{\tilde{0}}(E) \otimes \hat{\rho}^{\text{eq}}_{SC}$, hence upon tracing out the superconductor we get to second order in L_{T_S}

$$\hat{\rho}_{\tilde{0}}(E) \approx \big(W_{\tilde{0}}(E) + W_{\tilde{0}}(E)\text{Tr}_{SC}\left[L_{T_S}W_0(E)L_{T_S}\hat{\rho}^{\text{eq}}_{SC}\right] W_{\tilde{0}}(E)\big) i\hbar\hat{\rho}_{\tilde{0}}(t_0), \tag{A.45}$$

where $\hat{H}_{\tilde{0}} = \hat{H}_0 - \hat{H}_{SC}$ in $W_{\tilde{0}}(E)$, and we have used that terms with an odd number of L_{T_S} vanish and that higher-order terms are suppressed in the large gap limit from $W_0(E)$. Similarly, upon expanding $\hat{\rho}_{\tilde{0}}(E) = (E + i\eta - L_{\tilde{0}} - \overline{\Sigma}_S)^{-1} i\hbar\hat{\rho}_{\tilde{0}}(t_0)$ to first order in $\hat{\overline{\Sigma}}_S$ [45], we recognize

$$\overline{\Sigma}_S = \text{Tr}_{SC}\left[\Sigma_S \hat{\rho}^{\text{eq}}_{SC}\right], \qquad \Sigma_S = L_{T_S}W_0(E)L_{T_S}. \tag{A.46}$$

Next, we introduce the Bogoliubov transformation, $\hat{\boldsymbol{\gamma}}_q^\dagger = (\hat{\gamma}_{q\uparrow}^\dagger, \hat{\gamma}_{-q\downarrow}) = \hat{\boldsymbol{a}}_q^\dagger \boldsymbol{U}_q^\dagger$, where $\hat{\boldsymbol{a}}_q^\dagger = (\hat{a}_{q\uparrow}^\dagger, \hat{a}_{-q\downarrow})$ and

$$\boldsymbol{U}_q^\dagger = \begin{pmatrix} u_q^* & v_q \\ -v_q^* & u_q \end{pmatrix}, \tag{A.47}$$

is a unitary matrix with $u_q = (1+\epsilon_q/E_q)^{1/2}/\sqrt{2}$ and $v_q = (1-\epsilon_q/E_q)^{1/2}/\sqrt{2}e^{i\theta_S}$ where $E_q = \sqrt{\epsilon_q^2 + |\Delta|^2}$ and θ_S is the phase of the superconductor. With this transformation, we get $\hat{H}_{SC} = \sum_{q\sigma} E_q \hat{\gamma}_{q\sigma}^\dagger \hat{\gamma}_{q\sigma}$ (plus a constant which does not contribute to the von Neumann equation), and the tunneling Hamiltonian (A.39) becomes

$$\hat{H}_{T_S} = \sum_{\xi=\pm,\ell q\sigma} \xi t_{S\ell q}^\xi \left(u_q^\xi \hat{\gamma}_{q\sigma}^\xi + \sigma v_q^{(-\xi)} \hat{\gamma}_{-q-\sigma}^{(-\xi)} \right) \hat{d}_{\ell\sigma}^\xi, \tag{A.48}$$

where we have defined $t_{S\ell q}^{(+)-} = t_{S\ell q}^{(\ )*}$, $u_q^{(+)-} = u_q^{(\ )*}$, $v_q^{(+)-} = v_q^{(\ )*}$, $\hat{\gamma}_{q\sigma}^{+(-)} = \hat{\gamma}_{q\sigma}^{\dagger(\ )}$, $\hat{d}_{\ell\sigma}^{(+)-} = \hat{d}_{\ell\sigma}^{(\ )\dagger}$. We can furthermore write L_{T_S} in the compact form

$$\tilde{L}_{T_S} = \sum_{\xi,\theta=\pm,\ell q\sigma} \xi t_{S\ell q}^\xi \left(u_q^\xi \Gamma_{q\sigma}^{\xi\theta} + \sigma v_q^{(-\xi)} \Gamma_{-q-\sigma}^{(-\xi)\theta} \right) D_{\ell\sigma}^{\xi\theta}, \tag{A.49}$$

where $\theta = \pm$ determines if the operator acts to the left $(+)$ or right $(-)$, for instance

$$\Gamma_{q\sigma}^{\xi+}\hat{\rho}(E) = \hat{\gamma}_{q\sigma}^\xi \hat{\rho}(E), \quad \Gamma_{q\sigma}^{\xi-}\hat{\rho}(E) = \hat{\rho}(E)\hat{\gamma}_{q\sigma}^\xi, \tag{A.50}$$

and

$$D_{\ell\sigma}^{\xi+}\hat{\rho}(E) = \hat{d}_{\ell\sigma}^\xi \hat{\rho}(E), \quad D_{\ell\sigma}^{\xi-}\hat{\rho}(E) = \hat{\rho}(E)\hat{d}_{\ell\sigma}^\xi. \tag{A.51}$$

With these transformations, we readily obtain

$$\Sigma_S = \sum_{\xi\theta\ell q\sigma} \sum_{\xi'\theta'\ell'q'\sigma'} \xi\xi' t_{S\ell q}^\xi t_{S\ell' q'}^{\xi'} D_{\ell'\sigma'}^{\xi'\theta'} \left(u_{q'}^{\xi'} \Gamma_{q'\sigma'}^{\xi'\theta'} + \sigma' v_{q'}^{(-\xi')} \Gamma_{-q'-\sigma'}^{(-\xi')\theta'} \right) W_0(E) D_{\ell\sigma}^{\xi\theta} \left(u_q^\xi \Gamma_{q\sigma}^{\xi\theta} + \sigma v_q^{(-\xi)} \Gamma_{-q-\sigma}^{(-\xi)\theta} \right), \tag{A.52}$$

where we have used the commutation relation $\Gamma^{\chi\theta} D^{\chi'\theta'} = -\theta\theta' D^{\chi'\theta'} \Gamma^{\chi\theta}$ (suppressing the subscripts). Having expressed the tunneling Hamiltonian in terms of the Bogoliubov transformation that diagonalizes the superconducting Hamiltonian, we have

$$\Gamma_{q\sigma}^{\xi\theta} L_0 = (L_0 - \xi E_q)\Gamma_{q\sigma}^{\xi\theta}, \tag{A.53}$$

and thus

$$\begin{aligned} \Sigma_S = -\sum \xi\xi'\theta\theta' t_{S\ell q}^\xi t_{S\ell' q'}^{\xi'} D_{\ell'\sigma'}^{\xi'\theta'} \Big(& W_0(E+\xi' E_{q'}) D_{\ell\sigma}^{\xi\theta} u_{q'}^{\xi'} \Gamma_{q'\sigma'}^{\xi'\theta'} + W_0(E-\xi' E_{q'}) D_{\ell\sigma}^{\xi\theta} \sigma' v_{q'}^{(-\xi')} \Gamma_{-q'-\sigma'}^{(-\xi')\theta'} \Big) \\ & \times \left(u_q^\xi \Gamma_{q\sigma}^{\xi\theta} + \sigma v_q^{(-\xi)} \Gamma_{-q-\sigma}^{(-\xi)\theta} \right), \end{aligned} \tag{A.54}$$

where we have left the summation indices implicit. Upon tracing out the superconductor we obtain

$$\overline{\Sigma}_S = \sum_{\xi\theta\theta'\ell\ell'\sigma} \theta\theta' \left(D_{\ell'\sigma}^{(-\xi)\theta'} I_{\xi\theta\ell\ell'}^{(1)} + \sigma D_{\ell'-\sigma}^{\xi\theta'} I_{\xi\theta\ell\ell'}^{(2)} \right) D_{\ell\sigma}^{\xi\theta}, \tag{A.55}$$

where

$$I_{\xi\theta\ell\ell'}^{(1)} = \sum_q t_{S\ell q}^\xi t_{S\ell' q}^{(-\xi)} \left(|u_q|^2 n_F^{(-\xi\theta)}(E_q) W_{\tilde{0}}(E-\xi E_q) + |v_q|^2 n_F^{(\xi\theta)}(E_q) W_{\tilde{0}}(E+\xi E_q) \right), \tag{A.56}$$

$$I_{\xi\theta\ell\ell'}^{(2)} = \sum_q t_{S\ell q}^\xi t_{S\ell' -q}^\xi u_q^\xi v_q^{(-\xi)} \left(n_F^{(-\xi\theta)}(E_q) W_{\tilde{0}}(E-\xi E_q) - n_F^{(\xi\theta)}(E_q) W_{\tilde{0}}(E+\xi E_q) \right), \tag{A.57}$$

and we have used that $\mathrm{Tr}_{SC}\left[\Gamma^{\xi'\theta'}_{q'\sigma'}\Gamma^{\xi\,\theta}_{q\,\sigma}\hat{\rho}^{\mathrm{eq}}_{SC}\right] = \delta_{qq'}\delta_{\sigma\sigma'}\delta_{\xi,-\xi'}n_F^{(-\xi\theta)}(E_q)$, $n_F^+ = n_F$ and $n_F^- = 1-n_F \equiv \bar{n}_F$ with n_F being the Fermi–Dirac distribution, and $\epsilon_q = \epsilon_{-q}$. In the limit of large superconducting gap and in the long-time steady state limit, $W_{\bar{0}}(E \pm \xi E_q)$ is dominated by the constant factor $\pm\xi E_q^{-1}$, whereby

$$I^{(1)}_{\xi\theta\ell\ell'} \simeq -\sum_q t^{\xi}_{S\ell q}t^{(-\xi)}_{S\ell' q}\xi E_q^{-1}\left(|u_q|^2 n_F^{(-\xi\theta)}(E_q) - |v_q|^2 n_F^{(\xi\theta)}(E_q)\right), \tag{A.58}$$

$$I^{(2)}_{\xi\theta\ell\ell'} \simeq I^{(2)}_{\xi\ell\ell'} = -\sum_q t^{\xi}_{S\ell q}t^{\xi}_{S\ell' -q}u^{\xi}_q v^{(-\xi)}_q \xi E_q^{-1}. \tag{A.59}$$

Using that $I^{(1)}_{(-\xi)\theta\ell'\ell} = I^{(1)}_{\xi(-\theta)\ell\ell'}$ and $I^{(2)}_{\xi\ell'\ell} = I^{(2)}_{\xi\ell\ell'}$ we find upon performing the sum over θ and θ' in Eq. (A.55), $\overline{\Sigma}_S[\,\cdot\,] = [\hat{H}_{\Sigma_S},\,\cdot\,]$, where

$$\hat{H}_{\Sigma_S} = \sum_{\xi\ell\ell'\sigma}\left(I^{(1)}_{\xi+\ell\ell'}\hat{d}^{(-\xi)}_{\ell'\sigma}\hat{d}^{\xi}_{\ell\sigma} + \sigma I^{(2)}_{\xi\ell\ell'}\hat{d}^{\xi}_{\ell'-\sigma}\hat{d}^{\xi}_{\ell\sigma}\right). \tag{A.60}$$

Carrying out the remaining sums gives the terms in Eq. (3.31) where we have defined the amplitudes $\hbar\gamma_{\mathrm{CPS}} = -(I^{(2)}_{-LR} + I^{(2)}_{-RL})$ and $\hbar\gamma_{\mathrm{EC}} = I^{(1)}_{-+LR} - I^{(1)}_{++RL}$, corresponding to Cooper pair splitting and elastic cotunneling, respectively, absorbed the constant self-energy into a redefinition of the dot levels, and have omitted the term corresponding to a Cooper pair occupying a single dot which is prohobited in the large U limit. The momentum integrals from $I^{(1)}_{\xi\theta\ell\ell'}$ and $I^{(2)}_{\xi\ell\ell'}$ are calculated explicitly in Ref. [43] assuming point-like contacts between each dot and the superconductor (at zero temperature) separated by a distance δr, however, we treat the amplitudes as the tunable parameters.

A.4 Full counting statistics

In this appendix, we provide a brief introduction to full counting statistics. Inherited from photonics, full counting statistics has now become an important methodology to characterize transport properties in mesoscopic systems. It is most easily formulated for unidirectional transport where the key quantity is the probability distribution, $P(\mathbf{n},t) = \mathrm{Tr}\hat{\rho}(\mathbf{n},t)$, for having transferred $\mathbf{n} = (n_i, n_j, \dots)$ electrons of type $i, j, \dots$ to a collector system (i, j could for example refer to two distinguishable collector leads as considered in Sec. 3.2) during a time span t, which in steady-state does not depend on the starting time. To this end, we partition $\mathcal{L} = \mathcal{L}_0 + \sum_j \mathcal{J}_j$, where $\mathcal{J}_j$ describes a transition that we wish to count. From the von Neumann equation we obtain the number-resolved master equation

$$\frac{d}{dt}\hat{\rho}(n_1, n_2, \dots, t) = \mathcal{L}_0\hat{\rho}(n_1, n_2, \dots, t) + \sum_j \mathcal{J}_j\hat{\rho}(\dots, n_j - 1, \dots, t), \quad t > t_0, \quad \hat{\rho}(\dots, -1, \dots, t) = 0. \tag{A.61}$$

It is convenient to introduce a vector of counting fields $\boldsymbol{\chi} = (\chi_1, \chi_2, \dots)$ that couples to the number of transitions by defining

$$\hat{\rho}(\boldsymbol{\chi}, t) = \sum_{\boldsymbol{n}}\hat{\rho}(\boldsymbol{n}, t)e^{i\boldsymbol{n}\cdot\boldsymbol{\chi}}. \tag{A.62}$$

This is convenient for two reasons: First, $\hat{\rho}(\boldsymbol{\chi}, t)$ is a moment generating function for the expected number of events

$$\sum_{\boldsymbol{n}}(n_1^{m_1}n_2^{m_2}\dots)P(n_1, n_2, \dots, t) = (\partial^{m_1}_{i\chi_1}\partial^{m_2}_{i\chi_2}\dots)\mathrm{Tr}\hat{\rho}(\boldsymbol{\chi}, t)|_{\boldsymbol{\chi}\to\mathbf{0}}. \tag{A.63}$$

Secondly, $\hat{\rho}(\boldsymbol{\chi}, t)$ solves the number-resolved master equation

$$\frac{d}{dt}\hat{\rho}(\boldsymbol{\chi}, t) = \left[\mathcal{L}_0 + \sum_j \mathcal{J}_j e^{i\chi_j}\right]\hat{\rho}(\boldsymbol{\chi}, t) \equiv \mathcal{L}(\boldsymbol{\chi})\hat{\rho}(\boldsymbol{\chi}, t) = \left[\mathcal{L}(0) + \sum_j \mathcal{J}_j(e^{i\chi_j} - 1)\right]\hat{\rho}(\boldsymbol{\chi}, t). \tag{A.64}$$

A.4.1 Steady-state transport statistics

Let us consider the expected steady-state current from transitions of type j. In the stationary steady state, the expected number of events of type j in the time-interval $t - t_0$, $n_j(t)$, is related to the steady-state current, I_j, as $-en_j(t) = (t - t_0)I_j$, which upon Laplace-transforming becomes $I_j = e(E/\hbar)^2 n_j(E)$, where

$$n_j(E) = \mathrm{Tr}\left[\partial_{i\chi_j}\hat{\rho}(\boldsymbol{\chi}, E)\right]\Big|_{\boldsymbol{\chi}\to\mathbf{0}} = \mathrm{Tr}\left[\left[-\frac{i}{\hbar}E - \mathcal{L}(0)\right]^{-1}\mathcal{J}_j\left[-\frac{i}{\hbar}E - \mathcal{L}(0)\right]^{-1}\hat{\rho}^{(S)}\right], \tag{A.65}$$

and $\hat{\rho}^{(S)}$ is the steady-state density matrix, and the latter equality follows from the Laplace-transform of Eq. (A.64). Following C. Flindt et. al [199], it is convenient to introduce the projectors $\mathcal{P}[\,\cdot\,] = \hat{\rho}_S\mathrm{Tr}[\,\cdot\,]$ and $\mathcal{Q} = \mathbf{1} - \mathcal{P}$. Hence, using that $\mathcal{L}(0)\mathcal{P} = \mathcal{P}\mathcal{L}(0) = 0$, we get

$$\left[-\frac{i}{\hbar}E - \mathcal{L}(0)\right]^{-1} = \left[-\frac{i}{\hbar}E\mathcal{P} + \mathcal{Q}\left(-\frac{i}{\hbar}E - \mathcal{L}(0)\right)\mathcal{Q}\right]^{-1} = \frac{i\hbar}{E}\mathcal{P} + \mathcal{Q}\left[-\frac{i}{\hbar}E - \mathcal{L}(0)\right]^{-1}, \tag{A.66}$$

where the latter equality follows after some algebra using the properties of the projectors $\mathcal{P}^2 = \mathcal{P}$, $\mathcal{Q}^2 = \mathcal{Q}$, $\mathcal{P}\mathcal{Q} = \mathcal{Q}\mathcal{P} = 0$, and $\mathcal{Q}\mathcal{L}(0) = \mathcal{L}(0)\mathcal{Q}$. Hence, using the cyclic property of the trace and the properties of the projectors, we find $n_j(E) = -(\hbar/E)^2\mathrm{Tr}[\mathcal{J}_j\hat{\rho}^{(S)}]$, whereby the steady-state current becomes

$$I_j = (-e)\mathrm{Tr}[\mathcal{J}_j\hat{\rho}^{(S)}]. \tag{A.67}$$

Indeed, we could have written this expression immediately. However, the formalism become useful when evaluating correlation functions, such as the noise correlation function. In particular, the derivation of the expression for the noise correlation function in Eq. (3.40) is derived straightforwardly by transforming to Laplace-space and following similar steps as above. Since the derivation is provided in detail in e.g. Refs. [88, 93], we will not reproduce the derivation here, but refer to these references. We note, however, that the expression in Eq. (3.40) in the main text only governs the real part of the cross-correlation noise. This appears not to be discussed in Ref. [93], however, is required to ensure the symmetry $S_{\ell\ell'}(\omega) = S_{\ell'\ell}(\omega)$ used in the derivation.

A.5 Gaussian integrals

For convenient referencing we list the following identities of Gaussian integrals from Ref. [121, Secs. 2.3, 9.1]:

Bosonic fields

The Gaussian integral over a set of complex variables z_j, $j = 1, \ldots, N$, is given by [121, Eq. (2.20)]

$$\mathcal{Z}[\bar{J}, J] = \int \Pi_{j=1}^N \mathrm{d}[\bar{z}_j, z_j] e^{-\sum_{ij}^N \bar{z}_i \hat{A}_{ij} z_j + \sum_j^N [\bar{z}_j J_j + \bar{J}_j z_j]} = \frac{e^{\sum_{ij}^N \bar{J}_i (\hat{A}^{-1})_{ij} J_j}}{\det\hat{A}}, \tag{A.68}$$

for $\hat{A}_{ij}$ a complex $N \times N$ matrix with eigenvalues having non-negative real parts, J_j is an arbitrary complex vector, and $\mathrm{d}[\bar{z}_j, z_j] = \mathrm{d}(\mathrm{Re}z_j)\mathrm{d}(\mathrm{Im}z_j)/\pi$. From this, pair-wise averages are given by [121, Eq. (2.21)]

$$\langle z_a \bar{z}_b\rangle \equiv \frac{1}{\mathcal{Z}[0,0]}\left.\frac{\delta^2 Z[\bar{J}, J]}{\delta\bar{J}_a \delta J_b}\right|_{J=0} = (A^{-1})_{ab}. \tag{A.69}$$

Fermionic fields

The Gaussian integral over two sets of independent Grassmann variables $\bar{\psi}_j$ and ψ_j, $j = 1, \ldots, N$, is given by [121, Eq. (9.11)]

$$\mathcal{Z}[\bar{\chi}, \chi] = \int \Pi_{j=1}^{N} \mathrm{d}[\bar{\psi}_j, \psi_j] e^{-\sum_{ij}^{N} \bar{\psi}_i \hat{A}_{ij} \psi_j + \sum_j^N [\bar{\psi}_j \chi_j + \bar{\chi}_j \psi_j]} = \det \hat{A} e^{\sum_{ij}^{N} \bar{\chi}_i (\hat{A}^{-1})_{ij} \chi_j}, \tag{A.70}$$

for $\hat{A}_{ij}$ an invertible complex $N \times N$ matrix, and $\bar{\chi}_j$ and χ_j are two additionally mutually independent sets of Grassmann numbers. From this, pair-wise averages are given by [121, Eq. (9.12)]

$$\left\langle \psi_a \bar{\psi}_b \right\rangle \equiv \frac{1}{\mathcal{Z}[0,0]} \left. \frac{\delta^2 Z[\bar{\chi}, \chi]}{\delta \bar{\chi}_b \delta \chi_a} \right|_{\chi=0} = (A^{-1})_{ab}. \tag{A.71}$$

A.6 Block matrix inversion

Consider a nonsingular square matrix M with inverse M^{-1} which is partitioned into 2×2 blocks as

$$M = \left[\begin{array}{c|c} M^{++} & M^{+-} \\ \hline M^{-+} & M^{--} \end{array} \right]. \tag{A.72}$$

If M^{--} is non-singular, then M is invertible if and only if $M^{++} - M^{+-}(M^{--})^{-1} M^{-+}$ is invertible, and [200]

$$M^{-1} = \left[\begin{array}{c|c} \left[M^{++} - M^{+-}(M^{--})^{-1} M^{-+}\right]^{-1} & -\left[M^{++} - M^{+-}(M^{--})^{-1} M^{-+}\right]^{-1} M^{+-}(M^{--})^{-1} \\ \hline -(M^{--})^{-1} M^{-+} \left[M^{++} - M^{+-}(M^{--})^{-1} M^{-+}\right]^{-1} & (M^{--})^{-1} + (M^{--})^{-1} M^{-+} \left[M^{++} - M^{+-}(M^{--})^{-1} M^{-+}\right]^{-1} M^{+-}(M^{--})^{-1} \end{array} \right]. \tag{A.73}$$

A.7 Coupling to a fermionic reservoir

In this appendix, we discuss the coupling to a fermionic reservoir for the two-dimensional lattice model discussed in Sec. 5.3 and Ch. 6 in the main text. We consider the simple model in Ref. [25] and assume that the system is coupled diagonally to external electron reservoirs, i.e. that spin and momentum $\boldsymbol{k}$ is conserved during tunneling [185]

$$\hat{H}_{\mathrm{res}} = \hat{H}_{\mathcal{E}} + \hat{H}_{\mathcal{T}}, \quad \hat{H}_{\mathcal{E}} = \sum_{\ell \boldsymbol{k} k_z \sigma} \epsilon_{\ell \boldsymbol{k} k_z} \hat{c}^{\dagger}_{\ell \boldsymbol{k} k_z \sigma} \hat{c}_{\ell \boldsymbol{k} k_z \sigma}, \quad \hat{H}_{\mathcal{T}} = \sum_{\ell \boldsymbol{k} k_z \sigma} \left(t_\ell \hat{c}^{\dagger}_{\ell \boldsymbol{k} k_z \sigma} \hat{c}_{\boldsymbol{k}\sigma} + \mathrm{h.c.} \right), \tag{A.74}$$

where k_z is a continuum reservoir degree of freedom, and the coupling element t_ℓ is assumed to be independent of momentum and spin. We furthermore assume that $\epsilon_{\ell \boldsymbol{k} k_z} = \epsilon_{\ell \boldsymbol{k}} + \epsilon_{\ell k_z}$, and that $dk_z / d\epsilon_{\ell k_z}$ is constant (wide-band approximation). The coupling between the system of interest and the environment is modeled by the action

$$\begin{aligned} S_{\mathcal{T}} &= -\int_{\mathcal{C}} d\tau \sum_{\ell \boldsymbol{k} k_z \sigma} \left(t_\ell \bar{\psi}_{\ell \boldsymbol{k} k_z \sigma}(\tau) \psi_{\boldsymbol{k}\sigma}(\tau) + t^*_\ell \bar{\psi}_{\boldsymbol{k}\sigma}(\tau) \psi_{\ell \boldsymbol{k} k_z \sigma}(\tau) \right) \\ &= -\int_{-\infty}^{\infty} dt \sum_{\ell \boldsymbol{k} k_z \sigma} \left(t_\ell (\bar{\psi}^+_{\ell \boldsymbol{k} k_z \sigma}(t), \psi^-_{\ell \boldsymbol{k} k_z \sigma}(t)) \hat{\tau}_3 \begin{pmatrix} \psi^+_{\boldsymbol{k}\sigma}(t) \\ \psi^-_{\boldsymbol{k}\sigma}(t) \end{pmatrix} + t^*_\ell (\bar{\psi}^+_{\boldsymbol{k}\sigma}(t), \psi^-_{\boldsymbol{k}\sigma}(t)) \hat{\tau}_3 \begin{pmatrix} \psi^+_{\ell \boldsymbol{k} k_z \sigma}(t) \\ \psi^-_{\ell \boldsymbol{k} k_z \sigma}(t) \end{pmatrix} \right), \end{aligned} \tag{A.75}$$

Using Eq. (A.70) we integrate out the environment to obtain an effective contribution to the action from the coupling to the environment. Upon taking the continuous time limit and Keldysh rotating, we find

$$S_{\mathrm{res}} = -\int dt dt' \sum_{\boldsymbol{k}\sigma} \hat{\bar{\Psi}}_{\boldsymbol{k}\sigma}(t) \hat{R}_{\boldsymbol{k}}(t,t') \hat{\Psi}_{\boldsymbol{k}\sigma}(t'), \quad \hat{R}_{\boldsymbol{k}}(t,t') = \sum_\ell t_\ell^2 \sum_{k_z} \hat{G}_{0,\ell \boldsymbol{k} k_z}(t,t'), \tag{A.76}$$

as in e.g. Refs. [185, 125, 201].

A.7.1 Reservoir self-energy in Floquet space

Upon transforming $\hat{R}_{\boldsymbol{k}}(t,t')$ in Eq. (A.76) to Floquet space (notice that the non-driven reservoirs also satisfies the condition (5.2)) we have

$$\hat{R}_{\boldsymbol{k},mn}(\omega) = \sum_{\ell} t_{\ell}^2 \sum_{k_z} \hat{G}_{0,\ell\boldsymbol{k}k_z,mn}(\omega). \tag{A.77}$$

Using Eq. (5.18) for time-independent reservoir Hamiltonians, the retarded/advanced component of the reservoir self-energy becomes

$$\begin{aligned} R^{R/A}_{\boldsymbol{k},mn}(\omega) &= \sum_{\ell} t_{\ell}^2 \sum_{k_z} G^{R/A}_{0,\ell\boldsymbol{k}k_z,mn}(\omega) \\ &= \sum_{\ell} t_{\ell}^2 \nu_{\ell z} \int d\epsilon_{\ell k_z} \frac{1}{\hbar\omega + n\Omega - \epsilon_{\ell\boldsymbol{k}} - \epsilon_{\ell k_z} \pm i0^+} \delta_{mn} \\ &= \mp i\Gamma\delta_{mn}, \end{aligned} \tag{A.78}$$

where we have defined $\Gamma \equiv \frac{1}{2}\sum_{\ell}\gamma_{\ell}$ with $\gamma_{\ell} \equiv 2\pi t_{\ell}^2 \nu_{\ell z}$. Similarly, the Keldysh component of the reservoir self-energy becomes

$$\begin{aligned} R^{K}_{\boldsymbol{k},mn}(\omega) &= \sum_{\ell} t_{\ell}^2 \sum_{k_z} G^{K}_{0,\ell\boldsymbol{k}k_z,mn}(\omega) \\ &= \sum_{\ell} t_{\ell}^2 \sum_{k_z} F_{\ell}(\epsilon_{\ell\boldsymbol{k}k_z}) \left[G^{R}_{0,\ell\boldsymbol{k}k_z,mn}(\omega) - G^{A}_{0,\ell\boldsymbol{k}k_z,mn}(\omega) \right] \\ &= \sum_{\ell} t_{\ell}^2 \nu_{\ell z} \int d\epsilon_{\ell k_z} F_{\ell}(\epsilon_{\ell\boldsymbol{k}k_z}) \left[\frac{1}{\hbar\omega + n\hbar\Omega - \epsilon_{\ell\boldsymbol{k}} - \epsilon_{\ell k_z} + i0^+} - \frac{1}{\hbar\omega + n\hbar\Omega - \epsilon_{\ell\boldsymbol{k}} - \epsilon_{\ell k_z} - i0^+} \right] \\ &= -i \sum_{\ell} \gamma_{\ell} F_{\ell}(\hbar\omega + n\hbar\Omega)\delta_{mn}, \end{aligned} \tag{A.79}$$

in agreement with Ref. [125, Eq. (192)], and where F was defined below Eq. (4.33).

Bibliography

[1] N. Walldorf, A.-P. Jauho, and K. Kaasbjerg, *Thermoelectrics in Coulomb-coupled quantum dots: Cotunneling and energy-dependent lead couplings*. Physical Review B **96**(11), 115415 (2017).

[2] N. Walldorf, C. Padurariu, A.-P. Jauho, and C. Flindt, *Electron waiting times of a Cooper pair splitter*. Physical Review Letters **120**, 087701 (2018).

[3] N. Walldorf, D. M. Kennes, J. Paaske, and A. J. Millis, *The antiferromagnetic phase of the Floquet-driven Hubbard model*. Physical Review B **100**, 121110 (2019).

[4] N. Walldorf, F. Brange, C. Padurariu, and C. Flindt, *Noise and full counting statistics of a Cooper pair splitter*. Physical Review B **101**, 205422 (2020).

[5] N. R. Speiden, *Thomas A. Edison: Sketch of activities, 1874-1881*. Science **105**(2719), 137–150 (1947).

[6] *Quantum phases on demand*. Nature Physics **16**(1), 1 (2020).

[7] A. Altland and B. D. Simons, *Condensed matter field theory* (Cambridge University Press), 2nd edn. (2010).

[8] D. C. Mattis and E. H. Lieb, *Exact solution of a many-fermion system and its associated boson field*. Journal of Mathematical Physics **6**(2), 304 (1965).

[9] C. J. Gorter, *A possible explanation of the increase of the electrical resistance of thin metal films at low temperatures and small field strengths*. Physica **17**(17), 777–780, 777–780 (1951).

[10] J. Kondo, *Resistance minimum in dilute magnetic alloys*. Progress of Theoretical Physics **32**(1), 37–49 (1964).

[11] D. N. Basov, R. D. Averitt, and D. Hsieh, *Towards properties on demand in quantum materials*. Nature Materials **16**(11), 1077–1088 (2017).

[12] G. B. Lesovik, T. Martin, and G. Blatter, *Electronic entanglement in the vicinity of a superconductor*. The European Physical Journal B **24**(3), 287 (2001).

[13] P. Recher, E. V. Sukhorukov, and D. Loss, *Andreev tunneling, Coulomb blockade, and resonant transport of nonlocal spin-entangled electrons*. Physical Review B **63**(16), 165314 (2001).

[14] R. Sánchez and M. Büttiker, *Optimal energy quanta to current conversion*. Physical Review B **83**, 085428 (2011).

[15] H. Thierschmann, R. Sánchez, B. Sothmann, F. Arnold, C. Heyn, W. Hansen, H. Buhmann, and L. W. Molenkamp, *Three-terminal energy harvester with coupled quantum dots*. Nature Nanotechnology **10**(10), 854–858 (2015).

[16] J. V. Koski, A. Kutvonen, I. M. Khaymovich, T. Ala-Nissila, and J. P. Pekola, *On-chip Maxwell's demon as an information-powered refrigerator*. Physical Review Letters **115**, 260602 (2015).

[17] H. J. Kimble, *The quantum internet*. Nature **453**(7198), 1023–1030 (2008).

[18] R. Mankowsky, M. Först, and A. Cavalleri, *Non-equilibrium control of complex solids by nonlinear phononics*. Reports on Progress in Physics **79**(6), 064503 (2016).

[19] Y. Tokura, M. Kawasaki, and N. Nagaosa, *Emergent functions of quantum materials*. Nature Physics **13**(11), 1056–1068 (2017).

[20] L. J. Li, E. C. T. O'Farrell, K. P. Loh, G. Eda, B. Özyilmaz, and A. H. Castro Neto, *Controlling many-body states by the electric-field effect in a two-dimensional material*. Nature **534**(7607), 1 (2016).

[21] T. Oka and H. Aoki, *Photovoltaic hall effect in graphene*. Physical Review B **79**, 081406 (2009).

[22] D. Fausti, R. I. Tobey, N. Dean, S. Kaiser, A. Dienst, M. C. Hoffmann, S. Pyon, T. Takayama, H. Takagi, and A. Cavalleri, *Light-induced superconductivity in a stripe-ordered cuprate*. Science **331**(6014), 189–191 (2011).

[23] H. Ehrke, R. I. Tobey, S. Wall, S. A. Cavill, M. Först, V. Khanna, T. Garl, N. Stojanovic, D. Prabhakaran, A. T. Boothroyd, M. Gensch, A. Mirone, P. Reutler, A. Revcolevschi, S. S. Dhesi, and A. Cavalleri, *Photoinduced melting of antiferromagnetic order in* $La_{0.5}Sr_{1.5}MnO_4$ *measured using ultrafast resonant soft x-ray diffraction*. Physical Review Letters **106**, 217401 (2011).

[24] N. D. Mermin and H. Wagner, *Absence of ferromagnetism or antiferromagnetism in one- or two-dimensional isotropic Heisenberg models*. Physical Review Letters **17**, 1133 (1966).

[25] A. Mitra, S. Takei, Y. B. Kim, and A. J. Millis, *Nonequilibrium quantum criticality in open electronic systems*. Physical Review Letters **97**(23), 236808 (2006).

[26] S. Stefanucci and R. van Leeuwen, *Nonequilibrium many-body theory of quantum systems* (Cambridge University Press) (2013).

[27] H.-P. Breuer and F. Petruccione, *The theory of open quantum systems* (Oxford University Press) (2002).

[28] B. H. Bransden and C. J. Joachain, *Quantum mechanics* (Prentice Hall,), 2nd edn. (2000).

[29] H. Haug and A.-P. Jauho, *Quantum Kinetics in Transport and Optics of Semiconductors* (Springer Berlin Heidelberg) (2008).

[30] L. E. Ballentine, *Quantum mechanics: A modern development* (World Scientific) (2010).

[31] H. Bruus and K. Flensberg, *Many-body quantum theory in condensed matter physics - An Introduction* (Oxford University Press) (2004).

[32] S. A. Gurvitz and Y. S. Prager, *Microscopic derivation of rate equations for quantum transport*. Physical Review B **53**, 15932–15943 (1996).

[33] C. Timm, *Time-convolutionless master equation for quantum dots: Perturbative expansion to arbitrary order*. Physical Review B **83**, 115416 (2011).

[34] J. König, H. Schoeller, and G. Schön, *Resonant tunneling and Coulomb oscillations*. Europhysics Letters **31**(1), 31–36 (1995).

[35] S. Koller, M. Grifoni, M. Leijnse, and M. R. Wegewijs, *Density-operator approaches to transport through interacting quantum dots: Simplifications in fourth-order perturbation theory.* Physical Review B **82**, 235307 (2010).

[36] J. N. Pedersen, *Tunneling through nanostructures - interactions, intereference and broadening.* Ph.D. thesis, Lund University (2008).

[37] M. Turek and K. A. Matveev, *Cotunneling thermopower of single electron transistors.* Physical Review B **65**, 115332 (2002).

[38] J. Koch, F. von Oppen, Y. Oreg, and E. Sela, *Thermopower of single-molecule devices.* Physical Review B **70**, 195107 (2004).

[39] S. Nakajima, *On quantum theory of transport phenomena - steady diffusion.* Progress of Theoretical Physics **20**(6), 948–959 (1958).

[40] R. Zwanzig, *Ensemble method in the theory of irreversibility.* Journal of Chemical Physics **33**(5), 1338–1341 (1960).

[41] M. R. Wegewijs and Y. V. Nazarov, *Resonant tunneling through linear arrays of quantum dots.* Physical Review B **60**, 14318–14327 (1999).

[42] C. Flindt, T. Novotný, A. Braggio, M. Sassetti, and A.-P. Jauho, *Counting Statistics of Non-Markovian Quantum Stochastic Processes.* Physical Review Letters **100**, 150601 (2008).

[43] O. Sauret, D. Feinberg, and T. Martin, *Quantum master equations for the superconductor-quantum dot entangler.* Physical Review B **70**(24), 1 (2004).

[44] U. Harbola, M. Esposito, and S. Mukamel, *Quantum master equation for electron transport through quantum dots and single molecules.* Physical Review B **74**, 235309 (2006).

[45] C. Emary, *Theory of nanostructures* (2009), `http://www1.itp.tu-berlin.de/skripte/cemary/nanoskript.pdf`, last accessed March 24, 2020.

[46] H. Schoeller, *A perturbative nonequilibrium renormalization group method for dissipative quantum mechanics.* The European Physical Journal Special Topics **168**(1), 179–266 (2009).

[47] S. Gustavsson, R. Leturcq, B. Simovič, R. Schleser, T. Ihn, P. Studerus, K. Ensslin, D. C. Driscoll, and A. C. Gossard, *Counting statistics of single electron transport in a quantum dot.* Physical Review Letters **96**, 076605 (2006).

[48] L. P. Kouwenhoven, D. G. Austing, and S. Tarucha, *Few-electron quantum dots.* Reports on Progress in Physics **64**(6), 701–736 (2001).

[49] J. P. Pekola, O.-P. Saira, V. F. Maisi, A. Kemppinen, M. Möttönen, Y. A. Pashkin, and D. V. Averin, *Single-electron current sources: Toward a refined definition of the ampere.* Review of Modern Physics **85**, 1421–1472 (2013).

[50] N. Walldorf, *Thermoelectric effects in capacitively coupled quantum dots.* Master's thesis, Technical University of Denmark (2016).

[51] H. Thierschmann, R. Sánchez, B. Sothmann, H. Buhmann, and L. W. Molenkamp, *Thermoelectrics with Coulomb-coupled quantum dots.* Comptes Rendus Physique **17**(10), 1109 – 1122 (2016).

[52] P. Wang, *A theory of nonequilibrium steady states in quantum chaotic systems.* Journal of Statistical Mechanics: Theory and Experiment **2017**(9), 093105 (2017).

[53] H. L. Edwards, Q. Niu, G. A. Georgakis, and A. L. de Lozanne, *Cryogenic cooling using tunneling structures with sharp energy features*. Physical Review B **52**, 5714–5736 (1995).

[54] A. A. M. Starring, L. W. Molenkamp, B. W. Alphenaar, H. van Houten, O. J. A. Buyk, M. A. A. Mabesonne, C. W. J. Beenakker, and C. T. Foxon, *Coulomb-blockade oscillations in the thermopower of a quantum dot*. Europhysics Letters **22**(1), 57–62 (1993).

[55] A. J. Keller, J. S. Lim, D. Sánchez, R. López, S. Amasha, J. A. Katine, H. Shtrikman, and D. Goldhaber-Gordon, *Cotunneling drag effect in Coulomb-coupled quantum dots*. Physical Review Letters **117**, 066602 (2016).

[56] D. Bischoff, A. Varlet, P. Simonet, M. Eich, H. C. Overweg, T. Ihn, and K. Ensslin, *Localized charge carriers in graphene nanodevices*. Applied Physics Reviews **2**, 031301 (2015).

[57] M. Leijnse, M. R. Wegewijs, and K. Flensberg, *Nonlinear thermoelectric properties of molecular junctions with vibrational coupling*. Physical Review B **82**, 045412 (2010).

[58] J. König, J. Schmid, H. Schoeller, and G. Schön, *Resonant tunneling through ultrasmall quantum dots: Zero-bias anomalies, magnetic-field dependence, and boson-assisted transport*. Physical Review B **54**, 16820–16837 (1996).

[59] A. Thielmann, M. H. Hettler, J. König, and G. Schön, *Cotunneling current and shot noise in quantum dots*. Physical Review Letters **95**, 146806 (2005).

[60] J. N. Pedersen and A. Wacker, *Tunneling through nanosystems: Combining broadening with many-particle states*. Physical Review B **72**, 195330 (2005).

[61] S. Amasha, A. J. Keller, I. G. Rau, A. Carmi, J. A. Katine, H. Shtrikman, Y. Oreg, and D. Goldhaber-Gordon, *Pseudospin-resolved transport spectroscopy of the Kondo effect in a double quantum dot*. Physical Review Letters **110**, 046604 (2013).

[62] K. Kaasbjerg and A.-P. Jauho, *Correlated Coulomb drag in capacitively coupled quantum-dot structures*. Physical Review Letters **116**, 196801 (2016).

[63] J. Koch, M. E. Raikh, and F. von Oppen, *Pair tunneling through single molecules*. Physical Review Letters **96**(5), 056803 (2006).

[64] M. Leijnse, M. R. Wegewijs, and M. H. Hettler, *Pair tunneling resonance in the single-electron transport regime*. Physical Review Letters **103**, 156803 (2009).

[65] G. B. Arfken, H.-J. Weber, and F. E. Harris, *Mathematical methods for physicists: A comprehensive guide* (Elsevier), seventh edn. (2013).

[66] Y. V. Nazarov and Y. M. Blanter, *Quantum Transport: Introduction to Nanoscience* (Cambridge University Press) (2009).

[67] J. Argüello-Luengo, D. Sánchez, and R. López, *Heat asymmetries in nanoscale conductors: The role of decoherence and inelasticity* **91**, 165431 (2015).

[68] A. V. Feshchenko, J. V. Koski, and J. P. Pekola, *Experimental realization of a Coulomb blockade refrigerator*. Physical Review B **90**, 201407 (2014).

[69] P. Strasberg, G. Schaller, T. Brandes, and M. Esposito, *Thermodynamics of a physical model implementing a Maxwell demon*. Physical Review Letters **110**, 040601 (2013).

[70] B. Sothmann, R. Sánchez, and A. N. Jordan, *Thermoelectric energy harvesting with quantum dots*. Nanotechnology **26**, 032001 (2014).

[71] R. Sánchez, R. López, D. Sánchez, and M. Büttiker, *Mesoscopic Coulomb drag, broken detailed balance, and fluctuation relations.* Physical Review Letters **104**, 076801 (2010).

[72] A. Kutvonen, J. Koski, and T. Ala-Nissila, *Thermodynamics and efficiency of an autonomous on-chip Maxwell's demon.* Scientific Reports **6**, 21126 (2016).

[73] A. Einstein, B. Podolsky, and N. Rosen, *Can quantum-mechanical description of physical reality be considered complete?* Physical Review **47**, 777–780 (1935).

[74] J. S. Bell, *On the Einstein Podolsky Rosen paradox.* Physics Physique Fizika **1**, 195–200 (1964).

[75] A. Aspect, P. Grangier, and G. Roger, *Experimental realization of Einstein-Podolsky-Rosen-Bohm gedankenexperiment: A new violation of Bell's inequalities.* Physical Review Letters **49**, 91–94 (1982).

[76] A. K. Ekert, *Quantum cryptography based on Bell's theorem.* Physical Review Letters **67**, 661–663 (1991).

[77] R. Ursin, F. Tiefenbacher, T. Schmitt-Manderbach, H. Weier, T. Scheidl, M. Lindenthal, B. Blauensteiner, T. Jennewein, J. Perdigues, P. Trojek, B. Ömer, M. Fürst, M. Meyenburg, J. Rarity, Z. Sodnik, C. Barbieri, H. Weinfurter, and A. Zeilinger, *Entanglement-based quantum communication over 144km.* Nature Physics **3**(7), 481–486 (2007).

[78] J. Yin, Y. Cao, Y. H. Li, S. K. Liao, L. Zhang, J. G. Ren, W. Q. Cai, W. Y. Liu, B. Li, H. Dai, G. B. Li, Q. M. Lu, Y. H. Gong, Y. Xu, S. L. Li, F. Z. Li, Y. Y. Yin, Z. Q. Jiang, M. Li, J. J. Jia, G. Ren, D. He, Y. L. Zhou, X. X. Zhang, N. Wang, X. Chang, Z. C. Zhu, N. L. Liu, Y. A. Chen, C. Y. Lu, R. Shu, C. Z. Peng, J. Y. Wang, and J. W. Pan, *Satellite-based entanglement distribution over 1200 kilometers.* Science **356**(6343), 1140–1144 (2017).

[79] F. Pulizzi, *Milestone 23: The rise of semiconductor spintronics.* Nature Physics **4**(S1), S20 (2008).

[80] D. Van Delft and P. Kes, *The discovery of superconductivity.* Europhysics News **42**(1), 21–25 (2011).

[81] J. Bardeen, L. N. Cooper, and J. R. Schrieffer, *Theory of superconductivity.* Physical Review **108**, 1175–1204 (1957).

[82] L. Hofstetter, S. Csonka, J. Nygård, and C. Schönenberger, *Cooper pair splitter realized in a two-quantum-dot Y-junction.* Nature **461**(7266), 960 (2009).

[83] L. G. Herrmann, F. Portier, P. Roche, A. L. Yeyati, T. Kontos, and C. Strunk, *Carbon nanotubes as Cooper-pair beam splitters.* Physical Review Letters **104**(2), 026801 (2010).

[84] V. F. Maisi, D. Kambly, C. Flindt, and J. P. Pekola, *Full counting statistics of Andreev tunneling.* Physical Review Letters **112**, 036801 (2014).

[85] J. Eldridge, M. G. Pala, M. Governale, and J. König, *Superconducting proximity effect in interacting double-dot systems.* Physical Review B **82**(18), 184507 (2010).

[86] T. Meng, S. Florens, and P. Simon, *Self-consistent description of Andreev bound states in Josephson quantum dot devices.* Physical Review B **79**(22), 224521 (2009).

[87] S. Gurvitz, *Wave-function approach to master equations for quantum transport and measurement.* Frontiers of Physics **12**(4), 120303 (2016).

[88] C. Flindt, T. Novotný, and A.-P. Jauho, *Current noise in a vibrating quantum dot array.* Physical Review B **70**, 205334 (2004).

[89] C. Flindt, T. Novotný, A. Braggio, and A.-P. Jauho, *Counting statistics of transport through Coulomb blockade nanostructures: High-order cumulants and non-Markovian effects*. Physical Review B **82**, 155407 (2010).

[90] Y. M. Blanter and M. Büttiker, *Shot noise in mesoscopic conductors*. Physics Report **336**(1-2), 1–166 (2000).

[91] T. Brandes, *Waiting times and noise in single particle transport*. Annalen Der Physik (leipzig) **17**(7), 477–496 (2008).

[92] C. Flindt, T. Novotný, and A.-P. Jauho, *Current noise spectrum of a quantum shuttle*. Physica E **29**(1), 411 (2005).

[93] N. Lambert, R. Aguado, and T. Brandes, *Nonequilibrium entanglement and noise in coupled qubits*. Physical Review B **75**(4), 045340 (2007).

[94] O. Sauret, T. Martin, and D. Feinberg, *Spin-current noise and Bell inequalities in a realistic superconductor-quantum dot entangler*. Physical Review B **72**, 024544 (2005).

[95] D. Chevallier, J. Rech, T. Jonckheere, and T. Martin, *Current and noise correlations in a double-dot Cooper-pair beam splitter*. Physical Review B **83**, 125421 (2011).

[96] N. Ubbelohde, C. Fricke, C. Flindt, F. Hohls, and R. J. Haug, *Measurement of finite-frequency current statistics in a single-electron transistor*. Nature Communications **3**(1), 612 (2012).

[97] A. Das, R. Ronen, M. Heiblum, D. Mahalu, A. V. Kretinin, and H. Shtrikman, *High-efficiency Cooper pair splitting demonstrated by two-particle conductance resonance and positive noise cross-correlation*. Nature Communications **3**, 1165 (2012).

[98] A. Delteil, W.-b. Gao, P. Fallahi, J. Miguel-Sanchez, and A. Imamoğlu, *Observation of quantum jumps of a single quantum dot spin using submicrosecond single-shot optical readout*. Physical Review Letters **112**, 116802 (2014).

[99] S. K. Gorman, Y. He, M. G. House, J. G. Keizer, D. Keith, L. Fricke, S. J. Hile, M. A. Broome, and M. Y. Simmons, *Tunneling Statistics for Analysis of Spin-Readout Fidelity*. Physical Review Applied **8**, 034019 (2017).

[100] M. Jenei, E. Potanina, R. Zhao, K. Y. Tan, A. Rossi, T. Tanttu, K. W. Chan, V. Sevriuk, M. Möttönen, and A. Dzurak, *Waiting time distributions in a two-level fluctuator coupled to a superconducting charge detector*. Physical Review Research **1**, 033163 (2019).

[101] S. Matsuo, K. Kuroyama, S. Yabunaka, S. R. Valentin, A. Ludwig, A. D. Wieck, and S. Tarucha, *Full counting statistics of spin-flip/conserving charge transitions in Pauli-spin blockade*. arXiv:1909.12027 .

[102] F. Brange, A. Schmidt, J. C. Bayer, T. Wagner, C. Flindt, and R. J. Haug, *Adiabatic-to-nonadiabatic crossover observed in the electron waiting times of a dynamically driven single-electron transistor*. arXiv:2005.06176v1 .

[103] D. Dasenbrook, P. P. Hofer, and C. Flindt, *Electron waiting times in coherent conductors are correlated*. Physical Review B **91**, 195420 (2015).

[104] H. J. Carmichael, S. Singh, R. Vyas, and P. R. Rice, *Photoelectron waiting times and atomic state reduction in resonance fluorescence*. Physical Review A **39**, 1200–1218 (1989).

[105] H. Carmichael, *An open systems approach to quantum optics*, vol. 18 (Springer Berlin Heidelberg) (1993).

[106] P. Trocha and I. Weymann, *Spin-resolved Andreev transport through double-quantum-dot Cooper pair splitters*. Physical Review B **91**, 235424 (2015).

[107] O. Malkoc, C. Bergenfeldt, and P. Samuelsson, *Full counting statistics of generic spin entangler with quantum dot-ferromagnet detectors*. Europhysics Letters **105**(4), 47013 (2014).

[108] P. Busz, D. Tomaszewski, and J. Martinek, *Spin correlation and entanglement detection in Cooper pair splitters by current measurements using magnetic detectors*. Physical Review B **96**(6), 064520 (2017).

[109] K. Wrześniewski, P. Trocha, and I. Weymann, *Current cross-correlations in double quantum dot based Cooper pair splitters with ferromagnetic leads*. Journal of Physics: Condensed Matter **29**(19), 195302 (2017).

[110] S. Gustavsson, R. Leturcq, M. Studer, I. Shorubalko, T. Ihn, K. Ensslin, D. C. Driscoll, and A. C. Gossard, *Electron counting in quantum dots*. Surface Science Reports **64**(6), 191 (2009).

[111] S. K. Gorman, Y. He, M. G. House, J. G. Keizer, D. Keith, L. Fricke, S. J. Hile, M. A. Broome, and M. Y. Simmons, *Tunneling statistics for analysis of spin-readout fidelity*. Physical Review Applied **8**, 034019 (2017).

[112] V. F. Maisi, O.-P. Saira, Y. A. Pashkin, J. S. Tsai, D. V. Averin, and J. P. Pekola, *Real-time observation of discrete Andreev tunneling events*. Physical Review Letters **106**, 217003 (2011).

[113] L. Rajabi, C. Pöltl, and M. Governale, *Waiting time distributions for the transport through a quantum-dot tunnel coupled to one normal and one superconducting lead*. Physical Review Letters **111**, 067002 (2013).

[114] P. Stegmann, B. Sothmann, J. König, and C. Flindt, *Real-time diagrammatic theory of electron waiting time distributions: Interaction effects and higher-order tunneling processes* (2020).

[115] R. Sánchez, P. Burset, and A. L. Yeyati, *Cooling by Cooper pair splitting*. Physical Review B **98**, 241414 (2018).

[116] Z. B. Tan, A. Laitinen, N. S. Kirsanov, A. Galda, M. Haque, A. Savin, D. S. Golubev, V. M. Vinokur, G. B. Lesovik, and P. J. Hakonen, *Thermoelectric current in a graphene Cooper pair splitter* (2020).

[117] Phys.org, *Producing spin-entangled electrons*. `https://phys.org/news/2015-07-spin-entangled-electrons.html`, accessed April 6, 2020.

[118] V. I. Yudin, A. V. Taichenachev, and M. Y. Basalaev, *Dynamic steady state of periodically driven quantum systems*. Physical Review A **93**, 013820 (2016).

[119] J. Rech, D. Chevallier, T. Jonckheere, and T. Martin, *Current correlations in an interacting Cooper-pair beam splitter*. Physical Review B **85**, 035419 (2012).

[120] R. Citro, *Out-of-equilibrium physics of correlated electron systems* (Springer International Publishing) (2018).

[121] A. Kamenev, *Field theory of non-equilibrium systems* (Cambridge University Press) (2011).

[122] J. Schwinger, *Brownian motion of a quantum oscillator*. Journal of Mathematical Physics **2**(3), 407 (1961).

[123] L. P. Kadanoff and G. Baym, *Quantum statistical mechanics* (New York: Benjamin) (1962).

[124] L. P. Keldysh, *Diagram technique for nonequilibrium processes*. Soviet Physics JETP **20**(4), 1018 (1965).

[125] H. Aoki, N. Tsuji, M. Eckstein, M. Kollar, T. Oka, and P. Werner, *Nonequilibrium dynamical mean-field theory and its applications*. Review of Modern Physics **86**, 779–837 (2014).

[126] S. G. Jakobs, *Functional RG for nonequilibrium transport through mesoscopic systems* (2015), lecture notes.

[127] M. E. Peskin and D. V. Schroeder, *An introduction to quantum field theory*. Frontiers in Physics (Avalon Publishing) (1995).

[128] F. Berezin, *The method of second quantization*, vol. 24 (Academic Press) (1966).

[129] W. H. Louisell, *Quantum statistical properties of radiation* (John Willey) (1973).

[130] C. Karrasch, *The functional renormalization group for zero-dimensional quantum systems in and out of equilibrium*. Ph.D. thesis, RWTH Aachen (2010).

[131] P. Coleman, *Introduction to many-body physics* (Cambridge University Press) (2015).

[132] E. Fradkin, *Field theories of condensed matter physics* (Cambridge University Press) (2013).

[133] J. A. Hertz, *Quantum critical phenomena*. Physical Review B **14**(3), 1165–84, 1165–1184 (1976).

[134] A. J. Millis, *Effect of a nonzero temperature on quantum critical-points in itinerant fermions systems*. Physical Review B **48**(10), 7183–7196 (1993).

[135] D. M. Kennes, *Dynamics in low-dimensional correlated quantum systems*. Ph.D. thesis, RWTH Aachen University (2014).

[136] S. Weiss, R. Huetzen, D. Becker, J. Eckel, R. Egger, and M. Thorwart, *Iterative path integral summation for nonequilibrium quantum transport*. Physica Status Solidi B **250**(11), 2298–2314 (2013).

[137] R. S. Souto, *Quench Dynamics in Superconducting Nanojunctions*. Springer Theses (Springer International Publishing) (2020).

[138] J. Rammer and H. Smith, *Quantum field-theoretical methods in transport-theory of metals*. Reviews of Modern Physics **58**(2), 323–359 (1986).

[139] E. Smith, *Quantum-classical correspondence principles for locally nonequilibrium driven systems*. Physical Review E **77**, 021109 (2008).

[140] E. Smith, *Doi-Peliti methods for non-commuting observables* (2017).

[141] R. L. Stratonovich, *On a method of calculating quantum distribution functions*. Soviet Physics Doklady **2**, 416 (1957).

[142] J. Hubbard, *Calculation of partition functions*. Physical Review Letters **3**(2), 77–78 (1959).

[143] G. Floquet, *Sur les équations différentielles linéaires à coefficients périodiques*. Annales scientifiques de l'École Normale Supérieure **12** (1883).

[144] D. H. Dunlap and V. M. Kenkre, *Dynamic localization of a charged particle moving under the influence of an electric field*. Physical Review B **34**, 3625–3633 (1986).

[145] K. W. Madison, M. C. Fischer, R. B. Diener, Q. Niu, and M. G. Raizen, *Dynamical Bloch band suppression in an optical lattice*. Physical Review Letters **81**, 5093–5096 (1998).

[146] R. Iyer, J. S. Aitchison, J. Wan, M. M. Dignam, and C. M. de Sterke, *Exact dynamic localization in curved AlGaAs optical waveguide arrays*. Optics Express **15**(6), 3212–3223 (2007).

[147] H. Lignier, C. Sias, D. Ciampini, Y. Singh, A. Zenesini, O. Morsch, and E. Arimondo, *Dynamical control of matter-wave tunneling in periodic potentials*. Physical Review Letters **99**, 220403 (2007).

[148] M. Mitrano, A. Cantaluppi, D. Nicoletti, S. Kaiser, A. Perucchi, S. Lupi, P. Di Pietro, D. Pontiroli, M. Riccò, S. R. Clark, D. Jaksch, and A. Cavalleri, *Possible light-induced superconductivity in K3 C60 at high temperature*. Nature **530**(7591), 461–464 (2016).

[149] A. Kirilyuk, A. V. Kimel, and T. Rasing, *Ultrafast optical manipulation of magnetic order*. Review of Modern Physics **82**, 2731–2784 (2010).

[150] L. D'Alessio and M. Rigol, *Long-time behavior of isolated periodically driven interacting lattice systems*. Physical Review X **4**, 041048 (2014).

[151] B. H. Wu and J. C. Cao, *A Floquet-Green's function approach to mesoscopic transport under ac bias*. Journal of Physics: Condensed Matter **20**(8), 085224 (2008).

[152] T. Kitagawa, T. Oka, A. Brataas, L. Fu, and E. Demler, *Transport properties of nonequilibrium systems under the application of light: Photoinduced quantum hall insulators without landau levels*. Physical Review B **84**, 235108 (2011).

[153] A. K. Eissing, V. Meden, and D. M. Kennes, *Functional renormalization group in Floquet space*. Physical Review B **94**, 245116 (2016).

[154] J.-R. Ohm and H. D. Lüke, *Signalübertragung: Grundlagen der digitalen und analogen nachrichtenübertragungssysteme* (Springer) (2014).

[155] J. H. Shirley, *Solution of the Schrödinger equation with a Hamiltonian periodic in time*. Physical Review **138**, B979–B987 (1965).

[156] A.-P. Jauho, N. S. Wingreen, and Y. Meir, *Time-dependent transport in interacting and noninteracting resonant-tunneling systems*. Physical Review B **50**, 5528–5544 (1994).

[157] C. O. Taberner, *Periodically driven S-QD-S junction: Floquet dynamics of Andreev bound states*. Master's thesis, University of Copenhagen (2017).

[158] A. Lubatsch and R. Frank, *Behavior of Floquet topological quantum states in optically driven semiconductors*. Symmetry **11**(10), 1246 (2019).

[159] M. Spiegel, S. Lipschutz, and J. Liu, *Schaum's outlines: Mathematical handbook of formulas and tables* (McGraw-Hill) (2009).

[160] P. A. Martin, *On functions defined by sums of products of Bessel functions*. Journal of Physics A: Mathematical and Theoretical **41**(1), 015207 (2008).

[161] D. M. Kennes, S. G. Jakobs, C. Karrasch, and V. Meden, *Renormalization group approach to time-dependent transport through correlated quantum dots*. Physical Review B **85**, 085113 (2012).

[162] A. K. Eissing, *Functional renormalization group in Floquet space applied to periodically driven quantum dots*. Ph.D. thesis, RWTH Aachen University (2017).

[163] *Bessel Functions*, chap. 9, 219–255 (John Wiley & Sons, Ltd) (2011).

[164] Y. H. Wang, H. Steinberg, P. Jarillo-Herrero, and N. Gedik, *Observation of Floquet-Bloch states on the surface of a topological insulator*. Science **342**(6157), 453–457 (2013).

[165] F. Mahmood, C.-K. Chan, Z. Alpichshev, D. Gardner, Y. Lee, P. A. Lee, and N. Gedik, *Selective scattering between Floquet-Bloch and Volkov states in a topological insulator*. Nature Physics **12**(4), 306–U137 (2016).

[166] E. Demler, *Physics of strongly correlated systems.* `http://cmt.harvard.edu/demler/layman.html`, last accessed August 14, 2020.

[167] N. D. Mathur, F. M. Grosche, S. R. Julian, I. R. Walker, D. M. Freye, R. K. W. Haselwimmer, and G. G. Lonzarich, *Magnetically mediated superconductivity in heavy fermion compounds.* Nature **394**(6688), 39–43 (1998).

[168] J. R. Schrieffer, X.-G. Wen, and S.-C. Zhang, *Spin-bag mechanism of high-temperature superconductivity.* Physical Review Letters **60**, 944–947 (1988).

[169] J. Hubbard, *Electron correlations in narrow energy bands.* Proceedings of the Royal Society of London Series A-mathematical and Physical Sciences **276**(1364) (1963).

[170] R. Singla, G. Cotugno, S. Kaiser, M. Först, M. Mitrano, H. Y. Liu, A. Cartella, C. Manzoni, H. Okamoto, T. Hasegawa, S. R. Clark, D. Jaksch, and A. Cavalleri, *Thz-frequency modulation of the Hubbard U in an organic Mott insulator.* Physical Review Letters **115**, 187401 (2015).

[171] M. Claassen, H. C. Jiang, B. Moritz, and T. P. Devereaux, *Dynamical time-reversal symmetry breaking and photo-induced chiral spin liquids in frustrated Mott insulators.* Nature Communications **8**(1), 1192 (2017).

[172] M. Babadi, M. Knap, I. Martin, G. Refael, and E. Demler, *Theory of parametrically amplified electron-phonon superconductivity.* Physical Review B **96**, 014512 (2017).

[173] J. R. Schrieffer, X. G. Wen, and S. C. Zhang, *Dynamic spin fluctuations and the bag mechanism of high-T_c superconductivity.* Physical Review B **39**, 11663–11679 (1989).

[174] A. Singh, *Spin-wave spectral properties of the Mott-Hubbard antiferromagnet: The intermediate-coupling regime.* Physical Review B **48**, 6668–6671 (1993).

[175] E. Fawcett, *Spin-density-wave antiferromagnetism in chromium.* Review of Modern Physics **60**, 209–283 (1988).

[176] L. Howald, E. Stilp, P. D. De Réotier, A. Yaouanc, S. Raymond, C. Piamonteze, G. Lapertot, C. Baines, and H. Keller, *Evidence for coexistence of bulk superconductivity and itinerant antiferromagnetism in the heavy fermion system CeCo(In1-x Cdx)5.* Scientific Reports **5**(1), 12528 (2015).

[177] P. C. Hohenberg, *Existence of long-range order in one and two dimensions.* Physical Review **158**(2), 383–386 (1967).

[178] A. Auerbach, *Interacting electrons and quantum magnetism* (Springer) (1998).

[179] N. Dupuis, *Notes on the many-body problem: Magnetism in lattice fermion systems.* `https://www.lptmc.jussieu.fr/files/chap_im.pdf`, last accessed July 9, 2020.

[180] M. V. Berry and K. E. Mount, *Semiclassical approximations in wave mechanics.* Reports on Progress in Physics **35**(1), 315–397, 315–397 (1972).

[181] A. Kamenev, *Keldysh and Doi-Peliti techniques for out-of-equilibrium systems.* eprint arXiv:cond-mat/0109316 (2001).

[182] S. Blundell, *Magnetism in condensed matter* (Oxford Univ. Press) (2003).

[183] A. M. Azurenko, C. S. Chiu, G. Ji, M. F. Parsons, M. Kanasz-Nagy, R. Schmidt, F. Grusdt, E. Demler, D. Greif, and M. Greiner, *A cold-atom Fermi-Hubbard antiferromagnet.* Nature **545**(7655), 462–+ (2017).

[184] M. Abramovitz and I. A. Stegun, *Handbook of mathematical functions with formulas, graphs and mathematical tables*. Tenth edn. (1972).

[185] S. Takei, *Dissipation and decoherence in open nonequilibrium electronic systems*. Ph.D. thesis, University of Toronto (2008).

[186] P. Ribeiro, A. E. Antipov, and A. N. Rubtsov, *Nonequilibrium breakdown of a correlated insulator through pattern formation*. Physical Review B **93**, 144305 (2016).

[187] W. Magnus, *On the exponential solution of differential equations for a linear operator*. Communications on Pure and Applied Mathematics **7**(4), 649–673 (1954).

[188] J. H. Mentink, K. Balzer, and M. Eckstein, *Ultrafast and reversible control of the exchange interaction in Mott insulators*. Nature Communications **6**, 6708 (2015).

[189] D. M. Kennes, S. G. Jakobs, C. Karrasch, and V. Meden, *Renormalization group approach to time-dependent transport through correlated quantum dots*. Physical Review B **85**, 085113 (2012).

[190] D. M. Kennes and V. Meden, *Quench dynamics of correlated quantum dots*. Physical Review B **85**, 245101 (2012).

[191] J. J. Mendoza-Arenas, F. J. Gómez-Ruiz, M. Eckstein, D. Jaksch, and S. R. Clark, *Ultrafast control of magnetic relaxation in a periodically driven Hubbard model*. Annalen Der Physik **529**(10), 1700024 (2017).

[192] F. Görg, M. Messer, K. Sandholzer, G. Jotzu, R. Desbuquois, and T. Esslinger, *Enhancement and sign change of magnetic correlations in a driven quantum many-body system*. Nature **553**(7689), 481–485 (2018).

[193] A. Mitra and A. J. Millis, *Current-driven quantum criticality in itinerant electron ferromagnets*. Physical Review B **77**, 220404 (2008).

[194] X. Liu, T. F. Seman, K. H. Ahn, M. van Veenendaal, D. Casa, D. Prabhakaran, A. T. Boothroyd, H. Ding, and J. P. Hill, *Strongly momentum-dependent screening dynamics in* $La_{0.5}Sr_{1.5}MnO_4$ *observed with resonant inelastic x-ray scattering*. Physical Review B **87**, 201103 (2013).

[195] S. Maekawa, *Nonlinear conduction of ZnS in strong electric fields*. Physical Review Letters **24**, 1175–1177 (1970).

[196] S. B. Wilkins, P. D. Spencer, P. D. Hatton, S. P. Collins, M. D. Roper, D. Prabhakaran, and A. T. Boothroyd, *Direct observation of orbital ordering in* $La_{0.5}Sr_{1.5}MnO_4$ *using soft x-ray diffraction*. Physical Review Letters **91**, 167205 (2003).

[197] N. Dasari and M. Eckstein, *Ultrafast electric field controlled spin correlations in the Hubbard model*. Physical Review B **100**, 121114 (2019).

[198] A. Ono and S. Ishihara, *Nonequilibrium susceptibility in photoinduced Floquet states*. Physical Review B **100**, 075127 (2019).

[199] C. Flindt, T. Novotny, and A.-P. Jauho, *Full counting statistics of nano-electromechanical systems*. Europhysics Letters **69**(3), 475–481 (2005).

[200] L. Tzon-Tzer and S. Sheng-Hua, *Inverses of 2 × 2 block matrices*. Computers & Mathematics with Applications **43**(1), 119 – 129 (2002).

[201] A. Altland and R. Egger, *Nonequilibrium transport and dephasing in Coulomb-blockaded quantum dots*. Lecture Notes in Physics **843**, 215–244 (2012).

B | Publications

B.1 Publication I

Thermoelectrics in Coulomb-coupled quantum dots: Cotunneling and energy-dependent lead couplings

Nicklas Walldorf, Antti-Pekka Jauho, and Kristen Kaasbjerg

Physical Review B 96, 115415 (2017)

Thermoelectrics in Coulomb-coupled quantum dots: Cotunneling and energy-dependent lead couplings

Nicklas Walldorf,* Antti-Pekka Jauho, and Kristen Kaasbjerg†
Center for Nanostructured Graphene (CNG), Dept. of Micro- and Nanotechnology, Technical University of Denmark, DK-2800 Kongens Lyngby, Denmark

We study thermoelectric effects in Coulomb-coupled quantum-dot (CCQD) systems beyond lowest-order tunneling processes and the often applied wide-band approximation. To this end, we present a master-equation (ME) approach based on a perturbative T-matrix calculation of the charge and heat tunneling rates and transport currents. Applying the method to transport through a non-interacting single-level QD, we demonstrate excellent agreement with the Landauer-Büttiker theory when higher-order (cotunneling) processes are included in the ME. Next, we study the effect of cotunneling and energy-dependent lead couplings on the heat currents in a system of two Coulomb-coupled QDs. We find that cotunneling processes (i) can dominate the off-resonant heat currents at low temperature and bias compared to the interdot interaction, and (ii) give rise to a pronounced reduction of the cooling power achievable with the recently demonstrated Maxwell's demon cooling mechanism. Furthermore, we demonstrate that the cooling power can be boosted significantly by carefully engineering the energy dependence of the lead couplings to filter out undesired transport processes. Our findings emphasize the importance of higher-order cotunneling processes as well as engineered energy-dependent lead couplings in the optimization of the thermoelectric performance of Coulomb-coupled QD systems.

I. INTRODUCTION

The experimental progress in control of single-electron transport[1] has spurred interest in nanosystems that utilize the associated heat currents for thermoelectric applications.[2–4] In particular, experiments with Coulomb-coupled quantum-dot (CCQD) systems have demonstrated a plethora of phenomena ranging from Coulomb drag[5,6] and electron pairing[7] to extraordinary thermoelectric effects.[8,9] This includes the realization of an energy harvester that converts a thermal gradient in a CCQD system into an electric current,[8] as well as an autonomous Maxwell's demon capable of cooling a current-carrying QD system at the cost of heating a "demon" QD system.[9]

In addition to the above, theoretical studies have predicted a wide range of novel thermoelectric effects in CCQD systems.[10–13] The mechanisms behind these effects rely on the presence of a strong Coulomb interaction between electrons in the otherwise decoupled QDs (see Fig. 1 for the case of two Coulomb-coupled QDs). The strong interaction can be utilized to tailor the thermoelectric properties of CCQD systems,[4,14] and it provides the opportunity to test fundamental thermodynamic aspects of heat transport in interacting nanoscale systems driven out of equilibrium.[15]

While the operation principles of the above-mentioned effects are governed by *incoherent* electron tunneling (sequential tunneling) processes between the leads and the QDs,[8–13] the importance of coherent higher-order tunneling (cotunneling) processes for nonlinear heat transport remains largely unexplored. Furthermore, when operated under strong non-equilibrium conditions in which linear-response theory breaks down, a theoretical treatment taking into account the full nonlinear properties is needed.[16–19] Only recently have these issues been discussed in strongly interacting QD systems.[9,20–22]

Another important factor for thermoelectric effects in CCQD systems is the coupling to the leads which is usually treated in the wide-band approximation assuming energy-independent couplings.[23] However, energy-dependent couplings to the leads occur naturally in many QD systems[5,6,8,24] and add an important degree of tunability to the system. This is as crucial for the thermoelectric properties[10,11,25] as it is for Coulomb drag.[5,6,26–28]

In this work, we present a master-equation approach for the calculation of the nonlinear electronic charge and heat currents in interacting QD systems that takes into account the above-mentioned factors. The charge and heat transfer rates produced by electron tunneling processes are obtained with a perturbative T-matrix approach,[23] which treats sequential and cotunneling processes on an equal footing. We resolve the technical challenges associated with the evaluation of the cotunneling rates with an implementation of the often applied regularization scheme,[29,30] which applies to the general case of energy-dependent lead couplings, applied biases, and temperature gradients in the system.

The main findings and the organization of the paper are as follows. In Sec. II, we introduce the model system of CCQDs. In Sec. III, we present the methodology, and we benchmark the approach in Sec. IV by comparing it to the Landauer-Büttiker result for transport through a non-interacting single-level QD. In Sec. V, we study nonlinear thermoelectric phenomena in CCQDs. We investigate the energy exchange mediated by the interdot Coulomb interaction which among other thermoelectric effects leads to the demon-induced cooling mechanism.[9,10] Our findings shed light on the limitations imposed by cotunneling processes on the performance of this mechanism. Furthermore, we demonstrate a strongly

enhanced performance of the demon-induced cooling effect by tuning the energy-dependence of the lead couplings. In such performance optimization, as we show, cotunneling processes are essential for a quantitative description of the thermoelectric properties. Finally, Sec. VI presents our conclusions, and the appendix provides technical details on the cotunneling rates and the regularization procedure.

II. COULOMB-COUPLED QD SYSTEMS

We consider CCQD systems like the one illustrated in Fig. 1, which can be described by the Hamiltonian

$$\hat{H} = \hat{H}_{\rm dots} + \hat{H}_{\rm leads} + \hat{H}_T, \tag{1}$$

and consists of a system of CCQDs with Hamiltonian $\hat{H}_{\rm dots}$ that is coupled to external leads with Hamiltonian $\hat{H}_{\rm leads}$ by tunnel couplings described by $\hat{H}_T$. We denote $\hat{H}_0 = \hat{H}_{\rm dots} + \hat{H}_{\rm leads}$.

We consider a spinless model of Coulomb-coupled single-level QDs described by the Hamiltonian

$$\hat{H}_{\rm dots} = \sum_\delta \epsilon_\delta \hat{c}_\delta^\dagger \hat{c}_\delta + \sum_{\langle \delta,\delta'\rangle} U_{\delta\delta'} \hat{n}_\delta \hat{n}_{\delta'}, \tag{2}$$

where $\hat{c}_\delta^\dagger$ ($\hat{c}_\delta$) creates (annihilates) an electron in QD δ with energy controlled by gate voltages $\epsilon_\delta = -eV_\delta$, where V_δ is the gate potential on dot δ, $\hat{n}_\delta = \hat{c}_\delta^\dagger \hat{c}_\delta$ is the occupation number operator, $U_{\delta\delta'}$ is the *interdot* Coulomb interaction, and the summation in the second term is over all QD pairs (specific systems are studied in Secs. IV–V). Intra-dot double occupancy can be neglected due to a large intra-dot Coulomb interaction.

The leads are described by non-interacting electron reservoirs, $\hat{H}_{\rm leads} = \sum_{\ell k} \epsilon_{\ell k} \hat{c}_{\ell k}^\dagger \hat{c}_{\ell k}$, where $\hat{c}_{\ell k}^\dagger$ ($\hat{c}_{\ell k}$) creates (annihilates) an electron with momentum k and energy $\epsilon_{\ell k}$ in lead ℓ, which is assumed to be in local equilibrium with temperature T_ℓ and electrochemical potential $\mu_\ell = \mu_0 - eV_\ell$, where μ_0 is the equilibrium chemical potential and V_ℓ is the voltage applied to lead ℓ. The tunneling Hamiltonian that couples the QD system to the leads is $\hat{H}_T = \sum_{\ell k\delta}(t_{\ell k\delta}\hat{c}_\delta^\dagger \hat{c}_{\ell k} + \text{h.c.})$, where $t_{\ell k\delta}$ is the tunneling amplitude, and we consider the case where each lead couples to one QD only. We define lead coupling strengths as $\gamma^\ell(\epsilon) \equiv 2\pi d_\ell(\epsilon)|t_\ell(\epsilon)|^2$, where $d_\ell(\epsilon)$ is the lead density of states. $\gamma^\ell(\epsilon)$ is allowed to be energy-dependent in contrast to the often applied wide-band approximation.

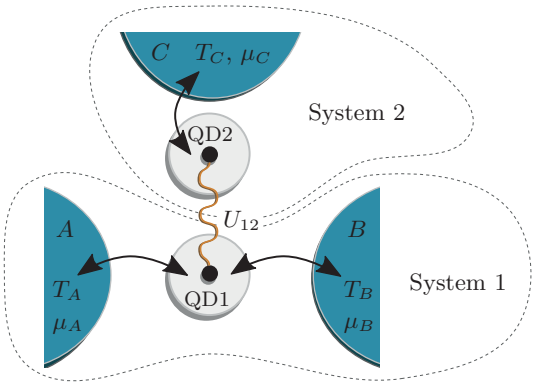

FIG. 1. Illustration of the CCQD system studied in Sec. V consisting of two Coulomb-coupled QDs with interdot Coulomb interaction U_{12} (no tunneling is allowed between the QDs) in a three-terminal configuration with leads $\ell \in \{A, B, C\}$ with temperatures T_ℓ and electrochemical potentials μ_ℓ.

III. MASTER EQUATION AND TRANSPORT CURRENTS

We describe the dynamics and transport in the CCQD system with a Pauli ME where the transitions between the QD states are governed by electron tunneling to and from the leads.[31] The tunneling-induced transition rates are calculated based on a perturbative T-matrix approach in which the tunneling Hamiltonian is treated as a perturbation to the decoupled QD system and leads. This allows for a systematic expansion in the tunnel couplings and the inclusion of high-order processes. However, quantum effects such as tunneling-induced level broadening and level shifts[32–34] are not captured by this perturbative approach, which is only valid in the weak-coupling regime $\gamma < k_B T, U$.

In the absence of tunnel coupling, the states of the decoupled QD system and leads are described by product states of the QD system occupation states $|m\rangle$ with energy $E_{{\rm dots},m} = \langle m|\hat{H}_{\rm dots}|m\rangle$ and the leads $|i\rangle$ with energy $E_{{\rm leads},i} = \langle i|\hat{H}_{\rm leads}|i\rangle$. The non-equilibrium occupations of the QD states are described by probabilities p_m (the diagonal components of the reduced density operator of the CCQD system), which are determined by the ME,

$$\dot{p}_m = \sum_{n\neq m} \left(\Gamma_{nm} p_n - \Gamma_{mn} p_m\right), \quad \sum_m p_m = 1, \tag{3}$$

where Γ_{mn} denotes the tunneling-induced transition rate from QD state $|m\rangle$ to $|n\rangle$. The ME is solved for the steady-state probabilities, $\dot{p}_m = 0$, in the following. The QD states are given explicitly in Secs. IV and V for the considered systems.

A. Transition rates

The rates for transitions between the QD states are obtained from the generalized Fermi's golden rule[23,35]

$$\begin{aligned}\tilde{\Gamma}_{mn} = \frac{2\pi}{\hbar}\sum_{ij} |\langle j|\langle n|\hat{T}|m\rangle|i\rangle|^2 \rho_i \\ \times \delta(\Delta_{mn} + E_{{\rm leads},j} - E_{{\rm leads},i}),\end{aligned} \tag{4}$$

where $\Delta_{mn} \equiv E_{\mathrm{dots},n} - E_{\mathrm{dots},m}$, ρ_i is the thermal probability of finding the leads in the initial state, the sum is over initial and final states of the leads, and the T matrix obeys

$$\hat{T} = \hat{H}_T + \hat{H}_T \frac{1}{E_{\mathrm{initial}} - \hat{H}_0 + i\eta} \hat{T}, \tag{5}$$

with $E_{\mathrm{initial}} = E_{\mathrm{dots},m} + E_{\mathrm{leads},i}$, and η is a positive infinitesimal.

The lowest-order contribution to the tunneling rates describes single-electron tunneling, or *sequential tunneling*, processes between the QD system and the leads:

$$\Gamma^{\vec{\ell}}_{mn} = \hbar^{-1}\gamma^{\ell}(\Delta_{mn}) f^{\ell}(\Delta_{mn}), \tag{6}$$

$$\Gamma^{\overleftarrow{\ell}}_{mn} = \hbar^{-1}\gamma^{\ell}(\Delta_{nm}) \bar{f}^{\ell}(\Delta_{nm}), \tag{7}$$

where Eq. (6) (Eq. (7)) is the sequential rate of tunneling out of, $\rightarrow$, (into, $\leftarrow$,) lead ℓ, thereby changing the state of the QD system from m to n, $f^{\ell}(\epsilon) = [\exp(\beta_\ell(\epsilon - \mu_\ell)) + 1]^{-1}$ is the Fermi-Dirac distribution in lead ℓ, $\bar{f}^{\ell}(\epsilon) = 1 - f^{\ell}(\epsilon)$, and $\beta_\ell = 1/(k_B T_\ell)$. The leads are assumed to equilibrate to the Fermi-Dirac distribution in between the tunneling events.

The next-to-leading order terms in the T matrix describe cotunneling processes. In conventional *local* elastic and inelastic cotunneling processes, a net electron is transferred between two leads attached to the same QD (e.g., System 1 in Fig. 1). Here we also consider (i) *nonlocal* cotunneling processes[27,36] in which a net electron is transferred between leads attached to different QDs, as well as (ii) pair-cotunneling processes where two electrons tunnel into/out of the CCQD system in one coherent process.[37,38]

For the thermoelectric effects in focus here, the process of nonlocal cotunneling is important. The (unregularized) rate for nonlocal cotunneling which net transfers an electron out of lead ℓ and into lead ℓ' is given by

$$\tilde{\Gamma}^{\vec{\ell}\,\overleftarrow{\ell'}}_{mn} = \int \frac{d\epsilon}{2\pi\hbar} \gamma^{\ell}(\epsilon)\gamma^{\ell'}(\epsilon - \Delta_{mn}) f^{\ell}(\epsilon) \bar{f}^{\ell'}(\epsilon - \Delta_{mn}) \times \left| \frac{1}{\Delta_{vm} + \epsilon + i\eta} + \frac{1}{\Delta_{v'n} - \epsilon + i\eta} \right|^2, \tag{8}$$

where v (v') refers to the virtually occupied intermediate state in the process where an electron initially tunnels from lead ℓ and into the QD system (from the QD system and into lead ℓ'). We refer the reader to the appendix for the expressions for the remaining cotunneling processes relevant for this study.

A well-known artifact of the cotunneling rates obtained with the T-matrix approach is that they formally diverge in the limit $\eta \to 0$. To deal with this divergence, different regularization schemes have been proposed.[29,30,35,39] Deep inside the Coulomb blockade, the discrepancy between the different regularization schemes vanishes.[39] In this work, we apply the by now standard regularization scheme in Ref. 29, but for future work, a detailed comparison of the heat currents obtained from different regularization schemes could be useful. We denote the regularized rates that enter into Eq. (3) without a tilde. To be explicit, we consider the processes $\Gamma_{mn} \equiv \sum_\ell (\Gamma^{\ell\leftarrow}_{mn} + \Gamma^{\ell\rightarrow}_{mn})$, $\Gamma^{\ell\leftarrow}_{mn} \equiv \Gamma^{\overleftarrow{\ell}}_{mn} + \sum_{\ell'} (\Gamma^{\overleftarrow{\ell}\,\vec{\ell}'}_{mn} + \Gamma^{\overleftarrow{\ell}\,\overleftarrow{\ell}'}_{mn})$, $\Gamma^{\ell\rightarrow}_{mn} \equiv \Gamma^{\vec{\ell}}_{mn} + \sum_{\ell'} (\Gamma^{\vec{\ell}\,\vec{\ell}'}_{mn} + \Gamma^{\vec{\ell}\,\overleftarrow{\ell}'}_{mn})$. A numerical procedure for the regularization is outlined in the appendix.

B. Charge and heat currents

The steady-state transport currents can be obtained from the occupation probabilities. The electric current going into lead ℓ is

$$I_\ell \equiv -e \left\langle \sum_k \frac{d\hat{n}_{\ell k}}{dt} \right\rangle = -e \sum_{mn} p_m \left(\Gamma^{\ell\leftarrow}_{mn} - \Gamma^{\ell\rightarrow}_{mn} \right), \tag{9}$$

where $\hat{n}_{\ell k} = \hat{c}^\dagger_{\ell k}\hat{c}_{\ell k}$, p_m is calculated from the steady-state solution of Eq. (3), and the rightmost form expresses the electric current in terms of the total rate of electrons tunneling into lead ℓ, minus the total rate of electrons tunneling out of lead ℓ.[40]

The heat current going into lead ℓ is[15,17,41]

$$J_\ell \equiv \left\langle \sum_k (\epsilon_{\ell k} - \mu_\ell) \frac{d\hat{n}_{\ell k}}{dt} \right\rangle = \sum_{mn} p_m \left(W^{\ell\leftarrow}_{mn} - W^{\ell\rightarrow}_{mn} \right), \tag{10}$$

where the rightmost form expresses the heat current in terms of heat rates W (using a similar notation to that for the tunneling rates).

The sequential-tunneling heat rate in lead ℓ is calculated as the tunneling rate multiplied by the energy of the tunneling electron relative to the chemical potential in the lead,

$$\begin{aligned} W^{\vec{\ell}}_{\ell,mn} &= (\Delta_{mn} - \mu_\ell)\Gamma^{\vec{\ell}}_{mn}, \\ W^{\overleftarrow{\ell}}_{\ell,mn} &= (\Delta_{nm} - \mu_\ell)\Gamma^{\overleftarrow{\ell}}_{mn}, \end{aligned} \tag{11}$$

where the indices follow the notation of the tunneling rates, and the additional subscript ℓ refers to the lead in which the heat rate is calculated.

Analogously, the cotunneling heat rates into/out of the leads are calculated *a posteriori* by multiplying the integrand in the cotunneling rate by the energy of the tunneling electron relative to the chemical potential of the lead. For example, for the nonlocal cotunneling process between lead ℓ and ℓ', the (unregularized) heat rate in lead ℓ reads

$$\tilde{W}^{\vec{\ell}\,\overleftarrow{\ell'}}_{\ell,mn} = \int \frac{d\epsilon}{2\pi\hbar} \gamma^{\ell}(\epsilon)\gamma^{\ell'}(\epsilon - \Delta_{mn}) f^{\ell}(\epsilon) \bar{f}^{\ell'}(\epsilon - \Delta_{mn}) \times (\epsilon - \mu_\ell) \left| \frac{1}{\Delta_{vm} + \epsilon + i\eta} + \frac{1}{\Delta_{v'n} - \epsilon + i\eta} \right|^2, \tag{12}$$

with the heat rate in lead ℓ', $\tilde{W}^{\vec{\ell}\,\overleftarrow{\ell'}}_{\ell',mn}$, given as above but with $(\epsilon-\mu_\ell)$ replaced by $(\epsilon-\Delta_{mn}-\mu_{\ell'})$. The remaining cotunneling heat rates follow similarly.

Whereas the calculation of charge currents involves the electron-tunneling rates that enter the ME (3), and therefore does not require any additional steps once the ME has been set up and solved, the heat currents must be calculated via the heat tunneling rates in a post-processing step, similar to the procedure in full density-matrix treatments.[20]

IV. COMPARISON TO THE LANDAUER-BÜTTIKER FORMALISM

In this section, we benchmark the approach by comparing the charge and heat currents in a spinless non-interacting single-level QD system with those obtained from the Landauer-Büttiker (LB) formalism (see Ref. 42 for a comparison of the electric current in the case of equal temperatures in the leads). For non-interacting systems, the LB result is exact. However, for the thermoelectric effects discussed in Sec. V, which require the presence of strong Coulomb interaction, an alternative method such as the ME approach is needed.

We consider a single-level QD coupled to two leads $\ell \in \{A, B\}$ (such as System 1 in Fig. 1 when decoupled from System 2). For simplicity, we assume wide-band lead couplings $\gamma^\ell(\epsilon) = \gamma^\ell$ in this case. The Hamiltonian of the QD reduces to

$$\hat{H}_{\rm dots} = \epsilon_1 \hat{c}_1^\dagger \hat{c}_1, \tag{13}$$

with states labeled by the occupancy, $|n_1\rangle \in \{|0\rangle, |1\rangle\}$.

In the LB formalism, the electric current and heat current going into lead A are given by,[18,43]

$$I_A^{\rm LB} = \frac{-e}{h}\int d\epsilon\, T(\epsilon)[f^B(\epsilon) - f^A(\epsilon)], \tag{14}$$

and

$$J_A^{\rm LB} = \frac{1}{h}\int d\epsilon\, (\epsilon-\mu_A) T(\epsilon)[f^B(\epsilon) - f^A(\epsilon)], \tag{15}$$

respectively. For a non-interacting single-level QD, the transmission function $T(\epsilon)$ is

$$T(\epsilon) = \frac{\gamma^A\gamma^B}{(\epsilon-\epsilon_1)^2 + (\gamma/2)^2}, \tag{16}$$

where $\gamma = \gamma^A + \gamma^B$ and we have omitted the tunneling-induced energy shift, which is not captured by the T-matrix approach.

The transport currents calculated with the two approaches with a finite bias and temperature difference ($T_B = 2T_A \equiv 2T$) between the leads are plotted in Figs. 2(a) and 2(b) as a function of the gate voltage for two different lead coupling strengths. To demonstrate the importance of cotunneling processes, we have included ME results based on sequential tunneling only (black dotted curves) that do not depend on γ^ℓ in the units shown, as well as sequential plus cotunneling (dashed curves). The results based purely on sequential tunneling differ significantly from the LB results unless $\gamma^\ell \ll k_BT$. However, for $\gamma^\ell < k_BT$, the ME results with cotunneling are in excellent agreement with the LB formalism. For $\gamma^\ell > k_BT$, which is outside the regime of validity of the ME approach, the two approaches deviate as expected.

In the following discussion of thermoelectric effects, the heat current is of particular interest. As seen in Fig. 2(b), when the dot level is above the electrochemical potential in lead A, the heat current becomes negative (for sufficiently small lead coupling strength). In this case, electrons above the electrochemical potential tunnel out of the lead and thereby cool the lead [cf. Eq. (10)]. Such cooling mechanisms due to energy-selective tunneling have been confirmed experimentally in metallic QD systems.[9,44] The energy-selective tunneling gives rise to an asymmetry in the energy dissipation between the source and drain leads that was recently observed in molecular junctions.[45]

V. THERMOELECTRIC EFFECTS IN COULOMB-COUPLED QDS

In the remaining part of the paper, we study the thermoelectric properties of the system illustrated in Fig. 1, i.e., two single-level QDs with QD1 tunnel-coupled to leads A and B and QD2 tunnel-coupled to lead C. The CCQD system is described by the Hamiltonian

$$\hat{H}_{\rm dots} = \epsilon_1 \hat{c}_1^\dagger \hat{c}_1 + \epsilon_2 \hat{c}_2^\dagger \hat{c}_2 + U\hat{n}_1\hat{n}_2, \tag{17}$$

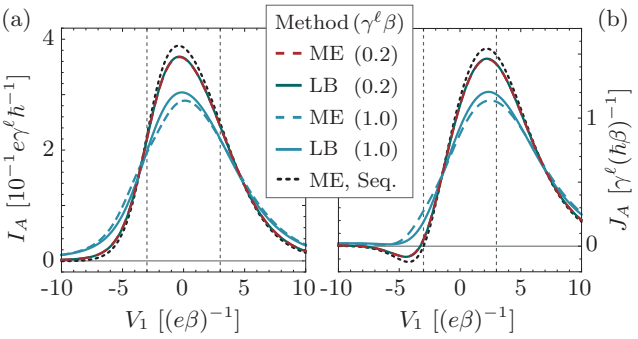

FIG. 2. Comparison of the electric current (a) and heat current (b) calculated with the ME and LB approaches. Currents are plotted as function of gate voltage V_1 for two different lead coupling strengths $\gamma^A = \gamma^B = \gamma^\ell$ (energy-independent). The ME result including only sequential tunneling is shown for reference (black dotted), and the vertical dashed lines mark the alignment of the dot level with the electrochemical potentials of leads A (left) and B (right). Parameters: $T_B = 2T_A \equiv 2/(k_B\beta)$, $\mu_A = 3\,\beta^{-1}$, $\mu_B = -3\,\beta^{-1}$, and $\eta = 10^{-3}\,\beta^{-1}$.

where we have used the simplified notation $U_{12} \equiv U$, and the occupation states are $|m\rangle = |n_1 n_2\rangle \in \{|00\rangle, |10\rangle, |01\rangle, |11\rangle\}$. We consider situations in which a source-drain bias V is applied to System 1, $\mu_A = \mu_0 + eV/2$, $\mu_B = \mu_0 - eV/2$ (we set $\mu_0 = 0$ for reference).

As pointed out above, we allow here for energy-dependent lead couplings. For small bias voltages and temperature differences compared to the energy scale at which the lead couplings vary, it suffices to consider the expansion of the lead couplings around their value at μ_0,[46]

$$\gamma^\ell(\epsilon) = \gamma_0^\ell + (\epsilon - \mu_0)\partial\gamma^\ell, \tag{18}$$

where $\gamma_0^\ell = \gamma^\ell(\mu_0)$, $\partial\gamma^\ell \equiv \frac{\partial\gamma^\ell(\epsilon)}{\partial\epsilon}|_{\epsilon=\mu_0}$.

A. Current and energy exchange

In Fig. 3(a) we show the electric current through QD1, $I \equiv I_A = -I_B$, at low temperature $k_B T_\ell = 10^{-2}U$ (for illustrative convenience) and bias $eV = 0.3U$ as a function of gate detuning $V_2 - V_1$ and total gating $V_1 + V_2$ in the vicinity of the honeycomb vertex of the stability diagram.[47] Here, we initially assume energy-independent lead couplings which is sufficient to get an overall understanding of the behavior of the system. The large current near the degeneracy lines defined by $\Delta_{00,10} = 0$ and $\Delta_{01,11} = 0$ is due to sequential tunneling processes. Away from these degeneracy lines where sequential tunneling is exponentially suppressed, cotunneling processes give rise to a weak background current. At the degeneracy line $\Delta_{10,01} = 0$ connecting the two triple points at $(V_1, V_2) = (0, 0), (U, U)$, respectively, *nonlocal* cotunneling processes are responsible for the enhanced cotunneling current.[27]

The heat currents that accompany the electric current are shown in Figs. 3(b)–3(d) for different temperatures in the leads. Figure 3(b) shows the heat current in lead A for $k_B T_\ell = 0.1U$. Near the degeneracy lines where $\Delta_{00,10} = 0$ and $\Delta_{01,11} = 0$ and only the occupation of QD1 fluctuates, the heat current shows a behavior similar to that in Fig. 2(b) for a single-level QD. However, at the center of the stability diagram, Coulomb-mediated energy exchange due to the strong Coulomb interaction between the QDs becomes significant. This manifests itself in a cooling of System 1 inside the region bounded by the solid lines at the center of Fig. 3(b) (notice that the color scale is dominated by the heat current with larger magnitude outside this region). From the heat current in lead C shown in Fig. 3(c), the cooling of System 1 is seen to be at the cost of heating System 2. This Coulomb-mediated energy exchange between the two QD systems occurs in spite of the fact that no electrons are exchanged, and it is the driving force behind demon-induced cooling,[9,10] energy harvesting,[4,8,11,12] and Coulomb drag.[26,27]

A simple analytical result for the energy exchange can be found when considering sequential tunneling processes

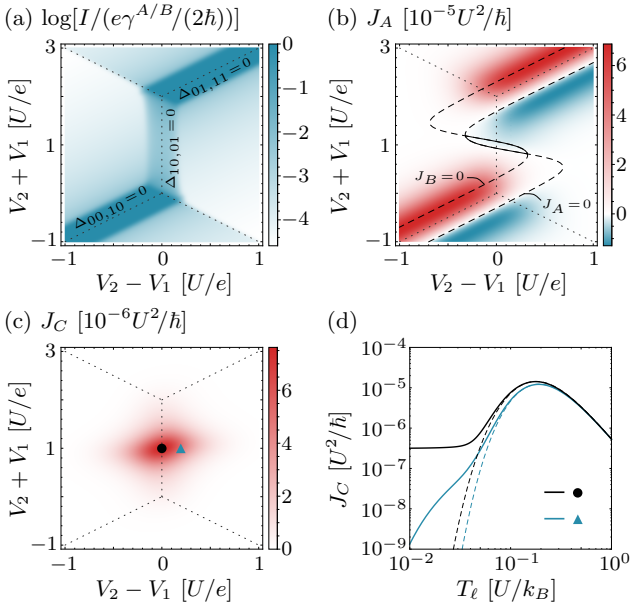

FIG. 3. Electric current and heat currents. (a) Electric current in System 1 as a function of gate detuning $V_2 - V_1$ and total gating $V_2 + V_1$ at low temperature, $k_B T_\ell = 10^{-2}\,U$. (b) Heat current in lead A, J_A, at high temperature, $k_B T_\ell = 10^{-1}\,U$ (contours indicate where J_A and J_B are zero). (c) Heat current in lead C, J_C, for $k_B T_\ell = 10^{-1}\,U$. (d) J_C as a function of temperature with (solid) and without (dashed) cotunneling for the gate configurations marked in (c): $eV_{1,2} = 0.5\,U$ (black circle) and $eV_1 = 0.4\,U$, $eV_2 = 0.6\,U$ (blue triangle). In plots (a)–(c), the degeneracy lines of the honeycomb vertex are indicated with dotted lines. Parameters: $\gamma^{A/B}(\epsilon) = 10^{-3}\,U$, $\gamma^C(\epsilon) = 10^{-2}\,U$, and $eV = 0.3\,U$.

only (indicated by the superscript s). In this case, the total heat currents in System 1, $J_1^s \equiv J_A^s + J_B^s$, and System 2, $J_2^s \equiv J_C^s$, become[11]

$$J_1^s = \frac{U}{\tau^s}(\Gamma^+ - \Gamma^-) + \frac{\mu_A - \mu_B}{e} I^s, \tag{19a}$$

$$J_2^s = \frac{U}{\tau^s}(\Gamma^- - \Gamma^+), \tag{19b}$$

where $\Gamma^- \equiv \Gamma_{00,01}\Gamma_{01,11}\Gamma_{11,10}\Gamma_{10,00}$ and $\Gamma^+ \equiv \Gamma_{00,10}\Gamma_{10,11}\Gamma_{11,01}\Gamma_{01,00}$. The factor τ^s depends on the various sequential tunneling rates, however it is merely a normalization factor and is not reproduced here. The two terms proportional to U in Eq. (19) describe the energy exchange, whereas the last term in Eq. (19a) describes the contribution from Joule heating in System 1. The direction of the energy transfer is determined by the sign of $\Gamma^- - \Gamma^+$. It is therefore convenient to consider the ratio

$$\frac{\Gamma^-}{\Gamma^+} = \Omega e^{U(\beta_2 - \beta_1)}, \tag{20}$$

which describes whether energy is transferred from System 1 to 2 ($\Gamma^-/\Gamma^+ > 1$) or vice versa ($\Gamma^-/\Gamma^+ < 1$).[48]

On the right-hand side of (20), we have taken $\beta_{A/B} = \beta_1$ and $\beta_C = \beta_2$, and have expressed the ratio in terms of an exponential factor, which depends on the temperature in System 1 and System 2, and

$$\Omega \equiv \frac{(\gamma_1^A f_1^A + \gamma_1^B f_1^B)(\gamma_0^A f_0^A e^{-\beta_1\mu_A} + \gamma_0^B f_0^B e^{-\beta_1\mu_B})}{(\gamma_0^A f_0^A + \gamma_0^B f_0^B)(\gamma_1^A f_1^A e^{-\beta_1\mu_A} + \gamma_1^B f_1^B e^{-\beta_1\mu_B})}, \tag{21}$$

which depends on the temperature and bias in System 1 only. The subscript 0 (1) in Eq. (21) indicates that the corresponding function is evaluated at $\Delta_{00,10}$ ($\Delta_{01,11}$) [see Eqs. (6) and (7)].

The exponential factor in (20) shows that a temperature gradient between the two QD systems can generate a net heat flow from the hot to the cold system. This is the mechanism behind the heat engine studied in Ref. 11. On the other hand, a closer inspection of the Ω factor reveals that it is, in fact, possible to generate a net heat flow in the opposite direction, i.e. from the cold to the hot system, and this is the cause of the negative heat current at the center of Fig. 3(b). This so-called demon-induced cooling effect will be discussed further in Sec. V B below.

When the applied bias and temperature are small compared to the interdot Coulomb interaction, $eV, k_BT \ll U$, cotunneling processes start to dominate the heat currents in the center of the stability diagram. This is demonstrated in Fig. 3(d) which shows the heat current J_C as a function of temperature for the two different gate tunings marked with symbols in Fig. 3(c). Considering sequential tunneling only (dashed curves), the heat current is quenched at $k_BT \ll U$ as $\Gamma_{01,11}$ and $\Gamma_{10,00}$ in Γ^- become exponentially suppressed. This can also be understood from the illustration in Fig. 4(a), which shows the sequence of sequential tunneling processes corresponding to Γ^-. However, nonlocal cotunneling processes allow the system to fluctuate between the two states $10 \leftrightarrow 01$, as illustrated in Fig. 4(b), and thereby transfer heat between the systems. The nonlocal cotunneling channel is open for $|\Delta_{01,10}| \lesssim \max\{|eV/2|, k_BT\}$, and the associated heat current is thus also suppressed at low temperature when $\Delta_{01,10} \neq 0$ as illustrated by the blue curve (triangle) in Fig. 3(d). For zero detuning, $\Delta_{01,10} = 0$ (circle), the nonlocal cotunneling rates, and hence also the heat current, saturate at $k_BT \ll eV$. In Sec. V B, we demonstrate that nonlocal cotunneling processes have a significant effect on the demon-induced cooling mechanism.

B. Demon-induced cooling

The effect of cooling System 1 at the cost of heating System 2 has recently been discussed in the context of a Maxwell's demon, where System 2 plays the role of the demon that performs the necessary feedback to cool System 1.[9,10] To maximize the achievable cooling power for refrigeration purposes,[49] large tunneling rates, $\gamma^\ell(\epsilon) \sim k_BT, U$, are desirable [cf. Eq. (19)].

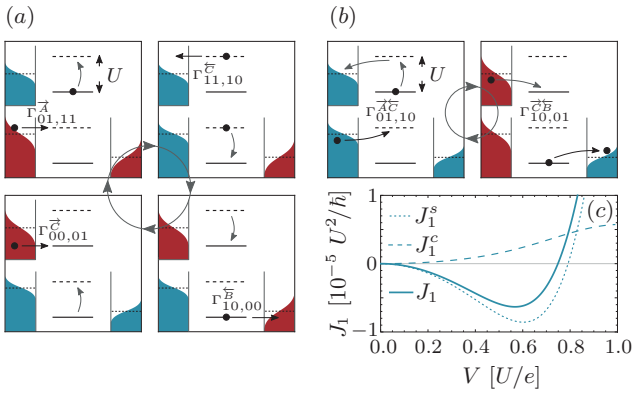

FIG. 4. Cooling cycle and effect of cotunneling. (a) Sequence of sequential tunneling processes that cool System 1. The positions of the dot levels when the other dot is empty (occupied) is illustrated with solid (dotted) lines. (b) Sequence of nonlocal cotunneling processes. (c) Heat current J_1 as a function of bias voltage. The individual contributions from sequential (J_1^s) and cotunneling (J_1^c) are also shown. Parameters: $eV_1 = eV_2 = U/2$, $\gamma^{A/B}(\epsilon) = 10^{-3}\,U$, $\gamma^C(\epsilon) = 10^{-2}\,U$, and $k_BT = 0.1\,U$.

However, large tunneling rates increase the contribution from higher-order tunneling processes, thus emphasizing the importance of including cotunneling processes in the analysis.

In the following, we consider the case of uniform temperature $T_\ell \equiv T$ whereby the exponential factor in (20) becomes unity. This allows us to focus on the Ω factor in the optimization of the performance. Equation (19) shows that the cooling mechanism is governed by Γ^- since, as illustrated in Fig. 4(a), in a full sequential cycle an amount of energy U is transferred from System 1 to System 2, thereby cooling System 1. In the following, we discuss how to increase the cooling power by maximizing the success rate for completing the cooling cycle in Fig. 4(a).

1. *Cotunneling limitations*

Although the cycle of nonlocal cotunneling processes illustrated in Fig. 4(b) gives the same net transfer of electrons as the sequential tunneling cycle in Fig. 4(a), the net energy transfer is different for the two cases. As illustrated, in a cotunneling process also electrons below (above) the electrochemical potential can tunnel out of lead A (into lead B), and thus reduce the demon-induced cooling effect.

In Fig. 4(c), we show the heat current $J_1 = J_A + J_B$ together with its individual contributions from sequential (J_1^s) and cotunneling (J_1^c) processes. Overall, System 1 cools at low bias, while at higher bias, Joule heating becomes dominant. The minimum in J_1 as a function of bias voltage is referred to as the maximum cooling power, $J_{1,\max} \equiv \min J_1(V)$. As the figure shows, cotunneling

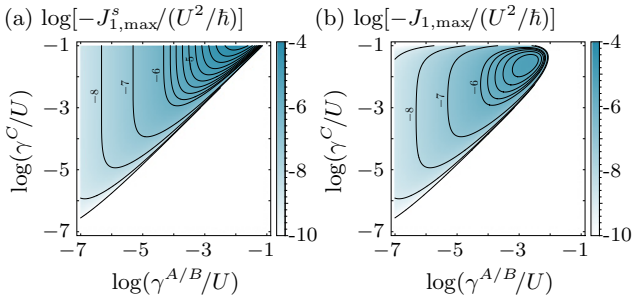

FIG. 5. Maximum cooling power, $J_{1,\max}$, as a function of the lead coupling strengths for energy-independent couplings. (a) Sequential tunneling, and (b) sequential plus cotunneling. Parameters: $eV_1 = eV_2 = U/2$ and $k_BT = 0.1\,U$.

reduces the maximum cooling power.

Figure 5 shows how the maximum cooling power $J_{1,\max}$ scales with the lead coupling strengths. As the figure demonstrates, the rates must satisfy $\gamma^C > \gamma^{A/B}$ to ensure that System 2 acts sufficiently fast to perform the desired feedback such that the cooling cycle in Fig. 4(a) is completed when an electron tunnels between leads A and B.[49] In the region of large cooling power, cotunneling processes start to become important, and hence there is a trade-off between sequential tunneling which improves the cooling effect, and nonlocal cotunneling, which limits the effect. In addition, the area in the lead coupling parameter space where refrigeration is possible is also reduced when cotunneling is included.

2. *Performance boosting*

Here we demonstrate that energy-dependent lead couplings can enhance the demon-induced cooling power significantly. We restrict the discussion to lead couplings with a linear energy dependence [cf. Eq. (18)].

By inspecting the Ω factor in Eq. (21), we find that for $\mu_A > \mu_B$, the configuration illustrated in the inset of Fig. 6, where γ_0^A, γ_1^B are reduced compared to γ_1^A, γ_0^B, boosts the Ω factor (and thereby Γ^-/Γ^+). This results in an enhancement of the cooling power by suppressing tunneling between leads A and B via two sequential tunneling processes, while at the same time promoting the processes of the cooling cycle in Fig. 4(a).

In Fig. 6 we show the maximum cooling power as a function of temperature for different situations for the energy dependence of the lead couplings, from the top (black) curve showing the result for energy *independent* lead couplings, to increasing energy dependence, i.e., increasing $|\partial\gamma^{A/B}|$, towards the bottom (light blue) curve. When tuning the energy dependence of the lead couplings, a significant enhancement of the cooling power is achieved. Again, the effect of cotunneling processes is to reduce the attainable cooling power (solid lines) relative to the cooling power obtained when only considering sequential tunneling processes (dashed lines).

VI. CONCLUSIONS

In summary, we have studied thermoelectric effects in CCQD systems with a T-matrix based master-equation approach for the calculation of charge and heat currents. The method (i) treats *incoherent* sequential tunneling processes and *coherent* cotunneling processes on an equal footing, and (ii) can account for energy-dependent tunnel couplings to the leads. Both are important for quantitative predictions and optimization of the thermoelectric properties of CCQDs.

To benchmark the master-equation method, we considered a non-interacting single-level QD coupled to source and drain leads for which the Landauer-Büttiker formalism is exact. In the regime of validity of our method, i.e. small tunnel couplings to the leads, $\gamma < k_BT$, we demonstrated excellent agreement with the results from the Landauer-Büttiker method when cotunneling processes are included in the master equation.

Furthermore, we studied the effect of cotunneling processes and energy-dependent lead couplings on the thermoelectric properties of a CCQD system consisting of two QDs exhibiting a Maxwell's demon-like cooling mechanism.[9,10] First of all, we showed that cotunneling processes reduce the cooling effect since they do not share the delicate energy selectivity inherent to sequential tunneling processes. This results in a significant reduction of the achievable cooling power compared to the sequential tunneling result when the lead couplings are increased

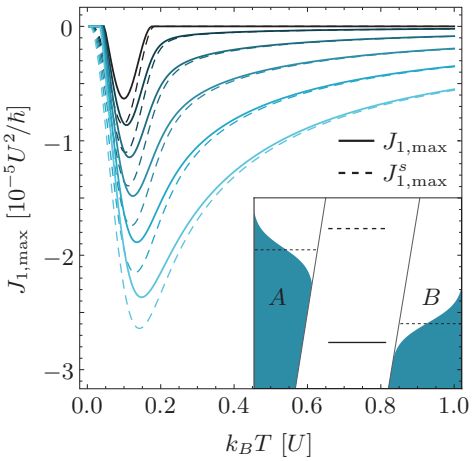

FIG. 6. Performance boosting with energy-dependent lead couplings. Maximum cooling power as function of temperature for different lead coupling strengths: $\partial\gamma^A = -\partial\gamma^B = x\gamma_0^{A/B}/U$ (sketched in the inset), with $x = 0$ (black) to $x = 1$ (light blue) in steps of 0.2. The full (dashed) lines show the result obtained with (without) cotunneling. Parameters: $\gamma^C(\epsilon) = 10^{-2}\,U$, $\gamma_0^{A/B} = 10^{-3}\,U$, $eV_1 = eV_2 = U/2$, and $\eta = 10^{-4}\,U$.

to maximize the cooling power from sequential tunneling processes. Secondly, we demonstrated that it is possible to boost the cooling power significantly via other means by introducing energy-dependent lead couplings and properly tuning their energy dependence. In this case, we showed that cotunneling still reduces the cooling power significantly, thus emphasizing the importance of cotunneling processes in quantitative analyses.

Applying the methodology to other mesoscopic systems allows for testing of new thermoelectric device ideas beyond sequential tunneling estimates, as well as for improved comparison with experiments.

ACKNOWLEDGMENTS

We would like to thank J. P. Pekola, M. Leijnse, C. Timm, and N. M. Gergs for valuable discussions. K.K. acknowledges support from the European Union's Horizon 2020 research and innovation programme under the Marie Sklodowska-Curie grant agreement no. 713683 (COFUNDfellowsDTU). The Center for Nanostructured Graphene (CNG) is sponsored by the Danish Research Foundation, Project DNRF103.

Appendix A: Cotunneling rates and regularization procedure

The rate for elastic cotunneling through a single-level QD is given by

$$\tilde{\Gamma}^{\vec{\ell}\,\vec{\ell'}}_{mm} = \int \frac{d\epsilon}{2\pi\hbar}\gamma^{\ell}(\epsilon)\gamma^{\ell'}(\epsilon)f^{\ell}(\epsilon)\bar{f}^{\ell'}(\epsilon)\left|\frac{1}{\Delta_{vm}\pm\epsilon+i\eta}\right|^2, \tag{A1}$$

where v refers to the virtually occupied intermediate state created in the process in which an initially empty level is filled ($+\epsilon$) or an initially filled level is emptied ($-\epsilon$).

In pair-cotunneling processes, two electrons tunnel simultaneously out of (into) the QD system and into (out of) the leads ℓ and ℓ'. The rate for such processes takes the form

$$\tilde{\Gamma}^{\overleftarrow{\ell}\,\overleftarrow{\ell'}}_{mn} = \int \frac{d\epsilon}{2\pi\hbar}\gamma^{\ell}(\epsilon)\gamma^{\ell'}(\Delta_{nm}-\epsilon)\bar{f}^{\ell}(\epsilon)\bar{f}^{\ell'}(\Delta_{nm}-\epsilon) \times\left|\frac{1}{\Delta_{vm}-\epsilon+i\eta}+\frac{1}{\Delta_{v'n}+\epsilon+i\eta}\right|^2, \tag{A2}$$

where v (v') refers to the virtually occupied intermediate state in a process in which an electron initially tunnels from the QD system and into lead ℓ (ℓ'). Similarly,

$$\tilde{\Gamma}^{\vec{\ell}\,\vec{\ell'}}_{mn} = \int \frac{d\epsilon}{2\pi\hbar}\gamma^{\ell}(\epsilon)\gamma^{\ell'}(\Delta_{mn}-\epsilon)f^{\ell}(\epsilon)f^{\ell'}(\Delta_{mn}-\epsilon) \times\left|\frac{1}{\Delta_{vn}-\epsilon+i\eta}+\frac{1}{\Delta_{v'm}+\epsilon+i\eta}\right|^2, \tag{A3}$$

where v (v') refers to the virtually occupied intermediate state in a process in which an electron initially tunnels from lead ℓ' (ℓ) and into the QD system.

The bare cotunneling rates are formally divergent in the limit $\eta \to 0$. The divergence stems from factors involving $|x+i\eta|^{-2}$, $x,\eta\in\mathbb{R}$. Using that[29]

$$\left|\frac{1}{x+i\eta}\right|^2 \to \frac{\pi}{\eta}\delta(x)+\mathcal{P}\frac{1}{x^2}, \quad \eta\to 0^+, \tag{A4}$$

where $\mathcal{P}$ denotes the principal value, we can identify the divergent contributions, e.g. from Eq. (8),

$$\tilde{\Gamma}^{\vec{\ell}\,\overleftarrow{\ell'}}_{mn} \to \frac{\hbar}{2\eta}\left(\Gamma^{\vec{\ell}}_{mv}\Gamma^{\overleftarrow{\ell'}}_{vn}+\Gamma^{\overleftarrow{\ell'}}_{mv'}\Gamma^{\vec{\ell}}_{v'n}\right)+\Gamma^{\vec{\ell}\,\overleftarrow{\ell'}}_{mn}, \tag{A5}$$

where $\Gamma^{\vec{\ell}\,\overleftarrow{\ell'}}_{mn}$ denotes the regularized cotunneling rate, and we have used the fact that the cross-terms from the absolute squared in Eq. (8) do not contribute to any divergences. The divergent contribution is proportional to products of two sequential tunneling rates. These correspond to two energy-conserving (sequential) transitions that can be identified with the intermediate processes in the cotunneling process. The sum is over the possible sequences of intermediate transitions. Similarly, for the cotunneling heat rates, e.g. Eq. (12),

$$\tilde{W}^{\vec{\ell}\,\overleftarrow{\ell'}}_{\ell,mn} \to \frac{\hbar}{2\eta}\left[W^{\vec{\ell}}_{\ell,mv}\Gamma^{\overleftarrow{\ell'}}_{vn}+\Gamma^{\overleftarrow{\ell'}}_{mv'}W^{\vec{\ell}}_{\ell,v'n}\right]+W^{\vec{\ell}\,\overleftarrow{\ell'}}_{\ell,mn}, \tag{A6}$$

or the corresponding heat rate in lead ℓ',

$$\tilde{W}^{\vec{\ell}\,\overleftarrow{\ell'}}_{\ell',mn} \to \frac{\hbar}{2\eta}\left[\Gamma^{\vec{\ell}}_{mv}W^{\overleftarrow{\ell'}}_{\ell',vn}+W^{\overleftarrow{\ell'}}_{\ell',mv'}\Gamma^{\vec{\ell}}_{v'n}\right]+W^{\vec{\ell}\,\overleftarrow{\ell'}}_{\ell',mn}. \tag{A7}$$

We apply the regularization scheme in Ref. 29 and subtract the terms scaling as η^{-1}.

In the case of identical temperatures in the leads, using the identity $f(\epsilon_1)[1-f(\epsilon_2)] = n(\epsilon_1-\epsilon_2)[f(\epsilon_2)-f(\epsilon_1)]$, where $f(\epsilon)$ is the Fermi-Dirac distribution and $n(\epsilon)$ is the Bose-Einstein distribution, the cotunneling rates can be written in the form

$$I = \int_{-\infty}^{\infty} d\epsilon P(\epsilon)\left[f^{\ell'}(\epsilon)-f^{\ell}(\epsilon+\Delta_3)\right] \times\left|\frac{k_1}{\epsilon-\Delta_1+i\eta}+\frac{k_2}{\Delta_2-\epsilon+i\eta}\right|^2, \tag{A8}$$

where $P(\epsilon)$ is assumed to be a polynomial, $P(\epsilon) = \sum_{i=0}^{n} c_i\epsilon^n$, of maximum order $n=2$ for $k_1-k_2\neq 0$ and $n=4$ for $k_1-k_2=0$ to ensure that the result below is well-defined. The derivation is in line with the one in Ref. 27, and the integral becomes

$$
\begin{aligned}
I =& k_1^2 P'(\Delta_1)\mathrm{Re}\left[\psi^-_{\ell'}(\Delta_1) - \psi^-_{\ell}(\Delta_1+\Delta_3)\right] + \frac{k_1^2\beta}{2\pi}P(\Delta_1)\mathrm{Im}\left[\psi^-_{1_{\ell'}}(\Delta_1) - \psi^-_{1_{\ell}}(\Delta_1+\Delta_3)\right] \\
&+ k_2^2 P'(\Delta_2)\mathrm{Re}\left[\psi^-_{\ell'}(\Delta_2) - \psi^-_{\ell}(\Delta_2+\Delta_3)\right] + \frac{k_2^2\beta}{2\pi}P(\Delta_2)\mathrm{Im}\left[\psi^-_{1_{\ell'}}(\Delta_2) - \psi^-_{1_{\ell}}(\Delta_2+\Delta_3)\right] \\
&- \frac{2k_1k_2}{\Delta_1-\Delta_2}\left(P(\Delta_1)\mathrm{Re}\left[\psi^-_{\ell'}(\Delta_1) - \psi^-_{\ell}(\Delta_1+\Delta_3)\right] - P(\Delta_2)\mathrm{Re}\left[\psi^-_{\ell'}(\Delta_2) - \psi^-_{\ell}(\Delta_2+\Delta_3)\right]\right) + R + \mathcal{O}(\eta^{-1}) + \mathcal{O}(\eta),
\end{aligned}
\tag{A9}
$$

where

$$
\psi_{(1)}{}^{\pm}_{\ell}(\epsilon) \equiv \psi_{(1)}\left(\frac{1}{2} \pm i\frac{\beta}{2\pi}(\epsilon-\mu_\ell)\right), \tag{A10}
$$

with ψ (ψ_1) being the digamma (trigamma) function, and

$$
R = \begin{cases} c_2(\mu_{\ell'}-\mu_\ell+\Delta_3)(k_1-k_2)^2, \ k_1-k_2 \neq 0, \\ c_4(\mu_{\ell'}-\mu_\ell+\Delta_3)k_1^2(\Delta_1-\Delta_2)^2, \ k_1-k_2 = 0. \end{cases} \tag{A11}
$$

The term $\mathcal{O}(\eta^{-1})$ is omitted by regularization before taking the limit $\eta \to 0$. For $k_BT < \gamma$ (outside the regime of validity), the failure of the approach is seen as a logarithmic divergence of the digamma functions near the degeneracy points.

In studies of thermoelectric effects where different lead temperatures as well as more general energy dependence of the lead couplings become relevant, one must turn to a numerical procedure. In this case, we evaluate the cotunneling integrals numerically with a small but finite η, and subsequently subtract contributions of order η^{-1} as shown in, e.g., Eqs. (A5)–(A7). In particular, we have applied the numerical procedure in Figs. 2 and 6, and we have stated the values of η in the figure captions.

* nicwall@nanotech.dtu.dk
† kkaa@nanotech.dtu.dk

[1] J. P. Pekola, O.-P. Saira, V. F. Maisi, A. Kemppinen, M. Möttönen, Y. A. Pashkin, and D. V. Averin, "Single-electron current sources: Toward a refined definition of the ampere," Rev. Mod. Phys. **85**, 1421 (2013).

[2] F. Giazotto, T. T. Heikkilä, A. Luukanen, A. M. Savin, and J. P. Pekola, "Opportunities for mesoscopics in thermometry and refrigeration: Physics and applications," Rev. Mod. Phys. **78**, 217 (2006).

[3] M. S. Dresselhaus, G. Chen, M. Y. Tang, R. G. Yang, H. Lee, D. Z. Wang, Z. F. Ren, J.-P. Fleurial, and P. Gogna, "New directions for low-dimensional thermoelectric materials," Adv. Mater. **19**, 1043 (2007).

[4] H. Thierschmann, R. Sánchez, B. Sothmann, H. Buhmann, and L. W. Molenkamp, "Thermoelectrics with Coulomb-coupled quantum dots," C. R. Physique **17**, 1109 (2016).

[5] D. Bischoff, M. Eich, O. Zilberberg, C. Rössler, T. Ihn, and K. Ensslin, "Measurement back-action in stacked graphene quantum dots," Nano. Lett. **15**, 6003 (2015).

[6] A. J. Keller, J. S Lim, D. Sánchez, R. López, S. Amasha, J. A. Katine, H. Shtrikman, and D. Goldhaber-Gordon, "Cotunneling drag effect in Coulomb-coupled quantum dots," Phys. Rev. Lett. **117**, 066602 (2016).

[7] A. Hamo, A. Benyamini, I. Shapir, I. Khivrich, J. Waissman, K. Kaasbjerg, Y. Oreg, F. von Oppen, and S. Ilani, "Electron attraction mediated by Coulomb repulsion," Nature (London) **535**, 395 (2016).

[8] H. Thierschmann, R. Sánchez, B. Sothmann, F. Arnold, C. Heyn, W. Hansen, H. Buhmann, and L. W. Molenkamp, "Three-terminal energy harvester with coupled quantum dots," Nature Nanotech. **10**, 854 (2015).

[9] J. V. Koski, A. Kutvonen, I. M. Khaymovich, T. Ala-Nissila, and J. P. Pekola, "On-chip Maxwell's demon as an information-powered refrigerator," Phys. Rev. Lett. **115**, 260602 (2015).

[10] P. Strasberg, G. Schaller, T. Brandes, and M. Esposito, "Thermodynamics of a physical model implementing a Maxwell demon," Phys. Rev. Lett. **110**, 040601 (2013).

[11] R. Sánchez and M. Büttiker, "Optimal energy quanta to current conversion," Phys. Rev. B **83**, 085428 (2011).

[12] B. Sothmann, R. Sánchez, and A. N. Jordan, "Thermoelectric energy harvesting with quantum dots," Nanotechnology **26**, 032001 (2014).

[13] R. Sánchez, H. Thierschmann, and L. W. Molenkamp, "All-thermal transistor based on stochastic switching," Phys. Rev. B **95**, 241401 (2017).

[14] J. V. Koski and J. P. Pekola, "Maxwell's demons realized in electronic circuits," C. R. Physique **17**, 1130 (2016).

[15] G. Benenti, G. Casati, K. Saito, and R. S. Whitney, "Fundamental aspects of steady-state conversion of heat to work at the nanoscale," Phys. Rep. **694**, 1 (2017).

[16] F. Haupt, M. Leijnse, H. L. Calvo, L. Classen, J. Splettstoesser, and M. R. Wegewijs, "Heat, molecular vibrations, and adiabatic driving in non-equilibrium transport through interacting quantum dots," Phys. Status Solidi B **250**, 2315 (2013).

[17] M. Leijnse, M. R. Wegewijs, and K. Flensberg, "Nonlinear thermoelectric properties of molecular junctions with vibrational coupling," Phys. Rev. B **82**, 045412 (2010).

[18] J. Argüello-Luengo, D. Sánchez, and R. López, "Heat asymmetries in nanoscale conductors: The role of decoherence and inelasticity," Phys. Rev. B **91**, 165431 (2015).

[19] D. Sánchez and R. López, "Nonlinear phenomena in quantum thermoelectrics and heat," C. R. Physique **17**, 1060 (2016).

[20] N. M. Gergs, C. B. M. Hörig, M. R. Wegewijs, and D. Schuricht, "Charge fluctuations in nonlinear heat transport," Phys. Rev. B **91**, 201107(R) (2015).

[21] K. M. Seja, G. Kiršanskas, C. Timm, and A. Wacker, "Violation of Onsager's theorem in approximate master equation approaches," Phys. Rev. B **94**, 165435 (2016).

[22] A.-M. Daré and P. Lombardo, "Powerful Coulomb drag thermoelectric engine," (2017), arXiv:1704.04064.

[23] H. Bruus and K. Flensberg, *Many-body Quantum Theory in Condensed Matter Physics* (Oxford University Press,

2004).
[24] J. Waissman, M. Honig, S. Pecker, A. Benyamini, A. Hamo, and S. Ilani, "Realization of pristine and locally tunable one-dimensional electron systems in carbon nanotubes," Nature Nanotech. **8**, 569 (2013).
[25] Y. Zhang, G. Lin, and J. Chen, "Three-terminal quantum-dot refrigerators," Phys. Rev. E **91**, 052118 (2015).
[26] R. Sánchez, R. López, D. Sánchez, and M. Büttiker, "Mesoscopic Coulomb drag, broken detailed balance, and fluctuation relations," Phys. Rev. Lett. **104**, 076801 (2010).
[27] K. Kaasbjerg and A.-P. Jauho, "Correlated Coulomb drag in capacitively coupled quantum-dot structures," Phys. Rev. Lett. **116**, 196801 (2016).
[28] J. S. Lim, R. López, and D. Sánchez, "Engineering drag currents in Coulomb coupled quantum dots," (2016), arXiv:1612.06627.
[29] M. Turek and K. A. Matveev, "Cotunneling thermopower of single electron transistors," Phys. Rev. B **65**, 115332 (2002).
[30] J. Koch, F. von Oppen, Y. Oreg, and E. Sela, "Thermopower of single-molecule devices," Phys. Rev. B **70**, 195107 (2004).
[31] C. Timm, "Tunneling through molecules and quantum dots: Master-equation approaches," Phys. Rev. B **77**, 195416 (2008).
[32] J. König, J. Schmid, H. Schoeller, and G. Schön, "Resonant tunneling through ultrasmall quantum dots: Zero-bias anomalies, magnetic-field dependence, and boson-assisted transport," Phys. Rev. B **54**, 16820 (1996).
[33] A. Thielmann, M. H. Hettler, J. König, and G. Schön, "Cotunneling current and shot noise in quantum dots," Phys. Rev. Lett. **95**, 146806 (2005).
[34] J. N. Pedersen and A. Wacker, "Tunneling through nanosystems: Combining broadening with many-particle states," Phys. Rev. B **72**, 195330 (2005).
[35] C. Timm, "Time-convolutionless master equation for quantum dots: Perturbative expansion to arbitrary order," Phys. Rev. B **83**, 115416 (2011).
[36] S. Amasha, A. J. Keller, I. G. Rau, A. Carmi, J. A. Katine, H. Shtrikman, Y. Oreg, and D. Goldhaber-Gordon, "Pseudospin-resolved transport spectroscopy of the Kondo effect in a double quantum dot," Phys. Rev. Lett. **110**, 046604 (2013).
[37] J. Koch, M. E. Raikh, and F. von Oppen, "Pair tunneling through single molecules," Phys. Rev. Lett. **96**, 056803 (2006).
[38] M. Leijnse, M. R. Wegewijs, and M. H. Hettler, "Pair tunneling resonance in the single-electron transport regime," Phys. Rev. Lett. **103**, 156803 (2009).
[39] S. Koller, M. Grifoni, M. Leijnse, and M. R. Wegewijs, "Density-operator approaches to transport through interacting quantum dots: Simplifications in fourth order perturbation theory," Phys. Rev. B **82**, 235307 (2010).
[40] Notice that for the particular pair-cotunneling processes with $\ell = \ell'$ one should include a factor of two in the current, however, for single-level QDs discussed here such processes do not contribute.
[41] M. F. Ludovico, M. Moskalets, D. Sánchez, and L. Arrachea, "Dynamics of energy transport and entropy production in ac-driven quantum electron systems," Phys. Rev. B **94**, 035436 (2016).
[42] J. Koch, F. von Oppen, and A. V. Andreev, "Theory of the Franck-Condon blockade regime," Phys. Rev. B **74**, 205438 (2006).
[43] H. Haug and A.-P. Jauho, *Quantum Kinetics in Transport and Optics of Semiconductors* (Springer Berlin Heidelberg, 2008).
[44] A. V. Feshchenko, J. V. Koski, and J. P. Pekola, "Experimental realization of a Coulomb blockade refrigerator," Phys. Rev. B **90**, 201407 (2014).
[45] W. Lee, K. Kim, W. Jeong, L. A. Zotti, F. Pauly, J. C. Cuevas, and P. Reddy, "Heat dissipation in atomic-scale junctions," Nature **498**, 209 (2013).
[46] In the numerical calculations we take the absolute value of the lead coupling strengths to ensure that the linear expansion yields non-negative coupling strengths.
[47] W. G. van der Wiel, S. De Franceschi, J. M. Elzerman, T. Fujisawa, S. Tarucha, and L. P. Kouwenhoven, "Electron transport through double quantum dots," Rev. Mod. Phys. **75**, 1 (2002).
[48] R. Sánchez and M. Büttiker, "Detection of single-electron heat transfer statistics," EPL **100**, 47008 (2012).
[49] A. Kutvonen, J. Koski, and T. Ala-Nissila, "Thermodynamics and efficiency of an autonomous on-chip Maxwell's demon," Scientific Reports **6**, 21126 (2016).

B.2 Publication II

Electron Waiting Times of a Cooper Pair Splitter

Nicklas Walldorf, Ciprian Padurariu, Antti-Pekka Jauho, and Christian Flindt

Physical Review Letters 120, 087701 (2018)

Electron Waiting Times of a Cooper Pair Splitter

Nicklas Walldorf,[1] Ciprian Padurariu,[2] Antti-Pekka Jauho,[1] and Christian Flindt[2]

[1] *Center for Nanostructured Graphene (CNG), Department of Micro- and Nanotechnology, Technical University of Denmark, DK-2800 Kongens Lyngby, Denmark*
[2] *Department of Applied Physics, Aalto University, 00076 Aalto, Finland*

Electron waiting times are an important concept in the analysis of quantum transport in nano-scale conductors. Here we show that the statistics of electron waiting times can be used to characterize Cooper pair splitters that create spatially separated spin-entangled electrons. A short waiting time between electrons tunneling into different leads is associated with the fast emission of a split Cooper pair, while long waiting times are governed by the slow injection of Cooper pairs from a superconductor. Experimentally, the waiting time distributions can be measured using real-time single-electron detectors in the regime of slow tunneling, where conventional current measurements are demanding. Our work is important for understanding the fundamental transport processes in Cooper pair splitters and the predictions may be verified using current technology.

Introduction.— Quantum technologies that exploit non-classical phenomena such as the discreteness of physical observables, coherent superpositions, and quantum entanglement promise solutions to current challenges in communication, computation, sensing, and metrology [1]. For solid-state quantum computers, an important building block is a device that can generate pairs of entangled electrons [2]. In one prominent approach, Cooper pairs in a superconductor are converted into spatially separated electrons that preserve the entanglement of their spins [3, 4]. Cooper pair splitters have been realized in architectures based on superconductor–normal-state hybrid systems [5–7], InAs nanowires [8–11], carbon nanotubes [12–16], and recently graphene structures [17–19].

The efficiency of Cooper pair splitters can be determined using conductance measurements [8–17]. For some setups, the efficiency is approaching unity [10, 14], indicating that Cooper pair splitters may be suited for electronics-based quantum technologies. One may now hope to detect the entanglement of the outgoing electrons by measuring the cross-correlations of the currents in the output channels [10, 20–22]. However, while these approaches are based on conventional current measurements, recent progress in the real-time detection of single electrons is opening another promising avenue for understanding quantum transport in nano-scale devices [23].

In this Letter we propose to characterize Cooper pair splitters using the distribution of electron waiting times. The electron waiting time is the time that passes between subsequent tunneling events. Waiting time distributions (WTDs) have in recent years been investigated theoretically for quantum transport in quantum dots [24–38], mesoscopic conductors [39–46], and superconducting devices [47–51]. Moreover, in a very recent experiment, the distribution of electron waiting times was measured for a quantum dot [52]. Here, we show that the WTD is a sensitive tool to understand the working principle of the Cooper pair splitter in Fig. 1(a). As we discuss below, WTDs such as those in Fig. 1(b) and (c) provide clear signatures of the Cooper pair splitting. Specifically, the

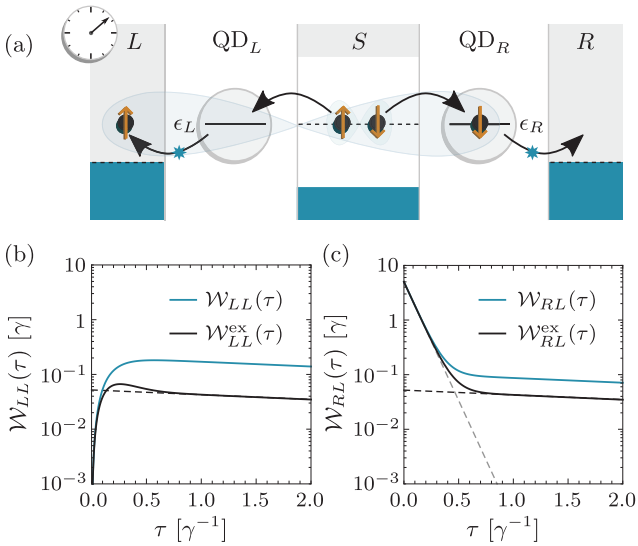

Figure 1. Electron waiting times of a Cooper pair splitter. (a) Two QDs are coupled to a superconducting source of Cooper pairs and two normal-metal drains. A tunneling event (star) starts the clock, which symbolizes the measurement scheme based on single-electron detectors [23, 52–54]. A subsequent tunneling event stops it. WTDs for tunneling into the same/different leads are shown in panels (b) and (c). The WTDs $\mathcal{W}_{ji}(\tau)$ [$\mathcal{W}^{\rm ex}_{ji}(\tau)$] are evaluated using Eq. (4) [(5)]. Parameters are $\xi := \gamma_L = \gamma_R = 10\gamma$, $\gamma_{\rm CPS} = \gamma_{\rm EC} = \gamma$, and $\epsilon_L = \epsilon_R = 0$. Dashed lines are exponentials with decay rates ξ (grey) and $2\gamma^2_{\rm CPS}/\xi$ (black). Corresponding to the recent experiments, the rate γ would be on the order of kilo-hertz, and the waiting times would be in the millisecond range [52–54].

splitting of Cooper pairs is associated with a large peak at short times in the WTD for tunneling into different drains, Fig. 1(c). This information is complementary to what can be learned from conventional current and noise measurements. In addition, with the ability to detect single electrons participating in Andreev tunneling across normal-state–superconductor interfaces [53, 54], a measurement of the electron waiting times in a Cooper pair splitter appears feasible with current technology. More

precisely, in the recent experiment on WTDs, the typical waiting times were on the order of milliseconds [52], which corresponds well to the kilo-hertz tunneling rates reported in Refs. [53, 54]. Importantly, such low tunneling rates do not produce electrical currents that can be measured using standard techniques. On the other hand, the tunneling of electrons can be detected in real-time, and the distribution of waiting times can be measured.

Cooper pair splitter.— The Cooper pair splitter consists of two quantum dots (QDs) coupled to a superconductor and two normal leads [4]. The grounded superconductor acts as a source of Cooper pairs. The negatively biased leads serve as drains for electrons in the QDs. Coulomb interactions are so strong that each QD cannot be occupied by more than one electron at a time. With a large superconducting gap, we may focus on the subgap transport (the working regime is specified below). The superconductor can then be included in an effective Hamiltonian of the QDs reading [55–61]

$$\begin{aligned}\hat{H}_{\rm QDs} =& \sum_{\ell\sigma} \epsilon_\ell \hat{d}^\dagger_{\ell\sigma}\hat{d}_{\ell\sigma} - \gamma_{\rm EC}\sum_{\sigma}\Big(\hat{d}^\dagger_{L\sigma}\hat{d}_{R\sigma} + \text{h.c.}\Big) \\ &- \frac{\gamma_{\rm CPS}}{\sqrt{2}}\Big(\hat{d}^\dagger_{L\downarrow}\hat{d}^\dagger_{R\uparrow} - \hat{d}^\dagger_{L\uparrow}\hat{d}^\dagger_{R\downarrow} + \text{h.c.}\Big),\end{aligned} \tag{1}$$

Here, the operator $\hat{d}^\dagger_{\ell\sigma}$ ($\hat{d}_{\ell\sigma}$) creates (annihilates) an electron in QD_ℓ, $\ell \in \{L, R\}$ with spin $\sigma \in \{\uparrow, \downarrow\}$ and energy ϵ_ℓ relative to the chemical potential of the superconductor, $\mu_S = 0$. The amplitudes $\gamma_{\rm CPS}$ and $\gamma_{\rm EC}$ correspond to Cooper pair splitting (CPS) and elastic cotunneling (EC) processes, respectively, and can be expressed in terms of microscopic parameters following Ref. [55]. We have excluded direct coupling between the QDs as in the experiment of Ref. [17], but such processes can easily be incorporated within our formalism. In the CPS processes, a Cooper pair in the superconductor is converted into two spin-entangled electrons in a singlet state with one electron in each QD, or vice versa. Such processes are favored when the empty state of the QDs is energetically degenerate with the doubly occupied state, $\epsilon_L + \epsilon_R = 0$ [62–65]. In the spin-preserving EC processes, an electron in one of the QDs is transferred via the superconductor to the other QD. These processes are on resonance when the QD levels are energetically aligned, $\epsilon_L = \epsilon_R$.

Transport through each QD is described by resonant tunneling and must be treated to all orders in the coupling to the leads. When the resonant level is deep inside the transport energy window, the transport can be described by a Markovian quantum master equation for the reduced density matrix $\hat{\rho}$ of the QDs (with $\hbar = 1$) [55, 66]

$$\frac{d}{dt}\hat{\rho} = \mathcal{L}\hat{\rho} = -i[\hat{H}_{\rm QDs}, \hat{\rho}] + \mathcal{D}\hat{\rho}. \tag{2}$$

Here, the Liouvillian $\mathcal{L}$ describes both coherent processes governed by $\hat{H}_{\rm QDs}$, and incoherent single-electron jumps to the normal metals captured by the Lindblad dissipator

$$\mathcal{D}\hat{\rho} = \sum_{\ell\sigma}\gamma_\ell\left[\hat{d}_{\ell\sigma}\hat{\rho}\hat{d}^\dagger_{\ell\sigma} - \frac{1}{2}\{\hat{\rho}, \hat{d}^\dagger_{\ell\sigma}\hat{d}_{\ell\sigma}\}\right]. \tag{3}$$

We take the rate γ_ℓ at which electrons leave via lead ℓ to be independent of the spin. To summarize, we work in the regime $U, \Delta \gg |V| \gg \epsilon_\ell, \gamma_\ell, \gamma_{\rm CPS}, \gamma_{\rm EC}$, where U is the Coulomb interaction energy, Δ is the superconducting gap, and V is the negative voltage. Due to the large negative bias, the electron transport from the QDs to the drain electrodes is unidirectional and the thermal smearing of the distribution functions in the leads becomes unimportant. Thus, the temperature can be considered as the smallest energy-scale in the system.

Electron waiting times.— We characterize the Cooper pair splitter by the distribution of electron waiting times. Given that an electron with spin σ has just tunneled into lead ℓ, the electron waiting time τ is the time that passes until another electron with spin σ' tunnels into lead ℓ'. The electron waiting time is a fluctuating quantity that must be characterized by a probability distribution. The terms in Eq. (3) of the form $\mathcal{J}_{\ell\sigma}\hat{\rho} \equiv \gamma_\ell \hat{d}_{\ell\sigma}\hat{\rho}\hat{d}^\dagger_{\ell\sigma}$ describe incoherent tunneling processes in which an electron with spin σ in QD_ℓ tunnels into lead ℓ. The distribution of waiting times between transitions of type $i = \ell\sigma$ and $j = \ell'\sigma'$ can then be expressed as [24, 44, 67]

$$\mathcal{W}_{ji}(\tau) = \frac{\text{Tr}[\mathcal{J}_j e^{(\mathcal{L}-\mathcal{J}_j)\tau}\mathcal{J}_i\hat{\rho}_S]}{\text{Tr}[\mathcal{J}_i\hat{\rho}_S]}, \tag{4}$$

where $\hat{\rho}_S$ is the stationary density matrix given as the normalized solution to the equation $\mathcal{L}\hat{\rho}_S = 0$. The expression above for the WTD can be understood as follows: after a transition of type i has occurred, the system is evolved until the next transition of type j happens. The denominator ensures that the WTD is normalized to unity when integrated over all possible waiting times.

Figures 1(b) and 1(c) show WTDs for transitions into the same lead and different leads, respectively. Experimentally, transitions between different charge states can be monitored using charge detectors that measure the occupation of each QD [23, 52–54]. In Fig. 1(b), we consider the waiting time between transitions into the left lead. Here, the coupling to the drain electrodes is much larger than the coupling to the superconductor, $\gamma_L, \gamma_R \gg \gamma_{\rm CPS}, \gamma_{\rm EC}$. As the QDs cannot be doubly-occupied, the WTD is strongly suppressed at short times, $\tau \ll \gamma^{-1}_{\rm CPS}$, and vanishes completely at $\tau = 0$, since simultaneous transitions into the same lead are not possible. At long times, the WTD is governed by the slow refilling of the left QD and the subsequent tunneling of an electron into the left lead. This WTD resembles what one would expect for single-electron tunneling through a single QD without any Cooper pair splitting [24].

A very different picture emerges from the waiting time between transitions into different leads. In Fig. 1(c), the

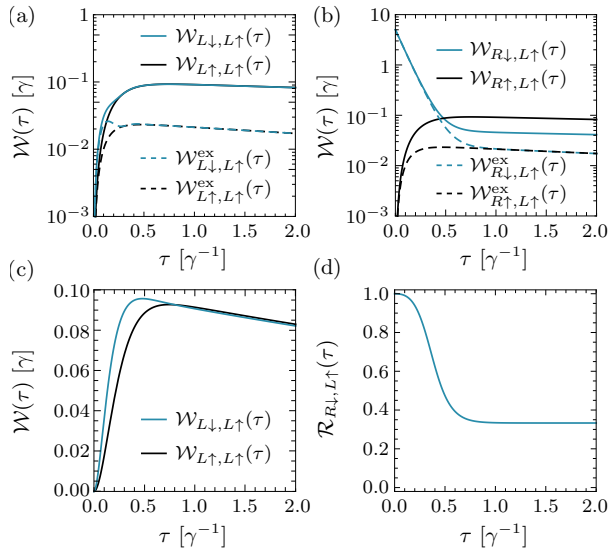

Figure 2. Spin-resolved WTDs. (a) Spin-revolved WTDs for tunneling into the same lead. (b) Spin-revolved WTDs for tunneling into different leads. In (a) and (b), the parameters are $\gamma_L = \gamma_R \equiv 10\gamma$, $\gamma_{\rm CPS} = \gamma_{\rm EC} = \gamma$, and $\epsilon_L = -\epsilon_R = 10\gamma$. (c) Spin-revolved WTDs for tunneling into the same lead with same parameters except that $\epsilon_L = \epsilon_R = 0$. (d) The branching ratio in Eq. (7) corresponding to the WTDs in panel (b).

splitting of a Cooper pair is signaled by a large peak in the WTD at short times, $\tau \ll \gamma^{-1}_{\rm CPS}$. In this case, the tunneling of an electron into the left lead is quickly followed by a transition into the right lead on a time-scale given by the coupling to the right lead, γ_R^{-1}. The slow decay of the WTD describes the waiting time between electrons originating from different Cooper pairs. This WTD clearly reflects the non-local nature of the CPS processes and it carries information about the *short* waiting times between electrons from the *same* Cooper pair and the *long* waiting times between electrons originating from *different* Cooper pairs. Experimentally, a measurement of the WTD in Fig. 1(c) would constitute a strong evidence of efficient Cooper pair splitting.

Exclusive WTDs.— To better understand the time-scales that enter the WTDs, we introduce *exclusive* WTDs. Again, we consider the waiting time that passes between transitions of types i and j. However, we now exclude cases, where any other transitions occur during the waiting time. This WTD is then defined as [24, 47]

$$\mathcal{W}^{\rm ex}_{ji}(\tau) = \frac{{\rm Tr}[\mathcal{J}_j e^{\mathcal{L}^{\rm ex}\tau}\mathcal{J}_i\hat{\rho}_S]}{{\rm Tr}[\mathcal{J}_i\hat{\rho}_S]}, \tag{5}$$

where $\mathcal{L}^{\rm ex} = \mathcal{L} - \sum_k \mathcal{J}_k$ removes all possible transitions from the full time evolution given by $\mathcal{L}$. In contrast to the WTD in Eq. (4), the exclusive WTD is only normalised upon integrating over all waiting times *and* summing over all types of final events. Due to its simpler structure, the exclusive WTD can be evaluated analytically. For example, with $\gamma_L = \gamma_R = \xi$ and $\epsilon_L = -\epsilon_R = \epsilon$, we find

$$\begin{aligned}
\mathcal{W}^{\rm ex}_{\ell\sigma,\ell'\sigma}(\tau) =& \frac{\xi}{2}e^{-\xi\tau}\alpha^2_{\rm CPS}[1-\cos(\omega_{\rm CPS}\tau)]\,,\\
\mathcal{W}^{\rm ex}_{\ell\sigma,\ell\bar{\sigma}}(\tau) =& \xi e^{-\xi\tau}\alpha^2_{\rm EC}[1-\cos(\omega_{\rm EC}\tau)] + \mathcal{W}^{\rm ex}_{\ell\sigma,\ell\sigma}(\tau),\\
\mathcal{W}^{\rm ex}_{\ell\sigma,\bar{\ell}\bar{\sigma}}(\tau) =& \frac{\xi}{2}e^{-\xi\tau} + 2\mathcal{W}^{\rm ex}_{\ell\sigma,\ell\sigma}(\tau) - \mathcal{W}^{\rm ex}_{\ell\sigma,\ell\bar{\sigma}}(\tau),
\end{aligned} \tag{6}$$

with $\bar{L} = R$ and $\bar{\uparrow} = \downarrow$ and vice versa, and we have identified the frequencies $\omega_{\rm CPS} = 2\sqrt{\gamma^2_{\rm CPS} - (\xi/2)^2}$ and $\omega_{\rm EC} = 2\sqrt{\gamma^2_{\rm EC} + \epsilon^2}$ associated with the coherent CPS and EC processes and introduced the ratios $\alpha_{\rm CPS} = \gamma_{\rm CPS}/\omega_{\rm CPS}$ and $\alpha_{\rm EC} = \gamma_{\rm EC}/\omega_{\rm EC}$. If $\gamma_{\rm CPS} \gg \gamma_L, \gamma_R$, the WTD exhibits oscillations with frequency $\omega_{\rm CPS} \simeq 2\gamma_{\rm CPS}$. By contrast, for $\gamma_{\rm CPS} \ll \gamma_L, \gamma_R$, the frequency becomes imaginary and now rather corresponds to an exponential decay. In Fig. 1, we show the exclusive WTDs $\mathcal{W}^{\rm ex}_{\ell\ell'}(\tau) = \sum_{\sigma,\sigma'}\mathcal{W}^{\rm ex}_{\ell\sigma,\ell'\sigma'}(\tau)/2$. For short times, we have $\mathcal{W}^{\rm ex}_{LL}(\tau) \simeq (\omega_{\rm CPS}\tau)^2$. By contrast, for the WTD in Fig. 1(c) the short-time behavior $\mathcal{W}^{\rm ex}_{RL}(\tau) \simeq e^{-\xi\tau}$ is governed by the escape rate, while the long-time decay $\mathcal{W}^{\rm ex}_{RL}(\tau) \simeq e^{-2\tau\gamma^2_{\rm CPS}/\xi}$ also involves the CPS amplitude.

Spin-resolved WTDs.— The splitting of Cooper pairs can be identified in the charge-resolved WTDs as we saw in Fig. 1(c). Still, further information can be obtained from the spin-resolved WTDs. Experimentally, one might measure spin-resolved WTDs using ferromagnetic detectors [58, 68–70]. In Fig. 2, we show WTDs that are resolved with respect to the spin degree of freedom. In Figs. 2(a) and (b), the levels are detuned so that only CPS processes are on resonance. Again, the WTDs for transitions into the same lead show essentially no signatures of the CPS processes. By contrast, the CPS processes can be identified in the WTD in Fig. 2(b) for transitions into different leads. Here, the CPS processes show up as a large enhancement at short times in the WTD for opposite spins. Due to the splitting of a Cooper pair, the tunneling of a spin-up electron into the left lead is likely followed by the tunneling of a spin-down electron into the right lead. A similar enhancement is not found for electrons with the same spin, since they must originate from different Cooper pairs.

In Fig. 2(c), both the CPS and EC processes are tuned into resonance. The combination of these processes lead to an enhancement at intermediate times in the WTD for electrons with opposite spins tunneling into the same lead. In this case, two electrons from a Cooper pair can exit into the same drain due to a spin-preserving EC process that transfers the second electron from the right to the left QD before it exits via the left drain. This is not possible for electrons with the same spin, since they cannot originate from the same Cooper pair, and the corresponding WTD is not enhanced in a similar way.

Importantly, from the spin-resolved WTDs, we can

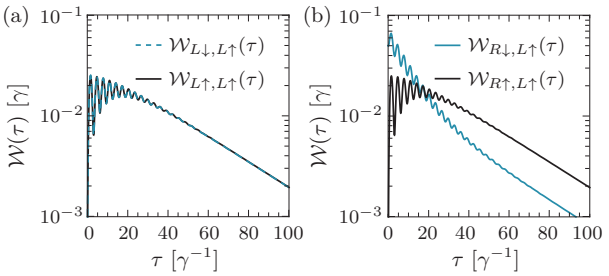

Figure 3. Coherent oscillations. (a) Spin-revolved WTDs for tunneling into the same lead. (b) Spin-revolved WTDs for tunneling into different leads. In both panels, the parameters are $\gamma_L = \gamma_R \equiv 0.1\gamma$, $\gamma_{\rm CPS} = \gamma_{\rm EC} = \gamma$, and $\epsilon_L = -\epsilon_R = 10\gamma$.

evaluate the branching ratio of the spins defined as

$$\mathcal{R}_{R\downarrow,L\uparrow}(\tau) \equiv \frac{\mathcal{W}_{R\downarrow,L\uparrow}(\tau)}{\mathcal{W}_{R\downarrow,L\uparrow}(\tau) + \mathcal{W}_{R\uparrow,L\uparrow}(\tau)}. \tag{7}$$

The branching ratio is the probability that two electrons, which tunnel into different leads separated by the waiting time τ, have opposite spins. Figure 2(d) shows that it is highly probable that electrons separated by a short waiting time have opposite spins and they likely originate from the same Cooper pair. This finding is important since it allows us to conclude that the large peak in Fig. 1(c) with near-unity probability corresponds to opposite spins originating from the same Cooper pair [71].

Until now, we have assumed that the coupling to the drains is much larger than the coupling to the superconductor. This regime may be most attractive for efficient Cooper pair splitting, since the split pair of electrons is quickly transferred to the drains. However, the opposite regime, $\gamma_{\rm CPS}, \gamma_{\rm EC} \gg \gamma_L, \gamma_R$, is also interesting. In Fig. 3, the rate of escape to the drains is so slow that several coherent oscillations between the QDs and the superconductor can be completed [24, 28, 47]. As discussed after Eq. (6), the frequency of the oscillations is given by $\omega_{\rm CPS} \simeq 2\gamma_{\rm CPS}$.

Joint WTDs.— The WTDs concern waiting times between subsequent tunneling events. However, they do not describe correlations between consecutive waiting times. Such correlations can be characterized by evaluating the joint distribution of electron waiting times [44, 49, 72]

$$\mathcal{W}_{kji}(\tau_1, \tau_2) = \frac{{\rm Tr}[\mathcal{J}_k e^{(\mathcal{L}-\mathcal{J}_k)\tau_2} \mathcal{J}_j e^{(\mathcal{L}-\mathcal{J}_j)\tau_1} \mathcal{J}_i \hat{\rho}_S]}{{\rm Tr}[\mathcal{J}_i \hat{\rho}_S]}, \tag{8}$$

which generalizes Eq. (4) to subsequent waiting times between transitions of type i, j, and k. For uncorrelated waiting times, the joint distribution factorizes as $\mathcal{W}_{kj}(\tau_2)\mathcal{W}_{ji}(\tau_1)$ in terms of the individual WTDs. Correlations can be quantified by the correlation function

$$\Delta\mathcal{W}_{kji}(\tau_1, \tau_2) = \frac{\mathcal{W}_{kji}(\tau_1, \tau_2) - \mathcal{W}_{kj}(\tau_2)\mathcal{W}_{ji}(\tau_1)}{\mathcal{W}_{kj}(\tau_2)\mathcal{W}_{ji}(\tau_1)}, \tag{9}$$

which is positive (negative) for positively (negatively) correlated waiting times and zero without correlations.

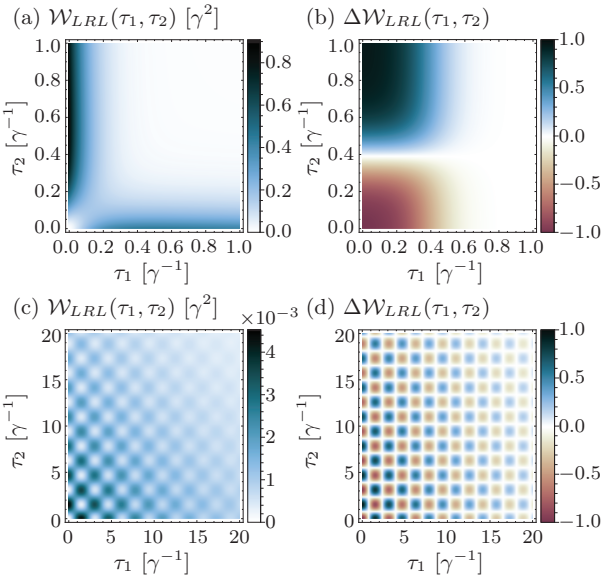

Figure 4. Joint WTDs and correlation functions. In panels (a) and (b), the parameters are $\gamma_L = \gamma_R = 10\gamma$, $\gamma_{\rm CPS} = \gamma_{\rm EC} \equiv \gamma$, and $\epsilon_L = \epsilon_R = 0$. In panels (c) and (d), the parameters are $\gamma_L = \gamma_R = 0.1\gamma$, $\gamma_{\rm CPS} = \gamma_{\rm EC} = \gamma$, and $\epsilon_L = \epsilon_R = 0$.

Figure 4 shows joint WTDs and correlation functions for electrons arriving in different leads. In panels (a) and (b), the coupling to the drains is much larger than the coupling to the superconductor. We see that a short waiting time is likely followed by a long waiting time, but unlikely followed by another short waiting time. A short waiting time corresponds to two electrons originating from the same Cooper pair, while a long waiting time is given by the slow refilling of the QDs by a split Cooper pair. The observed correlations reflect that the two processes, i.e. emission into the drains and refilling from the superconductor, follow one after another. A similar behavior is seen in panels (c) and (d), where the coupling to the superconductor is the largest. However, now the rate of escape to the drains is so slow that coherent oscillations between the QDs and the superconductor have time to form, giving rise to the oscillatory pattern in the joint WTD and the correlation function.

Conclusions.— We have proposed to use waiting time distributions to characterize Cooper pair splitters. The non-local nature of the Cooper pair splitting can be clearly identified in the distribution of waiting times. Based on the recent progress in the real-time detection of Andreev tunneling, we expect the predictions to be accessible in future experiments. Specifically, a measurement of the WTD would constitute a strong evidence of efficient Cooper pair splitting in the regime of slow tunneling, where conventional current measurements are demanding. Theoretically, it would be interesting to formulate a Bell-like inequality for the waiting times to certify the entanglement of the split Cooper pairs.

Acknowledgements.— We thank P. J. Hakonen,

G. B. Lesovik, M. V. Moskalets, J. P. Pekola, and B. Sothmann for valuable discussions. Authors at Aalto are associated with Centre for Quantum Engineering. The Center for Nanostructured Graphene is sponsored by the Danish Research Foundation (Project DNRF103).

[1] A. Zagoskin, *Quantum Engineering: Theory and Design of Quantum Coherent Structures* (Cambridge University Press, 2011).

[2] T. D. Ladd, F. Jelezko, R. Laflamme, Y. Nakamura, C. Monroe, and J. L. O'Brien, "Review: Quantum computers," Nature **464**, 45 (2010).

[3] G. B. Lesovik, T. Martin, and G. Blatter, "Electronic entanglement in the vicinity of a superconductor," Eur. Phys. J. B **24**, 287 (2001).

[4] P. Recher, E. V. Sukhorukov, and D. Loss, "Andreev tunneling, Coulomb blockade, and resonant transport of nonlocal spin-entangled electrons," Phys. Rev. B **63**, 165314 (2001).

[5] D. Beckmann, H. B. Weber, and H. v. Löhneysen, "Evidence for Crossed Andreev Reflection in Superconductor-Ferromagnet Hybrid Structures," Phys. Rev. Lett. **93**, 197003 (2004).

[6] S. Russo, M. Kroug, T. M. Klapwijk, and A. F. Morpurgo, "Experimental Observation of Bias-Dependent Nonlocal Andreev Reflection," Phys. Rev. Lett. **95**, 027002 (2005).

[7] R. S. Deacon, A. Oiwa, J. Sailer, S. Baba, Y. Kanai, K. Shibata, K. Hirakawa, and S. Tarucha, "Cooper pair splitting in parallel quantum dot Josephson junctions," Nat. Commun. **6**, 7446 (2015).

[8] L. Hofstetter, S. Csonka, J. Nygård, and C. Schönenberger, "Cooper pair splitter realized in a two-quantum-dot Y-junction," Nature **461**, 960 (2009).

[9] L. Hofstetter, S. Csonka, A. Baumgartner, G. Fülöp, S. d'Hollosy, J. Nygård, and C. Schönenberger, "Finite-Bias Cooper Pair Splitting," Phys. Rev. Lett. **107**, 136801 (2011).

[10] A. Das, R. Ronen, M. Heiblum, D. Mahalu, A. V. Kretinin, and H. Shtrikman, "High-efficiency Cooper pair splitting demonstrated by two-particle conductance resonance and positive noise cross-correlation," Nat. Commun. **3**, 1165 (2012).

[11] G. Fülöp, F. Domínguez, S. d'Hollosy, A. Baumgartner, P. Makk, M. H. Madsen, V. A. Guzenko, J. Nygård, C. Schönenberger, A. Levy Yeyati, and S. Csonka, "Magnetic Field Tuning and Quantum Interference in a Cooper Pair Splitter," Phys. Rev. Lett. **115**, 227003 (2015).

[12] L. G. Herrmann, F. Portier, P. Roche, A. Levy Yeyati, T. Kontos, and C. Strunk, "Carbon Nanotubes as Cooper-Pair Beam Splitters," Phys. Rev. Lett. **104**, 026801 (2010).

[13] L. G. Herrmann, P. Burset, W. J. Herrera, F. Portier, P. Roche, C. Strunk, A. Levy Yeyati, and T. Kontos, "Spectroscopy of non-local superconducting correlations in a double quantum dot," (2012), arXiv:1205.1972.

[14] J. Schindele, A. Baumgartner, and C. Schönenberger, "Near-Unity Cooper Pair Splitting Efficiency," Phys. Rev. Lett. **109**, 157002 (2012).

[15] G. Fülöp, S. d'Hollosy, A. Baumgartner, P. Makk, V. A. Guzenko, M. H. Madsen, J. Nygård, C. Schönenberger, and S. Csonka, "Local electrical tuning of the nonlocal signals in a Cooper pair splitter," Phys. Rev. B **90**, 235412 (2014).

[16] J. Schindele, A. Baumgartner, R. Maurand, M. Weiss, and C. Schönenberger, "Nonlocal spectroscopy of Andreev bound states," Phys. Rev. B **89**, 045422 (2014).

[17] Z. B. Tan, D. Cox, T. Nieminen, P. Lähteenmäki, D. Golubev, G. B. Lesovik, and P. J. Hakonen, "Cooper Pair Splitting by Means of Graphene Quantum Dots," Phys. Rev. Lett. **114**, 096602 (2015).

[18] I. V. Borzenets, Y. Shimazaki, G. F. Jones, M. F. Craciun, S. Russo, M. Yamamoto, and S. Tarucha, "High Efficiency CVD Graphene-lead (Pb) Cooper Pair Splitter," Sci. Rep. **6**, 23051 (2016).

[19] SK F. Islam and A. Saha, "Amplification of Cooper pair splitting current in a graphene-based Cooper pair beam splitter geometry," Phys. Rev. B **96**, 125406 (2017).

[20] S. Kawabata, "Test of Bell's Inequality using the Spin Filter Effect in Ferromagnetic Semiconductor Microstructures," J. Phys. Soc. Japan **70**, 1210 (2001).

[21] N. M. Chtchelkatchev, G. Blatter, G. B. Lesovik, and T. Martin, "Bell inequalities and entanglement in solid-state devices," Phys. Rev. B **66**, 161320 (2002).

[22] O. Sauret, T. Martin, and D. Feinberg, "Spin-current noise and Bell inequalities in a realistic superconductor-quantum dot entangler," Phys. Rev. B **72**, 024544 (2005).

[23] S. Gustavsson, R. Leturcq, M. Studer, I. Shorubalko, T. Ihn, K. Ensslin, D. C. Driscoll, and A. C. Gossard, "Electron counting in quantum dots," Surf. Sci. Rep. **64**, 191 (2009).

[24] T. Brandes, "Waiting times and noise in single particle transport," Ann. Phys. **17**, 477 (2008).

[25] S. Welack, M. Esposito, U. Harbola, and S. Mukamel, "Interference effects in the counting statistics of electron transfers through a double quantum dot," Phys. Rev. B **77**, 195315 (2008).

[26] S. Welack, S. Mukamel, and Y. J. Yan, "Waiting time distributions of electron transfers through quantum dot Aharonov-Bohm interferometers," Europhys. Lett. **85**, 57008 (2009).

[27] M. Albert, C. Flindt, and M. Büttiker, "Distributions of Waiting Times of Dynamic Single-Electron Emitters," Phys. Rev. Lett. **107**, 086805 (2011).

[28] K. H. Thomas and C. Flindt, "Electron waiting times in non-Markovian quantum transport," Phys. Rev. B **87**, 121405 (2013).

[29] G.-M. Tang, F. Xu, and J. Wang, "Waiting time distribution of quantum electronic transport in the transient regime," Phys. Rev. B **89**, 205310 (2014).

[30] G.-M. Tang and J. Wang, "Full-counting statistics of charge and spin transport in the transient regime: A nonequilibrium Green's function approach," Phys. Rev. B **90**, 195422 (2014).

[31] B. Sothmann, "Electronic waiting-time distribution of a quantum-dot spin valve," Phys. Rev. B **90**, 155315 (2014).

[32] R. Seoane Souto, R. Avriller, R. C. Monreal, A. Martín-Rodero, and A. Levy Yeyati, "Transient dynamics and waiting time distribution of molecular junctions in the polaronic regime," Phys. Rev. B **92**, 125435 (2015).

[33] V. Talbo, J. Mateos, S. Retailleau, P. Dollfus, and T. González, "Time-dependent shot noise in multi-level quantum dot-based single-electron devices," Semicond.

Sci. Technol. **30**, 055002 (2015).
[34] S. L. Rudge and D. S. Kosov, "Distribution of residence times as a marker to distinguish different pathways for quantum transport," Phys. Rev. E **94**, 042134 (2016).
[35] S. L. Rudge and D. S. Kosov, "Distribution of tunnelling times for quantum electron transport," J. Chem. Phys. **144**, 124105 (2016).
[36] K. Ptaszyński, "Nonrenewal statistics in transport through quantum dots," Phys. Rev. B **95**, 045306 (2017).
[37] E. Potanina and C. Flindt, "Electron waiting times of a periodically driven single-electron turnstile," Phys. Rev. B **96**, 045420 (2017).
[38] D. S. Kosov, "Non-renewal statistics for electron transport in a molecular junction with electron-vibration interaction," J. Chem. Phys. **147**, 104109 (2017).
[39] M. Albert, G. Haack, C. Flindt, and M. Büttiker, "Electron Waiting Times in Mesoscopic Conductors," Phys. Rev. Lett. **108**, 186806 (2012).
[40] G. Haack, M. Albert, and C. Flindt, "Distributions of electron waiting times in quantum-coherent conductors," Phys. Rev. B **90**, 205429 (2014).
[41] K. H. Thomas and C. Flindt, "Waiting time distributions of noninteracting fermions on a tight-binding chain," Phys. Rev. B **89**, 245420 (2014).
[42] D. Dasenbrook, C. Flindt, and M. Büttiker, "Floquet Theory of Electron Waiting Times in Quantum-Coherent Conductors," Phys. Rev. Lett. **112**, 146801 (2014).
[43] M. Albert and P. Devillard, "Waiting time distribution for trains of quantized electron pulses," Phys. Rev. B **90**, 035431 (2014).
[44] D. Dasenbrook, P. P. Hofer, and C. Flindt, "Electron waiting times in coherent conductors are correlated," Phys. Rev. B **91**, 195420 (2015).
[45] D. Dasenbrook and C. Flindt, "Quantum theory of an electron waiting time clock," Phys. Rev. B **93**, 245409 (2016).
[46] P. P. Hofer, D. Dasenbrook, and C. Flindt, "Electron waiting times for the mesoscopic capacitor," Physica E **82**, 11 (2016).
[47] L. Rajabi, C. Pöltl, and M. Governale, "Waiting Time Distributions for the Transport through a Quantum-Dot Tunnel Coupled to One Normal and One Superconducting Lead," Phys. Rev. Lett. **111**, 067002 (2013).
[48] S. Dambach, B. Kubala, V. Gramich, and J. Ankerhold, "Time-resolved statistics of nonclassical light in Josephson photonics," Phys. Rev. B **92**, 054508 (2015).
[49] S. Dambach, B. Kubala, and J. Ankerhold, "Time-resolved statistics of photon pairs in two-cavity Josephson photonics," Fortschr. Phys. **65**, 1600061 (2017).
[50] M. Albert, D. Chevallier, and P. Devillard, "Waiting times of entangled electrons in normal-superconducting junctions," Physica E **76**, 215 (2016).
[51] D. Chevallier, M. Albert, and P. Devillard, "Probing Majorana and Andreev bound states with waiting times," Europhys. Lett. **116**, 27005 (2016).
[52] S. K. Gorman, Y. He, M. G. House, J. G. Keizer, D. Keith, L. Fricke, S. J. Hile, M. A. Broome, and M. Y. Simmons, "Tunneling Statistics for Analysis of Spin-Readout Fidelity," Phys. Rev. Applied **8**, 034019 (2017).
[53] V. F. Maisi, O.-P. Saira, Yu. A. Pashkin, J. S. Tsai, D. V. Averin, and J. P. Pekola, "Real-Time Observation of Discrete Andreev Tunneling Events," Phys. Rev. Lett. **106**, 217003 (2011).
[54] V. F. Maisi, D. Kambly, C. Flindt, and J. P. Pekola, "Full Counting Statistics of Andreev Tunneling," Phys. Rev. Lett. **112**, 036801 (2014).
[55] O. Sauret, D. Feinberg, and T. Martin, "Quantum master equations for the superconductor-quantum dot entangler," Phys. Rev. B **70**, 245313 (2004).
[56] A. Braggio, M. Governale, M. G. Pala, and J. König, "Superconducting proximity effect in interacting quantum dots revealed by shot noise," Solid State Commun. **151**, 155 (2011).
[57] J. Eldridge, M. G. Pala, M. Governale, and J. König, "Superconducting proximity effect in interacting double-dot systems," Phys. Rev. B **82**, 184507 (2010).
[58] P. Trocha and I. Weymann, "Spin-resolved Andreev transport through double-quantum-dot Cooper pair splitters," Phys. Rev. B **91**, 235424 (2015).
[59] E. Amitai, R. P. Tiwari, S. Walter, T. L. Schmidt, and S. E. Nigg, "Nonlocal quantum state engineering with the Cooper pair splitter beyond the Coulomb blockade regime," Phys. Rev. B **93**, 075421 (2016).
[60] R. Hussein, L. Jaurigue, M. Governale, and A. Braggio , "Double quantum dot Cooper-pair splitter at finite couplings," Phys. Rev. B **94**, 235134 (2016).
[61] R. Hussein, A. Braggio, and M. Governale, "Entanglement-symmetry control in a quantum-dot Cooper-pair splitter," Phys. Status Solidi B **254**, 1600603 (2017).
[62] D. Chevallier, J. Rech, T. Jonckheere, and T. Martin, "Current and noise correlations in a double-dot Cooper-pair beam splitter," Phys. Rev. B **83**, 125421 (2011).
[63] B. Hiltscher, M. Governale, J. Splettstoesser, and J. König, "Adiabatic pumping in a double-dot Cooper-pair beam splitter," Phys. Rev. B **84**, 155403 (2011).
[64] M. Flöser, D. Feinberg, and R. Mélin, "Absence of split pairs in cross correlations of a highly transparent normal metal-superconductor-normal metal electron-beam splitter," Phys. Rev. B **88**, 094517 (2013).
[65] I. A. Sadovskyy, G. B. Lesovik, and V. M. Vinokur, "Unitary limit in crossed Andreev transport," New J. Phys. **17**, 103016 (2015).
[66] Sh. Gurvitz, "Wave-function approach to Master equations for quantum transport and measurement," Front. Phys, **12**, 120303 (2016).
[67] H. J. Carmichael, S. Singh, R. Vyas, and P. R. Rice, "Photoelectron waiting times and atomic state reduction in resonance fluorescence," Phys. Rev. A **39**, 1200 (1989).
[68] O. Malkoc, C. Bergenfeldt, and P. Samuelsson, "Full counting statistics of generic spin entangler with quantum dot-ferromagnet detectors," Europhys. Lett. **105**, 47013 (2014).
[69] P. Busz, D. Tomaszewski, and J. Martinek, "Spin correlation and entanglement detection in Cooper pair splitters by current measurements using magnetic detectors," Phys. Rev. B **96**, 064520 (2017).
[70] K. Wrześniewski, P. Trocha, and I. Weymann, "Current cross-correlations in double quantum dot based Cooper pair splitters with ferromagnetic leads," J. Phys.: Condens. Matter **29**, 195302 (2017).
[71] Z. Scherübl, A. Pályi, and S. Csonka, "Probing individual split Cooper pairs using the spin qubit toolkit," Phys. Rev. B **89**, 205439 (2014).
[72] X. H. H. Zhang and H. U. Baranger, "Photon Statistics in a Waveguide: Beyond Bunching and Antibunching," (2017), arXiv:1710.01543.

B.3 Publication III

The antiferromagnetic phase of the Floquet-driven Hubbard model

Nicklas Walldorf, Dante M. Kennes, Jens Paaske, and Andrew J. Millis

Physical Review B (Rapid Communication) 100, 121110(R) (2019)

The antiferromagnetic phase of the Floquet-driven Hubbard model

Nicklas Walldorf,[1] Dante M. Kennes,[2] Jens Paaske,[3] and Andrew J. Millis[4,5]

[1] *Center for Nanostructured Graphene (CNG), Department of Physics, Technical University of Denmark, DK-2800 Kongens Lyngby, Denmark*
[2] *Dahlem Center for Complex Quantum Systems and Fachbereich Physik, Freie Universität Berlin, 14195 Berlin, Germany*
[3] *Center for Quantum Devices, Niels Bohr Institute, University of Copenhagen, 2100 Copenhagen, Denmark*
[4] *Department of Physics, Columbia University, 538 West 120th Street, New Yok, NY 10027 USA*
[5] *Center for Computational Quantum Physics, Flatiron Institute, 162 5th Avenue, New York, NY 10010 USA*

A saddle point plus fluctuations analysis of the periodically driven half-filled two-dimensional Hubbard model is performed. For drive frequencies below the equilibrium gap, we find discontinuous transitions to time-dependent solutions. A highly excited, generically non-thermal distribution of magnons occurs even for drive frequencies far above the gap. Above a critical drive amplitude, the low-energy magnon distribution diverges as the frequency tends to zero and antiferromagnetism is destroyed, revealing the generic importance of collective mode excitations arising from a non-equilibrium drive.

The rapid development of stable, high-intensity, radiation sources has opened up new experimental horizons for non-equilibrium control of material properties by application of tailored radiation fields [1–3]. An applied radiation field affects a material in two fundamentally different ways: by changing the Hamiltonian, and creating excitations. The former, commonly referred to as "Floquet engineering", offers an exciting route towards engineering new phases of driven matter [4–17]. In some cases (e.g. integrable models with collisionless dynamics) mode excitation can lead to novel dynamical phases [18]. However, in the generic situation, if too many excitations are created, the interesting phases can be destabilized [19–22]. The general consensus in the field has been that if the drive frequency is sufficiently detuned from the electronic transition energies, excitations may be neglected, allowing a focus on "Floquet engineering" aspects.

In this paper we investigate the physics of ac driven systems with drive frequency detuned from electronic transitions via a theoretical study of the properties of the Hubbard model. This model is one of the paradigmatic systems of theoretical condensed matter physics, capturing the essential physics of electronic ordering and collective modes. We focus on the effect of the ac drive on the antiferromagnetic phase and the associated collective modes. We find that even in the 'detuned case', in which the ac drive does not produce a significant density of quasiparticle excitations, a highly non-equilibrium collective mode distribution is produced, with a remarkable dependence on the drive amplitude suggestive of a dynamical quantum phase transition. Above a critical drive amplitude, the non-equilibrium distribution of collective modes leads to a destruction of long-ranged antiferromagnetic order, possibly even for dimensions higher than two. These findings suggest that collective mode distribution effects may be important more broadly in the physics of Floquet-driven phases.

Model.— We consider the situation sketched in Fig. 1: the half-filled two-dimensional square-lattice Hubbard model with nearest-neighbor hopping, repulsive interaction, brought out of equilibrium via an applied electromagnetic field, and tunnel-coupled to a metallic reservoir to allow the system to reach a non-equilibrium steady state. The Hamiltonian is

$$\hat{H} = \sum_{\boldsymbol{k}\sigma} \epsilon_{\boldsymbol{k}}(t) \hat{c}^\dagger_{\boldsymbol{k}\sigma} \hat{c}_{\boldsymbol{k}\sigma} + U \sum_i \hat{n}_{i\uparrow}\hat{n}_{i\downarrow} + \hat{H}_{\rm res}, \qquad (1)$$

where $\epsilon_{\boldsymbol{k}}(t)$ is the electron dispersion and U the on-site repulsion. The operator $\hat{c}^\dagger_{i\sigma}$ creates an electron of spin σ at site i of a two-dimensional lattice of unit lattice constant, $c^\dagger_{\boldsymbol{k}\sigma}$ is its Fourier transform in the first Brillouin zone, and $\hat{n}_{i\sigma} = \hat{c}^\dagger_{i\sigma}\hat{c}_{i\sigma}$. $\hat{H}_{\rm res}$ is a weak tunnel coupling to an infinite-bandwidth reservoir with flat density of states [23] giving rise to a constant inverse electron lifetime, Γ (see Eq. (4) below). We set the chemical potential corresponding to half filling, set $\hbar = k_B = e = 1$, and include the electric field via the Peierls substitution with vector potential $A_{x,y}(t) = -E\sin(\Omega t)/\Omega$:

$$\epsilon_{\boldsymbol{k}}(t) = -2\tilde{t}\left\{\cos[k_x + A_x(t)] + \cos[k_y + A_y(t)]\right\}. \qquad (2)$$

Henceforth, all energies are given in units of the nearest-neighbor-hopping matrix element $\tilde{t}$.

The equilibrium properties of the model are well understood [24–26]: The ground state is antiferromagnetically

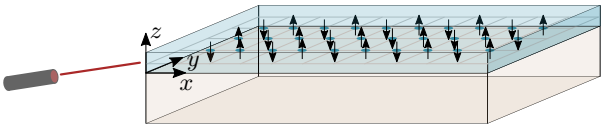

FIG. 1. Sketch of an antiferromagnetically ordered strongly correlated film (top layer, with spins indicated) driven by a radiation field and in contact with a metallic reservoir (bottom layer) kept at thermal equilibrium.

(Néel) ordered, has a gap to electronic excitations and supports gapless spin waves. The thermal population of magnons diverges as their energy goes to zero, which in turn leads to the destruction of long-ranged magnetic order at any non-zero temperature in dimension $d \leq 2$ [27–29]. These features are revealed by an appropriate interpretation of the results of a conventional mean field plus fluctuation analysis [24, 25], which is known to provide a qualitatively correct description of the equilibrium properties of the model.

We study the model for drive frequencies ranging from smaller than the equilibrium gap ("sub-gap drive regime") to larger than the highest electronic transition visible in linear response ("Magnus drive regime") [5, 7, 16, 30] by solving the non-equilibrium mean-field equations in the presence of the periodic drive and then computing one-loop corrections.

Saddle point approximation.— To generate the mean-field theory we write the model as a Keldysh-contour path-integral [31], decouple the interaction via a magnetic-channel Hubbard-Stratonovich field [32], $\boldsymbol{m}$, and consider $\boldsymbol{m}$ to have a mean-field part, $m_0 \hat{\boldsymbol{z}} e^{i\boldsymbol{Q}\cdot\boldsymbol{R}_i}$, identified with the Néel order parameter, $\boldsymbol{Q} = (\pi, \pi)$, and a fluctuation part, $\delta\boldsymbol{m}$, which when treated to one-loop order reveals the spin-wave physics.

In a non-equilibrium steady state the mean field is synchronized to the drive (see inset Fig. 2(b)) so the mean-field magnetization can be represented as a Fourier series $m_0(t) = \sum_n m_0^{(n)} e^{-in\Omega t}$. The mean-field equation, found as a saddle-point approximation for the classical magnetization field component [33], is then a nonlinear equation for the components $m_0^{(n)}$ of the Floquet-space vector representing $m_0(t)$

$$m_0^{(n)} = \frac{I}{4\pi N i} \sum_{\boldsymbol{k}}{}' \int_{-\infty}^{\infty} d\omega \, \mathrm{Tr}\Big[\hat{\mathcal{G}}_{\boldsymbol{k},n0}(\omega)(\hat{\tau}_1 \otimes \tau_1 \otimes \sigma_3)\Big], \quad (3)$$

where the primed sum is taken over the magnetic Brillouin zone (BZ), i.e. half of the electronic BZ, $I = U/3$ [32], and $\hat{\mathcal{G}}$, the mean-field Floquet Green function [34–37], is a matrix in Keldysh ($\hat{\tau}$), momentum-spinor (τ), spin (σ), and Floquet space. The retarded/advanced component of the electron Green's function dressed by the reservoir is given by

$$\mathcal{G}^{R/A\,-1}_{\boldsymbol{k},mn}(\omega) = (\omega + n\Omega \pm i\Gamma)\delta_{mn}\tau_0 \otimes \sigma_0 - h_{\boldsymbol{k},mn}, \quad (4)$$

where $h_{\boldsymbol{k},mn} = \epsilon_{\boldsymbol{k},m-n}\tau_3 \otimes \sigma_0 - m_0^{(m-n)}\tau_1 \otimes \sigma_3$, with $\epsilon_{\boldsymbol{k},m} = \frac{1}{T}\int_{-T/2}^{T/2} dt\, e^{im\Omega t}\epsilon_{\boldsymbol{k}}(t)$, describing electrons driven by the external field and moving in a time-periodic magnetization field. The Keldysh Green's function is given by $\mathcal{G}^K_{\boldsymbol{k},mn}(\omega) = \sum_{m'n'} \mathcal{G}^R_{\boldsymbol{k},mm'}(\omega)\Sigma^K_{\boldsymbol{k},m'n'}(\omega)\mathcal{G}^A_{\boldsymbol{k},n'n}(\omega)$, where $\Sigma^K_{\boldsymbol{k},mn}(\omega) = -2i\Gamma \tanh((\omega + n\Omega)/2T)\tau_0 \otimes \sigma_0\delta_{mn}$ is the self-energy from coupling to the reservoir. We solve Eqs. (3) and (4) numerically, choosing a Floquet cutoff $|n| \leq n_{\max}$, and iterate from an initial guess

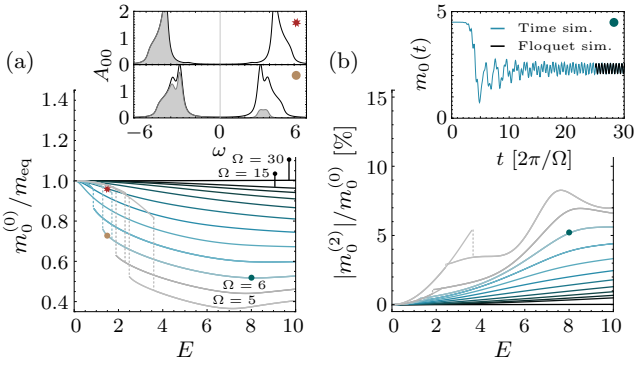

FIG. 2. Mean-field solutions for varying drive frequencies $\Omega = 5 - 15$ in steps of 1 as well as $\Omega = 30$. (a) Time-averaged mean field as a function of drive amplitude, and (inset) diagonal-component of the time-averaged spectral functions (solid lines) and occupation functions (shaded areas) for the mean-field solutions marked in (a). (b) Second mean-field Floquet component as a function of drive amplitude, and (inset) an explicit time-dependent mean-field solution for $\Omega = 7$ (see Refs. [38, 39] for computational details) ramped from the un-driven, to the driven state synchronized to the time-transformed Floquet mean-field solution. The parameters are $I = 5$, $T = 0.01$, $\Gamma = 0.2$ and $n_{\max} = 10$.

$m_0^{(n)} = 10^{-2}\theta(n_{max} - |n|)$. We use converged solutions as new starting points to explore multistability.

Representative results for the zeroth Floquet component, corresponding to the time-averaged dynamics, are shown in the left-hand panel of Fig. 2. For $I \gg \tilde{t}$ the qualitative physics does not depend on the interaction strength, so we present results only for a single typical case. In the high-frequency ('Magnus') limit, $\Omega \gg 2m_0^{(0)}$, theoretical arguments [30] suggest that the system is described by an effective Hamiltonian with hopping amplitude modified from the equilibrium value. We see that indeed on the mean-field level, the main features of the solution remain similar to equilibrium but with parameters renormalized as expected: a magnetic insulating state with the expected [30] small increase in the average staggered magnetization (barely visible in the $\Omega = 30$ trace in panel (a) of Fig. 2) arising from the Magnus-regime renormalization of $\tilde{t}$ by $J_0(E/\Omega)$ [7, 16]. However, as the drive frequencies are decreased towards the sub-gap regime (drive frequency within or below the region of particle-hole continuum excitations) we observe a change to a weak decrease of the order parameter with drive amplitude, and for still lower drive frequency the mean-field equation gives a discontinuous transition (within a regime of bistability) to a state of lower gap amplitude and significant occupation of the upper band (Fig. 2(a) inset). Within our mean-field theory, the state remains magnetically ordered on both sides of the transition; whether a more sophisticated approximation as in Ref. [22] would lead to a Mott or gapless state is an important open question.

Figure 2(b) presents the harmonic content of the order

parameter. The spin inversion symmetry of the drive implies that only even harmonics of the drive frequency appear in the order parameter, and we find generically that only the 0 and ± 2 Floquet components have appreciable amplitudes. The resulting 2Ω oscillation in the order parameter implies moderate second harmonic amplitude oscillations in the gap magnitudes (see inset Fig. 2(b)); the resulting nonlinear optical effects will be strongest for incident radiation at frequencies near the gap.

Fluctuations.— We now focus on the mean-field solutions at higher drive frequency, where the density of electron quasiparticle excitations is negligible. We introduce the fluctuation field as a Keldysh and momentum-spinor, $\delta \boldsymbol{m}^{\mu,i}_{\boldsymbol{q}}(t) = (\delta m^{\mu,i}_{\boldsymbol{q}}(t), \delta m^{\mu,i}_{\boldsymbol{q}+\boldsymbol{Q}}(t))$ with Keldysh index $i = c, q$ (classical, quantum [31]) and $\mu = \pm$ referring to the directional polar decomposition $x \pm iy$. The fluctuations are governed by the electron Green function bubble, which upon transforming to Floquet space reads

$$\Pi^{\mu\nu,ij}_{0/Q,\boldsymbol{q},mn}(\omega) = \frac{i}{2N}\sum_{\boldsymbol{k}}{}' \sum_{m'} \int_{-\infty}^{\infty} \frac{d\omega'}{2\pi} \mathrm{Tr}\left[(\hat{\gamma}_i \otimes \tau_0 \otimes \sigma_\mu) \times \hat{\mathcal{G}}_{\boldsymbol{k},mm'}(\omega')(\hat{\gamma}_j \otimes \tau_{0/1} \otimes \sigma_\nu)\hat{\mathcal{G}}_{\boldsymbol{k}+\boldsymbol{q},m'n}(\omega' - \omega - n\Omega)\right], \quad (5)$$

with Keldysh indices encoded in the matrices $\hat{\gamma}_{c/q} = \hat{\tau}_{0/1}$ [33]. Using the sublattice matrix structure [25]

$$\boldsymbol{\Pi}_{\boldsymbol{q}} = \begin{pmatrix} \Pi_{0,\boldsymbol{q}} & \Pi_{Q,\boldsymbol{q}} \\ \Pi_{Q,\boldsymbol{q}} & \Pi_{0,\boldsymbol{q}+\boldsymbol{Q}} \end{pmatrix}, \quad (6)$$

we define the corresponding transverse fluctuation matrix propagator, $\boldsymbol{\chi}^{\perp,ij}_{\boldsymbol{q}}(t,t') = (iN/\pi)\langle \delta m^{+,i}_{\boldsymbol{q}}(t) \delta m^{-,j}_{-\boldsymbol{q}}(t')\rangle$, as

$$\boldsymbol{\chi}^{\perp R/A}_{\boldsymbol{q},mn} = \left[(2I)^{-1} - \boldsymbol{\Pi}^{\perp R/A}_{\boldsymbol{q}}\right]^{-1}_{mn}, \quad (7)$$
$$\boldsymbol{\chi}^{\perp K}_{\boldsymbol{q},mn} = \left[(2I)^{-1} - \boldsymbol{\Pi}^{\perp R}_{\boldsymbol{q}}\right]^{-1}_{mm'} \boldsymbol{\Pi}^{\perp K}_{\boldsymbol{q},m'n'} \left[(2I)^{-1} - \boldsymbol{\Pi}^{\perp A}_{\boldsymbol{q}}\right]^{-1}_{n'n}.$$

The time-averaged (00-Floquet) fluctuation spectrum is revealed by $\mathrm{Im}\chi^{\perp,R}_{\boldsymbol{0},\boldsymbol{q},00}(\omega)$, shown in the left panel of Fig. 3. We see that the only low-lying excitations are very sharp peaks, corresponding to spin waves, with a small but non-zero broadening from the coupling to the reservoir. The peak energy vanishes and the peak amplitude grows as $\boldsymbol{q} \to \boldsymbol{Q}$. At energies below the charge gap, for positive frequencies $\mathrm{Im}\chi^{\perp R}_{0,\boldsymbol{q},00}(\omega) \approx Z_q \delta(\omega - \omega_q)$ for not too large Γ. Upon integrating over the peaks in Fig. 3(a), the inverse spectral weight Z_q^{-1} shows a linear $\delta q = |\boldsymbol{q} - \boldsymbol{Q}|$ dependence (Fig. 3(a) inset) which agrees well with the expanded equilibrium result, $Z_q^{-1} \approx \alpha \delta q$, $\alpha = 1/(8\sqrt{2}\pi m_0^2)[2 + t^2/m_0^2 + \mathcal{O}(t^4/m_0^4)]$. The ω_q is determined from the peak positions, and gives the dispersions presented in the right panel of Fig. 3. The dispersion exhibits the expected linear momentum dependence at lowest energies, $\omega = v\delta q$. The spin wave velocity is seen to compare well to the dissipative equilibrium result, $v = (2\sqrt{2}\tilde{t}^2/m_0)(1 - 5\tilde{t}^2/m_0^2 - 3\Gamma/\pi m_0 - \Gamma^2/2m_0^2) + \mathcal{O}\left(\tilde{t}^{2+n}\Gamma^{3-n}/m_0^5\right)$ for $n = 0, 1, 2, 3$ (consistent with Ref. [26] for $\Gamma = 0$), provided that the hopping amplitude $\tilde{t}$ is replaced by the Magnus-renormalized value $\tilde{t}J_0(E/\Omega)$ [7]. One may view this Bessel-function reduction of the spin-wave velocity as a particularly simple example of "Floquet engineering".

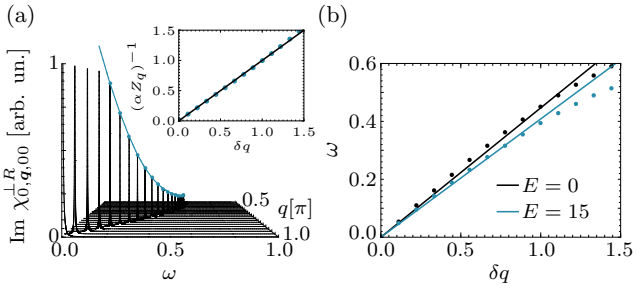

FIG. 3. Transverse spin wave modes. (a) Imaginary part of the retarded susceptibility as function of frequency and momentum $q_x = q_y = q$ for $E = 15$ showing the spin wave pole. Inset: Inverse spectral weight of the peaks in (a). (b) Location of the spin wave pole (points) as a function of frequency and δq together with the equilibrium linear spin wave dispersion, $\omega = v\delta q$, (solid lines) with $\tilde{t} \to \tilde{t}J_0(E/\Omega)$. The parameters are $I = 5$, $\Omega = 30$, $T = 0.01$, $\Gamma = 0.2$, and $n_{\max} = 3$.

The Keldysh component of the transverse propagator contains information about the non-equilibrium distribution of excitations. For low-lying spin waves with $\omega_q \ll \Omega$, this information resides in the zeroth Floquet component, from which we define a time-averaged distribution function, F, by the ansatz

$$\chi^{\perp K}_{0,\boldsymbol{q},00}(\omega) = 2i\,\mathrm{Im}\left[\chi^{\perp R}_{0,\boldsymbol{q},00}(\omega)\right] F(\boldsymbol{q},\omega) \approx 2iZ_q \delta(|\omega| - \omega_q) F_q. \quad (8)$$

The spin-wave pole approximation to $\mathrm{Im}\chi^R$ allows for a quasiclassical description in terms of an on-shell distribution function, $F_q = F(\boldsymbol{q}, \omega_q)$, referring only to the mode energy ω_q. In equilibrium, the fluctuation-dissipation theorem (FDT) ensures that $F_q = \coth(\omega_q/2T)$, which tends to unity at $\omega_q \gg T$ and diverges as ω_q^{-1} for $\omega_q \to 0$.

Figure 4(a) shows the inverse distribution function, F_q^{-1}, as a function of the mode energy, ω_q, at different drive amplitudes for a low reservoir temperature, $T = 0.01$. We plot the reciprocal to fit all data on the same panel. Because the reservoir temperature is substantially lower than the lowest ω_q included in our numerics, the equilibrium F_q (Fig. 4(b)) is indistinguishable from unity. We see that increasing the drive amplitude increases F_q (decreases F_q^{-1}) at all ω_q, with a larger increase for lower ω_q. Increasing either the drive frequency, Ω, or the reservoir coupling, Γ, for fixed drive amplitude reduces F_q (open symbols, left panel Fig. 4). For higher ω_q, F_q initially increases rapidly as the drive amplitude increases, but then saturates as the amplitude becomes large. For small ω_q, the situation is different. For the two weakest drive amplitudes, F_q appears to approach a finite, non-zero value as ω_q approaches zero; for the inter-

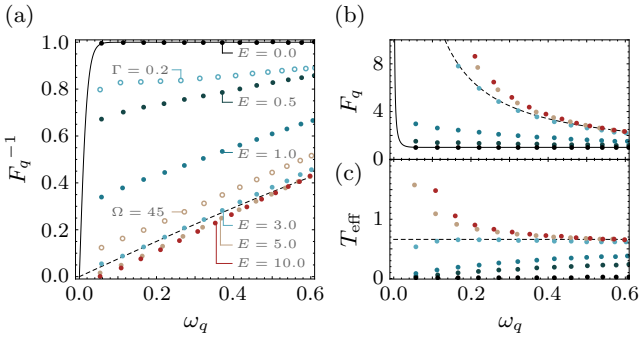

FIG. 4. (a) F_q^{-1} and (b) F_q as function of ω_q for increasing drive amplitude with $\Gamma = 0.02$ and $\Omega = 30$ together with the equilibrium curves for $T = 0.01$ (solid) and $T = 0.66$ (dashed). In (a) is also shown the result for $\Omega = 45$, $E = 5.0$, $\Gamma = 0.02$ and $\Gamma = 0.2$, $E = 3.0$, $\Omega = 30$. (c) $T_{\rm eff}$ corresponding to the curves in (b) together with the equilibrium $T = 0.66$ line (dashed). The parameters are $I = 5$, $T = 0.01$, and $n_{\rm max} = 3$.

mediate drive amplitude F_q^{-1} vanishes linearly as $\omega_q \to 0$ while for the two highest drive amplitudes, F_q^{-1} vanishes faster than linearly as $\omega_q \to 0$.

Apart from the intermediate drive amplitude ($E = 3$), these distribution functions depart markedly from the equilibrium distribution dictated by the FDT. To illustrate this more clearly, Fig. 4(c) shows the effective temperature $T_{\rm eff}$ as defined by $F_q = \coth(\omega_q/2T_{\rm eff}(q))$. We see that the results fall into two groups. For the two smallest drive amplitudes, $T_{\rm eff}$ is larger at high ω_q (very substantial excitation of high q spin waves above the equilibrium value), but decreases to a value consistent with the reservoir temperature as $\omega_q \to 0$. For the intermediate drive amplitude, $T_{\rm eff} \approx 0.66$ is essentially momentum-independent (i.e. F_q fits well to the equilibrium form) and much larger than the reservoir temperatures. For the two larger drive amplitudes, $T_{\rm eff}$ increases rapidly for small ω_q, indicating a super-thermal occupancy of the low-lying spin wave modes, in other words F_q diverging faster than $1/\omega_q$.

The site- and period-averaged mean squared fluctuations of the classical component of the order parameter are given by

$$\langle|\delta m^{+,c}|^2\rangle = \frac{1}{N}\sum_{\boldsymbol{q}}\int\frac{d\omega}{4\pi i}\chi^{\perp K}_{0,\boldsymbol{q},00}(\omega) \sim \int\frac{d^2q}{(2\pi)^2}Z_qF_q. \quad (9)$$

In thermal equilibrium at any non-zero temperature, both F_q and Z_q diverge as $1/\delta q$, and $\langle|\delta m^{+,c}|^2\rangle$ therefore diverges logarithmically with system size in two dimensions. This is the expression in the one-loop calculation of the well-known result [27, 28] that thermal fluctuations destabilize long-ranged magnetic order in continuous-symmetry systems of dimension $d \leq 2$. Our results indicate that the generalization to systems out of equilibrium is richer than expected from previous work. Unlike the dc current-driven ferromagnetic case [20, 21], a weak non-equilibrium drive would not destabilize the ordered state for $d = 2$, but larger drives lead to a super-thermal occupancy that can destabilize the order even in $d > 2$.

Conclusions.— We have used a mean field plus fluctuation analysis of the antiferromagnetic two-dimensional Hubbard model driven by an oscillating electric field to examine the accepted theoretical intuition, which suggests that if an ac drive is detuned from direct electronic transition energies, its main effect is to renormalize Hamiltonian parameters. Our solution of the full non-equilibrium problem shows rich additional physics: i) in the sub-gap drive regime, the drive is found to induce a substantial time-dependent component of the order parameter with first-order like transitions and coexistence regimes involving several locally stable (at least at the mean-field level) phases, and ii) in all cases, including the "Magnus" regime of very high frequency drive where the basic electronic state evolves smoothly with drive amplitude and no electronic quasiparticle excitations are created, we find a highly non-thermal distribution of magnons. Whereas the main focus in this paper is on the latter, an analysis of fluctuation effects on the bistability observed in the sub-gap drive regime is an interesting open question.

The interaction-mediated transfer of energy to the spin fluctuations may be thought of as a spin-charge coupling (albeit a weaker kind than considered e.g. in Ref. [40]). The dependence of the magnon distribution on the drive frequency and coupling to the reservoir indicates that the pathway to spin wave excitation involves reservoir states. The kinetics of this process, and the generalization to more realistic models of solids, are an important subject for future research. The distribution of fluctuations depends in a remarkable way on the drive amplitude. For small and moderate drive amplitude, there is substantial excitation of higher energy modes, but as the momentum tends to the ordering wave vector, the distribution tends towards the equilibrium one. However, at larger drive amplitude, the distribution diverges faster than ω_q^{-1} as momentum tends towards the ordering wave vector, which would indicate destabilization of order even in three dimensions. This apparent dynamical phase transition as a function of drive amplitude requires further study.

More generally, our findings show that the low-lying collective degrees of freedom are generically excited by the drive, and have a large, typically non-thermal, and drive amplitude-dependent occupancy that can lead to remarkable effects on physical properties. This finding calls into question the Floquet engineering paradigm in which applied radiation changes the Hamiltonian without changing the distribution function.

Acknowledgements.— The Center for Nanostructured Graphene (Proj. DNRF103) and the Center for Quantum Devices are sponsored by the Danish National Research Foundation. A.J.M. and D.M.K. were supported

by the US Department of Energy, Office of Basic Energy Sciences, Division of Materials Sciences and Engineering Grant DE SC0018218. D.M.K. additionally acknowledges support by the Deutsche Forschungsgemeinschaft through the Emmy Noether program (KA 3360/2-1). N.W. thanks Antti-Pekka Jauho for useful discussions.

[1] R. Mankowsky, M. Först, and A. Cavalleri, "Non-equilibrium control of complex solids by nonlinear phononics," Rep. on Prog. in Phys. **79**, 064503 (2016).

[2] D. N. Basov, R. D. Averitt, and D. Hsieh, "Towards properties on demand in quantum materials," Nature Mat. **16**, 1077–1088 (2017).

[3] Y. Tokura, M. Kawasaki, and N. Nagaosa, "Emergent functions of quantum materials," Nature Phys. **13**, 1056–1068 (2017).

[4] M. S. Rudner, N. H. Lindner, E. Berg, and M. Levin, "Anomalous edge states and the bulk-edge correspondence for periodically driven two-dimensional systems," Phys. Rev. X **3**, 031005 (2013).

[5] M. Bukov, L. D'Alessio, and A. Polkovnikov, "Universal high-frequency behavior of periodically driven systems: from dynamical stabilization to floquet engineering," Adv. in Phys. **64**, 139–226 (2015).

[6] R. Singla, G. Cotugno, S. Kaiser, M. Först, M. Mitrano, H. Y. Liu, A. Cartella, C. Manzoni, H. Okamoto, T. Hasegawa, S. R. Clark, D. Jaksch, and A. Cavalleri, "Thz-frequency modulation of the Hubbard U in an organic Mott insulator," Phys. Rev. Lett. **115**, 187401 (2015).

[7] J. H. Mentink, K. Balzer, and M. Eckstein, "Ultrafast and reversible control of the exchange interaction in Mott insulators," Nature Comm. **6**, 6708 (2015).

[8] M. Claassen, C. Jia, B. Moritz, and T. P. Devereaux, "All-optical materials design of chiral edge modes in transition-metal dichalcogenides," Nature Comm. **7**, 13074 (2016).

[9] M. Knap, M. Babadi, G. Refael, I. Martin, and E. Demler, "Dynamical Cooper pairing in nonequilibrium electron-phonon systems," Phys. Rev. B **94**, 214504 (2016), 1511.07874.

[10] D. A. Abanin, W. De Roeck, W. W. Ho, and F. Huveneers, "Effective hamiltonians, prethermalization, and slow energy absorption in periodically driven many-body systems," Phys. Rev. B **95**, 014112 (2017).

[11] D. M. Kennes, E. Y. Wilner, D. R. Reichman, and A. J. Millis, "Transient superconductivity from electronic squeezing of optically pumped phonons," Nature Phys. **13**, 479–483 (2017).

[12] M. A. Sentef, "Light-enhanced electron-phonon coupling from nonlinear electron-phonon coupling," Phys. Rev. B **95**, 205111 (2017).

[13] Y. Murakami, N. Tsuji, M. Eckstein, and P. Werner, "Nonequilibrium steady states and transient dynamics of conventional superconductors under phonon driving," Phys. Rev. B **96**, 045125 (2017).

[14] J. R. Coulthard, S. R. Clark, S. Al-Assam, A. Cavalleri, and D. Jaksch, "Enhancement of superexchange pairing in the periodically driven Hubbard model," Phys. Rev. B **96**, 085104 (2017).

[15] S. Kitamura, T. Oka, and H. Aoki, "Probing and controlling spin chirality in Mott insulators by circularly polarized laser," Phys. Rev. B **96**, 014406 (2017).

[16] D. M. Kennes, A. de la Torre, A. Ron, D. Hsieh, and A. J. Millis, "Floquet engineering in quantum chains," Phys. Rev. Lett. **120**, 127601 (2018).

[17] N. Tancogne-Dejean, M. A. Sentef, and A. Rubio, "Ultrafast modification of Hubbard U in a strongly correlated material: Ab initio high-harmonic generation in NiO," Phys. Rev. Lett. **121**, 097402 (2018).

[18] H. P. Ojeda Collado, José Lorenzana, Gonzalo Usaj, and C. A. Balseiro, "Population inversion and dynamical phase transitions in a driven superconductor," Phys. Rev. B **98**, 214519 (2018).

[19] F. Peronaci, M. Schiro, and O. Parcollet, "Resonant thermalization of periodically driven strongly correlated electrons," Phys. Rev. Lett. **120**, 197601 (2018).

[20] A. Mitra, S. Takei, Y. B. Kim, and A. J. Millis, "Nonequilibrium quantum criticality in open electronic systems," Phys. Rev. Lett. **97**, 236808 (2006).

[21] A. Mitra and A. J. Millis, "Current-driven quantum criticality in itinerant electron ferromagnets," Phys. Rev. B **77**, 220404(R) (2008).

[22] J. Jose Mendoza-Arenas, F. Javier Gomez-Ruiz, M. Eckstein, D. Jaksch, and S. R. Clark, "Ultra-fast control of magnetic relaxation in a periodically driven Hubbard model," Ann. Phys. **529**, 1700024 (2017).

[23] For details on the coupling to an infinite-bandwidth flat-band reservoir and how it leads to broadening, see e.g. [41].

[24] J. R. Schrieffer, X.-G. Wen, and S.-C. Zhang, "Spin-bag mechanism of high-temperature superconductivity," Phys. Rev. Lett. **60**, 944–947 (1988).

[25] J. R. Schrieffer, X. G. Wen, and S. C. Zhang, "Dynamic spin fluctuations and the bag mechanism of high-T_c superconductivity," Phys. Rev. B **39**, 11663–11679 (1989).

[26] A. Singh, "Spin-wave spectral properties of the Mott-Hubbard antiferromagnet: The intermediate-coupling regime," Phys. Rev. B **48**, 6668–6671 (1993).

[27] P. C. Hohenberg, "Existence of long-range order in one and two dimensions," Phys. Rev. **158**, 383–386 (1967).

[28] N. D. Mermin and H. Wagner, "Absence of ferromagnetism or antiferromagnetism in one- or two-dimensional isotropic Heisenberg models," Phys. Rev. Lett. **17**, 1133 (1966).

[29] A. Auerbach, *Interacting Electrons and Quantum Magnetism* (Springer, 1998).

[30] W. Magnus, "On the exponential solution of differential equations for a linear operator," Comm. on Pure and App. Math. **7**, 649–673 (1954).

[31] A. Kamenev, *Field Theory of Non-Equilibrium Systems* (Cambridge University Press, 2011).

[32] P. Coleman, *Introduction to Many-Body Physics* (Cambridge University Press, 2015).

[33] A. Kamenev and A. Levchenko, "Keldysh technique and non-linear sigma-model: basic principles and applications," Adv. in Phys. **58**, 197–319 (2009).

[34] T. Kitagawa, T. Oka, A. Brataas, L. Fu, and E. Demler, "Transport properties of nonequilibrium systems under the application of light: Photoinduced quantum Hall insulators without Landau levels," Phys. Rev. B **84**, 235108 (2011).

[35] H. Aoki, N. Tsuji, M. Eckstein, M. Kollar, T. Oka, and P. Werner, "Nonequilibrium dynamical mean-field theory and its applications," Rev. Mod. Phys. **86**, 779–837 (2014).

[36] A. K. Eissing, V. Meden, and D. M. Kennes, "Renormalization in periodically driven quantum dots," Phys. Rev. Lett. **116**, 026801 (2016).

[37] D. M. Kennes, "Transport through Periodically Driven Correlated Quantum Wires," (2018), arXiv:1801.02866.

[38] D. M. Kennes, S. G. Jakobs, C. Karrasch, and V. Meden, "Renormalization group approach to time-dependent transport through correlated quantum dots," Phys. Rev. B **85**, 085113 (2012).

[39] D. M. Kennes and V. Meden, "Quench dynamics of correlated quantum dots," Phys. Rev. B **85**, 245101 (2012).

[40] F. Dolcini, "Signature of interaction in dc transport of ac-gated quantum spin hall edge states," Phys. Rev. B **85**, 033306 (2012).

[41] S. Takei, *Dissipation and decoherence in open nonequilibrium electronic systems*, Ph.D. thesis, University of Toronto (2008).

B.4 Publication IV

Noise and full counting statistics of a Cooper pair splitter

Nicklas Walldorf, Fredrik Brange, Ciprian Padurariu, and Christian Flindt

Physical Review B 101, 205422 (2020)

Noise and full counting statistics of a Cooper pair splitter

Nicklas Walldorf,[1] Fredrik Brange,[2] Ciprian Padurariu,[3] and Christian Flindt[2]

[1] *Center for Nanostructured Graphene (CNG), Department of Physics, Technical University of Denmark, DK-2800 Kongens Lyngby, Denmark*
[2] *Department of Applied Physics, Aalto University, 00076 Aalto, Finland*
[3] *Institute for Complex Quantum Systems and IQST, University of Ulm, 89069 Ulm, Germany*

We investigate theoretically the noise and the full counting statistics of electrons that are emitted from a superconductor into two spatially separated quantum dots by the splitting of Cooper pairs and further on collected in two normal-state electrodes. With negatively-biased drain electrodes and a large superconducting gap, the dynamics of the Cooper pair splitter can be described by a Markovian quantum master equation. Using techniques from full counting statistics, we evaluate the electrical currents, their noise power spectra, and the power-power correlations in the output leads. The current fluctuations can be attributed to the competition between Cooper pair splitting and elastic cotunneling between the quantum dots via the superconductor. In one regime, these processes can be clearly distinguished in the cross-correlation spectrum with peaks and dips appearing at characteristic frequencies associated with elastic cotunneling and Cooper pair splitting, respectively. We corroborate this interpretation by analyzing the charge transport fluctuations in the time domain, specifically by investigating the $g^{(2)}$-function of the output currents. Our work identifies several experimental signatures of the fundamental transport processes involved in Cooper pair splitting and provides specific means to quantify their relative strengths. As such, our results may help guide and interpret future experiments on current fluctuations in Cooper pair splitters.

I. INTRODUCTION

Superconductors can serve as sources of entanglement in solid-state quantum circuits.[1,2] Electrons in the superconductor are paired up in spin-entangled states and by splitting these Cooper pairs, entanglement between distant electrons may be achieved. Specifically, electrons from a Cooper pair may tunnel into different normal-state electrodes, while preserving the entanglement of their spins. The process can be enhanced by using quantum dots with strong Coulomb interactions, which prevent electron pairs from tunneling into the same output lead, see Fig. 1. To certify the entanglement of the split Cooper pairs, it has been suggested that Bell inequalities can be formulated for the cross-correlations of the output currents, using ferromagnetic leads as spin filters.[3–8]

Following the theoretical proposals to generate nonlocal entanglement using Cooper pair splitters,[1,2] several experiments have realized these ideas in practice. Cooper pair splitters have been implemented in a variety of superconductor hybrid systems,[9–12] some of which employ InAs nanowires,[13–17] carbon nanotubes,[18–22] or graphene-based nanostructures.[23,24] The Cooper pair splitters can be characterized by measuring the conductance[14–23] or the noise,[13] and the splitting efficiency is in some cases approaching unity,[20,24] with one of the main competing processes being elastic cotunneling between the dots.[15,23] With this experimental progress, one may hope that Cooper pair splitters can soon be integrated into larger quantum circuits, aiming for solid-state quantum information processing.

On the theory side, Cooper pair splitters can be described using a variety of techniques depending on the specific device architecture and the operating conditions. For non-interacting systems, tight-binding models[25,26] or scattering theory[27] provide a convenient theoretical framework. Interactions can be included using Green function techniques,[28–32] quantum master equations,[5,33–38] or the real-time diagrammatic approach to quantum transport.[39–43] In most cases, these methods enable numerical calculations of the average currents

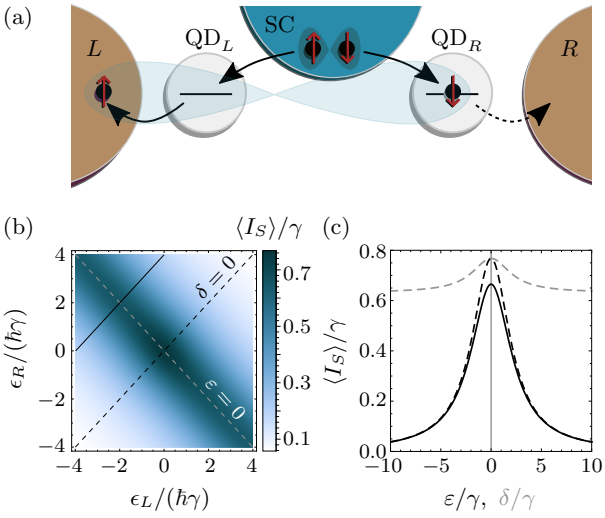

FIG. 1. Cooper pair splitter and average current. (a) Cooper pairs from a superconducting lead are split into two spin-entangled electrons that tunnel into separate quantum dots before reaching the output drains. (b) Average current from the superconductor into the drain electrodes as a function of the quantum dot levels. (c) The average current as a function of the sum, $\varepsilon = (\epsilon_L+\epsilon_R)/\hbar$, and the detuning, $\delta = (\epsilon_L-\epsilon_R)/\hbar$, of the quantum dot levels corresponding to the three cuts in the left panel. The results are obtained from Eq. (17) with the parameters $\gamma_{\rm CPS} = \gamma_{\rm EC} = \gamma$, $\gamma_L = 1.5\gamma$, $\gamma_R = 0.5\gamma$.

and the low-frequency noise in the output leads. On the other hand, analytic results for the current fluctuations in Cooper pair splitters are scarce.

In this work we investigate theoretically the current fluctuations in a Cooper pair splitter using techniques from full counting statistics.[44–50] In a recent article, some of us considered the distribution of waiting times between emitted electrons, and we showed that it contains a wealth of information about the Cooper pair splitter, for instance the characteristic time scales that govern the underlying tunneling processes.[51] Measurements of electron waiting times, however, require real-time detection of the individual tunneling events.[52–54] By contrast, conventional quantum transport experiments typically measure the electric currents and their fluctuations,[9–24] which are thus our main focus here. In particular, we consider the noise power spectra of the currents in the output leads[55–59] and their power-power correlations, which we use to analyze the physical processes involved in the splitting of Cooper pairs. We corroborate our findings by considering the $g^{(2)}$-function of the output currents,[60,61] which provides an alternative view on the charge transport in the time domain. While earlier works have analyzed the shot noise of Cooper pair splitters using numerical approaches, we here employ projection operator methods that have been developed in the context of full counting statistics[47–50] and which allow us to carry out all calculations analytically. We are hereby able to develop a detailed understanding of the process of Cooper pair splitting and the associated fluctuations, which is relevant for future experiments on Cooper pair splitters.

The rest of the paper is organized as follows. In Sec. II, we introduce the full Hamiltonian of the Cooper pair splitter, and we discuss how the combined system of a large-gap superconductor coupled to the quantum dots can be described by an effective Hamiltonian. In Sec. III, we derive a quantum master equation for the dynamics of electrons in the quantum dots, which is valid with large negative biases on the drains. By dressing the quantum master equation with counting fields, we gain access to the full statistics of electrons that have tunneled into the drains and the corresponding current fluctuations. In Sec. IV, we calculate the average currents and compare our results to earlier works before moving on to the noise power spectra of the output currents in Sec. V. Here, we first show how the zero-frequency noise allows for a simple and transparent interpretation of the charge transport in terms of contributions from elastic cotunneling between the quantum dots and the splitting of Cooper pairs, respectively. We then analyze the full frequency-dependent noise spectra and find that characteristic frequencies associated with Cooper pair splitting and elastic cotunneling, respectively, can be clearly identified in the finite-frequency noise spectra, thus providing experimental signatures of the two types of processes and their relative strengths. In Sec. VI, we consider higher-order cumulants of the currents. Our quantum master equation provides access to the full counting statistics of transferred electrons, and we here discuss the fourth cumulant of the currents, including the power-power correlations in the output leads. In Sec. VII, we turn to time-domain observables, and we show how our preceding analysis can be supported by investigations of the $g^{(2)}$-function of the output currents. Finally, in Sec. VIII, we give our conclusions, while technical details are provided in the Appendices.

II. COOPER PAIR SPLITTER

Figure 1 shows the Cooper pair splitter consisting of two quantum dots in proximity to a superconductor that acts as a source of Cooper pairs. Strong Coulomb interactions on the quantum dots ensure that split Cooper pairs tunnel into different dots and further on into the separate normal-metal leads that act as electronic drains. The eigenstates of the uncoupled quantum dots are given by the occupation of each dot including the spin-degree of freedom. With a large superconducting gap, the proximity to the superconductor coherently couples the occupation states with the same particle parity, that is, an even or an odd number of particles. The even states with zero or two electrons are coupled by the process of Cooper pair splitting, where two electrons enter the quantum dots from the superconductor or vice versa. The odd states with just a single electron on one of the dots are coupled by the process of elastic cotunneling, where an electron is transferred from one dot to the other via the superconductor. Under these conditions, the quantum dots and the superconductor can be described by an effective Hamiltonian as we discuss below.[33,34]

We start by specifying the full Hamiltonian

$$\hat{H} = \hat{H}_{QD} + \hat{H}_{SC} + \hat{H}_N + \hat{H}_{T_S} + \hat{H}_{T_N}, \tag{1}$$

which describes the quantum dots, the superconductor, and the normal-metal leads, given by the first three terms, as well as the coupling between them given by the two tunneling Hamiltonians, $\hat{H}_{T_S}$ and $\hat{H}_{T_N}$, which we detail below. The Hamiltonian of the dots reads

$$\hat{H}_{QD} = \sum_{\ell\sigma} \epsilon_\ell \hat{d}^\dagger_{\ell\sigma} \hat{d}_{\ell\sigma} + \sum_\ell U_\ell \hat{n}_{\ell\uparrow} \hat{n}_{\ell\downarrow}, \tag{2}$$

where we have defined the operators $\hat{d}^\dagger_{\ell\sigma}$ and $\hat{d}_{\ell\sigma}$ that create and annihilate electrons with energy ϵ_ℓ and spin σ in the left or right quantum dot, $\ell = L, R$. Here, the on-site interaction on the dots is denoted by U_ℓ, and $\hat{n}_{\ell\sigma} \equiv \hat{d}^\dagger_{\ell\sigma} \hat{d}_{\ell\sigma}$ counts electrons on the dots with spin σ. The superconductor is described by the BCS Hamiltonian

$$\hat{H}_{SC} = \sum_{q\sigma} \epsilon_q \hat{a}^\dagger_{q\sigma} \hat{a}_{q\sigma} - \left(\sum_q \Delta \ \hat{a}^\dagger_{q\uparrow} \hat{a}^\dagger_{-q\downarrow} + \text{h.c.} \right), \tag{3}$$

where the operators $\hat{a}^\dagger_{q\sigma}$ and $\hat{a}_{q\sigma}$ create and annihilate particles with momentum q single-particle energy ϵ_q in

the superconductor with the superconducting order parameter Δ. The normal-state leads are described by the Hamiltonian

$$\hat{H}_N = \sum_{\ell k\sigma} \epsilon_{\ell k} \hat{c}^\dagger_{\ell k\sigma} \hat{c}_{\ell k\sigma}, \tag{4}$$

while the coupling between the quantum dots and the external reservoirs are given by the tunneling Hamiltonians

$$\hat{H}_{T_S} = \sum_{\ell q\sigma} \left(t_{S\ell q} \hat{a}^\dagger_{q\sigma} \hat{d}_{\ell\sigma} + \text{h.c.} \right) \tag{5}$$

and

$$\hat{H}_{T_N} = \sum_{\ell k\sigma} \left(t_{\ell k} \hat{c}^\dagger_{\ell k\sigma} \hat{d}_{\ell\sigma} + \text{h.c.} \right), \tag{6}$$

where $t_{S\ell q}$ and $t_{\ell k}$ are the tunneling amplitudes.

In the following, we consider strong Coulomb interactions on the quantum dots, such that each of them can be occupied by maximally one electron at a time. With a large superconducting gap, the combined system of the quantum dots and the superconductor can then be described by the effective Hamiltonian[33,34]

$$\begin{aligned} \hat{H}_S = &\sum_{\ell\sigma} \epsilon_\ell \hat{d}^\dagger_{\ell\sigma} \hat{d}_{\ell\sigma} - \hbar\gamma_{\text{EC}} \sum_{\sigma} \left(\hat{d}^\dagger_{L\sigma} \hat{d}_{R\sigma} + \text{h.c.} \right) \\ &- \frac{\hbar\gamma_{\text{CPS}}}{\sqrt{2}} \left(\hat{d}^\dagger_{L\downarrow} \hat{d}^\dagger_{R\uparrow} - \hat{d}^\dagger_{L\uparrow} \hat{d}^\dagger_{R\downarrow} + \text{h.c.} \right) \end{aligned} \tag{7}$$

where $\hbar\gamma_{\text{EC}}$ and $\hbar\gamma_{\text{CPS}}$ are the amplitudes for elastic cotunneling and Cooper pair splitting. A detailed derivation of this Hamiltonian is provided in Appendix A.

In summary, we use the following operating conditions

$$k_B T, \epsilon_\ell, \hbar\gamma_{\text{EC}}, \hbar\gamma_{\text{CPS}}, \hbar\gamma_\ell \ll |eV_\ell| < \Delta < U_\ell, \tag{8}$$

where V_ℓ are the negative voltages applied to the drain electrodes, the temperature of the environment is denoted by T, and γ_ℓ are the tunneling rates from the quantum dots to the drains, which we introduce below. In this regime, we can trace out the normal-state electrodes and obtain a quantum master equation for the coupled quantum dots as shown in Appendix B.

III. QUANTUM MASTER EQUATION

Under the conditions specified above, the charge transport is unidirectional from the superconductor to the normal-state electrodes via the quantum dots. The system dynamics can then be described by a Markovian quantum master equation for the reduced density matrix $\hat{\rho}$, defined in the Hilbert space of $\hat{H}_S$, reading[62]

$$\frac{d}{dt}\hat{\rho} = \mathcal{L}\hat{\rho} = -\frac{i}{\hbar}[\hat{H}_S, \hat{\rho}] + \mathcal{D}[\hat{\rho}]. \tag{9}$$

The Liouvillian $\mathcal{L}$ is the sum of the coherent evolution of the system itself, given by the commutator of the Hamiltonian $\hat{H}_S$ and the density matrix, and the dissipator

$$\mathcal{D}[\hat{\rho}] = \sum_{\sigma,\ell=L,R} \gamma_\ell \left(\hat{d}_{\ell\sigma} \hat{\rho} \hat{d}^\dagger_{\ell\sigma} - \frac{1}{2}\{\hat{\rho}, \hat{d}^\dagger_{\ell\sigma} \hat{d}_{\ell\sigma}\} \right), \tag{10}$$

which describes the incoherent tunneling of electrons with spin $\sigma = \uparrow, \downarrow$ from the left (right) quantum dot to the left (right) electrode at the rate γ_ℓ, $\ell = L, R$.

To evaluate the charge transport statistics, we resolve the density matrix with respect to the number of electrons that have tunneled into each of the normal-state leads during the time span $[0, t]$.[63,64] Thus, we introduce the n-resolved density matrix, $\hat{\rho}(\mathbf{n})$, where the vector $\mathbf{n} = (n_L, n_R)$ contains the number of transferred electrons. By tracing over the system degrees of freedom, we obtain the full counting statistics of transferred charge as

$$P(\mathbf{n}, t) = \text{Tr}[\hat{\rho}(\mathbf{n}, t)]. \tag{11}$$

The unresolved density matrix is recovered as $\hat{\rho}(t) = \sum_{\mathbf{n}} \hat{\rho}(\mathbf{n}, t)$. Moreover, it is convenient to introduce a vector of counting fields, $\boldsymbol{\chi} = (\chi_L, \chi_R)$, that couple to the number of transferred charges, by defining

$$\hat{\rho}(\boldsymbol{\chi}, t) = \sum_{\mathbf{n}} \hat{\rho}(\mathbf{n}, t) e^{i\mathbf{n}\cdot\boldsymbol{\chi}}, \tag{12}$$

whose equation of motion follows from Eq. (9) and reads

$$\begin{aligned} \frac{d}{dt}\hat{\rho}(\boldsymbol{\chi}, t) &= \mathcal{L}(\boldsymbol{\chi})\hat{\rho}(\boldsymbol{\chi}, t) \\ &= \Big[\mathcal{L} + \sum_{\ell=L,R} (e^{i\chi_\ell} - 1)\mathcal{J}_\ell \Big] \hat{\rho}(\boldsymbol{\chi}, t). \end{aligned} \tag{13}$$

Here we have identified the jump operators that describe the transfer of an electron into lead ℓ as

$$\mathcal{J}_\ell \hat{\rho} = \gamma_\ell \sum_\sigma \hat{d}_{\ell\sigma} \hat{\rho} \hat{d}^\dagger_{\ell\sigma}. \tag{14}$$

Equation (13) provides us with a complete description of the charge transfer statistics on all relevant time scales, and it allows us to evaluate quantities such as the distribution of electron waiting times,[51,65,66] the noise power spectra of the currents,[55–59] and the full counting statistics of the transferred charge.[47–50] In the following sections, we use Eq. (13) to investigate the current fluctuations in the Cooper pair splitter.

IV. AVERAGE CURRENT

We start by considering the mean current flowing from the superconductor into the drain electrodes. Throughout this work, we consider particle currents instead of electrical currents, since it allows us to omit powers of

the electron charge. Due to charge conservation, the current from the superconductor can be written as

$$\langle I_S\rangle = \langle I_L\rangle + \langle I_R\rangle \tag{15}$$

in terms of the currents running into the normal-state drains, $\langle I_\ell\rangle$, $\ell = L, R$, which can be expressed as

$$\langle I_\ell\rangle = \mathrm{Tr}[\mathcal{J}_\ell\hat{\rho}_S], \tag{16}$$

where the stationary state $\hat{\rho}_S$ is given by the normalized solution to $\mathcal{L}\hat{\rho}_S = 0$. The current from the superconductor then becomes

$$\langle I_S\rangle = \bar{\gamma}^2_{\mathrm{CPS}}\gamma_\Sigma, \tag{17}$$

where we have introduced the average rate

$$\gamma_\Sigma = (\gamma_L + \gamma_R)/2, \tag{18}$$

and defined the renormalized couplings

$$\bar{\gamma}^2_{\mathrm{CPS}} = \frac{4\gamma^2_{\mathrm{CPS}}}{\varepsilon^2 + \gamma^2_\Sigma + 4\gamma^2_{\mathrm{CPS}}/\eta}, \tag{19}$$

and

$$\bar{\gamma}^2_{\mathrm{EC}} = \frac{4\gamma^2_{\mathrm{EC}}}{\delta^2 + \gamma^2_\Sigma + 4\gamma^2_{\mathrm{EC}}}, \tag{20}$$

where $\delta = (\epsilon_L - \epsilon_R)/\hbar$ and $\varepsilon = (\epsilon_L + \epsilon_R)/\hbar$ are the detuning and the sum of the energy levels, respectively. In addition, we have introduced the parameter

$$\eta = 1 + \left(\frac{\gamma_L - \gamma_R}{2\gamma_\Sigma}\right)^2 \left[(\bar{\gamma}_{\mathrm{EC}})^2 - 1\right], \tag{21}$$

which reduces to one for a symmetric setup with $\gamma_L = \gamma_R$. We note that the expression for the current recovers the result of Ref. 33 obtained with $\gamma_{\mathrm{EC}} = 0$ and the energy renormalization absorbed into the dot levels as discussed at the end of Appendix A. In addition, for $\gamma_{\mathrm{CPS}} \ll \gamma_\Sigma$, we reproduce the result of Ref. 2 in that limit.

The average current is shown in Fig. 1b as a function of the quantum dot energies. The current is maximal along the line $\varepsilon = 0$, where the doubly occupied state is on resonance with the empty state, and Cooper pair splitting is energetically favorable. Along this resonance line, the current is only weakly dependent on the detuning of the energy levels, δ, as shown in Fig. 1c. Moreover, for a symmetric setup with $\gamma_L = \gamma_R$, the elastic cotunneling processes do not influence the average current, which becomes independent of the detuning (not shown). In Fig. 1c, we also show the average current away from the resonance condition $\varepsilon = 0$, and the process of Cooper pair splitting gets suppressed. The peak in the current is Lorentzian with a broadening given by the coupling to the external electrodes. We also note that the elastic cotunneling processes are enhanced, when the quantum dot levels are on resonance, meaning that the detuning vanishes, $\delta = 0$.

V. NOISE POWER SPECTRUM

We next investigate the fluctuations of the current. To this end, we consider the noise power spectrum of the tunnel currents between the quantum dots and the drains. The noise power spectrum reads[67]

$$S_{\ell\ell'}(\omega) = \frac{1}{2}\int_{-\infty}^{\infty} \mathrm{d}t e^{i\omega t}\langle\{\delta\hat{I}_\ell(t), \delta\hat{I}_{\ell'}(0)\}\rangle, \tag{22}$$

where the operator $\delta\hat{I}_\ell(t) = \hat{I}_\ell(t) - \langle\hat{I}_\ell(t)\rangle$, $\ell = L, R$, measures the deviation of the tunnel current from its average value, and curly brackets denote an anti-commutator. The autocorrelation spectrum, $S_{\ell\ell}(\omega)$, is always real and positive. By contrast, the cross correlations, $S_{\ell\neq\ell'}(\omega)$, can take complex values at finite frequencies, but we only consider the real part, and from now on we let $S_{\ell\neq\ell'}(\omega)$ denote the real part. Below, we do not need to specify the current operators. Instead, MacDonald's formula[68] allows us to relate the noise power spectrum to the quantum master equation (13) and express it as[49,55,65]

$$S_{\ell\ell'}(\omega) = \delta_{\ell\ell'}\mathrm{Tr}[\mathcal{J}_\ell\hat{\rho}_S] - \mathrm{Re}\{\mathrm{Tr}\left[\mathcal{J}_\ell\mathcal{R}(\omega)\mathcal{J}_{\ell'}\hat{\rho}_S\right] + (\ell\leftrightarrow\ell')\}, \tag{23}$$

where the pseudoinverse, $\mathcal{R}(\omega)$, is defined as[48–50,55]

$$\mathcal{R}(\omega) = \mathcal{Q}(\mathcal{L} + i\omega)^{-1}\mathcal{Q}, \tag{24}$$

in terms of the orthogonal projectors $\mathcal{Q} = 1 - \mathcal{P}$ and $\mathcal{P}[\,\cdot\,] = \hat{\rho}_S\mathrm{Tr}[\,\cdot\,]$. The pseudoinverse is well-defined even for $\omega = 0$, since the inversion is performed only in the subspace spanned by $\mathcal{Q} = 1 - \mathcal{P}$, where $\mathcal{L}$ is regular, since the null space has been projected away. Using the matrix representation of the Liouvillian in Appendix C, we can then evaluate the noise spectrum. Details on how to evaluate the pseudoinverse can be found on page 7 of Ref. 50.

Interestingly, the noise power spectrum can be determined analytically. Specifically, for a symmetric setup with $\gamma_L = \gamma_R = \gamma_N$, we find for the Fano factor, $F_{\ell\ell'}(\omega) = S_{\ell\ell'}(\omega)/I_N$, the expression

$$F_{\ell\ell'}(\omega) = \delta_{\ell\ell'} - I_N\gamma_N(\gamma^2_N + \omega^2_{\mathrm{CPS}})\left(\frac{5\gamma^2_N + \omega^2_{\mathrm{CPS}} + \omega^2}{h(\omega_{\mathrm{CPS}}, \omega)} - \frac{(1 - \delta_{\ell\ell'})}{2\gamma^2_{\mathrm{CPS}}(\gamma^2_N + \omega^2)} + (-1)^{\delta_{\ell\ell'}}\left[\frac{\gamma_{\mathrm{EC}}}{\gamma_{\mathrm{CPS}}}\right]^2 \frac{\gamma^2_N + \omega^2_{\mathrm{EC}} - 3\omega^2}{h(\omega_{\mathrm{EC}}, \omega)}\right), \tag{25}$$

having defined the average current $I_N \equiv \langle I_L\rangle = \langle I_R\rangle = \langle I_S\rangle/2$ and the characteristic frequencies $\omega_{\mathrm{CPS}} = \sqrt{4\gamma^2_{\mathrm{CPS}} + \varepsilon^2}$

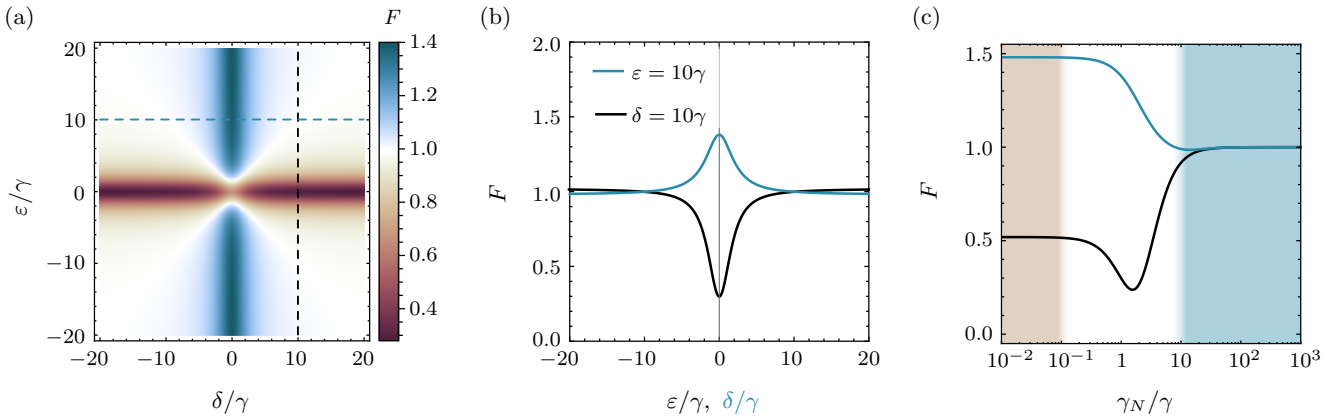

FIG. 2. Fano factor of the autocorrelations. (a) Fano factor as a function of the detuning, δ, and the total energy, ε, of the quantum dot levels with $\gamma_L = \gamma_R = \gamma_{\rm CPS} = \gamma_{\rm EC} \equiv \gamma$. (b) Fano factor along the cuts indicated in the left panel. (c) Fano factor as a function of $\gamma_L = \gamma_R \equiv \gamma_N$ with $\gamma_{\rm CPS} = \gamma_{\rm EC} \equiv \gamma$ and $\epsilon_L = -\epsilon_R = 5\hbar\gamma$ (black line) and $\epsilon_L = \epsilon_R = 5\hbar\gamma$ (blue line).

and $\omega_{\rm EC} = \sqrt{4\gamma_{\rm EC}^2 + \delta^2}$, as well as the function

$$h(\omega_0, \omega) = (\gamma_N^2 + \omega^2)^3 + 2(\gamma_N^4 - \omega^4)\omega_0^2 + (\gamma_N^2 + \omega^2)\omega_0^4. \tag{26}$$

With this expression in hand, we now discuss the information about the charge transport that we can extract.

To begin with, we consider the zero-frequency component of the current correlations. The zero-frequency noise of a Cooper pair splitter has previously been calculated numerically in Ref. 5. Here, we obtain a compact expression for the zero-frequency noise reading

$$F_{\ell\ell'} = 1 + \left(\delta_{\ell\ell'} - \frac{1}{2}\right)\tilde{\gamma}_{\rm EC}^2 - \frac{I_N}{\gamma_N}\left(1 + \frac{2I_N\gamma_N}{\gamma_{\rm CPS}^2}\right), \tag{27}$$

which provides an interesting interpretation of the charge transport. In the absence of elastic cotunneling and with large tunneling rates to the drains, only the first term survives, and the Fano factors equal unity. In this case, the separate flows of electrons into each drain resemble a Poisson process. However, the currents are correlated, since electrons are injected pairwise from the superconductor as split Cooper pairs. For this reason, the Fano factor of the cross-correlations is positive and not zero as one would expect for two uncorrelated processes.

This picture gradually breaks down as elastic cotunneling is included, and the second term becomes nonzero. Elastic cotunneling reduces the correlations between the currents in the drains, since electrons are allowed to transfer between the quantum dots. In this way, the separate flows of electrons into the drains get mixed, which both reduces their correlations and increases the fluctuations in each drain. Furthermore, as the coupling to the drain electrodes is lowered, also the third term becomes important, and it reduces both the auto and the cross correlations. In this case, the lowered coupling to the leads introduces a finite dwell time of electrons on the quantum dots, which reduces the fluctuations in the leads and the correlations between the currents.

To gain further insight into the current fluctuations, we show in Figs. 2 and 3 the Fano factors of the auto and cross correlations, respectively. In Fig. 2a, the splitting of Cooper pairs is favorable along the resonance line, $\varepsilon = 0$, and the Fano factor is suppressed well below one due to the tunnel barriers between the quantum dots and the drains. By contrast, along the other resonance line, $\delta = 0$, where elastic cotunneling is enhanced, the fluctuations are increased, since the separate flows of electrons get mixed. These effects are also illustrated in Fig. 2b, where we show the Fano factor along the cuts in the left panel, which both cross one of the resonance lines. In Fig. 2c, we show the Fano factor as a function of the coupling to the drain electrodes. In the blue-shaded region, electrons immediately leave the quantum dots via the drains because of the large coupling, and the Fano factor approaches unity, signaling that the injection of split Cooper pairs becomes a Poisson process. In the brown-shaded region, the coupling is very low, and the Fano factor now depends strongly on the energy levels of the quantum dots. For $\varepsilon = 0$ (black line), Cooper pair splitting is favorable, and the occupations of the quantum dots oscillate between being empty and doubly-occupied. In that case, the quantums dots are occupied half of the time, and the Fano factor is suppressed accordingly. For $\delta = 0$ (blue line), elastic cotunneling is enhanced, and the fluctuations are increased due to the mixing of the separate flows of electrons. In between these parameter regimes, the Fano factor develops a more complicated structure, since all possible processes are combined.

In Fig. 3, we turn to the Fano factor of the cross-

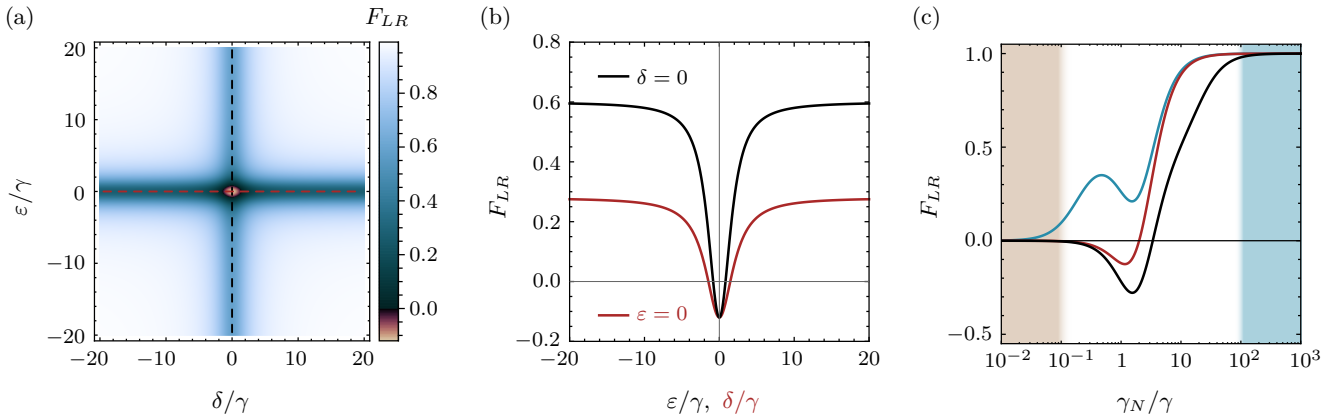

FIG. 3. Fano factor of the cross-correlations. (a) Fano factor as a function of the detuning, δ, and the total energy, ε, of the quantum dot levels with $\gamma_L = \gamma_R = \gamma_{\rm CPS} = \gamma_{\rm EC} \equiv \gamma$. (b) Fano factor along the cuts indicated in the left panel. (c) Fano factor as a function of $\gamma_L = \gamma_R \equiv \gamma_N$ with $\epsilon_L = \epsilon_R = 0$, $\gamma_{\rm CPS} \equiv \gamma$, and $\gamma_{\rm EC} = 0.1\gamma$ (blue line), 1γ (red line), 10γ (black line).

correlations. In Fig. 3a, we observe a large degree of correlation *away* from the resonance lines. In that case, neither Cooper pair splitting nor elastic cotunneling are favorable. Still, once a split Cooper pair is injected into the quantum dots and one electron tunnels out via a drain electrode, the other electron likely leaves via the other drain electrode, leading to the large correlations. However, despite the large correlations, the actual currents are of course small, since the system is operated away from any of the important resonance conditions. In Fig. 3b, we consider the cross-correlations along the two resonance lines, $\delta = 0$ (black line) and $\varepsilon = 0$ (red line), where either elastic cotunneling or Cooper pair splitting is favorable. Elastic cotunneling reduces the cross-correlations, since it mixes the separate flows of electrons. They also get reduced, if Cooper pair splitting is on resonance, and electrons quickly oscillate back and forth between the superconductor and the quantum dots. When the two processes are combined, we even observe negative cross-correlations between the output currents as seen in the figure.

Finally, in Fig. 3c, we consider the cross-correlations as a function of the coupling to the drain electrodes, and again we can identify three distinct regimes. For low couplings in the brown-shaded region, the tunneling events into the drains are rare and uncorrelated. By contrast, in the blue-shaded region, where the coupling is large, split Cooper pairs are immediately evacuated from the quantum dots via the drains, leading to strong correlations. In between these parameter regimes, the cross-correlations are more complicated as discussed above.

Next, we consider the full frequency-dependent noise spectra given by Eq. (25) and displayed in Fig. 4. In Fig. 4a, we show the Fano factor of the cross-correlations as a function of the observation frequency and the total energy of the quantum dots. Of particular interest are the dips and peaks in the cross-correlations that appear at the characteristic frequencies, $\omega_{\rm CPS}$ and $\omega_{\rm EC}$, associated with Cooper pair splitting and elastic cotunneling, respectively, thus providing a direct experimental method to distinguish the two types of processes. The figure also illustrates how $\omega_{\rm CPS}$ depends on the total energy, while $\omega_{\rm EC}$ remains constant. In Fig. 4b, we show both the auto and cross correlation spectra along the resonance line indicated in the left panel, and here we again see how the cross-correlations allow us to distinguish Cooper pair splitting from elastic cotunneling. By contrast, the two types of processes both lead to dips in the autocorrelation spectrum. We also see how a large coupling to the drain electrodes washes out these features, which might also not be robust against external decoherence and dephasing mechanisms that are not included here.

VI. POWER-POWER CORRELATIONS

Until now, we have focused on the average current and the noise power spectra, which at zero frequency correspond to the first and second cumulants of the currents. However, with the counting fields included in our quantum master equation, we can in principle access any cumulant of the full counting statistics. To this end, we formally solve the quantum master equation (13) as $\hat{\rho}(\boldsymbol{\chi}, t) = e^{\mathcal{L}(\boldsymbol{\chi})t}\hat{\rho}_S$, assuming that the system has reached its stationary state at the time $t = 0$, when the counting of particles begins. We also define the cumulant generating function for the charge transfer statistics as

$$S(\boldsymbol{\chi}, t) = \ln\left[\sum_{\mathbf{n}} P(\mathbf{n}, t)e^{i\mathbf{n}\cdot\boldsymbol{\chi}}\right] = \ln \mathrm{Tr}\left[e^{\mathcal{L}(\boldsymbol{\chi})t}\hat{\rho}_S\right]. \quad (28)$$

We then see that the scaled cumulant generating function

$$\Theta(\boldsymbol{\chi}) = \lim_{t\to\infty}\frac{S(\boldsymbol{\chi}, t)}{t} = \max_i\{\lambda_i(\boldsymbol{\chi})\}, \quad (29)$$

for long observation times is given by the eigenvalue of $\mathcal{L}(\boldsymbol{\chi})$ with the largest real part. For small values of the

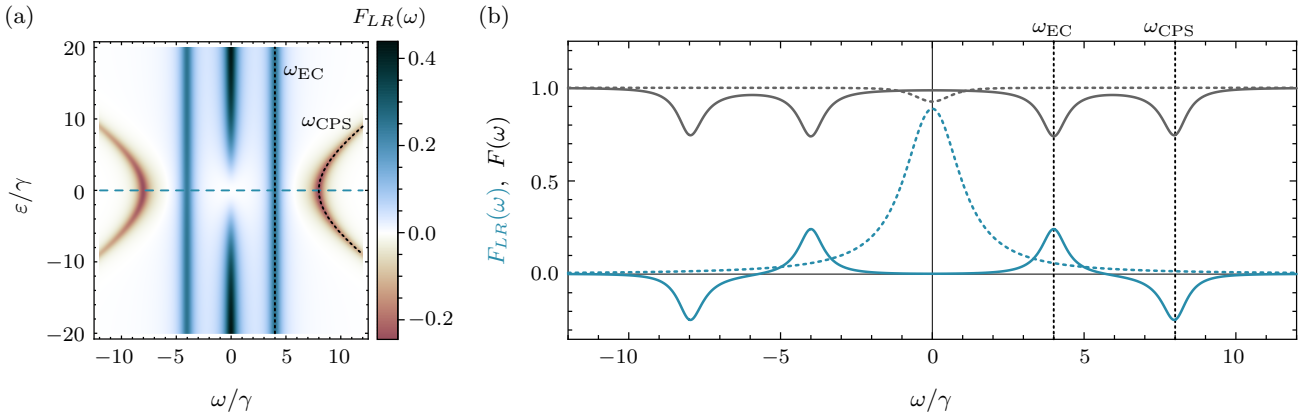

FIG. 4. Finite-frequency noise. (a) Fano factor of the cross-correlations as a function of the frequency and the total energy of the quantum dots. The other parameters are $\gamma_L = \gamma_R \equiv 0.5\gamma$, $\gamma_{\rm CPS} = 4\gamma$, $\gamma_{\rm EC} = 2\gamma$, and $\delta = 0$. (b) Auto (gray) and cross (blue) correlations as functions of the frequency for $\epsilon_L = \epsilon_R = 0$ and $\gamma_L = \gamma_R \equiv 0.5\gamma$, $\gamma_{\rm CPS} = 4\gamma$, $\gamma_{\rm EC} = 2\gamma$ (solid), given by the cut in the left panel, and $\gamma_L = \gamma_R \equiv \gamma$, $\gamma_{\rm CPS} = \gamma_{\rm EC} = 0.1\gamma$ (dotted). In both panels, we indicate $\omega_{\rm CPS}$ and $\omega_{\rm EC}$.

counting fields, this is the eigenvalue that develops adiabatically from the zero-eigenvalue corresponding to the stationary state. All other eigenvalues have negative real parts, causing the system to relax to its stationary state.

All zero-frequency cumulants of the (particle) current can now be obtained by differentiating the cumulant generating function with respect to the counting fields as

$$\langle\!\langle I_\ell^n I_{\ell'}^m \rangle\!\rangle = \partial_{\chi_\ell}^n \partial_{\chi_{\ell'}}^m \Theta(\boldsymbol{\chi})|_{\boldsymbol{\chi}=\mathbf{0}}, \tag{30}$$

where double brackets denote cumulant averages. The first and second cumulants are the average currents and the zero-frequency noise, respectively. Here, we focus on the power-power correlations in the drains, $\langle\!\langle I_\ell^2 I_{\ell'}^2 \rangle\!\rangle$, i.e., the correlations between the squared currents in the output leads. Such correlations have not received much attention in the past, but they can in principle be measured, and they can be evaluated using our quantum master equation dressed with counting fields. Technically, we have to evaluate the derivatives of the eigenvalue of $\mathcal{L}(\boldsymbol{\chi})$ with the largest real part according to Eq. (29). However, due to the large matrix size of $\mathcal{L}(\boldsymbol{\chi})$, we cannot directly evaluate its eigenvalues as functions of the counting fields. Instead, we find the derivatives of the largest eigenvalue using perturbation theory in the counting fields as discussed in Refs. 48–50. The method takes the zero-eigenvalue and the stationary state as the starting point and then calculates corrections to the eigenvalue order-by-order in the counting fields to obtain cumulants of any order. The details of this perturbation scheme are outlined in Appendix D, and below we just quote the final results.

For the autocorrelations of the power (or the fourth cumulant of the currents), we find

$$\langle\!\langle I_\ell^4 \rangle\!\rangle = \langle\!\langle I_\ell^2 \rangle\!\rangle - 12\mathrm{Tr}\big[\mathcal{J}_\ell \mathcal{R}\big\{1 + 2\mathcal{I}_\ell(1 + \mathcal{R}\mathcal{I}_\ell)\mathcal{R} + \mathcal{S}_\ell \mathcal{R}\big\}\mathcal{J}_\ell \hat{\rho}_S\big], \tag{31}$$

where $\mathcal{I}_\ell = \langle I_\ell \rangle - \mathcal{J}_\ell$ and $\mathcal{S}_\ell = \langle\!\langle I_\ell^2 \rangle\!\rangle - \mathcal{J}_\ell$ in terms of the zero-frequency noise, $\langle\!\langle I_\ell^2 \rangle\!\rangle = S_{\ell\ell}(0)$, and $\mathcal{R} = \mathcal{R}(0)$ is the pseudo-inverse in Eq. (24) evaluated at $\omega = 0$. (We note that the perturbation scheme also yields the noise power spectrum in Eq. (23) for $\omega = 0$.) For the power-power correlations, we arrive at the more complicated expression

$$\langle\!\langle I_\ell^2 I_{\ell'}^2 \rangle\!\rangle = \mathrm{Tr}\big[\mathcal{J}_\ell \mathcal{R}\big\{(1+2\mathcal{I}_\ell\mathcal{R})(1+2\mathcal{I}_{\ell'}\mathcal{R})\mathcal{I}_{\ell'} + 4\mathcal{I}_{\ell'}\mathcal{R}(\mathcal{I}_{\ell'}\mathcal{R}\mathcal{I}_\ell + \mathcal{I}_\ell\mathcal{R}\mathcal{I}_{\ell'}) + 4\langle\!\langle I_\ell I_{\ell'} \rangle\!\rangle \mathcal{R}\mathcal{I}_{\ell'} + 2\mathcal{S}_{\ell'}\mathcal{R}\mathcal{I}_\ell\big\}\hat{\rho}_S\big] + (\ell \leftrightarrow \ell'). \tag{32}$$

We can now evaluate these formulas based on the Liouvillian $\mathcal{L}$ and the jump operators in Eq. (14). The resulting expressions are lengthy, and here we only present analytical results in certain limits together with figures.

For a symmetric Cooper pair splitter, where the amplitude for Cooper pair splitting is much smaller than the total energy of the quantum dots, the average current is suppressed, and the Fano factor, $F_{\ell\ell'}^{(4)} = \langle\!\langle I_\ell^2 I_{\ell'}^2 \rangle\!\rangle / I_N$ for the power-power correlations simplify to the expression

$$F_{\ell\ell'}^{(4)} = 1 + \left(4\delta_{\ell\ell'} - \frac{1}{2}\right)\bar{\gamma}_{\rm EC}^2 + \mathcal{O}\left(\frac{\gamma_{\rm CPS}}{\sqrt{\gamma_N^2 + \varepsilon^2}}\right), \tag{33}$$

where the higher-order terms are different for the auto

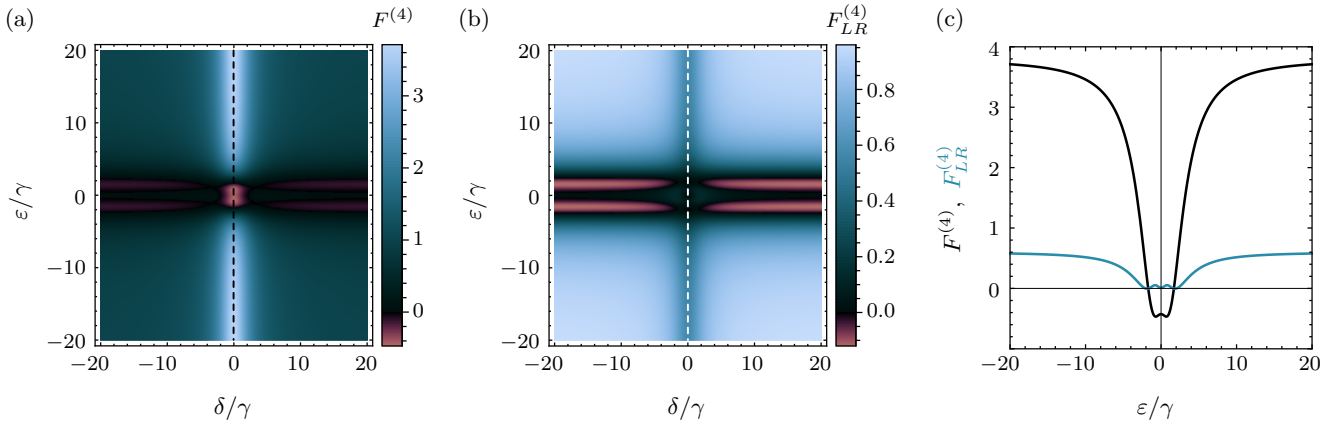

FIG. 5. Power-power correlations. (a) Fano factor of the power-power autocorrelations as a function of the detuning, δ, and the total energy, ε, of the quantum dot levels with $\gamma_L = \gamma_R = \gamma_{\rm CPS} = \gamma_{\rm EC} \equiv \gamma$. (b) Fano factor of the power-power cross-correlations for the same parameters. (c) Auto and cross correlations along the cuts indicated in the left panels, where $\delta = 0$.

and the cross correlation and depend on all parameters. Just as for the current-current correlations in Eq. (27) in that limit, we see that the autocorrelations are Poissonian, if elastic cotunneling is negligible. At the same time, the cross-correlations remain positive, since the two separate flows of electrons originate from the same random splitting of Cooper pairs. In this context, elastic cotunneling reduces the cross-correlations by mixing the two flows, and it also strongly increases the autocorrelations of the power fluctuations. More generally, we find that $F^{(4)}_{\ell\ell} = F^{(4)}_{\ell\ell'}$, if $\gamma_{\rm EC} \ll \sqrt{\gamma_N^2 + \delta^2}$, such that cotunneling is negligible.

In Fig. 5, we show the Fano factors of the auto and cross correlations of the power fluctuations as functions of the detuning and the total energy of the quantum dot levels. The fluctuations in each lead are generally large as we move along the resonance line, $\delta = 0$, where elastic cotunneling is favorable. However, the fourth cumulant of the current gets reduced, and even becomes negative, as also Cooper pair splitting comes into resonance. The cross-correlations also get reduced, even if the average current is large on resonance, since the elastic cotunneling processes mix the separate flows of electrons and thereby destroy the correlations.

VII. TIME-DOMAIN OBSERVABLES

Having investigated the current fluctuations in the frequency domain, we now change perspective and instead analyze the charge transport statistics in the time domain. In a recent work, we considered the distribution of waiting times between tunneling events into the drains.[51] As an alternative, we here consider the $g^{(2)}$-function of the output currents. Based on our quantum master equation, the $g^{(2)}$-function can be obtained as[60]

$$g^{(2)}_{\ell\ell'}(\tau) = \frac{{\rm Tr}\left[\mathcal{J}_\ell e^{\mathcal{L}\tau}\mathcal{J}_{\ell'}\hat{\rho}_S\right] + {\rm Tr}\left[\mathcal{J}_{\ell'} e^{\mathcal{L}\tau}\mathcal{J}_\ell\hat{\rho}_S\right]}{2\langle I_\ell\rangle\langle I_{\ell'}\rangle}, \quad (34)$$

where τ is the time between tunneling events described by the jump operators $\mathcal{J}_\ell$ and $\mathcal{J}_{\ell'}$. Here we consider a symmetrized $g^{(2)}$-function, although this makes no difference for the symmetric setup we consider below. The $g^{(2)}$-function is the probability that an electron tunnels into lead ℓ (or ℓ') at the time τ after an electron has tunneled into lead ℓ' (or ℓ), normalized with respect to the unconditional probability. Evaluating this expression for a symmetric setup, we find for the $g^{(2)}$-functions

$$g^{(2)}_{\ell\ell'}(\tau) = 1 - e^{-\gamma_N\tau}\left[\left(\cos\left[\frac{\omega_{\rm CPS}\tau}{2}\right] + \frac{\gamma_N}{\omega_{\rm CPS}}\sin\left[\frac{\omega_{\rm CPS}\tau}{2}\right]\right)^2 - g_x(1-\delta_{\ell\ell'}) + (-1)^{\delta_{\ell\ell'}} g_x\left(\frac{2\gamma_{\rm EC}\sin\left[\frac{\omega_{\rm EC}\tau}{2}\right]}{\omega_{\rm EC}}\right)^2\right], \quad (35)$$

where we have defined the parameter $g_x = (\gamma_N^2 + \omega_{\rm CPS}^2)/(2\gamma_{\rm CPS})^2$.

We start by analyzing the $g^{(2)}$-function of the individual currents. Here, we first notice that $g^{(2)}_{ll}(0) = 0$, which is a direct manifestation of the strong Coulomb interactions that prevent two electrons from being emitted from

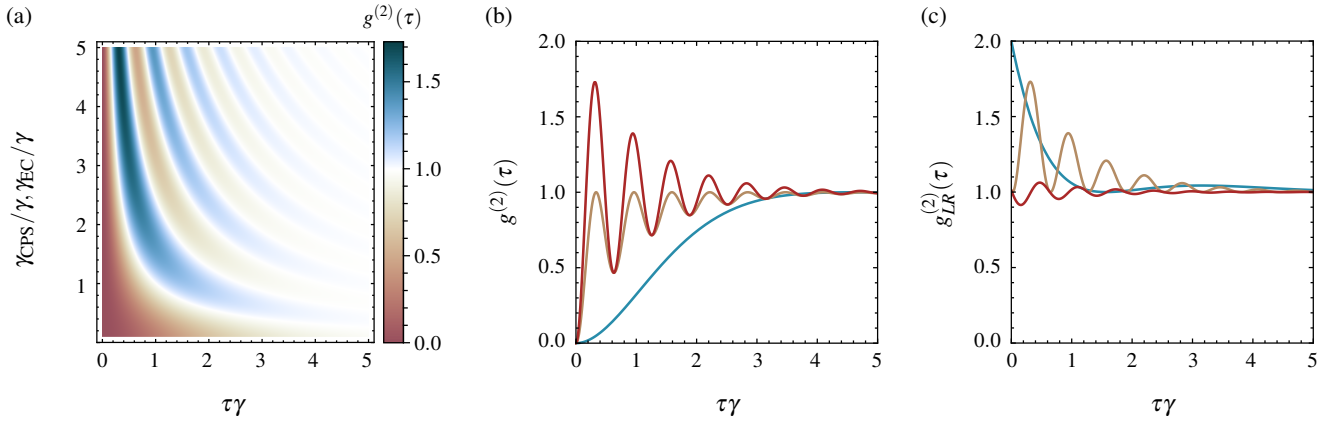

FIG. 6. Time-domain observables. (a) The $g^{(2)}$-correlation function of the output currents as a function of the time and the amplitudes for Cooper pair splitting and elastic cotunneling being equal, $\gamma_{\rm CPS} = \gamma_{\rm EC}$. The other parameters are $\delta = \varepsilon = 0$ and $\gamma_N = \gamma$. (b) Autocorrelation function, $g^{(2)}(\tau)$, for $\gamma_{\rm CPS} = 0.5\gamma$ and $\gamma_{\rm EC} = 0$ (blue), $\gamma_{\rm CPS} = 5\gamma$ and $\gamma_{\rm EC} = 0$ (yellow), and $\gamma_{\rm CPS} = 5\gamma$ and $\gamma_{\rm EC} = 5\gamma$ (red). (c) Cross-correlation function, $g^{(2)}_{LR}(\tau)$, for the same parameters as in the middle panel.

the same dot simultaneously. Furthermore, we find that $g^{(2)}_{ll}(0) < g^{(2)}_{ll}(\tau)$ for $\tau > 0$, implying that the electron emission from each quantum dot is always anti-bunched, even if the emission statistics may be super-Poissonian.[60]

In the first two panels of Fig. 6, we show the $g^{(2)}$-function of the individual currents and observe an oscillatory pattern that is washed out as the coupling to the drain electrodes is increased. In particular, if the coupling is much larger than the characteristic frequency associated with Cooper pair splitting, $\gamma_N \gg \omega_{\rm CPS}$, and the frequency associated with elastic cotunneling is small, $\omega_{\rm EC} \simeq 0$, we find

$$g^{(2)}_{\ell\ell}(\tau) \simeq 1 - e^{-\gamma_N \tau}\left(1 + \frac{\gamma_N \tau}{2}\right)^2, \qquad (36)$$

which increases monotonously with time. In the other extreme, where the coupling is smaller than the frequency of Cooper pair splitting, $\omega_{\rm CPS} \gtrsim \gamma_N$, an oscillatory pattern with frequency $\omega_{\rm CPS}$ appears due to the coherent oscillations between the quantum dots and the superconductor. Similarly, for $\omega_{\rm EC} \gtrsim \gamma_N$, elastic cotunneling leads to oscillations, however, with frequency $\omega_{\rm EC}$.

In Fig. 6c, we turn to the $g^{(2)}$-function of the cross-correlations. In this case, we find at short times

$$g^{(2)}_{\ell\neq\ell'}(0) = 1 + \frac{\gamma_N^2 + \omega_{\rm CPS}^2}{4\gamma_{\rm CPS}^2}, \qquad (37)$$

showing that the probability for simultaneous emissions into the left and right drain electrodes increases with the coupling to the leads, γ_N, and the total energy, $|\varepsilon|$. By contrast, as one might expect, elastic cotunneling has no effect on $g^{(2)}_{\ell\ell'}(\tau)$ on short timescales, $\tau \ll 1/\omega_{\rm EC}$. In the case, where the coupling to the leads is large, $\gamma_N \gg \omega_{\rm CPS}$, and the frequency of elastic cotunneling is small, $\omega_{\rm EC} \simeq 0$, we find

$$g^{(2)}_{l\neq l'}(\tau) \simeq 1 - e^{-\gamma_N \tau}\left[\left(1 + \frac{\gamma_N \tau}{2}\right)^2 - g_x\right]. \qquad (38)$$

Finally, we note that the $g^{(2)}$-correlation functions can be directly related to the noise spectra in Eq. (25) as[60]

$$F_{\ell\ell'}(\omega) = \delta_{\ell\ell'} + I_N \int_{-\infty}^{\infty} {\rm d}\tau e^{i\omega\tau}\left[g^{(2)}_{\ell\ell'}(|\tau|) - 1\right]. \qquad (39)$$

On the other hand, the charge transport is a non-renewal process, since the system does not return to the same state after each emission event. For this reason, there is no direct connection between the $g^{(2)}$-functions and the distribution of waiting times, and they contain different information about the charge transport statistics.[61]

VIII. CONCLUSIONS

We have theoretically investigated the noise and the full counting statistics of electrons emitted from a Cooper pair splitter. Working with negatively-biased drain electrodes and a large superconducting gap, the Cooper pair splitter can be described by a Markovian quantum master equation for the dynamics of electrons inside the quantum dots. Using methods from full counting statistics, we have then calculated not only the average current and the shot noise, but also the full frequency-dependent noise spectra, higher-order power-power correlations, as well as the $g^{(2)}$-correlation functions of the output currents. Based on our analytical results for these observables, we have presented a detailed investigation of the fundamental tunneling processes in Cooper pair splitters. Specifically, we have shown how the competing processes of Cooper pair splitting and elastic cotunneling are manifested in the low-frequency fluctuations of the currents and their cross-correlations. If the coupling to the normal-state leads is weak, the two types of processes show up as dips and peaks in the finite-frequency noise spectrum of the cross-correlations. These results are corroborated by an analysis of the $g^{(2)}$-correlation

functions in the time domain. Our work identifies several experimental signatures of the fundamental transport processes in Cooper pair splitters, and we expect that our results may help guide and interpret future experiments on Cooper pair splitting.

ACKNOWLEDGMENTS

We thank P. Burset, A.-P. Jauho, T. Novotný and M. Wegewijs for valuable discussions. The Center for Nanostructured Graphene (CNG) is sponsored by the Danish Research Foundation, Project DNRF103. The work was supported by the Academy of Finland (Projects No. 308515 and No. 312299).

Note added.— During the final preparations of our manuscript, we became aware of a related preprint that investigates the current fluctuations in a Cooper pair splitter based on three quantum dots.[69]

Appendix A: Effective Hamiltonian

In this appendix, we derive the effective Hamiltonian in Eq. (7), assuming a large superconducting gap and strong Coulomb interactions on the quantum dots. In this case, the quantum dots cannot be doubly occupied, and we can discard the double-occupied states in the density matrix and omit the double-occupancy contribution in Eq. (2).

We start by considering the von Neumann equation for the density matrix of the full system

$$i\hbar\frac{d}{dt}\hat{\rho}_H(t) = [\hat{H}, \hat{\rho}_H(t)]. \tag{A1}$$

Here $\hat{H} = \hat{H}_0 + \hat{H}_{T_S}$ is the time-independent Hamiltonian, with $\hat{H}_{T_S}$ the Hamiltonian describing the tunneling between the quantum dots and the superconductor, and $\hat{H}_0$ is the remaining part of the Hamiltonian. By Laplace-transforming the density matrix as

$$\hat{\rho}_H(E) = \int_{t_0}^{\infty} \mathrm{d}t \hat{\rho}_H(t) e^{i(E+i\eta)(t-t_0)/\hbar}, \tag{A2}$$

we can formally rewrite the von Neumann equation as

$$(E+i\eta)\hat{\rho}_H(E) - i\hbar\hat{\rho}_H(t_0) = L_0\hat{\rho}_H(E) + L_{T_S}\hat{\rho}_H(E), \tag{A3}$$

having defined $L_{0/T_S}[\,\cdot\,] = [\hat{H}_{0/T_S},\,\cdot\,]$. We can write the solution as the geometric series

$$\begin{aligned}\hat{\rho}_H(E) = (&W_0(E) + W_0(E)L_{T_S}W_0(E) \\ &+ W_0(E)L_{T_S}W_0(E)L_{T_S}W_0(E) + \cdots)i\hbar\hat{\rho}_H(t_0),\end{aligned} \tag{A4}$$

where $W_0(E) = [E - L_0 + i\eta]^{-1}$. The superconductor is in thermal equilibrium, $\hat{\rho}_H(E) \simeq \hat{\rho}_{\tilde{0}}(E) \otimes \hat{\rho}^{\mathrm{eq}}_{SC}$, hence by tracing out the superconductor, we get to second order in L_{T_S},

$$\hat{\rho}_{\tilde{0}}(E) \approx (W_{\tilde{0}}(E) + W_{\tilde{0}}(E)\mathrm{Tr}_{SC}[\Sigma_S\hat{\rho}^{\mathrm{eq}}_{SC}]W_{\tilde{0}}(E))i\hbar\hat{\rho}_{\tilde{0}}(t_0), \tag{A5}$$

where $\hat{H}_{\tilde{0}} = \hat{H}_0 - \hat{H}_{SC}$ in $W_{\tilde{0}}$, $\Sigma_S = L_{T_S}W_0(E)L_{T_S}$, and we have used that terms with an odd number of L_{T_S} vanish and that higher-order terms are suppressed in the large gap limit due to $W_0(E)$. Similarly, upon expanding $\hat{\rho}_{\tilde{0}}(E) = (E + i\eta - L_{\tilde{0}} - \overline{\Sigma}_S)^{-1}i\hbar\hat{\rho}_{\tilde{0}}(t_0)$ to first order in $\overline{\Sigma}_S$, we recognize that[70] $\overline{\Sigma}_S = \mathrm{Tr}_{SC}[\Sigma_S\hat{\rho}^{\mathrm{eq}}_{SC}]$.

Next, we introduce the Bogoliubov transformation, $\hat{\boldsymbol{\gamma}}^\dagger_q = (\hat{\gamma}^\dagger_{q\uparrow}, \hat{\gamma}_{-q\downarrow}) = \hat{\boldsymbol{a}}^\dagger_q\boldsymbol{U}^\dagger_q$, where $\hat{\boldsymbol{a}}^\dagger_q = (\hat{a}^\dagger_{q\uparrow}, \hat{a}_{-q\downarrow})$ and

$$\boldsymbol{U}^\dagger_q = \begin{pmatrix} u^*_q & v_q \\ -v^*_q & u_q \end{pmatrix}, \tag{A6}$$

is a unitary matrix with $u_q = (1 + \epsilon_q/E_q)^{1/2}/\sqrt{2}$ and $v_q = (1 - \epsilon_q/E_q)^{1/2}/\sqrt{2}e^{i\theta_S}$ where $E_q = \sqrt{\epsilon_q^2 + |\Delta|^2}$ and θ_S is the phase of the superconductor. With this transformation, we get $\hat{H}_{SC} = \sum_{q\sigma} E_q\hat{\gamma}^\dagger_{q\sigma}\hat{\gamma}_{q\sigma}$ (plus a constant, which does not contribute to the von Neumann equation), and the tunneling Hamiltonian (5) becomes

$$\hat{H}_{T_S} = \sum_{\xi=\pm,\ell q\sigma} \xi t^\xi_{S\ell q}\left(u^\xi_q\hat{\gamma}^\xi_{q\sigma} + \sigma v^{(-\xi)}_q\hat{\gamma}^{(-\xi)}_{-q-\sigma}\right)\hat{d}^\xi_{\ell\sigma}, \tag{A7}$$

where we have defined $t^{(+)-}_{S\ell q} = t^{(\,)*}_{S\ell q}$, $u^{(+)-}_q = u^{(\,)*}_q$, $v^{(+)-}_q = v^{(\,)*}_q$, $\hat{\gamma}^{+(-)}_{q\sigma} = \hat{\gamma}^{\dagger(\,)}_{q\sigma}$, $\hat{d}^{(+)-}_{\ell\sigma} = \hat{d}^{(\,)\dagger}_{\ell\sigma}$. We can furthermore write L_{T_S} in the compact form[70]

$$L_{T_S} = \sum_{\xi,\theta=\pm,\ell q\sigma} \xi t^\xi_{S\ell q}\left(u^\xi_q\Gamma^{\xi\theta}_{q\sigma} + \sigma v^{(-\xi)}_q\Gamma^{(-\xi)\theta}_{-q-\sigma}\right)D^{\xi\theta}_{\ell\sigma}, \tag{A8}$$

where $\theta = \pm$ determines if the operator acts to the left $(+)$ or right $(-)$, for instance

$$\Gamma^{\xi+}_{q\sigma}\hat{O} = \hat{\gamma}^\xi_{q\sigma}\hat{O}, \quad \Gamma^{\xi-}_{q\sigma}\hat{O} = \hat{O}\hat{\gamma}^\xi_{q\sigma}, \tag{A9}$$

and

$$D^{\xi+}_{\ell\sigma}\hat{O} = \hat{d}^\xi_{\ell\sigma}\hat{O}, \quad D^{\xi-}_{\ell\sigma}\hat{O} = \hat{O}\hat{d}^\xi_{\ell\sigma}, \tag{A10}$$

where $\hat{O}$ is an operator. With these transformations, we readily obtain

$$\Sigma_S = \sum_{\xi\theta\ell q\sigma}\sum_{\xi'\theta'\ell' q'\sigma'} \xi\xi' t^\xi_{S\ell q}t^{\xi'}_{S\ell' q'}D^{\xi'\theta'}_{\ell'\sigma'}\left(u^{\xi'}_{q'}\Gamma^{\xi'\theta'}_{q'\sigma'} + \sigma' v^{(-\xi')}_{q'}\Gamma^{(-\xi')\theta'}_{-q'-\sigma'}\right)W_0(E)D^{\xi\theta}_{\ell\sigma}\left(u^\xi_q\Gamma^{\xi\theta}_{q\sigma} + \sigma v^{(-\xi)}_q\Gamma^{(-\xi)\theta}_{-q-\sigma}\right), \tag{A11}$$

where we have used the commutation relation $\Gamma^{\chi\theta}D^{\chi'\theta'} = -\theta\theta' D^{\chi'\theta'}\Gamma^{\chi\theta}$ (suppressing the subscripts). Having expressed the tunneling Hamiltonian in terms of the Bogoliubov transformation that diagonalizes the superconducting Hamiltonian, we have

$$\Gamma^{\xi\theta}_{q\sigma} L_0 = (L_0 - \xi E_q)\Gamma^{\xi\theta}_{q\sigma}, \tag{A12}$$

and thus

$$\begin{aligned}\Sigma_S = -\sum \xi\xi'\theta\theta' t^{\xi}_{S\ell q} t^{\xi'}_{S\ell' q'} D^{\xi'\theta'}_{\ell'\sigma'} \Big(W_0(E + \xi' E_{q'}) D^{\xi\theta}_{\ell\sigma} u^{\xi'}_{q'} \Gamma^{\xi'\theta'}_{q'\sigma'} + W_0(E - \xi' E_{q'}) D^{\xi\theta}_{\ell\sigma} \sigma' v^{(-\xi')}_{q'} \Gamma^{(-\xi')\theta'}_{-q'-\sigma'} \Big) \\ \times \Big(u^{\xi}_{q} \Gamma^{\xi\theta}_{q\sigma} + \sigma v^{(-\xi)}_{q} \Gamma^{(-\xi)\theta}_{-q-\sigma} \Big),\end{aligned} \tag{A13}$$

where we have left the summation indices implicit. Upon tracing out the superconductor, we find

$$\overline{\Sigma}_S = \sum_{\xi\theta\theta'\ell\ell'\sigma} \theta\theta' \Big(D^{(-\xi)\theta'}_{\ell'\sigma} I^{(1)}_{\xi\theta\ell\ell'} + \sigma D^{\xi\theta'}_{\ell'-\sigma} I^{(2)}_{\xi\theta\ell\ell'} \Big) D^{\xi\theta}_{\ell\sigma}, \tag{A14}$$

where we have defined

$$I^{(1)}_{\xi\theta\ell\ell'} = \sum_q t^{\xi}_{S\ell q} t^{(-\xi)}_{S\ell' q} \left(|u_q|^2 f^{(-\xi\theta)}(E_q) W_{\tilde{0}}(E - \xi E_q) + |v_q|^2 f^{(\xi\theta)}(E_q) W_{\tilde{0}}(E + \xi E_q) \right), \tag{A15}$$

and

$$I^{(2)}_{\xi\theta\ell\ell'} = \sum_q t^{\xi}_{S\ell q} t^{\xi}_{S\ell' -q} u^{\xi}_q v^{(-\xi)}_q \left(f^{(-\xi\theta)}(E_q) W_{\tilde{0}}(E - \xi E_q) - f^{(\xi\theta)}(E_q) W_{\tilde{0}}(E + \xi E_q) \right), \tag{A16}$$

and we have used that $\mathrm{Tr}_{SC}\left[\Gamma^{\xi'\theta'}_{q'\sigma'}\Gamma^{\xi\,\theta}_{q\,\sigma}\,\hat{\rho}^{\mathrm{eq}}_{SC}\right] = \delta_{qq'}\delta_{\sigma\sigma'}\delta_{\xi,-\xi'} f^{(-\xi\theta)}(E_q)$, $f^+ = f$ and $f^- = 1 - f$ with f being the Fermi–Dirac distribution, and $\epsilon_q = \epsilon_{-q}$. In the limit of large superconducting gap at long times, $W_{\tilde{0}}(E \pm \xi E_q)$ is dominated by the constant factor $\pm\xi E_q^{-1}$, whereby

$$I^{(1)}_{\xi\theta\ell\ell'} \simeq -\sum_q t^{\xi}_{S\ell q} t^{(-\xi)}_{S\ell' q} \xi E_q^{-1} \Big(|u_q|^2 f^{(-\xi\theta)}(E_q) - |v_q|^2 f^{(\xi\theta)}(E_q) \Big), \tag{A17}$$

and

$$I^{(2)}_{\xi\theta\ell\ell'} \simeq I^{(2)}_{\xi\ell\ell'} = -\sum_q t^{\xi}_{S\ell q} t^{\xi}_{S\ell' -q} u^{\xi}_q v^{(-\xi)}_q \xi E_q^{-1}. \tag{A18}$$

Using that $I^{(1)}_{(-\xi)\theta\ell'\ell} = -I^{(1)}_{\xi(-\theta)\ell\ell'}$ and $I^{(2)}_{\xi\ell'\ell} = I^{(2)}_{\xi\ell\ell'}$ we find upon performing the sum over θ and θ' in Eq. (A14) $\overline{\Sigma}_S[\,\cdot\,] = [\hat{H}_{\Sigma_S},\,\cdot\,]$, where

$$\hat{H}_{\Sigma_S} = \sum_{\xi\ell\ell'\sigma} \Big(I^{(1)}_{\xi+\ell\ell'} \hat{d}^{(-\xi)\dagger}_{\ell'\sigma} \hat{d}^{\xi}_{\ell\sigma} + \sigma I^{(2)}_{\xi\ell\ell'} \hat{d}^{\xi}_{\ell'-\sigma} \hat{d}^{\xi}_{\ell\sigma} \Big). \tag{A19}$$

Carrying out the remaining sums, one obtains the terms in Eq. (7), where we have defined the amplitudes $\hbar\gamma_{\mathrm{CPS}} = -\sqrt{2}(I^{(2)}_{-LR} + I^{(2)}_{-RL})$ and $\hbar\gamma_{\mathrm{EC}} = I^{(1)}_{-+LR} - I^{(1)}_{++RL}$, corresponding to Cooper pair splitting and elastic cotunneling, respectively, absorbed the constant self-energy into a redefinition of the quantum dot levels, and omitted the term corresponding to a Cooper pair occupying a single dot, which is prevented in the large-U limit. The momentum integrals from $I^{(1)}_{\xi\theta\ell\ell'}$ and $I^{(2)}_{\xi\ell\ell'}$ are calculated explicitly in Ref. 33 assuming point-like contacts between each dot and the superconductor (with zero temperature), separated by the distance δr.

Appendix B: Quantum master equation

In this appendix, we derive the quantum master equation (9) with the dissipator given by Eq. (10). A microscopic approach for quantum transport in normal-state structures in the high-bias limit has been devised by Gurvitz and Prager[71–73] and later on extended to Cooper pair splitters in Ref. 33. The method uses an occupation-number representation of the many-body wave function, which is time-evolved under the Schrödinger equation. As an alternative and potentially more compact approach, we here derive the quantum master equation starting from the von Neumann equation for $\hat{\rho}_{\tilde{0}}$ (cf. App. A). The geometric series form of the von Neumann

equation as in Eq. (A4) can also be obtained by iterating as

$$\begin{aligned}\hat{\rho}_{\bar{0}}(E) &= W_{\bar{0}}(E)\left[L_{T_N}\hat{\rho}_{\bar{0}}(E) + i\hbar\hat{\rho}_{\bar{0}}(t_0)\right] \\ &= W_{\bar{0}}(E)\left[L_{T_N}W_{\bar{0}}(E)\left(L_{T_N}\hat{\rho}_{\bar{0}}(E) + i\hbar\rho_{\bar{0}}(t_0)\right)\right. \\ &\quad \left. + i\hbar\hat{\rho}_{\bar{0}}(t_0)\right] \\ &= \cdots,\end{aligned} \tag{B1}$$

where $\hat{H}_{\bar{0}} = \hat{H}_S + \hat{H}_N$ in $W_{\bar{0}}$. We now inspect the operator

$$\Sigma_N \equiv L_{T_N}W_{\bar{0}}(E)L_{T_N}, \tag{B2}$$

which appears after the first iteration. To this end, we express the tunneling Hamiltonian in the compact form

$$\hat{H}_{T_N} = \sum_{\xi=\pm,\ell k\sigma} \xi t^{\xi}_{\ell k}\hat{c}^{\xi}_{\ell k\sigma}\hat{d}^{\xi}_{\ell\sigma}, \tag{B3}$$

where we have defined $\hat{c}^{+(-)}_{\ell k\sigma} = \hat{c}^{\dagger(\,)}_{\ell k\sigma}$, $\hat{d}^{+(-)}_{\ell\sigma} = \hat{d}^{(\,)\dagger}_{\ell\sigma}$, and $t^{+}_{\ell k} = t_{\ell k}$, $t^{-}_{\ell k} = t^{*}_{\ell k}$. We also have

$$L_{T_N} = \sum_{\xi,\theta=\pm,\ell k\sigma} \xi t^{\xi}_{\ell k}C^{\xi\theta}_{\ell k\sigma}D^{\xi\theta}_{\ell\sigma}, \tag{B4}$$

in terms of superoperators as in App. A. With these definitions, we readily obtain

$$\Sigma_N = \sum_{\xi\theta\ell k\sigma}\sum_{\xi'\theta'\ell'k'\sigma'} \xi\xi' t^{\xi}_{\ell k}t^{\xi'}_{\ell' k'}D^{\xi'\theta'}_{\ell'\sigma'}C^{\xi'\theta'}_{\ell' k'\sigma'}W_{\bar{0}}(E)D^{\xi\theta}_{\ell\sigma}C^{\xi\theta}_{\ell k\sigma}, \tag{B5}$$

having used the commutation relation $C^{\xi\theta}D^{\xi'\theta'} = -\theta\theta' D^{\xi'\theta'}C^{\xi\theta}$, omitting the subscripts here.

The electrons in the normal-state reservoirs are non-interacting, such that

$$C^{\xi\theta}_{\ell k\sigma}L_{\bar{0}} = (L_{\bar{0}} - \xi\epsilon_{\ell k})C^{\xi\theta}_{\ell k\sigma}, \tag{B6}$$

and thus

$$\begin{aligned}\Sigma_N = &-\sum t^{\xi}_{\ell k}t^{\xi'}_{\ell' k'}D^{\xi'\theta'}_{\ell'\sigma'}W_{\bar{0}}(E+\xi'\epsilon_{\ell' k'})D^{\xi\theta}_{\ell\sigma}C^{\xi'\theta'}_{\ell' k'\sigma'}C^{\xi\theta}_{\ell k\sigma} \\ &\times \xi\xi'\theta\theta',\end{aligned} \tag{B7}$$

where we have left out the summation indices in the sum. The environment is not affected by the subsystem of interest, $\hat{\rho}_{\bar{0}}(E) \simeq \hat{\rho}(E)\otimes\hat{\rho}^{\rm eq}_N$, allowing us to trace out the environmental degrees of freedom as

$$\begin{aligned}\hat{\bar{\Sigma}}_\rho = &\sum_{\xi\theta\theta'\ell k\sigma}\theta\theta' t^{\xi}_{\ell k}t^{-\xi}_{\ell k}D^{(-\xi)\theta'}_{\ell\sigma}W_S(E-\xi\epsilon_{\ell k})D^{\xi\theta}_{\ell\sigma}\hat{\rho}(E) \\ &\times f^{(-\xi\theta)}_{\ell}(\epsilon_{\ell k}),\end{aligned} \tag{B8}$$

where $\hat{H}_S$ in W_S is given in Eq. (7), we have defined $\hat{\bar{\Sigma}}_\rho = {\rm Tr}_N\{\Sigma_N\hat{\rho}_{\bar{0}}(E)\}$ and used that ${\rm Tr}_N\{C^{\xi'\theta'}_{\ell' k'\sigma'}C^{\xi\theta}_{\ell k\sigma}\hat{\rho}^{\rm eq}_N\} = \delta_{\ell\ell'}\delta_{kk'}\delta_{\sigma\sigma'}\delta_{\xi,-\xi'}f^{(-\xi\theta)}_{\ell}(\epsilon_{\ell k})$, where $f^{+}_{\ell} = f_\ell$ is the Fermi–Dirac distribution, and $f^{-}_{\ell} = 1 - f_\ell$. Formally, inserting completeness relations in terms of the eigenstates of $\hat{H}_S = \sum_a \epsilon_a|a\rangle\langle a|$, we find

$$\hat{\bar{\Sigma}}_\rho = \sum_{\xi\theta\theta'\ell\sigma}\sum_{aa'}\theta\theta' D^{(-\xi)\theta'}_{\ell\sigma}|a\rangle\langle a|(D^{\xi\theta}_{\ell\sigma}\hat{\rho}(E))|a'\rangle\langle a'|I_{\delta\delta'\xi\theta aa'}, \tag{B9}$$

where the integral

$$I_{\ell\xi\theta aa'} = \int d\epsilon \frac{\nu_\ell(\epsilon)|t_\ell(\epsilon)|^2 f^{(-\xi\theta)}_{\ell}(\epsilon)}{E - \xi\epsilon + i\eta - (\epsilon_a - \epsilon_{a'})}, \tag{B10}$$

contains the density of states, ν_ℓ, of lead ℓ.

We now assume that large negative voltages are applied to the normal-state electrodes, so that they are completely empty, $f^{(-\xi\theta)}_{\ell}(\epsilon) = \delta_{-\xi\theta,-}$. In addition, we assume that the lead coupling,

$$\gamma_\ell \equiv \frac{2\pi}{\hbar}\nu_\ell|t_\ell|^2, \tag{B11}$$

is constant for the relevant energies. Hence,

$$I_{\ell\xi\theta aa'} = -i\hbar\gamma_\ell\delta_{-\xi\theta,-}/2 \equiv -i\hbar I_{\ell\xi\theta}/2. \tag{B12}$$

Since $I_{\ell\xi\theta}$ does not depend on a and a' we can remove the completeness relations from Eq. (B9) and write

$$\hat{\bar{\Sigma}}_\rho = -\frac{i\hbar}{2}\sum_{\xi\theta\theta'\ell\sigma}\theta\theta' D^{(-\xi)\theta'}_{\ell\sigma}D^{\xi\theta}_{\ell\sigma}I_{\ell\xi\theta}\hat{\rho}(E). \tag{B13}$$

Considering next the following iterations in Eq. (B1), we see that terms with an odd number of L_{T_N} vanish, once we trace out the environment. On the other hand, for terms with an even number of L_{T_N}, we see that as we commute all the C's to the right, the leftmost C will give rise to the substitution, $E \to E + \xi\epsilon$, in all the $W_{\bar{0}}$'s. Hence, the approximations used above lead to integrals over ϵ, as in Eq. (B10), involving products of simple fractions with poles in the same complex half-plane. For this reason, these integrals vanish.[71] As a result, the iteration loop terminates, and upon tracing out the environment, we can write Eq. (B1) as

$$(E + i\eta - L_S)\hat{\rho}(E) = i\hbar\mathcal{D}\hat{\rho}(E) + i\hbar\hat{\rho}(t_0), \tag{B14}$$

where we have defined the superoperator

$$\mathcal{D} = -\frac{1}{2}\sum_{\xi\theta\theta'\ell\sigma}\theta\theta' D^{(-\xi)\theta'}_{\ell\sigma}D^{\xi\theta}_{\ell\sigma}I_{\ell\xi\theta}. \tag{B15}$$

Finally, by transforming this expression back to the time domain, we arrive at Eqs. (9) and (10) by letting the dissipator $\mathcal{D}$ act on the reduced density matrix.

Appendix C: Matrix representation

To carry out our calculations, we need a matrix representation of the Liouvillian. In the basis

$$\{\rho_{(0)(0)},\rho_{(L\uparrow)(L\uparrow)},\rho_{(L\downarrow)(L\downarrow)},\rho_{(R\uparrow)(R\uparrow)},\rho_{(R\downarrow)(R\downarrow)},\rho_{(S)(S)},\rho_{(0)(S)},\rho_{(S)(0)},\rho_{(L\uparrow)(R\uparrow)},\rho_{(R\uparrow)(L\uparrow)},\rho_{(L\downarrow)(R\downarrow)},\rho_{(R\downarrow)(L\downarrow)}\}, \quad \text{(C1)}$$

where $\rho_{\psi\psi'}=\langle\psi|\hat{\rho}|\psi'\rangle$ and $|\psi\rangle,|\psi'\rangle\in\{|0\rangle,|\ell\sigma\rangle=\hat{d}^\dagger_{\ell\sigma}|0\rangle,|S\rangle=\frac{1}{\sqrt{2}}\left(\hat{d}^\dagger_{L\downarrow}\hat{d}^\dagger_{R\uparrow}-\hat{d}^\dagger_{L\uparrow}\hat{d}^\dagger_{R\downarrow}\right)|0\rangle\}$, the Liouvillian reads

$$\mathcal{L}=\begin{pmatrix}
0 & \gamma_L e^{i\chi_L} & \gamma_L e^{i\chi_L} & \gamma_R e^{i\chi_R} & \gamma_R e^{i\chi_R} & 0 & -i\gamma_{\rm CPS} & i\gamma_{\rm CPS} & 0 & 0 & 0 & 0\\
0 & -\gamma_L & 0 & 0 & 0 & \frac{\gamma_R}{2}e^{i\chi_R} & 0 & 0 & -i\gamma_{\rm EC} & i\gamma_{\rm EC} & 0 & 0\\
0 & 0 & -\gamma_L & 0 & 0 & \frac{\gamma_R}{2}e^{i\chi_R} & 0 & 0 & 0 & 0 & -i\gamma_{\rm EC} & i\gamma_{\rm EC}\\
0 & 0 & 0 & -\gamma_R & 0 & \frac{\gamma_L}{2}e^{i\chi_L} & 0 & 0 & i\gamma_{\rm EC} & -i\gamma_{\rm EC} & 0 & 0\\
0 & 0 & 0 & 0 & -\gamma_R & \frac{\gamma_L}{2}e^{i\chi_L} & 0 & 0 & 0 & 0 & i\gamma_{\rm EC} & -i\gamma_{\rm EC}\\
0 & 0 & 0 & 0 & 0 & -(\gamma_L+\gamma_R) & i\gamma_{\rm CPS} & -i\gamma_{\rm CPS} & 0 & 0 & 0 & 0\\
-i\gamma_{\rm CPS} & 0 & 0 & 0 & 0 & i\gamma_{\rm CPS} & i\varepsilon-\frac{\gamma_L+\gamma_R}{2} & 0 & 0 & 0 & 0 & 0\\
i\gamma_{\rm CPS} & 0 & 0 & 0 & 0 & -i\gamma_{\rm CPS} & 0 & -i\varepsilon-\frac{\gamma_L+\gamma_R}{2} & 0 & 0 & 0 & 0\\
0 & -i\gamma_{\rm EC} & 0 & i\gamma_{\rm EC} & 0 & 0 & 0 & 0 & -i\delta-\frac{\gamma_L+\gamma_R}{2} & 0 & 0 & 0\\
0 & i\gamma_{\rm EC} & 0 & -i\gamma_{\rm EC} & 0 & 0 & 0 & 0 & 0 & i\delta-\frac{\gamma_L+\gamma_R}{2} & 0 & 0\\
0 & 0 & -i\gamma_{\rm EC} & 0 & i\gamma_{\rm EC} & 0 & 0 & 0 & 0 & 0 & -i\delta-\frac{\gamma_L+\gamma_R}{2} & 0\\
0 & 0 & i\gamma_{\rm EC} & 0 & -i\gamma_{\rm EC} & 0 & 0 & 0 & 0 & 0 & 0 & i\delta-\frac{\gamma_L+\gamma_R}{2}
\end{pmatrix}, \quad \text{(C2)}$$

where we have introduced the counting fields χ_L and χ_R that couple to transitions into the left and right leads.

Appendix D: Power-power correlations

To evaluate the cumulants of the full counting statistics, we need to find the derivatives of the eigenvalue $\lambda_0(\boldsymbol{\chi})$ of $\mathcal{L}(\boldsymbol{\chi})$ with the largest real part. For $\boldsymbol{\chi}=\mathbf{0}$, this is the zero-eigenvalue, $\lambda_0(\mathbf{0})=0$, corresponding to the stationary state $\hat{\rho}_S$, defined as the normalized solution to $\mathcal{L}\hat{\rho}_S=0$, which constitutes our unperturbed problem.

We now follow Refs. 48–50 and calculate $\lambda_0(\boldsymbol{\chi})$ perturbatively in the counting fields, $\boldsymbol{\chi}=(\chi_L,\chi_R)$. Our starting point is the perturbed eigenvalue problem

$$\mathcal{L}(\boldsymbol{\chi})\hat{\rho}_S(\boldsymbol{\chi})=[\mathcal{L}+\mathcal{L}'(\boldsymbol{\chi})]\hat{\rho}_S(\boldsymbol{\chi})=\lambda_0(\boldsymbol{\chi})\hat{\rho}_S(\boldsymbol{\chi}), \quad \text{(D1)}$$

where $\mathcal{L}'(\boldsymbol{\chi})$ is the perturbation due to the counting fields. Following the steps of Refs. 48–50, we find

$$\lambda_0(\boldsymbol{\chi})=\mathrm{Tr}\left\{\mathcal{L}'(\boldsymbol{\chi})\hat{\rho}_S(\boldsymbol{\chi})\right\}, \quad \text{(D2)}$$

and

$$\hat{\rho}_S(\boldsymbol{\chi})=\hat{\rho}_S+\mathcal{R}[\lambda_0(\boldsymbol{\chi})-\mathcal{L}'(\boldsymbol{\chi})]\hat{\rho}_S(\boldsymbol{\chi}), \quad \text{(D3)}$$

where $\mathcal{R}=\mathcal{R}(0)$ is the pseudo-inverse in Eq. (24) evaluated at $\omega=0$. Next, we expand all quantities as

$$\begin{aligned}
\lambda_0(\boldsymbol{\chi})&=\sum_{n,m=0}^{\infty}\frac{(i\chi_L)^n}{n!}\frac{(i\chi_R)^m}{m!}\langle\!\langle I_L^n I_R^m\rangle\!\rangle,\\
\hat{\rho}_S(\boldsymbol{\chi})&=\sum_{n,m=0}^{\infty}\frac{(i\chi_L)^n}{n!}\frac{(i\chi_R)^m}{m!}\hat{\rho}_S^{(n,m)},\\
\mathcal{L}'(\boldsymbol{\chi})&=\sum_{n,m=0}^{\infty}\frac{(i\chi_L)^n}{n!}\frac{(i\chi_R)^m}{m!}\mathcal{L}^{(n,m)},
\end{aligned} \quad \text{(D4)}$$

recalling that the cumulants of the currents are given by the derivatives of the largest eigenvalue. We also note that $\mathcal{L}^{(0,0)}=\mathcal{L}'(\mathbf{0})=0$ by definition.

Inserting these expansions into Eqs. (D2) and (D3) and collecting terms to same order in the counting fields, we obtain the recursive formulas[49,50]

$$\langle\!\langle I_L^n I_R^m\rangle\!\rangle=\sum_{i,j=0}^{n,m}\binom{n}{i}\binom{m}{j}\mathrm{Tr}\left\{\mathcal{L}^{(i,j)}\hat{\rho}_S^{(n-i,m-j)}\right\}, \quad \text{(D5)}$$

and

$$\hat{\rho}_S^{(n,m)}=\mathcal{R}\sum_{i,j=0}^{n,m}\binom{n}{i}\binom{m}{j}\left[\langle\!\langle I_L^i I_R^j\rangle\!\rangle-\mathcal{L}^{(i,j)}\right]\hat{\rho}_S^{(n-i,m-j)}. \quad \text{(D6)}$$

From these expressions, we can in principle calculate any cumulant of the currents. For the Cooper pair splitter, the calculations are simplified by the fact that $\mathcal{L}^{(n,m)}=0$, if both $n>0$ and $m>0$. As an illustration of the recursive scheme, we find for some of the corrections to the eigenstate the following expressions

$$\begin{aligned}
\hat{\rho}_S^{(0,1)}&=-\mathcal{R}\mathcal{J}_R\hat{\rho}_S,\\
\hat{\rho}_S^{(0,2)}&=-\mathcal{R}\left[2\mathcal{I}_R\mathcal{R}+1\right]\mathcal{J}_R\hat{\rho}_S,\\
\hat{\rho}_S^{(1,1)}&=-\mathcal{R}\left[\mathcal{I}_R\mathcal{R}\mathcal{J}_L+\mathcal{I}_L\mathcal{R}\mathcal{J}_R\right]\hat{\rho}_S,\\
\hat{\rho}_S^{(1,2)}&=-\mathcal{R}\big[2\mathcal{I}_R\mathcal{R}\left[\mathcal{I}_R\mathcal{R}\mathcal{J}_L+\mathcal{I}_L\mathcal{R}\mathcal{J}_R\right]+\mathcal{S}_R\mathcal{R}\mathcal{J}_L\\
&\quad+\mathcal{I}_L\mathcal{R}\left[2\mathcal{I}_R\mathcal{R}+1\right]\mathcal{J}_R+2\langle\!\langle I_L I_R\rangle\!\rangle\mathcal{R}\mathcal{J}_R\big]\hat{\rho}_S,
\end{aligned} \quad \text{(D7)}$$

where $\mathcal{I}_\ell=\langle I_\ell\rangle-\mathcal{J}_\ell$ and $\mathcal{S}_\ell=\langle\!\langle I_\ell^2\rangle\!\rangle-\mathcal{J}_\ell$ is given in terms of the noise, $\langle\!\langle I_\ell^2\rangle\!\rangle=\mathrm{Tr}\big[\mathcal{J}_\ell\hat{\rho}_S\big]-2\mathrm{Tr}\big[\mathcal{J}_\ell\mathcal{R}\mathcal{J}_\ell\hat{\rho}_S\big]=S_{\ell\ell}(0)$. Based on these expressions and Eq. (D5), we obtain Eqs. (31) and (32) for the power-power correlations.

[1] G. B. Lesovik, T. Martin, and G. Blatter, "Electronic entanglement in the vicinity of a superconductor," Eur. Phys. J. B **24**, 287 (2001).

[2] P. Recher, E. V. Sukhorukov, and D. Loss, "Andreev tunneling, Coulomb blockade, and resonant transport of nonlocal spin-entangled electrons," Phys. Rev. B **63**, 165314 (2001).

[3] S. Kawabata, "Test of Bell's Inequality using the Spin Filter Effect in Ferromagnetic Semiconductor Microstructures," J. Phys. Soc. Jap. **70**, 1210 (2001).

[4] N. M. Chtchelkatchev, G. Blatter, G. B. Lesovik, and T. Martin, "Bell inequalities and entanglement in solid-state devices," Phys. Rev. B **66**, 161320 (2002).

[5] O. Sauret, T. Martin, and D. Feinberg, "Spin-current noise and Bell inequalities in a realistic superconductor-quantum dot entangler," Phys. Rev. B **72**, 024544 (2005).

[6] O. Malkoc, C. Bergenfeldt, and P. Samuelsson, "Full counting statistics of generic spin entangler with quantum dot-ferromagnet detectors," EPL **105**, 47013 (2014).

[7] H. Soller, "Generic model for Cooper pair splitting," Int. J. Mod. Phys. B **28**, 1450137 (2014).

[8] F. Brange, O. Malkoc, and P. Samuelsson, "Minimal Entanglement Witness from Electrical Current Correlations," Phys. Rev. Lett. **118**, 036804 (2017).

[9] D. Beckmann, H. B. Weber, and H. v. Löhneysen, "Evidence for Crossed Andreev Reflection in Superconductor-Ferromagnet Hybrid Structures," Phys. Rev. Lett. **93**, 197003 (2004).

[10] S. Russo, M. Kroug, T. M. Klapwijk, and A. F. Morpurgo, "Experimental Observation of Bias-Dependent Nonlocal Andreev Reflection," Phys. Rev. Lett. **95**, 027002 (2005).

[11] R. S. Deacon, A. Oiwa, J. Sailer, S. Baba, Y. Kanai, K. Shibata, K. Hirakawa, and S. Tarucha, "Cooper pair splitting in parallel quantum dot Josephson junctions," Nature Commun. **6**, 7446 (2015).

[12] L. E. Bruhat, T. Cubaynes, J. J. Viennot, M. C. Dartiailh, M. M. Desjardins, A. Cottet, and T. Kontos, "Circuit QED with a quantum-dot charge qubit dressed by Cooper pairs," Phys. Rev. B **98**, 155313 (2018).

[13] A. Das, R. Ronen, M. Heiblum, D. Mahalu, A. V. Kretinin, and H. Shtrikman, "High-efficiency Cooper pair splitting demonstrated by two-particle conductance resonance and positive noise cross-correlation," Nature Commun. **3**, 1165 (2012).

[14] L. Hofstetter, S. Csonka, J. Nygård, and C. Schönenberger, "Cooper pair splitter realized in a two-quantum-dot Y-junction," Nature **461**, 960 (2009).

[15] L. Hofstetter, S. Csonka, A. Baumgartner, G. Fülöp, S. d'Hollosy, J. Nygård, and C. Schönenberger, "Finite-Bias Cooper Pair Splitting," Phys. Rev. Lett. **107**, 136801 (2011).

[16] G. Fülöp, F. Domínguez, S. d'Hollosy, A. Baumgartner, P. Makk, M. H. Madsen, V. A. Guzenko, J. Nygård, C. Schönenberger, A. Levy Yeyati, and S. Csonka, "Magnetic Field Tuning and Quantum Interference in a Cooper Pair Splitter," Phys. Rev. Lett. **115**, 227003 (2015).

[17] K. Ueda, S. Matsuo, H. Kamata, S. Baba, Y. Sato, Y. Takeshige, K. Li, S. Jeppesen, L. Samuelson, H. Xu, and S. Tarucha, "Dominant nonlocal superconducting proximity effect due to electron-electron interaction in a ballistic double nanowire," Science Adv. **5**, eaaw2194 (2019).

[18] L. G. Herrmann, F. Portier, P. Roche, A. Levy Yeyati, T. Kontos, and C. Strunk, "Carbon Nanotubes as Cooper-Pair Beam Splitters," Phys. Rev. Lett. **104**, 026801 (2010).

[19] L. G. Herrmann, P. Burset, W. J. Herrera, F. Portier, P. Roche, C. Strunk, A. Levy Yeyati, and T. Kontos, "Spectroscopy of non-local superconducting correlations in a double quantum dot," arXiv:1205.1972.

[20] J. Schindele, A. Baumgartner, and C. Schönenberger, "Near-Unity Cooper Pair Splitting Efficiency," Phys. Rev. Lett. **109**, 157002 (2012).

[21] G. Fülöp, S. d'Hollosy, A. Baumgartner, P. Makk, V. A. Guzenko, M. H. Madsen, J. Nygård, C. Schönenberger, and S. Csonka, "Local electrical tuning of the nonlocal signals in a Cooper pair splitter," Phys. Rev. B **90**, 235412 (2014).

[22] J. Schindele, A. Baumgartner, R. Maurand, M. Weiss, and C. Schönenberger, "Nonlocal spectroscopy of Andreev bound states," Phys. Rev. B **89**, 045422 (2014).

[23] Z. B. Tan, D. Cox, T. Nieminen, P. Lahteenmaki, D. Golubev, G. B. Lesovik, and P. J. Hakonen, "Cooper Pair Splitting by Means of Graphene Quantum Dots," Phys. Rev. Lett. **114**, 096602 (2015).

[24] I. V. Borzenets, Y. Shimazaki, G. F. Jones, M. F. Craciun, S. Russo, M. Yamamoto, and S. Tarucha, "High Efficiency CVD Graphene-lead (Pb) Cooper Pair Splitter," Sci. Rep. **6**, 23051 (2016).

[25] P. Burset, W. J. Herrera, and A. L. Yeyati, "Microscopic theory of Cooper pair beam splitters based on carbon nanotubes," Phys. Rev. B **84**, 115448 (2011).

[26] B. Braunecker, P. Burset, and A. Levy Yeyati, "Entanglement Detection from Conductance Measurements in Carbon Nanotube Cooper Pair Splitters," Phys. Rev. Lett. **111**, 136806 (2013).

[27] I. A. Sadovskyy, G. B. Lesovik, and V. M. Vinokur, "Unitary limit in crossed Andreev transport," New J. Phys. **17**, 103016 (2015).

[28] R. Mélin, C. Benjamin, and T. Martin, "Positive cross correlations of noise in superconducting hybrid structures: Roles of interfaces and interactions," Phys. Rev. B **77**, 094512 (2008).

[29] D. Chevallier, J. Rech, T. Jonckheere, and T. Martin, "Current and noise correlations in a double-dot Cooper-pair beam splitter," Phys. Rev. B **83**, 125421 (2011).

[30] J. Rech, D. Chevallier, T. Jonckheere, and T. Martin, "Current correlations in an interacting Cooper-pair beam splitter," Phys. Rev. B **85**, 035419 (2012).

[31] P. Burset, B. Lu, H. Ebisu, Y. Asano, and Y. Tanaka, "All-electrical generation and control of odd-frequency s-wave Cooper pairs in double quantum dots," Phys. Rev. B **93**, 201402 (2016).

[32] J. A. Celis Gil, P. S. Gomez, and W. J. Herrera, "Noise cross-correlation and Cooper pair splitting efficiency in multi-teminal superconductor junctions," Solid State Commun. **258**, 25 (2017).

[33] O. Sauret, D. Feinberg, and T. Martin, "Quantum master equations for the superconductor-quantum dot entangler," Phys. Rev. B **70**, 245313 (2004).

[34] J. Eldridge, M. G. Pala, M. Governale, and J. König, "Superconducting proximity effect in interacting double-dot systems," Phys. Rev. B **82**, 184507 (2010).

[35] E. Amitai, R. P. Tiwari, S. Walter, T. L. Schmidt, and S. E. Nigg, "Nonlocal quantum state engineering with the Cooper pair splitter beyond the Coulomb blockade regime," Phys. Rev. B **93**, 075421 (2016).

[36] R. Hussein, A. Braggio, and M. Governale, "Entanglement-symmetry control in a quantum-dot Cooper-pair splitter," Phys. Status Solidi B **254**, 1600603 (2017).

[37] SK F. Islam and A. Saha, "Amplification of Cooper pair splitting current in a graphene-based Cooper pair beam splitter geometry," Phys. Rev. B **96**, 125406 (2017).

[38] R. Sánchez, P. Burset, and A. Levy Yeyati, "Cooling by Cooper pair splitting," Phys. Rev. B **98**, 241414 (2018).

[39] B. Hiltscher, M. Governale, J. Splettstoesser, and J. König, "Adiabatic pumping in a double-dot Cooper-pair beam splitter," Phys. Rev. B **84**, 155403 (2011).

[40] B. Sothmann, S. Weiss, M. Governale, and J. König, "Unconventional superconductivity in double quantum dots," Phys. Rev. B **90**, 220501 (2014).

[41] P. Trocha and I. Weymann, "Spin-resolved Andreev transport through double-quantum-dot Cooper pair splitters," Phys. Rev. B **91**, 235424 (2015).

[42] K. Wrzeniewski, P. Trocha, and I. Weymann, "Current cross-correlations in double quantum dot based Cooper pair splitters with ferromagnetic leads," J. Phys. Conden. Mat. **29**, 195302 (2017).

[43] P. Trocha and K. Wrzeniewski, "Cross-correlations in a quantum dot Cooper pair splitter with ferromagnetic leads," J. Phys. Conden. Mat. **30**, 305303 (2018).

[44] D. A. Bagrets and Yu. V. Nazarov, "Full counting statistics of charge transfer in Coulomb blockade systems," Phys. Rev. B **67**, 085316 (2003).

[45] J. Börlin, W. Belzig, and C. Bruder, "Full Counting Statistics of a Superconducting Beam Splitter," Phys. Rev. Lett. **88**, 197001 (2002).

[46] A. Braggio, M. Governale, M. G. Pala, and J. König, "Superconducting proximity effect in interacting quantum dots revealed by shot noise," Solid State Commun. **151**, 155 (2011).

[47] C. Flindt, T. Novotný, and A.-P. Jauho, "Current noise in a vibrating quantum dot array," Phys. Rev. B **70**, 205334 (2004).

[48] C. Flindt, T. Novotný, and A.-P. Jauho, "Full counting statistics of nano-electromechanical systems," EPL **69**, 475 (2005).

[49] C. Flindt, T. Novotný, A. Braggio, M. Sassetti, and A.-P. Jauho, "Counting Statistics of Non-Markovian Quantum Stochastic Processes," Phys. Rev. Lett. **100**, 150601 (2008).

[50] C. Flindt, T. Novotný, A. Braggio, and A.-P. Jauho, "Counting statistics of transport through Coulomb blockade nanostructures: High-order cumulants and non-Markovian effects," Phys. Rev. B **82**, 155407 (2010).

[51] N. Walldorf, C. Padurariu, A.-P. Jauho, and C. Flindt, "Electron Waiting Times of a Cooper Pair Splitter," Phys. Rev. Lett. **120**, 087701 (2018).

[52] S. K. Gorman, Y. He, M. G. House, J. G. Keizer, D. Keith, L. Fricke, S. J. Hile, M. A. Broome, and M. Y. Simmons, "Tunneling Statistics for Analysis of Spin-Readout Fidelity," Phys. Rev. Applied **8**, 034019 (2017).

[53] M. Jenei, E. Potanina, R. Zhao, K. Y. Tan, A Rossi, T. Tanttu, K. W. Chan, V. Sevriuk, M. Möttönen, and A. Dzurak, "Waiting time distributions in a two-level fluctuator coupled to a superconducting charge detector," Phys. Rev. Research **1**, 033163 (2019).

[54] S. Matsuo, K. Kuroyama, S. Yabunaka, S. R. Valentin, A. Ludwig, A. D. Wieck, and S Tarucha, "Full Counting Statistics of Spin-Flip/Conserving Charge Transitions in Pauli-Spin Blockade," arXiv:1909.12027.

[55] C. Flindt, T. Novotný, and A.-P. Jauho, "Current noise spectrum of a quantum shuttle," Physica E **29**, 411 (2005).

[56] N. Lambert, R. Aguado, and T. Brandes, "Nonequilibrium entanglement and noise in coupled qubits," Phys. Rev. B **75**, 045340 (2007).

[57] C. Emary, D. Marcos, R. Aguado, and T. Brandes, "Frequency-dependent counting statistics in interacting nanoscale conductors," Phys. Rev. B **76**, 161404 (2007).

[58] D. Marcos, C. Emary, T. Brandes, and R. Aguado, "Finite-frequency counting statistics of electron transport: Markovian theory," New J. Phys. **12**, 123009 (2010).

[59] N. Ubbelohde, C. Fricke, C. Flindt, F. Hohls, and R. J. Haug, "Measurement of finite-frequency current statistics in a single-electron transistor," Nature Commun. **3**, 612 (2012).

[60] C. Emary, C. Pöltl, A. Carmele, J. Kabuss, A. Knorr, and T. Brandes, "Bunching and antibunching in electronic transport," Phys. Rev. B **85**, 165417 (2012).

[61] F. Brange, P. Menczel, and C. Flindt, "Photon counting statistics of a microwave cavity," Phys. Rev. B **99**, 085418 (2019).

[62] H.-P. Breuer and F. Petruccione, *The theory of open quantum systems* (Oxford University Press, 2003).

[63] M. B. Plenio and P. L. Knight, "The quantum-jump approach to dissipative dynamics in quantum optics," Rev. Mod. Phys. **70**, 101 (1998).

[64] Yu. Makhlin, G. Schön, and A. Shnirman, "Quantum-state engineering with Josephson-junction devices," Rev. Mod. Phys. **73**, 357 (2001).

[65] T. Brandes, "Waiting times and noise in single particle transport," Ann. Physik **17**, 477 (2008).

[66] K. H. Thomas and C. Flindt, "Electron waiting times in non-Markovian quantum transport," Phys. Rev. B **87**, 121405 (2013).

[67] Ya. M. Blanter and M. Bttiker, "Shot noise in mesoscopic conductors," Phys. Rep. **336**, 1 (2000).

[68] D. K. C. MacDonald, *Noise and Fluctuations: An Introduction* (Wiley, New York, 1962).

[69] K. Wrzeniewski and I. Weymann, "Current cross-correlations and waiting time distributions in Andreev transport through Cooper pair splitters based on triple quantum dots," Phys. Rev. B **101**, 155409 (2020).

[70] C. Emary, *Theory of Nanostructures* (lecture notes, TU-Berlin, 2009).

[71] S. A. Gurvitz and Ya. S. Prager, "Microscopic derivation of rate equations for quantum transport," Phys. Rev. B **53**, 15932 (1996).

[72] S. A. Gurvitz, "Rate equations for quantum transport in multidot systems," Phys. Rev. B **57**, 6602 (1998).

[73] S. Gurvitz, "Wave-function approach to master equations for quantum transport and measurement," Front. Phys. **12**, 120303 (2016).

Technical
University of
Denmark

Fysikvej, 2800 Kongens Lyngby
Denmark
www.fysik.dtu.dk